Mehmet ÖZDEMİR

DESIGN, SYNTHESIS, AND CHARACTERIZATION OF FUNCTIONAL ORGANIC MATERIALS FOR OPTOELECTRONIC APPLICATIONS

AGU 2018

DESIGN, SYNTHESIS, AND CHARACTERIZATION OF FUNCTIONAL ORGANIC MATERIALS FOR OPTOELECTRONIC APPLICATIONS

A Ph.D. Thesis

By

Mehmet ÖZDEMİR

December 2018

ABDULLAH GÜL UNIVERSITY

DESIGN, SYNTHESIS, AND CHARACTERIZATION OF FUNCTIONAL ORGANIC MATERIALS FOR OPTOELECTRONIC APPLICATIONS

A THESIS
SUBMITTED TO THE DEPARTMENT OF MATERIALS SCIENCE AND MECHANICAL ENGINEERING OF ABDULLAH GÜL UNIVERSITY
IN PARTIAL FULFILLMENT OF THE REQUIREMENTS
FOR THE DEGREE OF
DOCTOR OF PHILOSOPHY

By
Mehmet ÖZDEMİR
December 2018

SCIENTIFIC ETHICS COMPLIANCE

I hereby declare that all information in this document has been obtained in accordance with academic rules and ethical conduct. I also declare that, as required by these rules and conduct, I have fully cited and referenced all materials and results that are not original to this work.

Mehmet ÖZDEMİR

REGULATORY COMPLIANCE

Ph.D. thesis titled “DESIGN, SYNTHESIS, AND CHARACTERIZATION OF FUNCTIONAL ORGANIC MATERIALS FOR OPTOELECTRONIC APPLICATIONS” has been prepared in accordance with the Thesis Writing Guidelines of the Abdullah Gül University, Graduate School of Engineering and Science.

Prepared By

Mehmet ÖZDEMİR

Advisor

Assoc. Prof. Hakan USTA

Head of the Materials Science and Mechanical Engineering Program

Prof. Murat DURANDURDU

ACCEPTANCE AND APPROVAL

Ph.D. thesis titled "Design, Synthesis, And Characterization Of Functional Organic Materials For Optoelectronic Applications" was prepared by Mehmet ÖZDEMİR, which has been accepted by the jury in the Materials Science and Mechanical Engineering Graduate Program at Abdullah Gül University, Graduate School of Engineering and Science.

26/12/2018

JURY:

Advisor: Assoc. Prof. Hakan USTA

Member: Prof. Murat DURANDURDU

Member: Prof. Ertuğrul ŞAHMETLİOĞLU

Member: Assoc. Prof. Evren MUTLUGÜN

Member: Assoc. Prof. M. Serdar ÖNSES

APPROVAL:

The acceptance of this Ph.D. thesis has been approved by the decision of the Abdullah Gül University, Graduate School of Engineering and Science, Executive Board dated ….. /….. / …….. and numbered ……..……. .

Graduate School Dean
Prof. İrfan ALAN

ABSTRACT

DESIGN, SYNTHESIS, AND CHARACTERIZATION OF FUNCTIONAL ORGANIC MATERIALS FOR OPTOELECTRONIC APPLICATIONS

Mehmet ÖZDEMİR

Ph.D. in Materials Science and Mechanical Engineering

Supervisor: Assoc. Prof. Hakan USTA

December 2018

The development of π-conjugated semiconducting small molecules and polymers as functional organic materials is an emerging and continuously growing research area in (opto)electronics. Semiconducting small molecules and polymers are envisioned as key components of high-performance organic thin-film transistors (OTFTs) and photovoltaics (OPVs) for next-generation (opto)electronic technologies such as plastic logic circuits, flexible displays, rollable solar panels, and electronic skins. The main motivations in continuously designing and synthesizing new π-frameworks in the past few decades do not only include improving charge-transport and device characteristics and realizing novel functions, but also better understanding and addressing molecular structure-(opto)electronic property-electrical performance relationships. This thesis studies and explores the rational design, synthesis, and characterization of novel π-conjugated semiconductors with varied chemical structures for OTFT and OPV applications.

In the first chapter, the general concepts and fundamentals of π-conjugated semiconducting materials and organic electronic devices are discussed along with a deep literature review focusing on most up-to-date results in the field. OTFTs are classified and described based on the major charge carrier type as *n*-channel, *p*-channel, and ambipolar devices, which is closely related to the semiconductor's π-structure. The mechanism of OPVs' working principle is also reviewed describing the electronic/structural effects of semiconductor π-structure on these devices.

The second chapter deals with the design, synthesis, and characterization of a series of new indeno[1,2-b]fluorene-6,12-dione-thiophene small molecules, **DD-TIFDKT**, **2EH-TIFDKT**, and **2OD-TIFDKT** that consist of highly π-conjugated donor–acceptor molecular architectures based on indeno[1,2-b]fluorene-6,12-dione

acceptor unit and thiophene donor units. The semiconductor structures have low band gaps of 1.7–1.8 eV, and they are α,ω-end-functionalized with linear –n-$C_{12}H_{25}$ chains or swallow-tail 2-ethylhexyl-/2-octyldodecyl chains. The detailed study on the effects of alkyl chain size and orientation on the optoelectronic properties, intermolecular cohesive forces, thin-film microstructures, and charge transport performances of the new semiconductors, which revealed crucial structure–property–function relationships. The solution-processed OTFT devices of the current semiconductors, **2EH-TIFDKT** and **2OD-TIFDKT**, exhibit excellent ambipolar behavior with carrier mobilities of 0.04–0.12 $cm^2/V \cdot s$ and 0.0003–0.02 $cm^2/V \cdot s$ for electrons and holes, respectively, and I_{on}/I_{off} ratios of 10^5 to 10^6, which indicates two–three orders of carrier mobility enhancement compared to those of solution-processed β-substituted counterparts. In the rational design of the new molecules, the repositioning of the insulating β-substituents to molecular termini is found to significantly enhance the π-core planarity while maintaining a good solubility, which improved the charge-transport characteristics.

In the third chapter, three novel solution-processable BODIPY-based semiconducting materials (**BDY-3T-BDY, BDY-4T-BDY**, and **BDY-PhAc-BDY**) were synthesized. All these materials displayed *n*-channel OTFT device operation. **BDY-4T-BDY** based bottom-gate/top-contact devices exhibited extremely high I_{on}/I_{off} ratios of $>10^8$ and electron mobilities of up to 0.01 $cm^2/V \cdot s$. Up to now, this result is one of the best charge-carrier mobilities among the known BODIPY based materials in the literature. **BDY-3T-BDY** showed electron mobilities of 2.7×10^{-4} $cm^2/V \cdot s$ and I_{on}/I_{off} ratio of 9.6×10^5 . **BDY- PhAc –BDY** displayed electron mobilities of 0.004 $cm^2/V \cdot s$ and I_{on}/I_{off} ratio of 10^5-10^6. The chemical structures, optical/electrochemical properties, and thin-film microstructures for these semiconductors were fully characterized by $^1H/^{13}C$ NMR, mass spectrometry, cyclic voltammetry, UV-Vis absorption spectroscopy, thermogravimetric, atomic force microscope (AFM) and X-ray diffraction (XRD) analysis.

In the fourth chapter, boron containing polymers **P(2OD-TBDY-T)** and **P(2OD-TBDY-TT)** were synthesized and their optoelectronic properties in OTFT and OPV devices were investigated. **P(2OD-TBDY-T)** based bottom-gate/top-contact OTFT devices exhibited I_{on}/I_{off} ratios of $>10^8$ and hole mobilities of 0.005 $cm^2/V \cdot s$. Inverted BHJ-OPVs employing **(P(2OD-TBDY-T):PC_{71}BM** active layer exhibited excellent power conversion efficiencies (PCE) of 6.2% with a short-circuit current of 16.6 mA/cm^2. These results showed that rationally designed BODIPY based donor copolymers could be used in high-performance OPVs.

The findings presented in this thesis suggest that through computational modeling guided rational design and synthetic tailoring, physicochemical/optoelectronic properties and electron/hole transport characteristics of molecular and polymeric semiconductors can be significantly improved realizing new functions. We believe that our results will provide key structural/electronic information and additional motivation in the field to investigate and optimize structurally varied semiconductors for high-performance organic (opto)electronic applications.

Keywords: Organic Semiconductors, Solution-Processable Molecules and Polymers, Organic Thin-Film Transistors (OTFTs), Organic Photovoltaics (OPVs)

ÖZET

OPTOELEKTRONİK UYGULAMALAR İÇİN FONKSİYONEL ORGANİK MAZLEMELERİN DİZAYNI, SENTEZİ VE KARAKTERİZASYONU

Mehmet ÖZDEMİR
Malzeme Bilimi ve Makine Mühendisliği Doktora Programı
Tez Yöneticisi: Doç. Dr. Hakan USTA

Aralık 2018

π-konjuge yarıiletken küçük molekül ve polimerlerin fonksiyonel organik malzemeler olarak geliştirilmesi optoelektronikte ortaya çıkan ve aralıksız büyümeye devam eden bir araştırma alanıdır. Gelecek nesil optoelektronik teknolojisinde mantık devreleri, esnek ekranlar, bükülebilir güneş panellerinde ve elektronik derilerde, yarı iletken küçük moleküller ve polimerler, yüksek performanslı organik ince-film transistörler (OTFT) ve fotovoltaiklerin (OPV) ana öğesi olarak öngörülmektedir. Ana motivasyon, son birkaç on yıldır devam eden yeni π-sistemlerin tasarlanıp sentezlenmesi sadece yük-taşımayı iyileştirmek, cihaz karakteristiği ve yeni fonksiyonelleri keşfetmeyi içermez aynı zamanda belirlenen molekülün optoelektronik özelliği ve elektrik performansı arasındaki ilişkiyi daha iyi anlamaktır. Bu tezde, OTFT ve OPV uygulamalar için, yeni π-konjuge yarıiletkenlerin teorik tasarım, sentez ve karakterizasyonuyla birlikte farklı kimyasal yapıları çalışılmış ve araştırılmıştır.

Birinci bölümde π-konjuge yarıiletken malzemeler ve organik elektronik aygıtların genel konsepti ve temel kavramlar üzerinde durulmuş ve kapsamlı bir literatür taramasıyla bu alandaki en güncel sonuçlara erişilmiştir. OTFT'lerin sınıflandırılması yarıiletken malzemenin π yapısına bağlı olarak belirlenen n-kanal, p-kanal ve çift kanallı olmak üzere ana yük taşıyıcı tipine göre yapılmaktadır. Ayrıca, OPV'lerin çalışma mekanizması kullanılan yarıiletkenin π yapısının elektronik/yapısal özelliklere etkisi üzerinden incelenmiştir.

İkinci bölümde yeni indeno[1,2-b]fluorene-6,12-dione-thiophene temelli yüksek π-konjuge donor-akseptör moleküler mimariye sahip **DD-TIFDKT**, **2EH-TIFDKT** ve

2OD-TIFDKT küçük molekülleri tasarlanmış, sentezlenmiş ve karakterize edilmiştir. Indeno[1,2-b]fluorene-6,12-dione akseptör olarak tiyofen de donor olarak kullanılmıştır. Yarı iletken yapıları lineer –n-$C_{12}H_{25}$ veya 2-ethylhexyl-/2-octyldodecyl dallanmış α,ω-son fonksiyonel gruplu alkil zincirlerine sahip olup 1.7–1.8 eV düzeyinde düşük enerji bant aralığına sahiptir. Yeni yarıiletkenlerin alkil zincir boyutu ve yöneliminin optoelektronik özellikler, moleküller arası kohezif kuvveti, ince-film yapısı ve yük taşınım performansı üzerindeki etkisinin araştırılması yapı-özellik-fonksiyonellik bağıntısını ortaya koymuştur. **2EH-TIFDKT** ve **2OD-TIFDKT** yarı iletken malzemelerin çözücü ile proses edildiği yarı iletken OTFT cihazlar elektronlar için 0.04–0.12 $cm^2/V{\cdot}s$ ve deşikler için 0.0003–0.02 $cm^2/V{\cdot}s$ taşınım değerleri ve 10^5 - 10^6 düzeyindeki I_{on}/I_{off} oranı ile mükemmel çift yönlü davranış göstermekte; çözücü ile proses edilebilen β-pozisyonundakine oranla taşıyıcı iletkenliğinde 2-3 kat artış sağlamıştır. β-pozisyonundaki değişim önemli biçimde π-yapı düzlemselliğini arttırmışken çözünürlük daha iyi hale gelmiş ve yük taşınım karakteristiği artmıştır.

Üçüncü bölümde, 3 farklı yeni solüsyondan proses edilebilen BODIPY temelli yarıiletken malzemeler (**BDY-3T-BDY, BDY-4T-BDY** ve **BDY-PhAc-BDY**) sentelenmiş. Tüm malzemeler n-karakterli OTFT cihazda çalıştı. BDY-4T-BDY temelli alt kapı/üst kontak cihazda I_{on}/I_{off} $>10^8$ electron hareketliliği ise 0.01 $cm^2/V{\cdot}s$ den yüksek çıkmıştır. Bu sonuç bugüne kadar ki literatürde bilinen BODIPY temelli malzemelerde yüksek yük-taşıma hareketliliği ne sahiptir. **BDY-3T-BDY** ise elektron hareketliliği 2.7×10^{-4} $cm^2/V{\cdot}s$ ve 9.6×10^5 I_{on}/I_{off} oranına sahiptir. **BDY- PhAc –BDY** ise elektron hareketliliği 0.004 $cm^2/V{\cdot}s$ ve $I_{on}/I_{off}10^5$-10^6'dur. Bu moleküllerin kimyasal yapıları, optik/elektrokimyasal özellikleri ve ince-film yapıları $^1H/^{13}C$ NMR, kütle spektrometresi, siklik voltametri, UV-Vis absorbsiyon spektroskopisi, termogravimetrik , atomik kuvvet misroskopisi (AFM) ve X-ray kırılım(XRD) analizi ile karakterize edilmiştir.

Dördüncü bölümde, Boron içeren **P(2OD-TBDY-T)** ve **P(2OD-TBDY-TT)** polimerleri sentezlenmiş ve OTFT ile OPV'de ki optoelektronik özellikleri araştırılmıştır. **P(2OD-TBDY-T)** temelli polimer, alt kapı/üst kontak OTFT cihazda I_{on}/I_{off} oranı $>10^8$ ve deşik hareketliliği 0.005 $cm^2/V{\cdot}s$ sergilemiştir. Ters çevrilmiş BHJ-Güneş pillerinin aktif tabakasında **(P(2OD-TBDY-T):PC_{71}BM** kullanımı ile % 6,2 güneş enerjisi çevirme verimi (PCE) ve 16.6 mA/cm^2 kısa devre akımı ile harika sonuçlar elde edilmiştir. Bu sonuçlar mantıklı tasarımlarla BODIPY temelli donor kopolimerlerin yüksek performanslı OPV'ler için kullanılabileceğini göstermektedir.

Bu tez kapsamında yapılan çalışmaların bulguları matematiksel modelleme ışığında gerçekleştirilen sentez dizaynları ile moleküler ve polimerik yarıiletkenlerin fizyokimyasal/optoelektronik özelliklerinin yanında elektron/deşik taşınım karakteristiklerinin de büyük ölçüde geliştirilerek yeni fonksiyonlar kazandırılabileceğini ortaya koymaktadır. Elde ettiğimiz sonuçların yüksek performanslı optoelektronik uygulamalarında kullanılacak farklı yapılardaki yarıiletken malzemelerin araştırılması ve optimize edilmesi için önemli bilgiler ve motivasyon sağlayacağını düşünmekteyiz.

Anahtar kelimeler: Çözücüde Proses Edilebilen, Ambipolar, N-tipi, Organik Yarı İletken, Organik Güneş Pili

Acknowledgements

At first, I would like to express my deepest appreciation to my advisor, Assoc. Prof. Hakan Usta. His support and encouragement gave me strength and assurance. Prof. Usta's assiduousness, deep knowledge, and enthusiasm for science has had such an intense impact on me and my career. My research would not have been possible without his guidance and efforts.

I would like to thank my jury members, Assoc. Prof. Evren MUTLUGÜN and Assoc. Prof. M. Serdar ÖNSES for their support and suggestions.

All the members of the Usta research group: Hüsniye, İbrahim, Ayşe, Furkan and especially Resul, I will never forget the bozlak music and I promise I'll listen again. Thanks to Hüsniye for all help with device fabrication and your effort about device fabricating.

To my family: thanks to my wife, Özlem for her endless love, infinite patience and supports for every step on my life. And mom thank you your support and your patience.

I would like to acknowledge that this study was supported by Research Fund of Abdullah Gül University (AGU-BAP), Project No: FDK-2017- 97, Turkish Academy of Sciences, The Young Scientists Award Program (TUBA-GEBIP 2015), The Science Academy, Young Scientist Award Program (BAGEP 2014) and The Scientific and Technologial Research Council of Turkey (Tubitak 114M226).

Table of Contents

List of Figures

List of Tables

Chapter 1

Introduction

1.1. The History of Organic Semiconductor Materials

One of the most important inventions in the twentieth century are integrated circuits, which have been used in modern electronic devices including computers, telecommunication equipments, health devices, and many others. An integrated circuit, also named as a microchip, is a small electronic circuit in which all the components (e.g., transistors, capacitors, resistors) are on the same single chip. The main building block of an electronic circuit is thin-film transistor, which is a semiconductor device used to amplify or switch electronic signals and electrical power. Although thin-film transistors were large and discrete in their size in the beginning five decades ago, advances in materials science and nanotechnology have enabled packing billions of them on a few square centimeters of a single chip area.

In 1855, German scientist Heinrich Geissler - who made the first vacuum tubes (Geissler tubes) - also realized that applying an electric field across the vacuum between two electrodes caused a strange glow of colored light in 1857. Vacuum tubes were used as the main component of such bulky devices, and they have different functions such as amplification, rectification, and switching. These bulky devices were used as electronic circuits before thin-film transistors and microchips. [2]

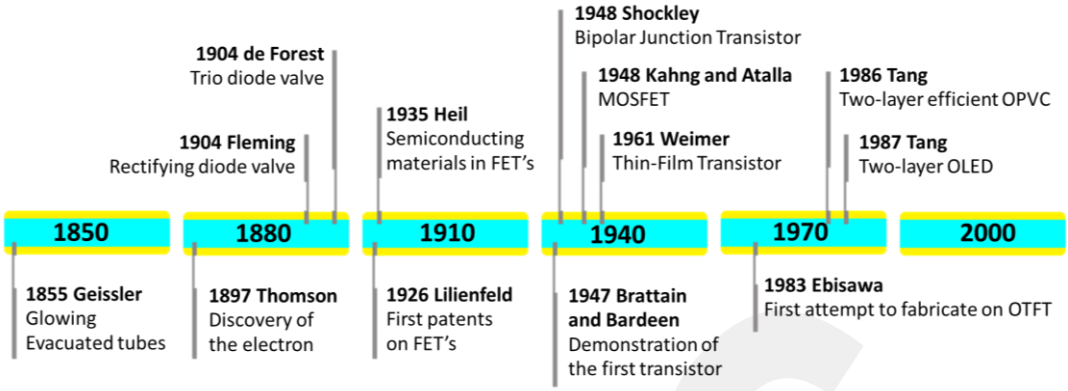

Figure 1.1.1 Historical development of electronic devices from the introduction of vacuum tubes to the first use of organic compounds in transistors, light-emitting diodes, and photovoltaic cells.[3]

The concept of a field-effect transistor (FET) was first demonstrated by Lilienfeld and Heil, which was simply a three-electrode amplifying device relying on the semiconducting properties of copper sulfide (Cu_2O). Later in 1947, John Bardeen, William Shockley, and Walter Brattain invented the world's first transistor. For the history of transistors four most important milestones are, John Bardeen and Walter Brattain, which are American physicists, have used germanium point-contact device, and they have demonstrated the first transistor action in 1947. However, the mechanical configuration of transistors was difficult for high volume manufacture; William Shockley invented the first bipolar junction transistor (BJT). Shockley was leading Bell Labs with Bardeen and Brattain, these three scientists worked on solid-state physics. Their invention was awarded the Nobel Prize Physics in 1956; Egyptian engineer Martin M. Atalla and Korean physicist Dawon Kahng invented the first metal-oxide semiconductor field-effect transistor (MOSFET) in 1959, which had been long projected by Heil and Lilienfelt. Basically, MOSFETs have three layers that are silicon semiconductor for base material, thermally-grown native oxide for insulator, and metallic gate electrode for controlling terminals. After the invention of MOSFETs, the usage of BJTs decreased day by day since silicon offers superior properties including more controllable and stable surface oxide. Until today, MOSFETs have grown as the dominant devices used in electronic industry and integrated circuits. This device is similar to FETs developed by Heil and Lilienfelds. Weimer used a polycrystalline cadmium-sulfite as semiconducting material and glass to insulate the substrate.[2]

Using organic semiconductor-based thin-film circuits are an alternative approach to reach functionality and complexity in future electronic technologies. The processing of organic materials is typically much lower than 200 °C that could enable to use of plastics as a substrate introducing flexible electronics. Also, using solution processable organic materials in the fabrication processes of active materials could significantly reduce the fabrication costs and allow for large-area coverage. The first study on photoconductivity of organic materials was reported by Pochettino and Volmer, which was based on anthracene, which was followed by the demonstration of electroluminescence characteristics of organic compounds by Bernanose in 1955. In that time, organic semiconductors were still very limited in technological applications since their charge-carrier mobilities were low, they require very high voltages (400 V) for operation, and structural versatility was very limited.[4]

Despite all these drawbacks, Hideki Shirakawa's post-doc student serendipitously added excess iodine and synthesized halogen (iodine)-doped polyacetylene in 1977 that showed metallic conductivity. In 2000, Nobel Prize in Chemistry was given to Alan G. MacDiarmid, Alan J. Heeger, Hideki Shirakawa for the discovery of conductive polymers, which is considered a major breakthrough that has led to exciting new era of organic electronics. Ever since the report of the first OTFT, a great deal of interest in this field has been steadily rising. Indeed organic semiconductors allow producing low-cost and flexible circuits through the combination of low-temperature and high-throughput processing/fabrication techniques such as roll-to-roll process and ink-jet printing. To give some examples, the future potential applications embedding OTFTs could include flexible active matrix displays (electrophoretic or OLED) displays (Figure 1.1.2), disposable flexible radio frequency identification (RFID) tags, analog/digital or digital/analog converters, and other analog building blocks opening the way to front-end signal processing in smart disposable sensors (e.g. for medical diagnostics). [3]

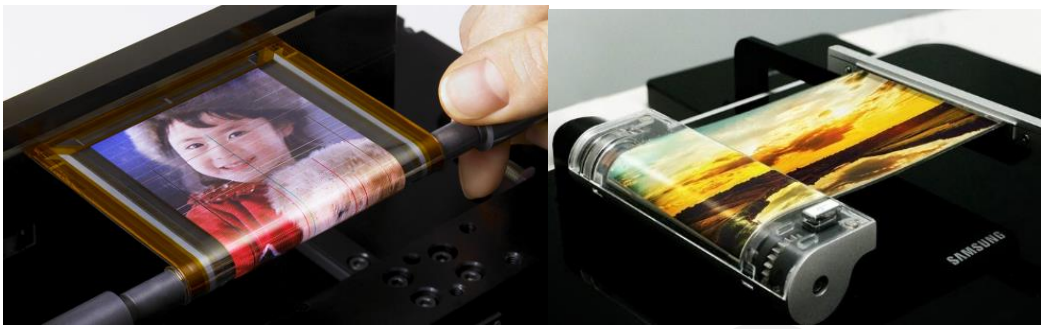

Figure 1.1.2 Rollable OTFT used OLED displays manufactured by Sony and Samsung.

1.2. Organic Electronics Market

Organic molecules have opened a rapidly growing market in the field of optoelectronics and they bring in a new point of view for flexibility and functionality of electronics in everyday life. IDTechEx expects that the total market for printed, flexible and organic electronics will grow from $42.03 billion to $76.79 billion by end of 2024. One of the most attractive organic electronic devices realized to date is organic light-emitting diodes (OLEDs), which have been commercialized in a wide range of applications as lighting devices, touch sensors, and displays for consumer electronics. Organic electronic applications were divided into five different categories in 2017 by Organic and Printed Electronics Association (OE-A7), which are OLED Lighting, Organic Photovoltaic (OPV), flexible and OLED display, electronics and components, and integrated smart systems (Figure 1.2.1). The future research and developments in each of these categories require the design and synthesis of new high performance organic materials which is the main focus of this thesis.

	OLED Lighting	OPV	Flexible & OLED Display	Electronics & Components	Integrated Smart Systems
Short Term 2018-2020	Flexible OLEDs (color); flexible OLEDs (white)	Large area OPV foil; OPV objects; opaque OPV for building integration	EPD wrist band; transparent displays; conformable OLCD; enhanced display integration in werables	Printed mobile communication device based on antennas, light sensor; stretchable conductors/ resistors; 3D touch sensors	Smart labels (discrete); HMIs (embedded electronics & displays)
Medium Term 2021-2023	Transparent OLEDs; flexible red OLED for automotive applications	OPV integrated in building products	Curved displays for automotive interior; integration into clothing; white goods displays	Printed lithium ion battery; printed super caps; active touch & gesture sensors	Human monitoring patches (single parameter, point of care, on-skin); disposable & quantative sensors for food safety; biomedical sensors
Long Term 2024+	3D OLEDs; dynamic OLED signage (segmented); long stripes; OLED in general lighting	OPV in packaging; energy harvesting combined with storage	wallpaper displays; display in everyday objects; foldable displays	Printed complex logic; 3D & large area flexible electronics	Fully printed RFID / NFC label; ambient intelligence (connected); sensors for security (explosives)

Figure 1.2.1 The OE-A Roadmap for organic and printed electronics applications including a forecast for the market entry in large volumes for the different applications.

1.3. Charge Carrier Transport in Organic Semiconductors

1.3.1. Hybridization and Molecular Orbital Theory

The electronic configuration of C is $1s^2$, $2s^2$, $2p^2$, which means the first shell is filled with a pair of electrons, the 2s orbital accommodates two electrons while remaining two electrons occupy the two of three energetically degenerate 2p orbitals according to Hund's rule. The experimental fact that carbon atoms can make four bonds could be simply explained by the valence bond theory using hybridization of atomic orbitals. In carbon, the linear combination of the 2s orbital and the three degenerate 2p orbitals generates four equivalent orbitals named sp^3 hybrid orbitals. There are three different types of hybridization for the linear combination of s and p orbitals: sp, sp^2, and sp^3 hybridizations. Among these, sp and sp^2 hybridizations are the most crucial types for electrical conductivity and photon-molecule interactions to be exploited in organic optoelectronic devices since these types of hybridizations could generate energetically accessible p-orbitals as shown in Figure 1.3.1.1.

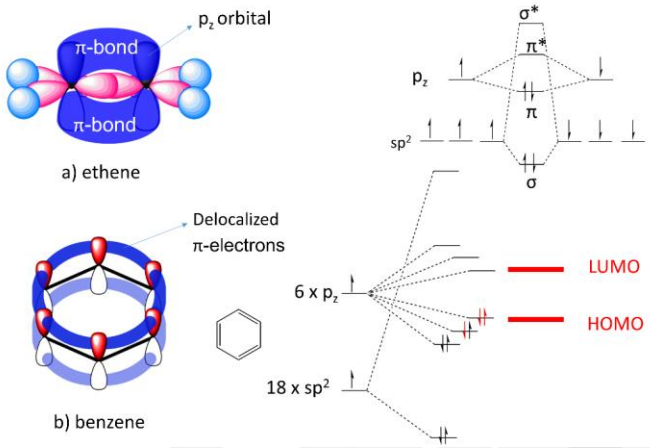

Figure 1.3.1.1 Illustration of the formation of delocalized π orbitals in a) ethene and b) benzene. In each carbon atom contributing to the system, the s and two p orbitals form three sp^2 hybrid orbitals, which align in a plane (xy-plane) with an angle of 120°, corresponding to the preferred bond angle. The remaining p_z orbital is aligned perpendicular to the sp2 plane. The bond between two such atoms is a double bond consisting of a σ bond between sp2 hybrid orbitals and a π bond formed by the overlap of the atomic p_z orbitals. When composing several of these carbon-carbon units, as e. g. shown in benzene, the p_z orbitals of all atoms overlap equally, forming π and π* orbitals which are delocalized over all carbon atoms. The highest occupied molecular orbital (HOMO) and the lowest unoccupied molecular orbital (LUMO) confine the "energy gap", which determines the semiconducting behavior of the material.

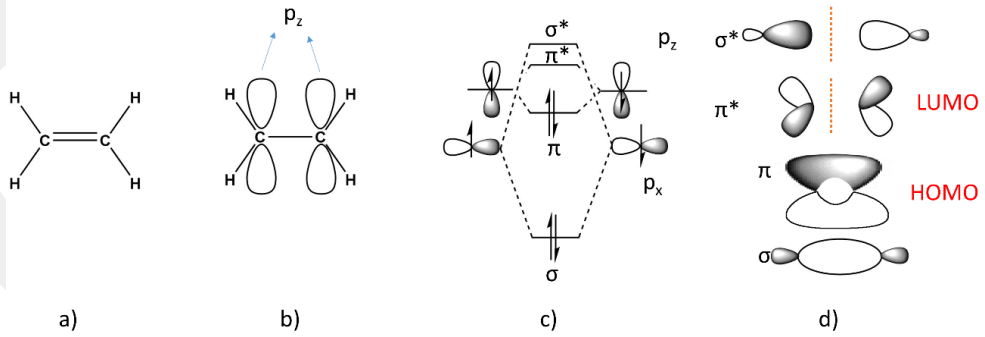

Figure 1.3.1.2 Chemical structure of ethene (a) its geometric configuration (b) and its orbital configuration with two overlapping sp^2 and p_z-orbitals (c) yielding four molecular orbitals (d) the atomic orbitals of the carbon atoms.

Conductive polymers and small molecules require “conjugated double bonds” to enable electrical conductivity throughout the molecular structure. Small molecular and polymeric π-conjugated systems result from alternating double and single bonds between the neighboring carbon atoms. These structures can be observed in Figure 1.3.1.3.

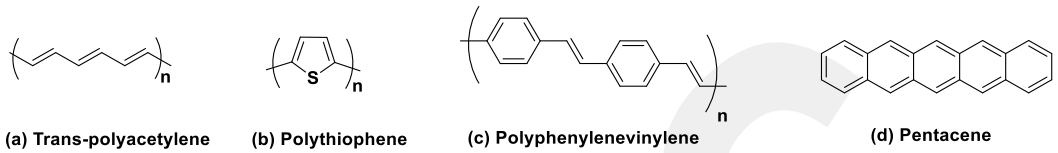

Figure 1.3.1.3 Chemical structure of polymers and small molecules: (a) polyacetylene, (b) polythiophene and (c) polyphenylenevinylene (d) pentacene

Single and double bonds of sp^2-hybridized carbons are alternating in conjugated double bond structure which causes π-electrons delocalization throughout the whole π-system. These delocalizations provide the conduction of charge carriers along the entire conjugated small molecules and/or polymers. The energy band diagram of an organic semiconducting molecule is shown in Figure 1.3.1.6.

The HOMO (highest occupied molecular orbital) is analogous to the valence band (highest energy filled band) in silicon and arises from bonding states of the π-orbitals with filled electrons. The LUMO (lowest unoccupied molecular orbital) is analogous to the conduction band and arise from empty higher energy anti-bonding (π^*) orbitals. The energy difference between the HOMO and LUMO defines the E_G (band-gap energy). Typically, the band gap energy is in the range of 1-4 eV in conjugated polymers. This band-like structure is the reason behind the semiconducting conjugated polymers. Conduction mainly takes place via polaron-assisted tunneling and phonon-assisted hopping between localized states as a result of disordered nature of organic materials.

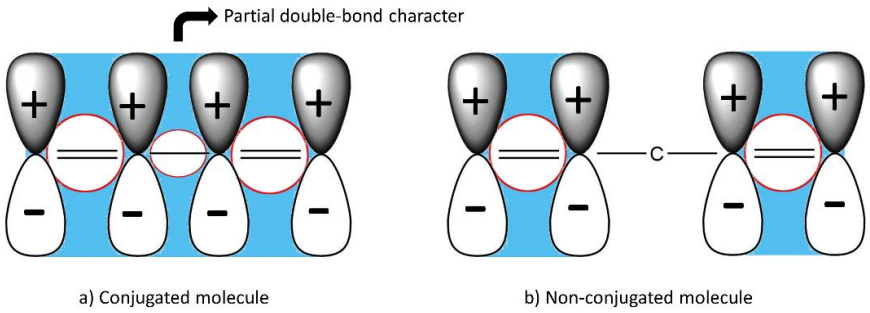

Figure 1.3.1.4 a) conjugated and b) non-conjugated structure of an organic molecule

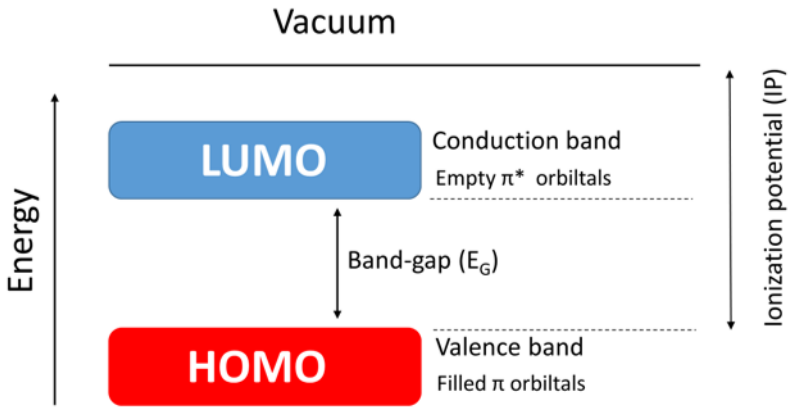

Figure 1.3.1.5 Representative energy band diagram of an organic semiconductor.[5]

Thanks to strong π-orbital overlap, highly conjugated organic materials could show semiconducting characteristics. However, wide band-gap semiconducting polymers exhibit very low conductivities in their neutral state. Therefore, they require additional doping to increase the electrical conductivity. Chemical doping or electrochemical doping techniques could tune the conductivity of conjugated polymers. For this purpose, oxidation and reduction reactions are used to achieve p-type and n-type doping, respectively. These processes provide additional mobile charge carriers into the π-systems.

1.3.2. Microstructure and Molecular Alignment

Most of the organic semiconductor thin films are composed of a mixture of amorphous and polycrystalline phases. The charge carrier mobility in amorphous regions is limited due to intervention of hopping. Therefore, it is significant to remove disordered phases and grain boundaries to achieve efficient charge transport. Proper solid-state arrangements of organic molecules and polymers lead to enhanced charge carrier mobility along thin-films. In additionally, rational molecular designs and surface/interface treatments are desired to achieve well-ordered and well-stacked structures.

Organic thin-film morphologies/microstructures can be characterized via atomic force microscopy, transmission electron microscopy, transmission electron diffraction, and X-ray diffraction measurements. These devices provide information about intermolecular spacing, stacking structure, and distance of π–π stacking structures (Figure 1.3.2.1).[6]

The alignment and orientation of small molecules and polymer chains through the active layer of organic thin-film transistors have significant influence on the device performance. For instance, the mobility of Poly(3-hexylthiophene) (P3HT) is dramatically increased more than 100 times by changing molecular orientation from face-on to edge-on as shown in Figure 1.3.2.2. In face-on orientation, π–π stacking alignment is parallel to dielectric surface. On the other hand, in edge-on orientation π–π stacking is aligned perpendicular to dielectric surface (Figure 1.3.2.2).[7]

Dielectric surface modification is an important step in organic thin-film transistor device fabrication processes. Prior to depositing organic semiconducting layer, functionalization and careful preparation of dielectric surface is essential to achieve high device performance especially in the case of top-contact/bottom-gate device architecture.

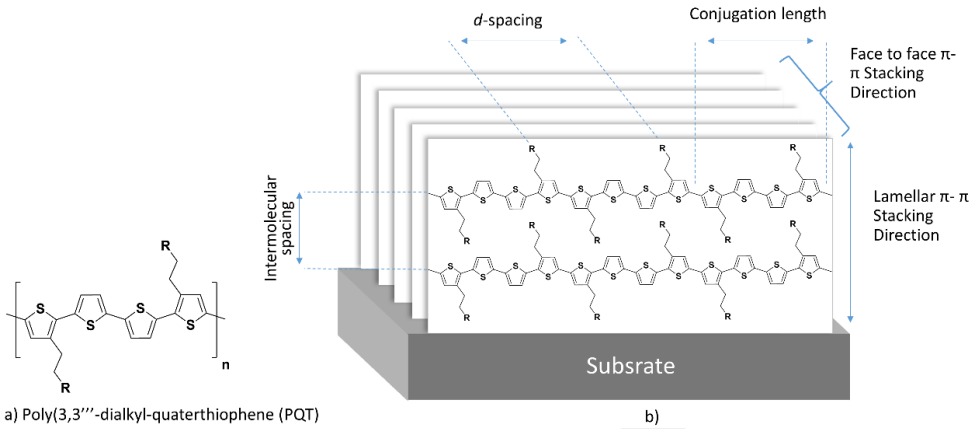

Figure 1.3.2.1 a) Chemical structure of PQT-12 organic semiconductor. b) Schematic illustration of lamellar π–π stacking in a PQT-12 film.

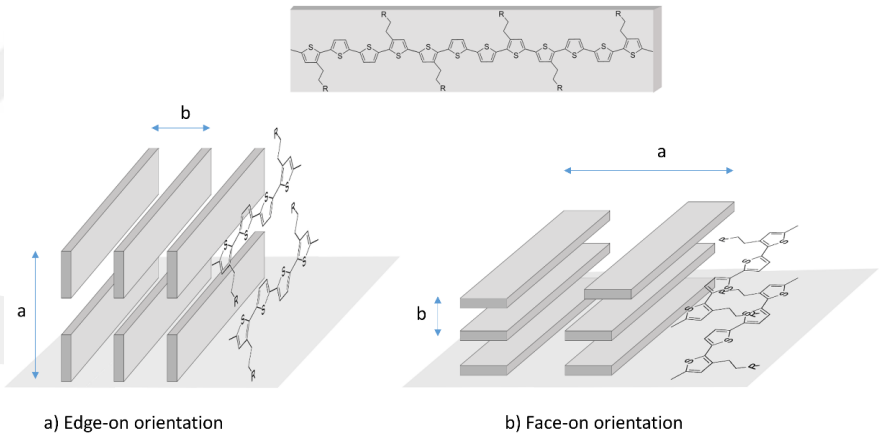

Figure 1.3.2.2 (a,b) Two different orientations of ordered P3HT domains with respect to the dielectric substrate surface.

1.4. Device Operating Principles

Organic semiconducting materials are highly important and promising materials for electronic device applications. Two of the most extensively used electronic devices are organic photovoltaics (OPVs) and organic thin-film transistors (OTFTs).

1.4.1. Organic Thin Film Transistor

OTFT devices have three electrodes that are gate, source, and drain. The semiconducting layer is parallel to substrate surface and the direction of charge carrier movement is from source to drain. Gate controls the charge carrier movement through the channel based on the relationship between source, drain, and gate (figure 1.4.1.1). When there is no gate voltage in the system, no charge carrier transport will occur through channel, and no current will be observed between source and drain. Owing to polarization in the dielectric layer charge carriers could be induced in the semiconducting layers there is applied voltage on the gate electrode. OTFT devices can be classified depending on the charge carrier types:

- p-type (hole conduction)
- n-type (electron conduction)
- ambipolar (hole and electron conduction) (Figure 1.4.1.2).

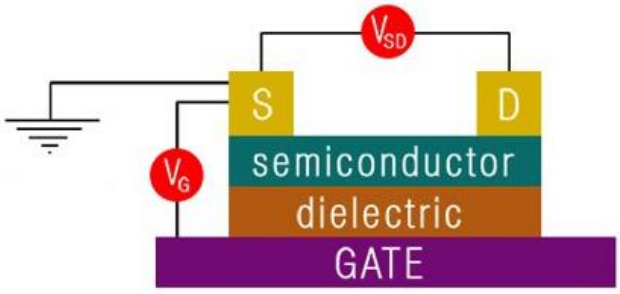

Figure 1.4.1.1 Schematic diagram of an OFET device structure.

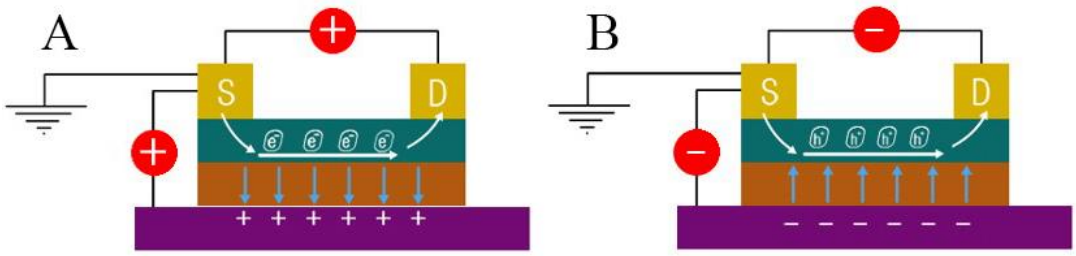

Figure 1.4.1.2 Schematic diagram of *p*-channel OFET (a) and *n*-channel OFET (b).

Three figures of merit of OTFT devices are threshold voltage (V_T), current on/off ratio (I_{ON}/I_{OFF}) and charge carrier mobility (μ). Threshold voltage and charge carrier mobilities can be extracted from the saturation region which can be extracted with the following equation:

$$\mu_{sat} = (2I_{DS}L)/[WC_i(V_G - V_T)^2]$$

In this formula, I_{DS} stands for the drain current, L and W refers to the channel length and channel width, respectively, C_i is the areal capacitance of the gate dielectric, V_G is the gate voltage, and V_T is the threshold voltage.

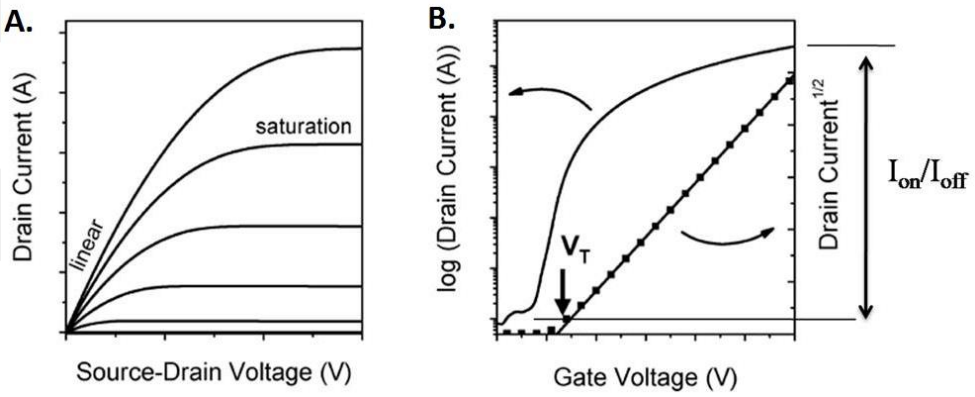

Figure 1.4.1.3 Typical OFET transfer (a) and output (b) curve.

1.4.2. Organic Photovoltaics

The generation of charge carriers upon absorption of sunlight in organic photovoltaics is different from inorganic photovoltaics. The dielectric constant of organic materials is very low. Upon light absorption, the formed exciton has a hole and an electron that are tightly bound to each other (Fig. 1.4.2.1). The exciton must be separated in order to generate free charge carriers. Electron-acceptor and electron-donor materials in the active layer of OPVs have high electron affinities and low ionization potentials, respectively. When an electron is excited by a photon of sun light, it transfers from HOMO to LUMO. The electron will transfer to the LUMO of acceptor if the energy of the latter is below that of the donor's LUMO by an amount at least as large as the exciton binding energy, which is typically several hundred meV (Fig. 1.4.2.1). Optical band gap is fundamentally the energy difference between LUMO and HOMO, which is an important parameter of the absorbing species. The exciton must survive for a long time at the interface of donor and acceptor layers to enable this charge transfer. In ordinary organic semiconductors exciton lifetimes range from 100 picoseconds to 1 ns. After this time elapses, if the exciton is not separated completely, recombination will occur. The exciton moves along a diffusion distance on the order of 10 nm. This length cause limitation on the morphology of the active layer, therefore acceptor and donor species must perfectly mix. Organic materials contain a complex series of intramolecular and intermolecular movements. These movements are often available as polarons, they must be transported to their corresponding electrodes. A combination of drift and diffusion is driving force for transport, the relative roles of which are determined by the electrode materials, applied voltage and other parameters.

OPV devices have a number of different layers (Fig. 1.4.2.2). A plastic or glass transparent substrate is coated with a transparent anode conductor in a standard architecture (Fig. 1.4.2.2a). Hole transport buffer layer blocks electrons from reaching the anode in between the absorbing active layer and the anode. In the same way, active layer is between electron-transport buffer layer and hole transport buffer layer. Active layer is serving an electron-transport buffer layer for supplementary role, followed by the cathode. On the other side, inverted architectures are generally more coherent with roll-to-roll process and low-

work function metals, which could be used for electron-transport layer in this architecture. Inverted architectures are highly susceptible to device degradation (Fig. 1.4.2.2b).[8]

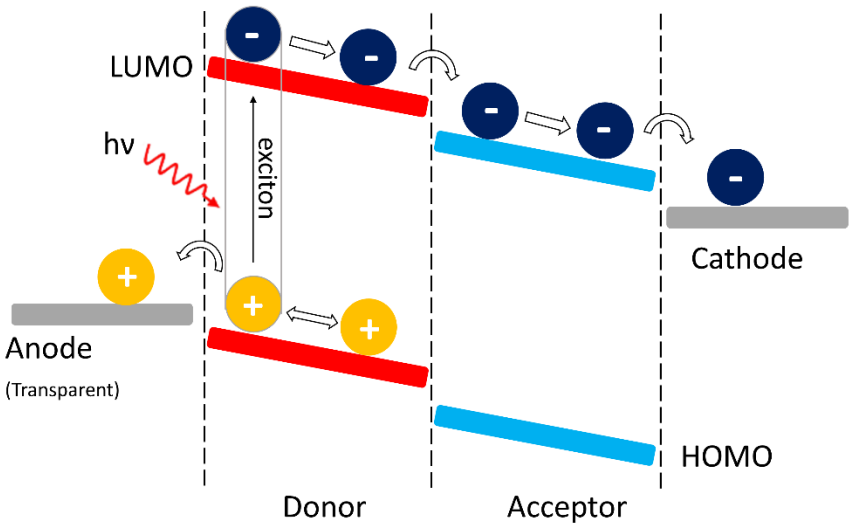

Figure 1.4.2.1 Simplified schematic showing the principal internal processes taking place in OPVs.

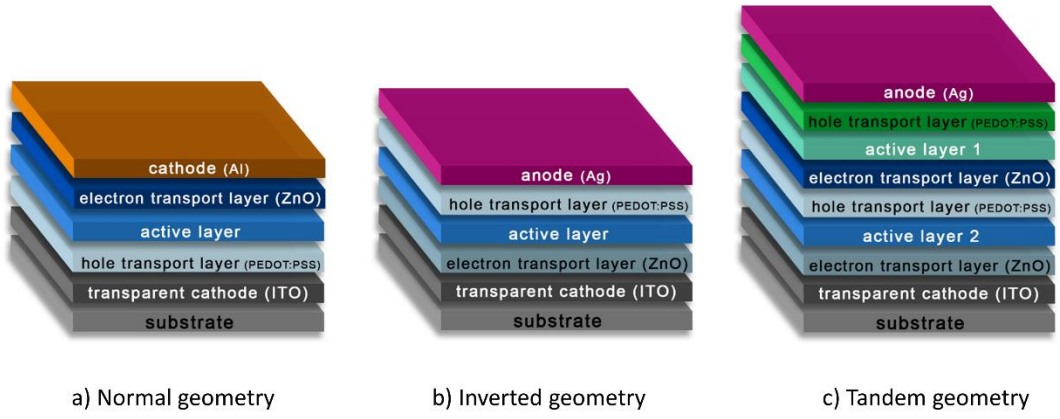

Figure 1.4.2.2 Schematics of common layer structure of OPV devices in (a) normal, (b) inverted, and (c) tandem geometries with typical materials noted.

1.5. Material Development and Classification

1.5.1. Polymeric and Small-Molecule p-Channel Semiconductors for OFETs

Thiophene-based materials are favorable in organic optoelectronics applications after the invention of polythiophene. Polythiophene (PT) has poor π-π stacking in the solid state and the mobility of $\approx 10^{-5}$ cm^2/Vs. The poly(3-alkylthiophene)-based OTFTs performance have been investigated in several research groups for different types of parameters, for instance the length of the core substituent and the effects of the molecular weight.[9] These studies give us information about the charge-transport properties. However, Ong et al. reported a class of solution-processable regioregular polyquaterthiophenes (PQTs). Their structure has long alkyl side chain to enable solubility, structural order to allow molecular self-assembly and control of the π-conjugation elongation. In this way, PQT-12 (P2, Figure 1.5.1) layers exhibited high field-effect mobility of up to 0.14 $cm^2\ V^{-1}\ s^{-1}$ and high I_{on}/I_{off} ratios of $>10^7$ under ambient atmosphere.[10][11]

Fused aromatic system based devices which has good π-conjugation across the rings showed greater p-channel TFT performances because of its coplanar crystal structure. Takimiya and his colleagues reported a lot of advanced molecular and polymeric heteroarene semiconductors for TFTs (Figure 1.5.1). The twist between the thiophene and adjacent thiophene units would reduce the π-π stacking. This polymer P3 exhibited the one of the highest field-effect mobilities observed to date for semiconducting polymers (>0.3–0.5 $cm^2\ V^{-1}\ s^{-1}$).[12]

Isoindigo has strong electron-withdrawing property. Because of this, indigo-based materials are highly popular among scientists. Pei *et al*. reported the first air-stable isoindigo-based polymer (P4, Figure 1.5.1) in OFETs. This copolymer showed hole mobilities of up to 0.79 $cm^2\ V^{-1}\ s^{-1}$. Branched solubilizing groups which are placed further away from the

polymer π-backbone enable polymer chains to pack more closely together, and to increase hole mobility to 3.62 $cm^2 V^{-1} s^{-1}$ for P4 (Figure 1.5.1).[13]

The first Diketopyrrolopyrrole (DPP)-based polymer was reported in 2008, and DPP polymers have shown high charge-carrier mobilities (≥1 $cm^2 V^{-1} s^{-1}$). Ong *et al*. recently reported long-term air-stable DPP polymer which has an extremely high hole mobility of 10.5 $cm^2 V^{-1} s^{-1}$ for P5 (Figure 1.5.1). P5 has planar thienothiophene moiety, thus promotes molecular orbital delocalization along the π backbone, allowing intermolecular packing and lower conformational energy disorder.[14] Kim and his coworkers developed a new DPP-based polymer P6 (Figure 1.5.1). P6 has side chains having extended branching positions and leads to a long-range-ordered, edge-on lamellar crystalline microstructure in the polymer π backbone. These polymers showed high hole mobilities of up to 5 $cm^2 V^{-1} s^{-1}$ with room-temperature processing and of up to 12 $cm^2 V^{-1} s^{-1}$ after thermal annealing.[15]

Takimiya *et al.* adopted a different type of design strategy. They placed heterocycle or alkyl chain at the terminal positions of the center π-core. This strategy provides higher mobility compared to other heteroacene-based semiconductors. These semiconductors have low-lying HOMO energy level. P9 was prepared with phenyl substituents, and it showed hole mobilities of 2.0 $cm^2 V^{-1} s^{-1}$ and I_{on}/I_{off} ratios of 10^7 (Figure 1.5.1).[16] After this work, P10 was prepared with various alkyl chain lengths (n=5–14). BTBTs with alkyl chain were found to be highly soluble in common organic solvents. P10 (n=5–14) showed p-channel behavior with the field-effect mobilities as high as 2.75 $cm^2 V^{-1} s^{-1}$ and I_{on}/I_{off} ratios of 10^7. Recently it has been achieved hole mobility as high as 5 $cm^2 V^{-1} s^{-1}$ for P10 (Figure 1.5.1).[12]

Lee and coworkers reported pyrene-based organic semiconductors, which have been rarely studied in the literature of OFETs (Figure 1.5.1). 5′-octyl-2,2′-bithiophene-5-yl aromatic units were positioned at 1 and 6 positions on the pyrene core, resulting in FET mobility of 2.1 $cm^2 V^{-1} s^{-1}$ and I_{on}/I_{off} ratio of $\sim 10^7$. This work showed that pyrene-based semiconductors are promising materials for high-performance optoelectronic applications.[17]

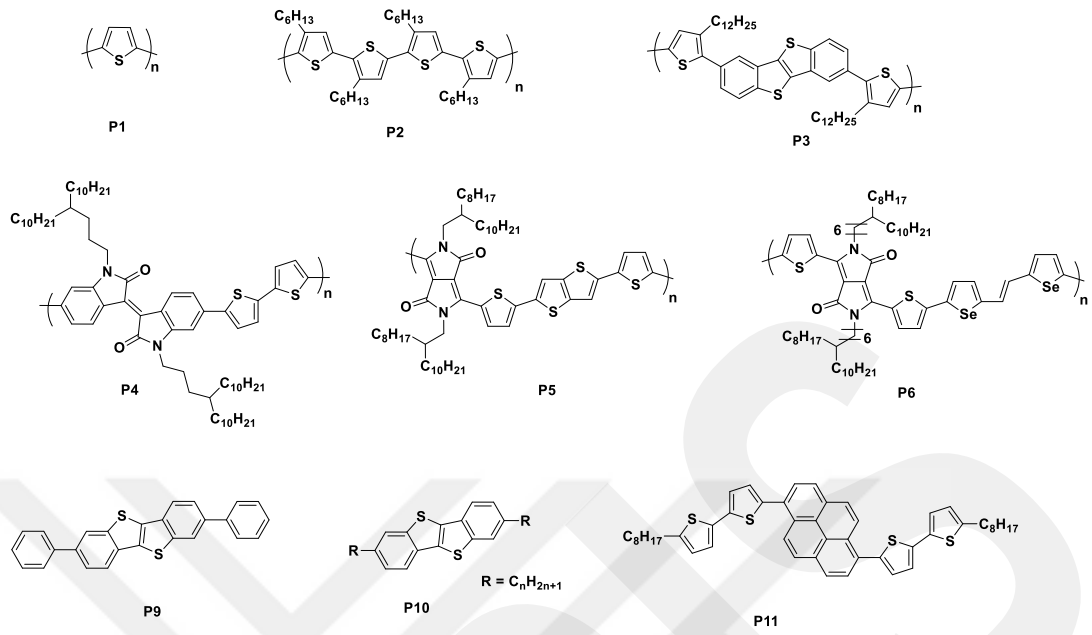

Figure 1.5.1 Chemical structures of *p*-channel polymeric semiconductors.

1.5.2. Polymeric and Small-Molecule n- Channel Semiconductors for OFETs

Since the intrinsic properties of *p*-channel materials compatible with gold electrode (work function of 5.1 eV) most of research in the field of organic semiconducting materials is focused on this type semiconductors. On the other hand, most of *n*-type semiconductors in the literature suffer from low charge-carrier mobility and air stability issue. Babel and coworkers discovered and reported the first *n*-channel polymeric semiconductor which was poly(benzobisimidazobenzophenanthroline) (BBL, N1).[18] This polymer exhibits a high electron mobility of 0.1 $cm^2\ V^{-1}\ s^{-1}$. Letizia and coworkers reported dithenodiimide-based homopolymer (N2, Figure 1.5.2).[19] This solution-processable homopolymer poly(N-(2-octyldodecyl)-2,2′-bithiophene-3,3′-dicarboximide) (P(DTI), N2 exhibited electron mobility of >0.01 $cm^2\ V^{-1}\ s^{-1}$ and I_{on}/I_{off} ratio of 10^7. The first perylene-based polymer (P(PDI2DD-

DTT), N3 in Figure 1.5.2 was reported by Zhan *et al*., and it exhibited electron mobility as high as ~0.01 $cm^2\ V^{-1}\ s^{-1}$ and I_{on}/I_{off} >10^4. [20]

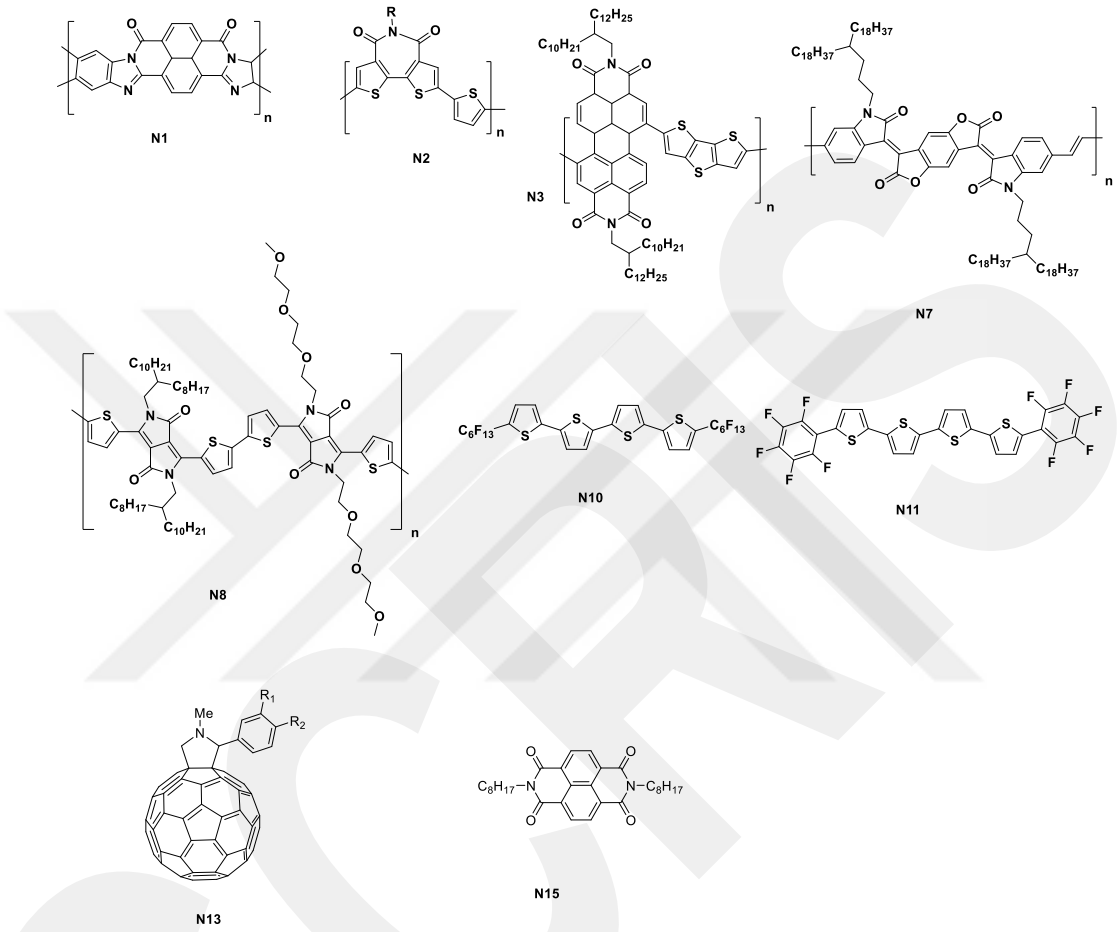

Figure 1.5.2 Chemical structures of *n*-channel polymeric semiconductors.

Pei *et al.* reported new highly electron-deficient benzodifurandione-based poly(p-phenylenevinylene) (PPV) derivative N7 (Figure 1.5.2). This polymer includes solubilizing alkyl groups (4-octadecyldocosyl) and carbonyl functional groups which is a strong electron-withdrawing group. Using N7 as an active layer in OFET device, electron mobility of 1.1 $cm^2\ V^{-1}\ s^{-1}$ was observed. This polymer has one of the highest electron mobility reached to date in *n*-channel polymer OFETs literature.[21]

Patil and coworkers reported an *n*-channel polymeric semiconductor based diketopyrrolopyrrole (DPP) π-core, N8 (Figure 1.5.2). Before their report, DPP and DPP-

based polymers have been used in ambipolar and *p*-channel OFET devices. N8 was incorporated with triethylene glycol side chain (Figure 1.5.2), and these chains provide good solubility. The electron mobilities of DPP-based OFET are up to 3 $cm^2 V^{-1} s^{-1}$.[22]

Facchetti et al. reported the first *n*-channel oligothiophene-based materials included terminal diperfluorohexyl chains (DFH-nTs, N10, in Figure 1.5.2). DFH-4T, was shown to exhibit one of the highest small molecular *n*-type mobility (0.22 cm2 V−1 s−1). [23] After this work they reported arene-thiophene and fluoroarene-thiophene (FTnF (N11), n=2–4, Figure 1.5.2) based semiconductors which exhibited electron mobilities of 0.00001–0.5 $cm^2 V^{-1} s^{-1}$ and I_{on}/I_{off} ratios of 10^1–10^8,respectively. [24]

Chikamatsu and coworkers have synthesized soluble C60-fused N-methylpyrrolidine-meta-C12 phenyl (C60MC12, N13, Figure 1.5.2). N13-based OFET device showed electron mobility of ∼0.07 $cm^2 V^{-1} s^{-1}$. [25]

Rylenediimide-based small molecule *n*-channel OFET was fabricated by Katz *et al*. which exhibited electron mobility of ∼10^{-4} $cm^2 V^{-1} s^{-1}$. They took this work forward and added n-octyl groups on the nitrogen atoms of NDI core. The compound N15 (or NDI-8, Figure 1.5.2) showed an electron mobility of ∼0.16 $cm^2 V^{-1} s^{-1}$.[26] In addition to this, several *n*-type semiconducting materials are still of great interest such as rylenedicarboximide, tetraazabenzodifluoranthenediimide, lutetiumphthalocyanine, and quinomethane terthiophene-based materials to achieve high performing organic optoelectronic devices.

1.5.3. Polymeric and Small-Molecule Ambipolar Semiconductors for OFETs

Although the majority of common organic semiconductors are electron-transporting (n-type) or hole-transporting (p-type) materials, recent work show that ambipolar organic semiconductors have been conspicuous for their potential use. These studies could help us to understand their distinctive properties and their crucial role in specific applications

including CMOS-type organic logic circuits, light-sensing organic thin-film transistors (LS-OTFTs), and organic light emitting transistors (OLETs). All of these devices are based on simultaneous transfer of hole and electrons through the active layer. Ambipolar materials generally have lower band gap compared to unipolar semiconductors.

Sirringhaus and coworkers synthesized polyselenophene-based polymers poly(3,3″-di-n-alkylterselenophene) (A1, Figure 1.5.3). A1-based polymer has an effective performance and presents ambipolarity with balanced hole and electron mobilities (>0.01 $cm^2\ V^{-1}\ s^{-1}$).[27] Naphthalenebiscarboximidebithiophene copolymer ambipolar semiconductor was reported by Watson and coworkers A2 (Figure 1.5.3). [28]Naphthalene bisimide was used as electron-accepting unit, and dialkoxybithiophene as electron-donating unit. A2-based polymer OTFT exhibited electron and hole mobilities up to 0.04 and 0.003 $cm^2\ V^{-1}\ s^{-1}$, respectively. Reynolds *et al*. reported benzo[1,2-c;4,5-c′]bis[1,2,5]thiadiazole (BBT) based polymer A4 (Figure 1.5.3), which contains dithieno[3,2-b:2′,3′- d]pyrrole (DTP) donor and trialkoxyphenyl acceptor units. This polymer has long-chain alkoxy substituents for solubility and this strategy provided a high-lying HOMO. The polymer bandgap was 0.5–0.6 eV, and this result is one of the lowest band gap reported among the other solution processable polymer. However, A4-based OTFT exhibited electron mobility of 5.8×10^{-4} $cm^2\ V^{-1}\ s^{-1}$ and hole mobility of 1.2×10^{-3}. Pei and coworkers synthesized the first isoindigo-based donor–acceptor polymers.[29] This polymer A5 (Figure 1.5.3) was consisting of electron-donating bithiophene and electron-accepting isoindigo units. P99 showed high hole mobility of up to 1.85 $cm^2\ V^{-1}\ s^{-1}$ and electron mobilities from 10^{-2} to 0.43 $cm^2\ V^{-1}\ s^{-1}$ under ambient conditions. [30]

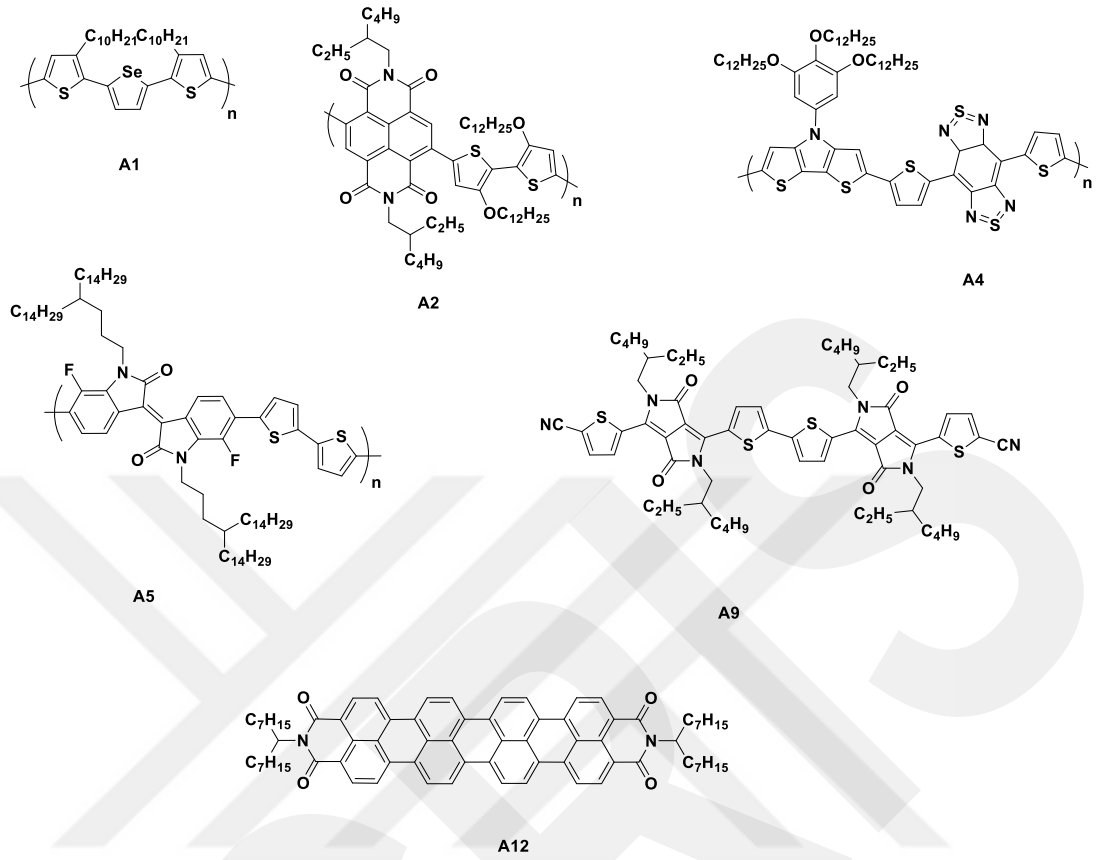

Figure 1.5.3 Chemical structures of ambipolar polymeric semiconductors.

DPP-based oligomer A9 (Figure 1.5.3) was reported by Wang *et al*. This small molecule has cyano terminal functional groups and it was operable in air. A9 showed electron mobilities of 0.03 $cm^2\ V^{-1}\ s^{-1}$ and hole mobilities of 0.07 $cm^2\ V^{-1}\ s^{-1}$ which is one of the highest results for air-stable, solution-processable small molecular ambipolar semiconductors.[31] Quaterrylenediimide-based solution-processable ambipolar semiconductor was synthesized by Müllen and coworkers A12 (Figure 1.5.3).[32] In this material, while HOMO energy level was increasing, LUMO stayed unchanged as a result of π-conjugation extension. Solution-processed OTFT based on M16 molecule displayed both hole and electron mobilities of 10^{-3} $cm^2\ V^{-1}\ s^{-1}$. The most important part of this report was, after the thermal annealing ambipolarity disappeared which shows that there is a strong relation between device performance and morphology.

1.5.4. Molecular Donors Based on OPV Materials

Oligothiophenes are important materials for organic semiconductors and they have been widely used in OFETs. In 1974, quinquethiophene (OP1) (Figure 1.5.4) was synthesized by Khunan and his collegues, and they studied their photoelectrical behavior.[33] After this work, the first prototype of bilayer D/A heterojunction cell was reported by Shirota and coworkers, which was based on octithiophene (OP2). In this work octithiophene was used as donor, and perylenebasedpigment was used as acceptor. Under white light illumination at 10^5 mW cm^{-2} the cell exhibited a fill-factor (FF) of 0.50, leading to a conversion efficiency of 0.59%, a short-circuit current density (Jsc) of 2.90 mA cm^{-2}, and an open circuit voltage (V_{oc}) of 0.42 V (Figure 1.5.4).[34] Liu and coworkers reported cyano-substituted terthiophenes (OP3) (Figure 1.5.4). Terthiophenes was used as donor and perylenetetracarboxilicdianhydride (PTCD) as acceptor. An unspecified active area of simple devices ITO/16/PCDT/Al showed PCE of 1.51 %, J_{sc} of 7.60, and V_{oc} of 0.65.[35] Fitzner and coworkers reported a 4T terminal group including a dicyanovinyl functional group (OP4). OPV device based C60 exhibited Jsc of 6.50 mA cm^{-2} and a PCE of 3.80%.[36] After this work they synthesized 5Ts with 10 methyl groups and reported its PV performance (OP5).[37] OPV device exhibited better performance PCE of (6.90% and Js of 11.10 mA cm^{-2}) compared with their former study. Steinberger et al. reported five-ring system with two benzothiadiazole (BzT), OP6 with PCE of 3.10%. (Figure 1.5.4).[38]

Demeter et al. synthesized 3,4-ethylenedioxythiophene (EDOT). EDOT building block was revisited with terminal dicyanovinyl group (OP7-OP8) (Figure 1.5.4). They tried to diminish the size of oligothiophene because of the strong donor properties of EDOT group. The compound OP7 showed a low V_{oc} of 0.35 V, a J_{sc} of 3.51 mA cm^{-2}, and its low FF caused to a poor PCE of 0.41%. Afterwards, they switch the thiophene with an EDOT group and reported the compound of OP8 having PCE of 2.02%, a V_{oc} of 0.83 V and a J_{sc} of 5.40 mA cm^{-2}.[39]

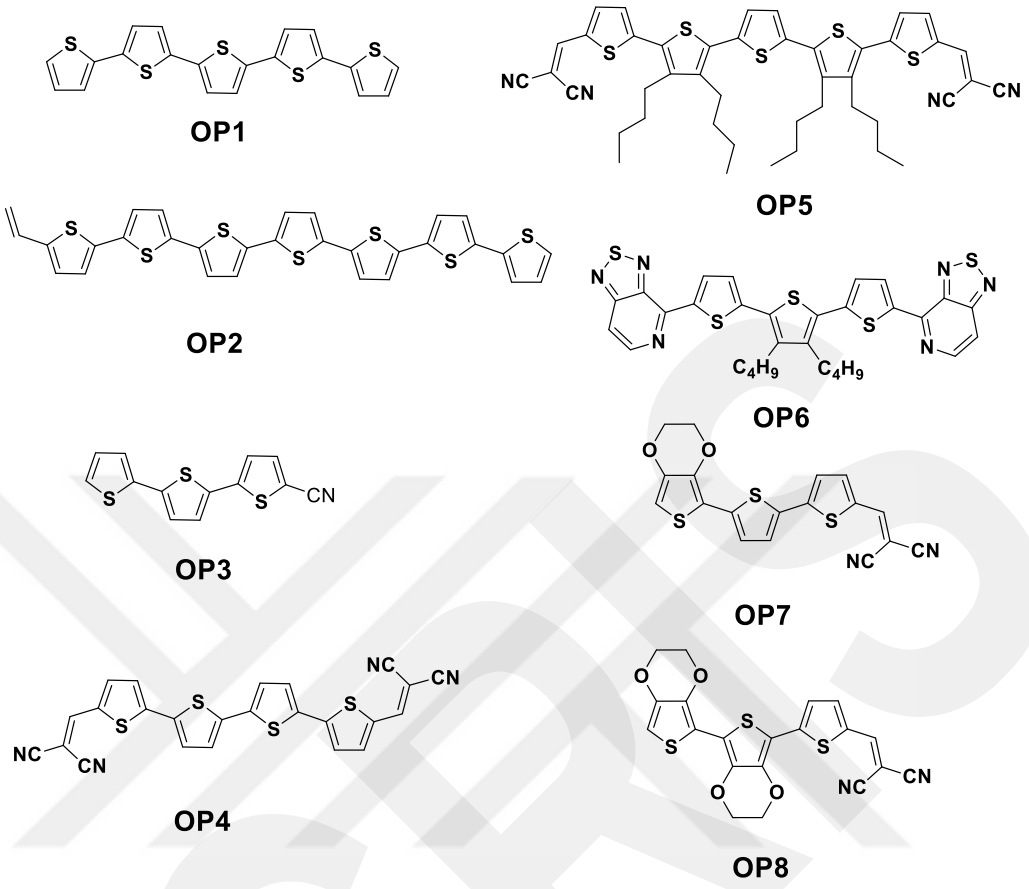

Figure 1.5.4. Chemical structures of molecular donors based on OPV materials.

1.6. Research Strategy and Overview of This Thesis

The small molecular π-conjugated semiconducting materials have attracted widespread scientific and technological interest during the last few decades to realize low-cost, mechanically flexible, large-area, and printable optoelectronics. Nowadays, numerous commercial products, for example organic light-emitting diode (OLED)-based displays, employ molecular semiconductors as a electroactive layer. The π-conjugated small molecules are advantageous when compared to polymeric π-systems in terms of facile synthesis, higher purity levels, good solubility, enhanced thin-film crystallinity, and

relatively small batch-to-batch variations. To this end, various molecular design strategies have been extensively explored to optimize the physicochemical and optoelectronic characteristics, and to meet the specific measures of a particular application. One of these design approaches is to manipulate the effective π-conjugation of the molecules with the goal of achieving a favorable balance between solution-processability, solid-state packing, HOMO–LUMO energetics, and optical band gaps. This is particularly important for the design of low band-gap ambipolar semiconductors, which are crucial for the development of single component OLETs and integrated microelectronic organic logic circuits, and as well as fundamental understanding of hole vs. electron transport in molecular solids. The rationale for obtaining a low band-gap molecular semiconductor relies on building a small energetic separation between HOMO and LUMO, which leads to simultaneous injections of both holes and electrons with low energy barriers. The most practical technique to achieve low band-gap and to enhance π-conjugation is to build donor–acceptor molecular architectures, and to minimize the inter-ring torsions between electron-deficient (acceptor) and electron-rich (donor) moieties.

In the second chapter of the thesis, a series of solution processable ambipolar indeno[1,2-b]fluorene-6,12-dione-thiophene derivatives with alkyl substituents at α,ω-positions as side groups were designed and synthesized. These new compounds were fully characterized by $^{1}H/^{13}C$ NMR, mass spectrometry, cyclic voltammetry, UV-Vis absorption spectroscopy, differential scanning calorimetry, thermogravimetric analysis, and melting point measurement. The solid state structure of the indeno[1,2-b]fluorene-6,12-dione acceptor core was identified based on single-crystal X-ray diffraction (XRD). The structural and electronic properties were also studied using density functional theory calculations, which were found to be in excellent agreement with the experimental findings and provided further insight. The detailed effects of alkyl chain size and orientation on the optoelectronic properties, intermolecular cohesive forces, thin-film microstructures, and charge transport performance of the new semiconductors were investigated. Two of the new solution-processable semiconductors, **2EH-TIFDKT** and **2OD-TIFDKT**, were deposited as thin-films via solution-shearing, drop-casting, and droplet-pinned crystallization methods, and their morphologies and microstructures were investigated by X-ray diffraction (XRD) and atomic force microscopy (AFM). The solution-processed thin-film transistors based on **2EH-**

TIFDKT and **2OD-TIFDKT** showed ambipolar device operations with electron and hole mobilities as high as 0.12 $cm^2/V \cdot s$ and 0.02 $cm^2/V \cdot s$, respectively, and I_{on}/I_{off} ratios of 10^5-10^6. Herein, we demonstrated that rational repositioning of the β-alkyl substituents to molecular termini provides π-core planarity while retaining a good solubility, resulting in favorable structural and optoelectronic characteristics for more efficient charge-transport in the solid-state. The ambipolar charge carrier mobilities were increased by two-three orders of magnitude in the new indeno[1,2-b]fluorene-6,12-dione-thiophene core on account of the rational side-chain engineering.

Electron-deficient π-conjugated small molecules can function as electron-transporting semiconductors in various optoelectronic applications. Despite their unique structural, optical, and electronic properties, the development of BODIPY-based organic semiconductors have lagged behind that of other π-deficient units.

In the third chapter, the design and synthesis of two novel solution-proccessable BODIPY-based small molecules (**BDY-3T-BDY** and **BDY-4T-BDY**) for organic thin-film transistors (OTFTs) were performed. The new semiconductors were fully characterized by $^1H/^{13}C$ NMR, mass spectrometry, cyclic voltammetry, UV-Vis spectroscopy, photoluminescence, differential scanning calorimetry, and thermogravimetric analysis. The single-crystal X-ray diffraction (XRD) characterization of a key intermediate reveals crucial structural properties. Solution-sheared top-contact/bottom-gate OTFTs exhibited electron mobilities of up to 0.01 $cm^2/V \cdot s$, and I_{on}/I_{off} $>10^8$. Film microstructural and morphological characterizations indicated the formation of relatively long (~0.1 mm) and micron-sized (1-2 μm) crystalline fibers for **BDY-4T-BDY**-based films along the shearing direction. Fiber-alignment-induced charge transport anisotropy ($\mu_{\parallel}/\mu_{\perp}$~10) was observed, and higher mobilities were achieved when the microfibers were aligned along the conduction channel, which allows for efficient long-range charge transport between source and drain electrodes. These OTFT performances are the highest reported to date for a BODIPY-based molecular semiconductor, and it indicates that BODIPY is a promising building block for solution-processable, electron-transporting semiconductor films.

A new solution-processable, acceptor-donor-acceptor (A-D-A) type small molecule, BDY-PhAc-BDY, consisting of BODIPY π-acceptors and rod-shaped 1,4-bis-(thienylethynyl)2,5-dialkoxybenzene π-donor, was synthesized and fully characterized as a

novel n-channel semiconductor in bottom-gate/top-contact organic field-effect transistors (OFETs). The new semiconductor exhibited an electrochemical band gap of 2.12 eV with highly stabilized HOMO/LUMO energy levels of -5.68 eV/-3.56 eV. Single-crystal X-ray diffraction (XRD) analysis of BDY-PhAc-BDY showed a relatively low "BODIPY-meso-thiophene" dihedral angle (θ = 44.94°), antiparallel π-stacked BODIPY dimers with an interplanar distance of 3.93 Å, and strong "C-H$\cdots\pi$ (2.85Å)" interactions. The OFET devices fabricated by solution processing showed the formation of highly-crystalline, one-dimensional (1-D) microribbons, resulting in n-channel semiconductivity with electron mobility of 0.004 cm2/V·s and the on-to-off current ratio of 10^5-10^6. This is the highest reported to date for BODIPY-based small molecular semiconductors having alkyne linkages. Our results clearly demonstrate that BODIPY is an effective π-acceptor unit for the design of solution-processable, electron-transporting organic semiconductors and easily fabricate 1-D semiconductor micro-/nano-structures for the fundamental and applied researches in organic optoelectronics.

In the last chapter, the synthesis, physicochemical, and optoelectronic properties of a new class of low band-gap (~1.3 eV) donor-acceptor copolymers based on a highly electron-deficient *meso*-5-(2-octyldodecyl)thiophene substituted BODIPY π-unit are presented. The polymeric solutions exhibited strong aggregation-dependent excitonic properties, indicating the presence of enhanced π-coherence as a result of strong inter-chain interactions. The polymeric semiconductor thin-films prepared by spin-coating showed isotropic nodule-like grains with essentially no ordering in the out-of-plane direction. Field-effect hole mobilities of 0.005 $cm^2/V\cdot s$ were observed in bottom-gate top-contact OFETs, and inverted BHJ-OPVs employing the polymer:$PC_{71}BM$ active layer exhibited excellent power conversion efficiencies of 6.2% with a short-circuit current of 16.6 mA/cm^2. To the best of our knowledge, this is the best OPV performance reported to date for a boron-containing donor polymer. Our findings indicate that BODIPY-based donor-acceptor copolymers designed in a rational way can be one of the important semiconductors in photovoltaic applications.

Chapter 2

Design, Synthesis, and Characterization of α,ω-Disubstituted Indeno[1,2-b]fluorene-6,12-dione-Thiophene Molecular Semiconductors. Enhancement of Ambipolar Charge Transport Through Synthetic Tailoring of Alkyl Substituents.

2.1. Introduction

π-conjugated small molecules constitute a highly investigated class of semiconductor materials that have attracted widespread scientific and technological interest during the last few decades to realize low-cost, mechanically flexible, large-area, and printed optoelectronics.[40]–[57] Today, numerous commercial products, such as organic light-emitting diode (OLED) based displays, employ functional small molecules as their electro-active layers. [58], [59] Compared to larger π-systems such as polymers and dendrimers, π-conjugated small molecules are advantageous in terms of facile synthesis, higher purity levels, good solubility, enhanced thin-film crystallinity, and relatively small batch-to-batch variations.[60], [61] To this end, various molecular design strategies have been extensively explored to optimize their physicochemical and optoelectronic characteristics, and to meet the specific measures of a particular application.[62]–[64] As a result of these studies, impressive performances have been realized with small molecules in organic thin-film transistors (OTFTs), organic photovoltaics (OPVs), OLEDs, and recently with organic light-emitting transistors (OLETs).[65]–[68] One of these design approaches is to manipulate the

effective π-conjugation of the molecules with the goal of achieving a favorable balance between solution-processibility, solid-state packing, HOMO-LUMO orbital energetics, and optical band gaps.[69]–[71] This has been particularly important in the design of low band-gap ambipolar semiconductors, which are crucial for the development of single-component OLETs and integrated microelectronic organic logic circuits, and as well as fundamental understanding of hole vs. electron transport in molecular solids.[72]–[75] The rationale for obtaining a low band-gap molecular semiconductor relies on building a small energetic separation between HOMO and LUMO, which leads to simultaneous injections of both holes and electrons with low energy barriers.[76] The most practical technique to achieve low band-gap and to enhance π-conjugation is to build donor-acceptor molecular architectures, and to minimize the inter-ring torsions between π-electron deficient (acceptor) and π-electron rich (donor) moieties.[77]–[79]

In a previous work, Marks and Facchetti et al. have reported a new family of indenofluorene and bisindenofluorene-based ladder-type semiconductors with good charge-transport properties and ambient-stability.[80] One of these semiconductors is a solution-processable ambipolar small molecule, **β-DD-TIFDKT** (Figure 2.1), which has a β-substituted donor-acceptor-donor type of molecular architecture with thiophene (donor) and indeno[1,2-b]fluorene-6,12-dione (acceptor) π-cores.[81] However, preliminary solution-based electron and hole mobilities were quite poor (~10^{-4} $cm^2/V \cdot s$). Therefore, in this study, we aim to further optimize the chemical structure of this π-core via tailoring alkyl substitutions. From a molecular design standpoint, the earlier semiconductor displays large inter-ring dihedral angles of ~47° between indeno[1,2-b]fluorene-6,12-dione core and the terminal thiophene units in its energy-minimized geometry due to the presence of β-substituents (vide infra). These twists undoubtedly contribute to the solubility of this large π-system, and enable the solvent-based chromatographic purification and device processing. However, we speculate that they also deteriorate intra-/intermolecular π-conjugation and π-delocalization, resulting in the observed poor charge-transport. The repositioning of the β-substituents to molecular termini (α,ω-substitutions) is expected to greatly benefit the π-core planarity of the semiconductor backbone as a result of reduced steric interactions. However, it is known that the solubility of π-conjugated systems decrease with enhancing π-conjugation and planarization as a result of better solid-state packing. Therefore, rational

alkyl chain engineering is required to establish a delicate balance of good solution processibility, effective π-conjugation, and favorable solid-state packing/charge-transport. Previously, similar side chain engineering approaches have been successfully employed to tune the optoelectronic and charge-transport properties of solution-processable semiconductor polymers.[82]–[85]

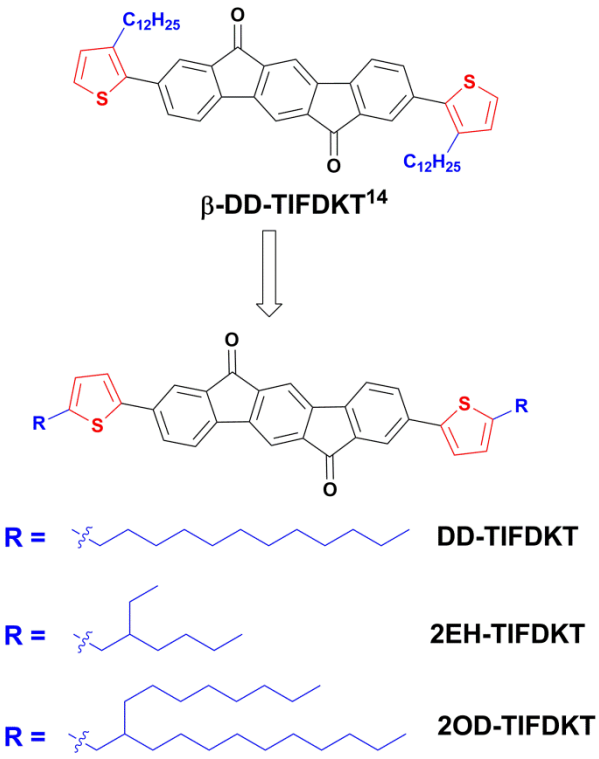

Figure 2.1.1 Chemical structures of **β-DD-TIFDKT**,[14] and **DD-TIFDKT**, **2EH-TIFDKT**, and **2OD-TIFDKT** developed in this study.

Here, we report on the design, synthesis, and characterization of three new α,ω-disubstituted molecules (**DD-TIFDKT**, **2EH-TIFDKT**, and **2OD-TIFDKT**) based on indeno[1,2-b]fluorene-6,12-dione and thiophene building blocks. Based on the solubility of these molecules, **2EH-TIFDKT** and **2OD-TIFDKT** are characterized by optical absorption spectroscopy, cyclic voltammetry, differential scanning calorimetry, and thermogravimmetric analysis. Corresponding thin-films are deposited via various solution processing methods including solution-shearing (SS), droplet-pinned crystallization (DPC), and drop-casting (DC), and they are studied by X-ray diffraction, atomic force microscopy

(AFM), and field-effect transistor measurements. Single-crystal analysis of the intermediate compound **2** reveals crucial structural features of the 2,8-dibromo-indeno[1,2-b]fluorene-6,12-dione acceptor core. In our attempts to develop new solution-processable semiconductors, we first synthesized **DD-TIFDKT** with linear -*n*-$C_{12}H_{25}$ chains at α,ω-positions, which resulted in complete insolubility. Therefore, our choice was to incorporate two different swallow tail alkyl chains of 2-ethylhexyl (2-EH) and 2-octyldodecyl (2-OD). The presence of swallow tails, which enhances the degrees of rotational freedom in the molecular backbone, would endow the new semiconductors with good solubility in common organic solvents. To this end, α,ω-disubstituted indeno[1,2-b]fluorene-6,12-dione-thiophene semiconductor was first synthesized with 2-octyldodecyl chains (**2OD-TIFDKT**), which has yielded good solubility, but also highly unbalanced electron and hole mobilities of up to 0.04 $cm^2/V{\cdot}s$ and ~3×10^{-4} $cm^2/V{\cdot}s$, respectively. Then, **2EH-TIFDKT** was developed with reduced insulating alkyl chain (2-ethylhexyl) density, which yields good solution processibility and relatively more balanced and higher charge carrier mobilities. Solution-processed OTFTs with **2EH-TIFDKT** exhibit electron and hole mobilities of up to 0.12 $cm^2/V{\cdot}s$ and 0.02 $cm^2/V{\cdot}s$, respectively with on/off ratios of 10^5– 10^6. This indicates an improvement of >100× in the ambipolar charge carrier mobilities compared to those of parent β-substituted semiconductor (**β-DD-TIFDKT**) as a result of superior structural and electronic properties.

2.2. Experimental

2.2.1. Materials and Methods

All reagents were purchased from commercial sources and used without further purification unless otherwise noted. Conventional Schlenk techniques were used, and reactions were carried out under N_2 unless otherwise noted. NMR spectra were recorded on a Bruker 400 spectrometer (^1H, 400 MHz; ^{13}C, 100 MHz). Elemental analyses were performed on a LecoTruspec Micro model instrument. MALDI-TOF was performed on a

Bruker Microflex LT MALDI-TOF-MS Instrument. Thermogravimetric analysis (TGA) and differential scanning calorimetry (DSC) measurements were performed on Perkin Elmer Diamond model instruments under nitrogen at a heating rate of 10 °C/min. UV-Vis absorption measurements were performed on a Shimadzu, UV-1800 UV-Vis Spectrophotometer. Electrochemistry was performed on a C3 Cell Stand electrochemical station equipped with BAS Epsilon software (Bioanalytical Systems, Inc., Lafayette, IN). Prior to the synthesis, the optimization of the molecular geometries and total energy calculations were carried out using density functional theory (DFT) at the B3LYP/6-31G** level by using Gaussian 09.[86]

2.2.2. Crystal Structure Determination

The intensity data for **IFDK-BR2** (**2**) were collected on an Bruker APEX II QUAZAR three-circle diffractometer using monochromatized Mo *Kα* X-radiation (λ = 0.71073 Å). Indexing was performed using APEX2 [Bruker (2014) APEX2, version 2014.11-0, Bruker AXS Inc., Madison, Wisconsin, USA]. Data integration and reduction were carried out with SAINT [Bruker (2013) SAINT, version V8.34A, Bruker AXS Inc., Madison, Wisconsin, USA]. Absorption correction was performed by multi-scan method implemented in SADABS [Bruker (2014) SADABS, version 2014/5, Bruker AXS Inc., Madison, Wisconsin, USA].The structures were solved and refined using the Bruker SHELXTL Software Package [Bruker (2010) SHELXTL, version 6.14, Bruker AXS Inc., Madison, Wisconsin, USA]. All non-hydrogen atoms were refined anisotropically using all reflections with $I > 2\sigma(I)$. The C-bound H atoms were positioned geometrically and refined using a riding mode. Crystallographic data and refinement details of the data collection are summarized in Table 2.2.2 The final geometrical calculations and the molecular drawings were carried out with Platon (version 1.17) and Mercury CSD (version 3.5.1) programs.

Table 2.2.2 Crystal data and refinement parameters for ***IFDK-BR2***.

Empirical Formula	$C_{20}H_8Br_2O_2$
Formula weight (g. mol^{-1})	440.08
Temperature (K)	300.(2)
Wavelength (Å)	0.71073
Crystal system	Monoclinic
Space group	*P* 2_1/c
a (Å)	3.8828(3)
b (Å)	13.5879(11)
c (Å)	14.1314(13)
α(°)	90
β(°)	95.032(6)
γ(°)	90
Crystal size (mm)	0.139 x 0.146 x 0.525
V (Å3)	742.69(11)
Z	2
ρcalcd (g. cm^{-3})	1.968
μ (mm^{-1})	5.467
F(000)	428
θ range for data collection (°)	3.00-25.68
h/k/l	-4/4, -15/16, -15/17
Reflections collected	5701
Independent reflections	1408 [R(int) = 0.0764]
Absorption correction	Multi-scan
Data/restraints/parameters	1408 / 0 / 109
Goodness-of-fit on F^2	1.009
Final R indices [I > 2σ(I)]	R_1= 0.0454, wR_2= 0.1093
R indices (all data)	R_1= 0.0566, wR_2= 0.1159
Largest diff. peak and hole (e.Å^{-3})	0.771 and -0.702

2.2.3. Synthesis and Characterization

2-Dodecyl bromide and 2-ethylhexyl bromide were purchased from commercial sources, and 2-octyldodecyl bromide is synthesized from 2-octyl-1-dodecanol in accordance with the following procedure:

2.2.3.1. 2-octyldodecyl bromide

A mixture of 2-octyl-1-dodecanol (9.0 g, 30 mmol) and triphenylphosphine (11.4 g, 120 mmol) was dissolved in 400 mL THF under ambient conditions. Bromine (18.0 g, 120 mmol) was added slowly to this mixture, and the resulting reaction solution was stirred at room temperature for 3 h. Then, 6 ml of methanol was added and the solvent was removed on the rotary evaporator. The residue is suspended in hexane, and the insoluble part was removed by filtration. Then, the resulting filtrate was concentrated on the rotary evaporator to give a crude oil, which was purified by column chromatography on silica gel using hexane as the eluent to give the pure product as a colorless oil (10.61 g, 97.5%). ^{1}H NMR (400 MHz, $CDCl_3$): δ 3.44 (2H, d, J = 4.8Hz), 1.58 (1H, m), 1.27 (32H, m), 0.88 (6H, t, J = 6.7 Hz).

2.2.3.2. 4,4’’-dibromo-2,2’’-methoxycarbonyl-[1,1’;4’,1’’]terphenyl (1)

A mixture of 1,4-benzenediboronic acid bis(pinacol) ester (1.0 g, 3.03 mmol), methyl 2-iodo-5-bromobenzoate (2.262 g, 6.64 mmol), and Aliquat 336 (0.347 g, 0.86 mmol) was suspended in 20 mL of dry toluene under nitrogen. Then, tetrakis(triphenylphosphine)palladium (0.21 g, 0.18 mmol) and 1M aqueous sodium carbonate solution (1.28 g in 12.2 mL of water), which was already deaerated for 2 h, were

added under N_2. The mixture was heated at reflux for 2 days under nitrogen. The mixture was then cooled to room temperature and quenched with water. The reaction mixture was extracted with hexanes, and the organic phase was washed with water, dried over Na_2SO_4, filtered, and evaporated to dryness to give the crude product. The crude was then purified by column chromatography on silica gel using chloroform as the eluent to give the pure product as a white solid (1.316 g, 86.0% yield). ^{1}H NMR (400 MHz, $CDCl_3$): δ 3.71 (s, 6H), 7.32 (m, 6H), 7.67 (dd, 2H, J = 8.0 Hz and J = 2.4 Hz), 8.00 (d, 2H, 2.4 Hz).

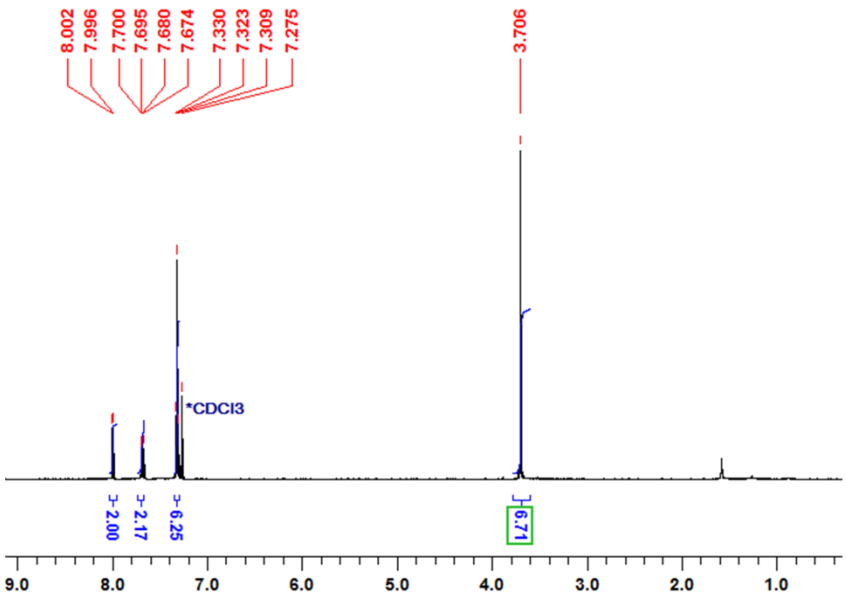

Fig. 2. 1.3.2 ^{1}H NMR spectra of compound 1 in $CDCl_3$ at room temperature.

2.2.3.3. 2,8-dibromo-indeno[1,2-b]fluorene-6,12-dione (2)

Compound **1** (0.61 g, 1.20 mmol) was added to 60.0 mL of 80% H_2SO_4 (prepared from 12mL of H_2O and 48 mL of concentrated (98%) H_2SO_4), and the reaction mixture was heated with stirring at 120 °C for 17 h. Then, the reaction mixture was poured into ice and stirred for 15 min to give a dark red solid, which was collected by filtration. The crude product was then washed with water, saturated sodium hydrogen carbonate ($NaHCO_3$) solution, and

methanol, respectively. The crude product was then purified by thermal gradient sublimation under high vacuum (2×10^{-5} Torr) to afford the pure product as a cherry red crystalline solid (0.395 g, 74.0% yield). Note that during the sublimation, single-crystals of this compound were also obtained. m.p. > 390 °C. Anal.calcd. for $C_{20}H_8O_2Br_2$: C, 54.58; H, 1.83 Found: C, 54.70; H, 1.96.

2.2.3.4. 2,8-bis(5-dodecylthien-2-yl)indeno[1,2-b]fluorene-6,12-dione (DD-TIFDKT).

The reagents 2,8-dibromo-indeno[1,2-b]fluorene-6,12-dione(2)(0.763 g, 1.73 mmol), 2-trimethylstannyl-5-dodecylthiophene (4) (1.58 g, 3.81 mmol), and Pd(PPh3)2Cl2 (0.202 g, 0.29 mmol) in anhydrous DMF (80 mL) were heated at 125 °C under nitrogen for 24 h. Then, the reaction mixture was cooled down to room temperature and evaporated to dryness. The crude product was filtered by using methanol, and then washed with methanol, acetone, and hexanes to give a dark crude solid (1.89 g, 87.5% crude yield). The crude product was insoluble in common organic solvents, and, thus, thermal gradient sublimation was performed under high vacuum (2×10-5 Torr), which resulted in complete decomposition of the crude material.

2.2.3.5. 2,8-bis(5-(2-ethylhexyl)thien-2-yl)indeno [1,2-b]fluorene-6,12-dione (2EH-TIFDKT).

The reagent 2,8-dibromo-indeno[1,2-b]fluorene-6,12-dione(**2**) (0.500 g, 1.136 mmol), 2-trimethylstannyl-5-(2-ethylhexyl)thiophene (**6**) (0.82 g, 2.272 mmol), and $Pd(PPh_3)_2Cl_2$ (79.4 mg, 0.113 mmol)in anhydrous DMF (65 mL) were heated at 125 °C under nitrogen for 18 h. Then, the reaction mixture was cooled down to room temperature and evaporated to dryness. The crude product was filtered by using methanol, and then washed with methanol, acetone, and hexanes to give a dark crude solid. The crude product was purified by column

chromatography on silica gel with $CHCl_3$/hexanes (9:1) as the eluent to give final product as a dark green solid (0.37 g, 48.5% yield). m.p. 292-293 °C. ^{1}H NMR (400 MHz, $CDCl_3$):δ 0.92 (t, 6H, J = 7.2 Hz), 1.26-1.40 (m, 9H), 2.74 (d, 2H, J = 6.4 Hz), 6.71 (d, 1H, J = 3.6 Hz), 7.15 (d, 1H, J = 3.6 Hz), 7.40 (d, 1H, J = 7.6 Hz), 7.63 (m, 2H), 7.75 (s, 1H).^{13}C NMR (100 MHz, $CDCl_3$):δ10.9, 14.2, 23.0, 25.5, 28.9, 32.4, 34.2, 41.4, 115.8, 120.9, 121.0, 123.6, 126.4, 131.4, 134.6, 136.2, 139.4, 140.2, 141.3, 145.5, 192.6. IR (KBr): 1710 cm^{-1} (C=O Stretching). MS(MALDI-TOF) m/z (M^+): calcd. for $C_{44}H_{46}O_2S_2$: 670, found: 671 $[M+H]^+$. Anal.calcd. for $C_{44}H_{46}O_2S_2$: C, 78.76; H, 6.91, Found: C, 78.43; H, 6.98.

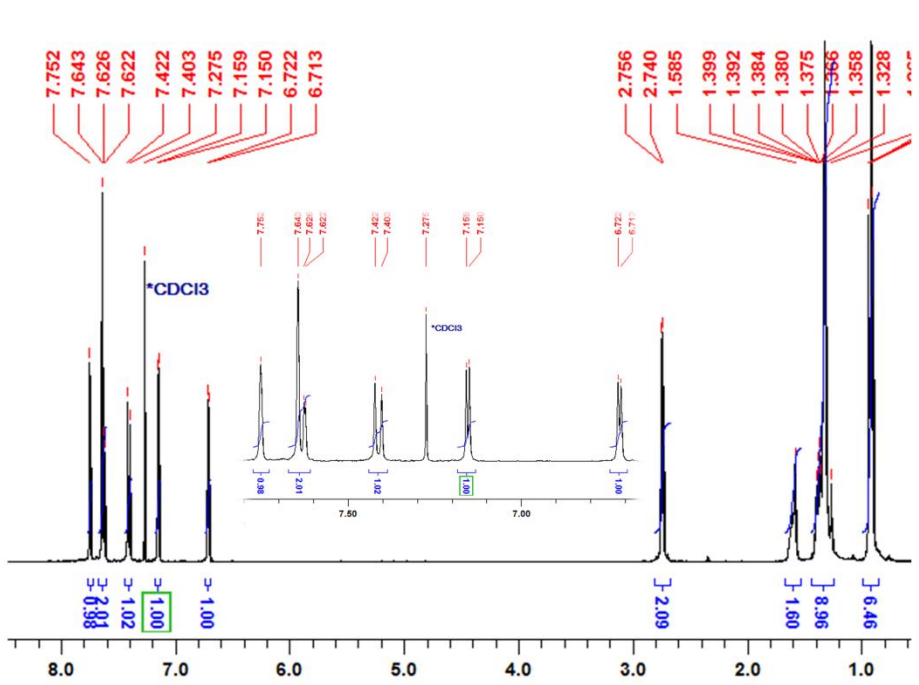

Figure 2.2.3.5.1 ^{1}H NMR spectra of **2EH-TIFDKT** in $CDCl_3$ at room temperature.

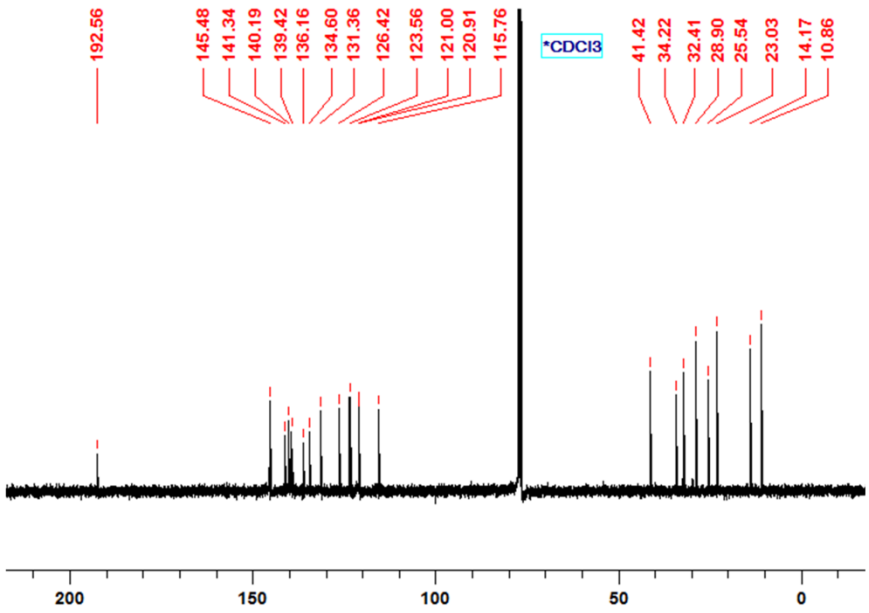

Figure 2.2.3.5.2 ^{13}C NMR spectra of **2EH-TIFDKT** in $CDCl_3$ at room temperature.

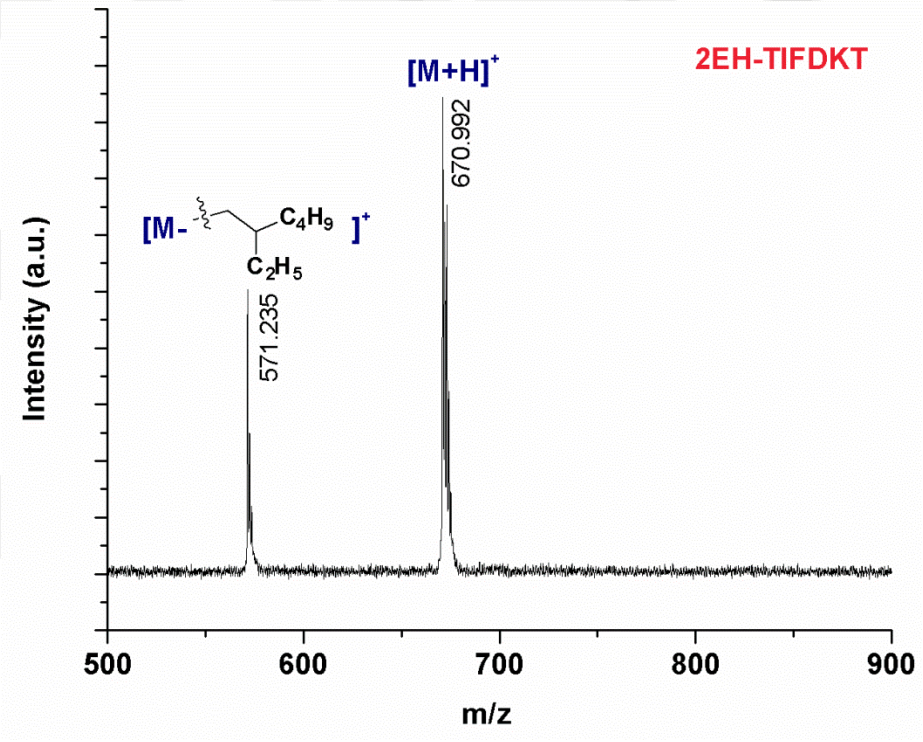

Figure 2.2.3.5.3 Positive ion and linear mode MALDI TOF-MS spectrum of **2EH-TIFDKT**.

2.2.3.6. 2,8-bis(5-(2-octyldodecyl)thien-2-yl)indeno [1,2-b]fluorene-6,12-dione (2OD-TIFDKT).

The reagent 2,8-dibromo-indeno[1,2-b]fluorene-6,12-dione (**2**) (0.682 g, 1.55 mmol), 2-trimethylstannyl-5-(2-octyldodecyl)thiophene (**8**) (1.80 g, 3.41 mmol), and $Pd(PPh_3)_2Cl_2$ (0.109 g, 0.155 mmol) in anhydrous DMF (75 mL) were heated at 125 °C under nitrogen for 24 h. Then, the reaction mixture was cooled down to room temperature and evaporated to dryness. The crude product was filtered by using methanol, and then washed with methanol, acetone, and hexanes to give a dark crude solid. The crude product was purified by column chromatography on silica gel with $CHCl_3$/hexanes (7:3) as the eluent to give final product as a dark green solid (0.531 g, 34.0% yield). m.p. 135-136 °C. ^{1}H NMR (400 MHz, $CDCl_3$): δ 0.90 (m, 6H), 1.28-1.31 (m, 33H), 2.74 (d, 2H, J = 6.4 Hz), 6.68 (d, 1H, J = 3.2 Hz), 7.12 (d, 1H, J = 3.6 Hz), 7.38 (d, 1H, J = 7.6 Hz), 7.60 (m, 2H), 7.70 (s, 1H).^{13}C NMR (100 MHz, $CDCl_3$): δ 14.1, 22.7, 26.6, 29.3, 29.4, 29.7, 29.8, 29.9, 30.0, 31.9, 33.2, 34.7, 40.0, 115.7, 120.8, 120.9, 123.5, 126.4, 131.3, 134.6, 136.1, 139.4, 140.2, 141.2, 145.4, 145.5, 192.5. IR (KBr): 1710 cm^{-1} (C=O Stretching). MS(MALDI-TOF) m/z (M^+): calcd. for $C_{68}H_{94}O_2S_2$: 1008, found: 1009 $[M+H]^+$. Anal.calcd. for $C_{68}H_{94}O_2S_2$: C, 81.06; H, 9.40, Found: C, 81.31; H, 9.52.

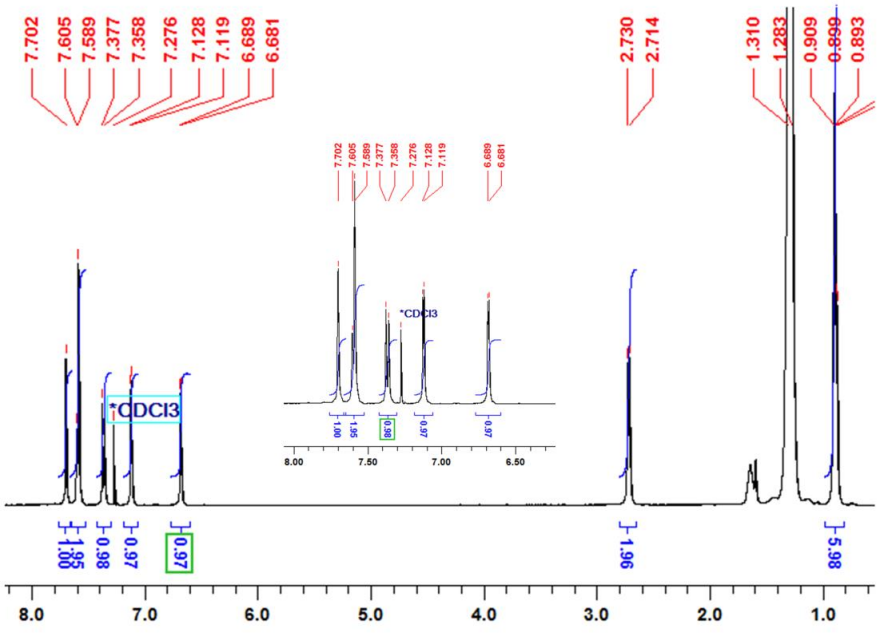

Figure 2.2.3.6.1 ^{1}H NMR spectra of **2OD-TIFDKT** in $CDCl_3$ at room temperature.

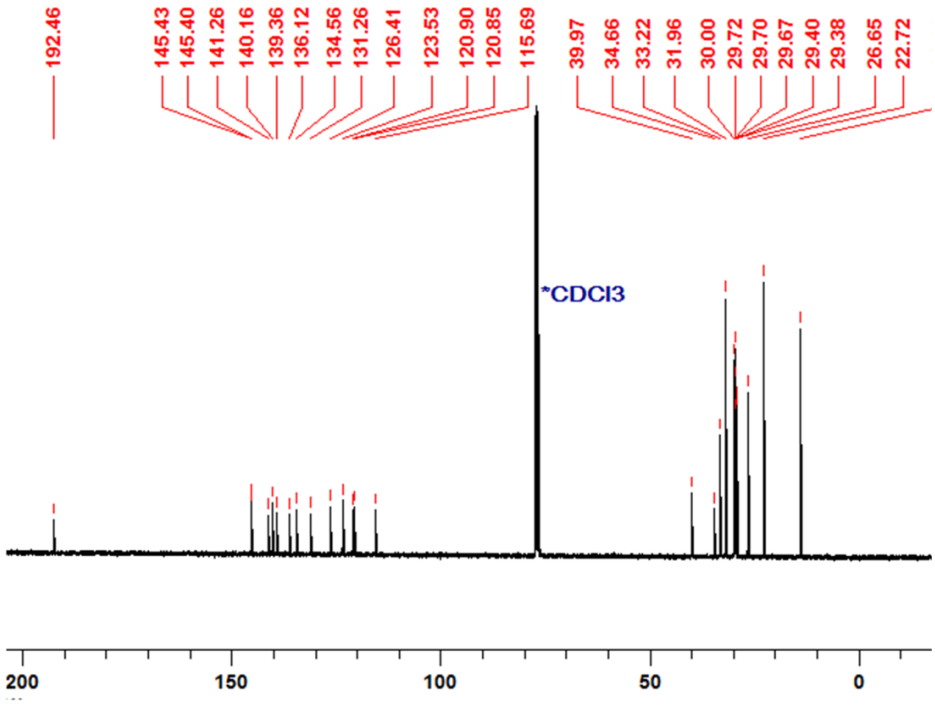

Figure 2.2.3.6.2 ^{13}C NMR spectra of **2OD-TIFDKT** in $CDCl_3$ at room temperature.

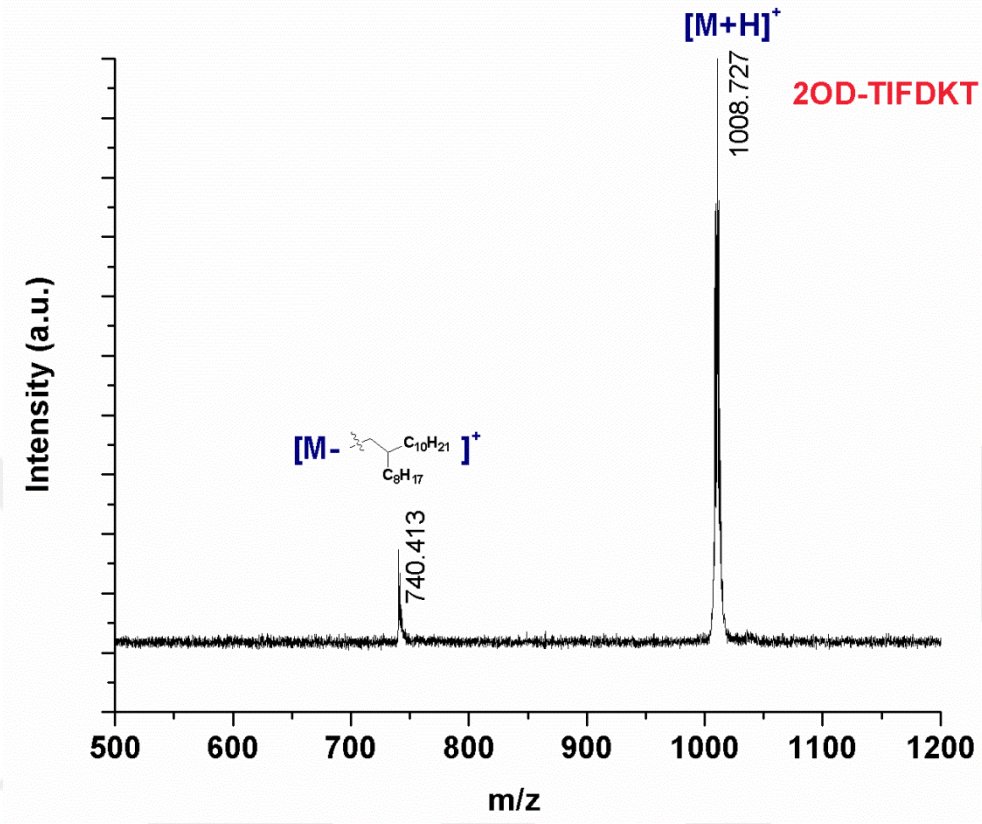

Figure 2.2.3.6.3 Positive ion and linear mode MALDI TOF-MS spectrum of **2OD-TIFDKT**.

2.2.3.7. 2-dodecylthiophene (3).

To a solution of thiophene (2.0 g, 23.76 mmol) in THF (24mL) at −78 °C was added 9.98 mL (24.95 mmol) of *n*-butyllithium (2.5 M in n-hexane) dropwise under nitrogen. The resulting mixture was stirred at −78 °C for 30 min and at room temperature for an additional 1 h. Then, 1-bromododecane (6.52 g, 26.15mmol) was added to this mixture slowly at −78 °C. The resulting reaction mixture was stirred at room temperature for 1 h, and then heated to reflux for 12 h. The reaction was quenched with water, and the product was extracted with chloroform. The organic phase was washed twice with water, dried over Na_2SO_4, filtered, and evaporated to dryness to yield a crude product, which was purified by vacuum distillation to give the pure product as a colorless oil (5.57 g, 93.0%).^{1}H NMR (400 MHz, $CDCl_3$): δ 0.90 (t, 3H, J = 6.8 Hz), 1.27-1.32 (m, 18H), 1.71 (m, 2H), 2.83 (t, 2H, J = 7.6 Hz), 6.79 (d, 1H, J = 3.6 Hz), 6.93 (dd, 1H, J = 5.0Hz, J = 3.6 Hz), 7.11 (d, 1H, J = 5.0 Hz).

2.2.3.8. 2-dodecyl-5-trimethylstannylthiophene (4).

To a solution of 2-dodecylthiophene (**3**) (2.0 g, 7.92 mmol) in THF (30 mL) at −78 °C was added 3.33 mL (8.32 mmol) of *n*-butyllithium (2.5 M in *n*-hexane) under nitrogen. The mixture was stirred at −78 °C for 30 min and at room temperature for 1 h. Then, trimethyltinchloride (1.74 g, 8.71 mmol) was added slowly at −78 °C, and the resulting reaction mixture was allowed to warm to room temperature and stirred at room temperature overnight. The reaction was quenched with water, and the product was extracted with hexane. The organic phase was washed with water, dried over Na_2SO_4, filtered, and evaporated to dryness to give the pure product as a colorless oil (2.96 g, 90.0%). ^{1}H NMR ($CDCl_3$, 400 MHz): δ 0.35 (s, 9H),0.90 (t, 3H, J = 6.8), 1.27-1.36 (m, 20H), 2.87 (t, 2H, J = 7.6 Hz), 6.92 (d, 1H, J = 3.2 Hz), 7.02 (d, 1H, J = 3.2 Hz).

2.2.3.9. 2-(2-ethylhexyl)thiophene (5)

To a solution of thiophene (3.0 g, 35.65 mmol) in THF (35 mL) at −78 °C was added 15.0 mL (37.44 mmol) of *n*-butyllithium (2.5 M in n-hexane) dropwise under nitrogen. The resulting mixture was stirred at −78 °C for 30 min and at room temperature for an additional 1 h. Then, 2-ethylhexylbromide (7.58 g, 0.039 mol) was added to this mixture slowly at −78 °C. The resulting reaction mixture was stirred at room temperature for 1 h, and then heated to reflux for 12 h. The reaction was quenched with water, and the product was extracted with chloroform. The organic phase was washed twice with water, dried over Na_2SO_4, filtered, and evaporated to dryness to yield a crude product, which was purified by vacuum distillation to give the pure product as a colorless oil (3.58 g, 51.0%). ^{1}H NMR (400 MHz, $CDCl_3$): δ 0.91 (m, 6H), 1.29-1.32 (m, 9H), 2.77 (d, 2H, J = 6.8 Hz), 6.77 (d, 1H, J = 3.6 Hz), 6.93 (dd, 1H, J = 5.2 Hz, J = 3.6 Hz), 7.13 (d, 1H, J = 5.2 Hz).

2.2.3.10. 2-(2-ethylhexyl)-5-trimethylstannyl thiophene (6).

To a solution of 2-(2-ethylhexyl)thiophene (**5**) (1.5 g, 7.64 mmol) in THF (30 mL) at −78 °C was added 3.2 mL (8.02 mmol) of *n*-butyllithium (2.5 M in *n*-hexane) under nitrogen. The mixture was stirred at −78 °C for 30 min and at room temperature for 1 h. Then, trimethyltinchloride (1.67 g, 8.4mmol) was added slowly at −78 °C, and the resulting reaction mixture was allowed to warm to room temperature and stirred at room temperature overnight. The reaction was quenched with water, and the product was extracted with hexane. The organic phase was washed with water, dried over Na_2SO_4, filtered, and evaporated to dryness to give the pure product as a colorless oil (2.37 g, 86.5%). ^{1}H NMR ($CDCl_3$, 400 MHz): δ 0.35 (s, 9H),0.90 (m, 6H), 1.25-1.35 (m, 9H), 2.81 (d, 2H, J = 6.4 Hz), 6.89 (d, 1H, J = 3.2 Hz), 7.01 (d, 1H, J = 3.2 Hz).

2.2.3.11. 2-(2-octyldodecyl) thiophene (7).

To a solution of thiophene (0.671 g, 7.98 mmol) in THF (10 mL) at −78 °C was added 3.35 mL (8.38 mmol) of *n*-butyllithium (2.5 M in n-hexane) dropwise under nitrogen. The resulting mixture was stirred at −78 °C for 30 min and at room temperature for an additional 1 h. Then, 1-bromo-2-octyldodecane (3.05 g, 8.78 mmol) was added to this mixture slowly at −78 °C. The resulting reaction mixture was stirred at room temperature for 1 h and then heated to reflux for 12 h. The reaction was quenched with water, and the product was extracted with chloroform. The organic phase was washed twice with water, dried over Na_2SO_4, filtered, and evaporated to dryness to yield a crude product, which was purified by column chromatography on silica gel using hexane as the eluent to give the pure product as a colorless oil (1.51 g, 52.0%). ^{1}H NMR (400 MHz, $CDCl_3$): δ 0.89 (m, 6H), 1.27-1.33 (m, 33H), 2.76 (d, 2H, J = 6.8 Hz),6.76 (d, 1H, J = 3.4 Hz), 6.92 (dd, 1H, J = 5.2 Hz, J = 3.4 Hz), 7.13 (d, 1H, J = 5.2 Hz).

2.2.3.12. 2-(2-octyldodecyl)-5-trimethylstannyl thiophene (8).

To a solution of 2-(2-octyldodecyl)thiophene (**7**) (1.4 g, 3.84 mmol) in THF (30 mL) at −78 °C was added 1.61 mL (4.03 mmol) of *n*-butyllithium (2.5 M in *n*-hexane) under nitrogen. The mixture was stirred at −78 °C for 30 min and at room temperature for 1 h. Then, trimethyltinchloride (0.841 g, 4.22 mmol) was added slowly at −78 °C, and the resulting reaction mixture was allowed to warm to room temperature and stirred at room temperature overnight. The reaction was quenched with water, and the product was extracted with hexanes. The organic phase was washed with water, dried over Na_2SO_4, filtered, and evaporated to dryness to give the pure product as a colorless oil (1.94 g, 95.9%). ^{1}H NMR ($CDCl_3$, 400 MHz): δ 0.35 (s, 9H), 0.91 (m, 6H), 1.25-1.33 (m, 33H), 2.80 (d, 2H, J = 6.0 Hz), 6.88 (d, 1H, J = 3.2 Hz), 7.02 (d, 1H, J = 3.2 Hz).

2.2.4. Device Fabrication and Characterization

For the fabrication of top-contact/bottom-gate organic thin film transistors (OTFTs), highly n-doped (100) silicon wafers (resistivity < 0.005Ω·cm) with a 300 nm thermally grown oxide gate dielectric film were used as device substrates. The Si/SiO_2 substrates were washed via sonication in acetone for 10 min, followed by oxygen plasma for 5 min (18 W). For the formation of PS-brush layer, hydroxyl end-functionalized polystyrenes (M_n =1.73, 10.0, and 28.6 kg/mol, Polymer Source) were spin-coated onto the Si/SiO_2 substrate from 0.5 wt% toluene solutions, then the substrates were heated at 170° for 48 h under vacuum to allow the hydroxyl end groups of the PS chains to react with silanol groups on the Si/SiO_2 substrate.[87] The PS brush-treated substrates were rinsed with toluene to remove unreacted PS chains and annealed at 100 °C for 24 h under vacuum. The water contact angle of the PS brush-treated substrates was ~74°. For the OTS treatment, a 0.1% solution of octadecyltrimethoxysilane in trichloroethylene was spin-coated onto the Si/SiO_2 substrate, and placed in the Schlenk line to react with ammonia vapor for overnight. Unreacted silanes were removed by sonication in toluene for 2 min, followed by rinsing with toluene, acetone

and isopropyl alcohol, and drying under a stream of nitrogen. The water contact angle of the OTS-treated substrates was ~96°. Semiconducting layers (**2EH-TIFDKT** and **2OD-TIFDKT**) were formed via three different solution-processing methods – solution-shearing (SS), droplet-pinned crystallization (DPC), and drop-casting (DC). For all solution processes, PS brush-treated substrates were employed. For the optimization of film-forming process, various solvents including toluene, chlorobenzene, chloroform, 1,2-dichlorobenzene, *p*-xylene, tetralin, 1,2,4-trichlorobenzene with various concentrations (0.5 – 2 mg/mL) were employed. For the DC process, the solutions were drop-cast onto the substrates at preset temperature in solvent-vapor saturated environment, and the substrates were annealed in vacuum oven at 110 °C overnight. For the DPC process, the solutions were dropped onto the substrates (1 × 1 cm^2) and a piece of silicon wafer (0.4 × 0.4 cm^2, pinner) was placed on the substrate to pin the solution droplet. The silicon substrate with the droplet was placed in a Petri dish sealed with parafilm on a hot plate at 30 °C until the solvent was evaporated. For the SS process, a few drops of semiconductor solution were cast onto a heated substrate (1 × 2 cm^2), and the substrate was covered with a dewetting OTS-modified top substrate. The top substrate was then translated by an electrically-controlled syringe pump at a constant rate relative to the bottom substrate, gradually uncovering the sandwiched solution, which quickly evaporated leaving behind a polycrystalline thin film seeding from the shearing substrate frontier. Solvent evaporation was controlled by different deposition temperature (50% - 80% of the solvent boiling point in centigrade) and different solution shearing speed (0.1 – 18 mm/min). The solution-sheared substrates were placed in a vacuum oven at 90 °C overnight to remove the residual solvent. Film thicknesses were characterized by profilometer (DEKTAK-XT, Brucker) as 40 – 90 nm (SS), 100 – 200 nm (DPC), and 25 – 70 nm (DC), respectively. Au layers (40 nm) were thermally evaporated through a shadow mask to define source and drain contacts with various channel lengths (L; 100 and 50 μm) and widths (W; 1000 and 500 μm). The electronic characteristics of OTFTs were measured using a Keithley 4200-SCS. Carrier mobilities (μ) were calculated in the saturation regime by the formula, $\mu_{sat} = (2I_{DS}L)/[WC_i(V_G - V_T)^2]$, where I_{DS} is the source-drain current, L is the channel length, W is the channel width, C_i is the areal capacitance of the gate dielectric (C_i =11.4 $nF \cdot cm^{-2}$), V_G is the gate voltage, and V_T is the threshold voltage. The microstructure and surface morphology of thin-films were characterized using an X-ray diffractometer

(XRD, SmartLab, Rigaku) and an atomic force microscope (AFM, NX10, Park Systems), respectively.

2.3. Results and Discussion

2.3.1. Computational Modeling, Synthesis and Characterization

Prior to the synthesis, the optimization of the molecular geometries and total energy calculations were carried out using density functional theory (DFT) at the B3LYP/6-31G** level. The molecular structure of the previously developed **β-DD-TIFDKT** is illustrated with the model compound **M1**, and **M2** and **M3** illustrates **DD-TIFDKT** and **2EH-TIFDKT/2OD-TIFDKT**, respectively (Figure 2.3.1.1). While **M1** and **M2** are modeled with *n*-butyl chains, **M3** is modeled with isobutyl ($-CH_2CH(CH_3)_2$) chains to demonstrate the structural/electronic differences between linear and swallow-tail alkyl chain systems, respectively. The optimized molecular geometries, HOMO-LUMO energy levels, and pictorial representations are shown in Figure 2.3.1.1 For the indeno[1,2-b]fluorene-6,12-dione core, good agreement is found between the calculated *gas-phase* and X-ray crystallographic geometries (vide infra) with perfect core planarity, although the DFT calculations generally lead to optimized geometries with slightly less bond-length alternations (i.e., more delocalization) for the fused carbon-carbon backbones. In the optimized geometries, relocating alkyl substituents from β-positions to the molecular termini (α,ω-locations) induces a planarization between indeno[1,2-b]fluorene-6,12-dione and thiophene units, and the inter-ring torsional angle is found to reduce from ~47° to ~23° (Figure 2.3.1.1.b). This planarization enhances the electronic communication between donor (thiophene) and acceptor (indeno[1,2-b]fluorene-6,12-dione) moieties, which leads to enhanced π-delocalization along the molecular backbone, lower HOMO-LUMO gaps (Δ = 0.1–0.2 eV), and possibly enhanced intermolecular π-π interactions. All these advantages are

expected to improve ambipolar charge carrier mobility of α,ω-disubstituted semiconductors compared to that of β-disubstituted semiconductors.

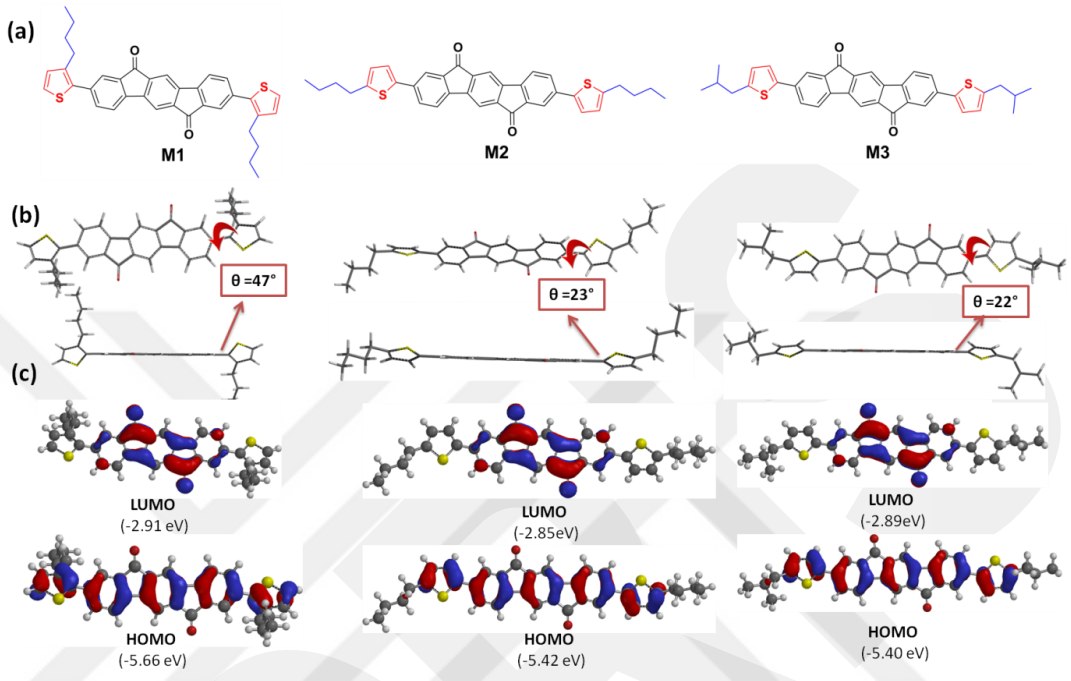

Figure 2.3.1.1 a) Chemical structures of the model compounds **M1**, **M2**, and **M3**. b) Optimized molecular geometries showing inter-ring dihedral angles. c) Computed HOMO and LUMO energy levels, and topographical representations (DFT, B3LYP/6-31G**)

The theoretical HOMO/LUMO energies were found to be −5.66/–2.91 eV for **M1**, −5.42/–2.85 eV for **M2**, and −5.40/–2.89 eV for **M3**. The LUMO electron density distributions of **M1**, **M2**, and **M3** are mostly identical, and mainly delocalized on the acceptor indeno[1,2-b]fluorene-6,12-dione core. Therefore, LUMO energy level shows minimal changes (<0.06 eV) upon alkyl chain tailoring, which is mainly attributed to the differences in the inductive effects of alkyl substituents. However, the HOMO energy level is found to increase by 0.2–0.3 eV since the HOMO electron density is delocalized over the entire π-backbone, and π-electron-rich thiophene moiety is getting more conjugated (enhancing π-delocalization) with the whole π-core in the new α,ω-disubstituted structures. The theoretical HOMO and LUMO energies for **M2** and **M3** are in the range of those calculated for previously reported *p*-channel and *n*-channel semiconductors, respectively,

indicating that, from a molecular orbital energetic perspective, the new molecules should be able to transport both holes and electrons.[81] In the new α,ω-disubstituted indeno[1,2-b]fluorene-6,12-dione-thiophene molecular semiconductors, HOMO-LUMO energy gaps are found to decrease by 0.1–0.3 eV compared to the β-substituted core, which may energetically further facilitate ambipolar charge transport. On the other hand, although symmetric carbonyl functionalization results in nearly zero total molecular dipole moment, each carbonyl site induces local dipoles of 3.31 D, which are effective to facilitate dipole-dipole interactions in the solid-state. This is evident in the single-crystal structure of the indeno[1,2-b]fluorene-6,12-dione core (vide infra, Figures 2.3.3.d and 2.3.3.e). In conclusion, for these new molecular systems, these theoretical results are in excellent agreement with the electrochemical, optical, and single-crystal characterizations (vide infra), and should favor efficient charge transport characteristics.

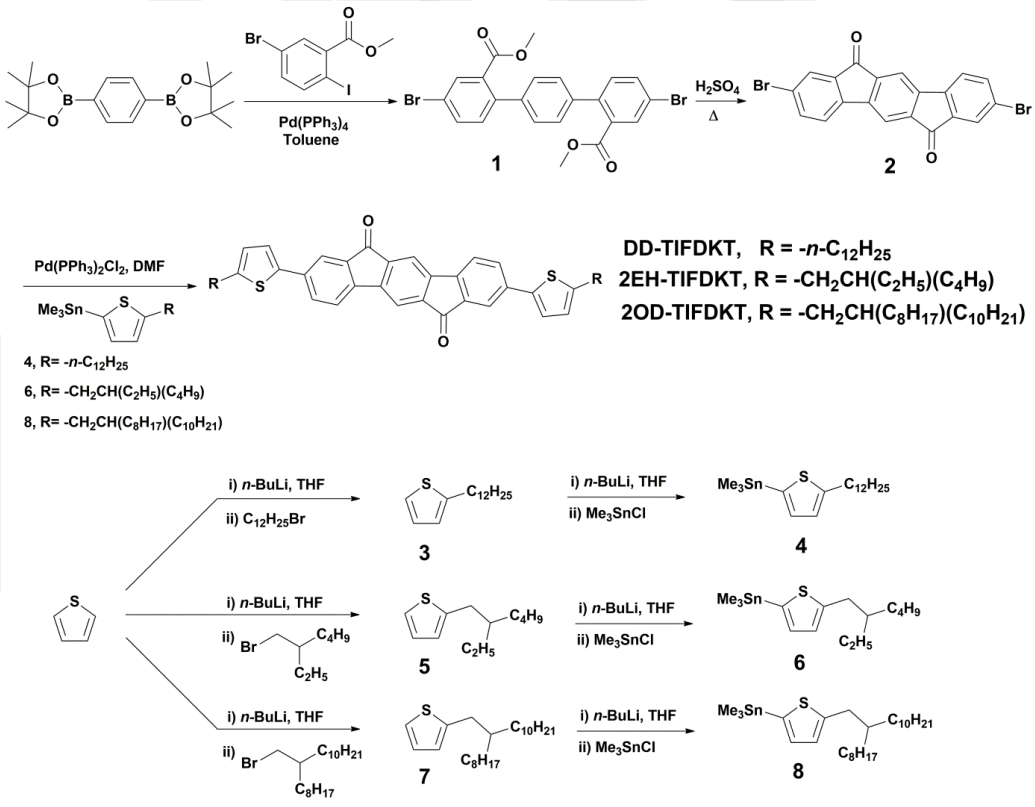

Scheme 2.3.1 Synthesis of α,ω-disubstituted indeno[1,2-b]fluorene-6,12-dione-thiophene molecular semiconductors **DD-TIFDKT**, **2EH-TIFDKT** and **2-OD-TIFDKT**.

In the synthesis of α,ω-disubstituted thiophene-indeno[1,2-b]fluorene-6,12-dione molecules, **DD-TIFDKT**, **2EH-TIFDKT** and **2-OD-TIFDKT**, acid-catalyzed intramolecular Friedel-Crafts acylation reaction is used as the key step for the formation of carbonyl functionalized ladder-type acceptor core. As shown in Scheme 1, Suzuki coupling of 1,4-benzenediboronic acid dipinacol ester with methyl 5-bromo-2-iodobenzoate yields terphenyl intermediate **1** in 86% yield, which undergoes a double intramolecular Friedel-Crafts acylation reaction in 80% H_2SO_4 at 120 °C to yield **2** in 74% yield. On the other hand, alkyl-substituted thiophene reagents **3**, **5**, and **7** are synthesized from thiophene via lithiations followed by alkylbromide subtitutions in 51–93% yields. It is noteworthy that for these reactions, swallow-tails give lower substitution yields compared to linear alkyl chains as a result of steric effects. The corresponding trimethylstannyl-functionalized thiophene reagents **4**, **6**, and **8** are synthesized from **3**, **5**, and **7**, respectively, by lithiation/stannylation reactions in 86–96% yields.

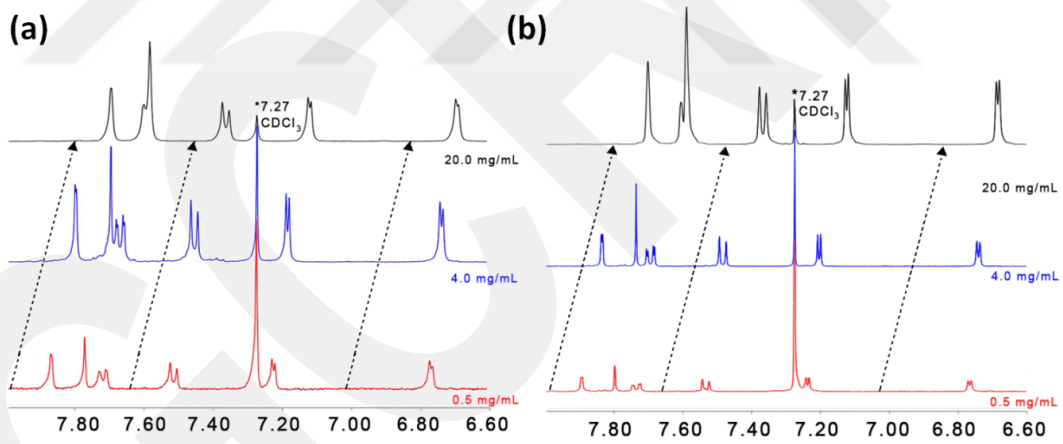

Figure 2.3.1.2 The concentration-dependent ^{1}H NMR spectra of **2EH-TIFDKT** (a) and **2OD-TIFDKT** (b) in $CDCl_3$.

The new semiconductors are synthesized by Stille cross-coupling reactions of dibromo compound **2** with distannylated derivatives **4** (for DD-TIFDKT), **6** (for 2-EH-TIFDKT), and **8** (for 2-OD-TIFDKT) in DMF using $Pd(PPh_3)_2Cl_2$ catalyst. **2EH-TIFDK** and **2OD-TIFDKT** are found to be freely soluble in common organic solvents ($CHCl_3$, CH_2Cl_2, THF, toluene), which allows the convenient purification by flash column chromatography to yield

pure semiconductors in 34–48% yields. However, **DD-TIFDKT** exhibits extremely low solubility, which prevents its solution-based purification. This indicates that enhanced core-planarity significantly lowers the solubility and it cannot be compensated by linear –*n*-$C_{12}H_{25}$ chains. It is noteworthy that linear –*n*-$C_{12}H_{25}$ chain substituted fused *p*-type semiconductors such as[1]benzothieno[3,2-b][1]benzothiophene (BTBT) have been previously reported to be highly soluble.[65] This indicates that in the current **DD-TIFDKT** molecular core, larger local dipole moments, enhanced molecular donor–acceptor characteristics, and improved molecular planarity plays a key role to facilitate intermolecular interactions, which significantly lowers the solubility. The purification of **DD-TIFDKT** was attempted via gradient sublimation under high vacuum (2×10^{-5} Torr), however it resulted in complete decomposition of the material with no observable pure product. This indicates that the current **TIFDKT** core may not be ideal for vacuum-based thermal evaporation methods, which is consistent with the OTFT inactivity and the formation of decomposed products after physical vapor deposition (vide infra). The Stille cross-coupling reaction was also performed with $Pd(PPh_3)_4$/toluene (catalyst/solvent) system, which yielded the desired products in similar yields (42–45%). This is in sharp contrast to our previous report, in which using $Pd(PPh_3)_4$ catalyst did not yield any product for sterically-encumbered Stille coupling of 2,8-dibromo-indeno[1,2-b]fluorene-6,12-dione (**2**) with 3-dodecyl-2-trimethylstannylthiophene reagent. This suggests that for the present sterically less-demanding coupling reaction, higher turnover frequencies of more coordinatively unsaturated $Pd(PPh_3)_2Cl_2$ catalyst is not essential.[81] For this particular Stille coupling, the similar yields obtained for **2EH-TIFDK** and **2OD-TIFDKT** indicates that the reaction is not particularly sensitive to alkyl substituent encumbrance on the thiophene reagent. The chemical structures and purities of **2EH-TIFDK** and **2OD-TIFDKT** were characterized by ^{1}H and ^{13}C NMR (Figures 2.2.3.5.1-2.2.3.6.1, 2.2.3.5.2-2.2.3.6.2), elemental analysis, IR (Figure 2.3.1.3), and mass spectroscopy (Maldi-TOF) (Figures 2.2.3.5.3, 2.2.3.6.3).

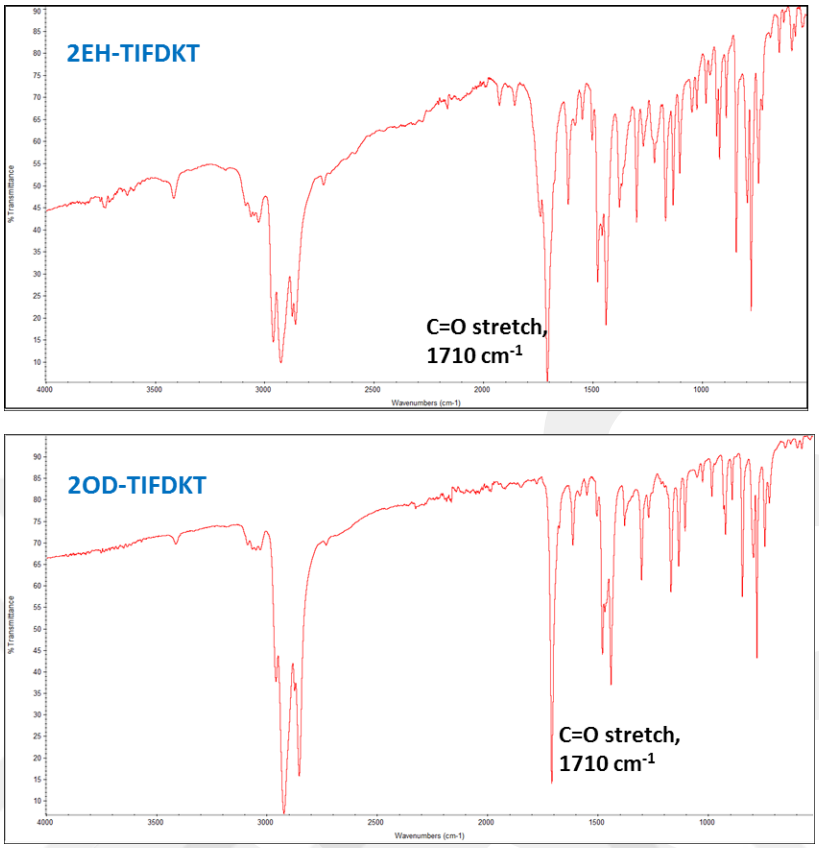

Figure 2.3.1.3 FTIR spectra of **2EH-TIFDKT** and **2OD-TIFDKT**.

The good solubility of these molecules is a consequence of the swallow-tail alkyl substituent and offers a significant advantage in OTFTs for the deposition of semiconductor layers from solution. As shown in Figure 2.3.1.2, in the ^{1}H NMR spectra of **2EH-TIFDKT** and **2OD-TIFDKT**, the chemical shifts of the aromatic protons are found to significantly shift upfield ($\Delta\delta$ = 0.15–0.20 ppm) with increasing concentration (0.5 mg/mL → 20 mg/mL), which indicates a shielding effect as a result of staggered molecular stacking in solution via π-π interactions. Based on the chemical shifts, both indeno[1,2-b]fluorene-6,12-dione and thiophene units appear to be involved in the molecular stack formation in solution. In addition, due to a greater number of local electronic environments, the aromatic peaks are broadened with concentration, which further supports this stacking model. Similar self-assembly characteristics in solution have been observed in the literature for a number of π-conjugated molecules,[71], [88] and it offers key advantages to efficient charger-carrier transport.

2.3.2. Thermal Properties

The thermal properties of the present compounds, **2EH-TIFDKT** and **2OD-TIFDKT** were characterized by differential scanning calorimetry (DSC), thermogravimetric analysis (TGA), and conventional melting point measurements. Thermal scans are shown in Figure 2.3.2 and data are presented in Table 1. A 5% mass loss in TGA scan is defined as the thermolysis threshold. For the present molecules, since the molecular architecture of the π-backbone (thiophene-indeno[1,2-b]fluorene-6,12-dione-thiophene) remains the same, alkyl substituents are found to have significant effects on thermal phase transitions by influencing two intermolecular forces: π-π stacking interactions between molecular backbones, and van der Waals' interactions between alkyl chains.

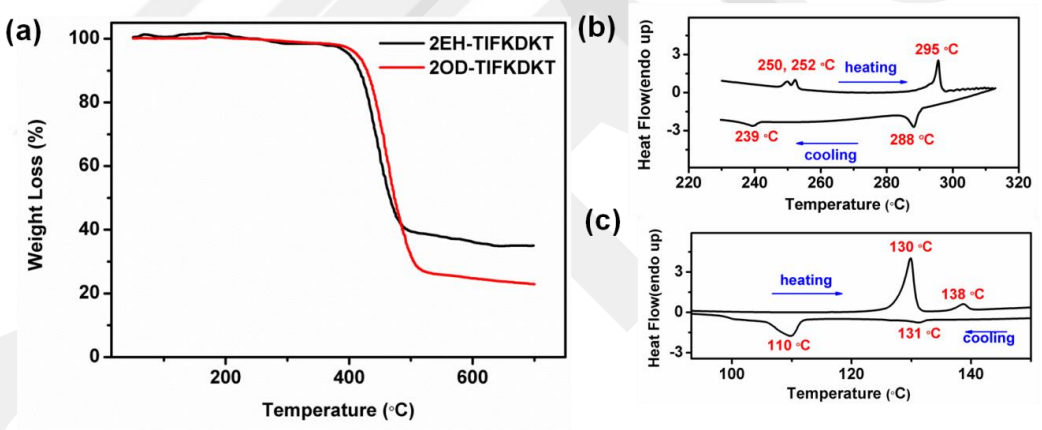

Figure 2.3.2 Thermogravimetric analysis (TGA) (a), and differential scanning calorimetry (DSC) of the compounds **2EH-TIFDKT** (b) and **2OD-TIFDKT** (c) at temperature ramps of 10 °C min^{-1} under N_2.

Table 2.3.2 Summary of Thermal, Optical Absorption, and Electrochemical Properties of Compounds 2EH-TIFDKT, 2OD-TIFDKT, and β-DD-TIFDKT[11] and Corresponding Estimated Frontier Molecular Orbital Energies.

Compounds	T_{mp} (°C)	T_{DSC}(°C)[a] heating (cooling)	T_{TGA}[b] (°C)	$E_{red}^{1/2}$ (V)[c]	E_{LUMO} (eV)[d]	E_{HOMO} (eV)[e]	$\lambda_{abs}^{sol.}$ (nm) (E_g (eV))[f]	$\lambda_{abs}^{film.}$ (nm) (E_g (eV))[g]
2EH-TIPDKT	292	250, 252, 295 (239, 288)	401	-0.75 (vs. Ag/AgCl)	-3.65	-5.60	383, 556 (1.95)	371, 630 (1.79)
2OD-TIFDKT	135	130, 138 (110, 131)	415	-0.77 (vs. Ag/AgCl)	-3.63	-5.57	384, 560 (1.94)	406, 648 (1.76)
β-DD-TIFDKT[14]	152	155 (128)	420	-0.74 (vs. SCE)	-3.70	-5.75	377, 525 (2.05)	365, 594 (1.89)

[a] From DSC scans under nitrogen at a scan rate of 10 °C/min. [b] Onset decomposition temperature measured by TGA under nitrogen. [c] 0.1 M $Bu_4N^+PF_6^-$ in THF at a scan rate of 50 mV/s. [d] Estimated from the equation $E_{LUMO} = -4.40$ eV - $E_{red}^{1/2}$. [e] E_{HOMO} is calculated from $E_g = E_{LUMO} - E_{HOMO}$. [f] From optical absorption in THF, optical band gap is estimated from the low energy band edge of the UV-Vis absorption spectrum. [g] From optical absorption as spin-coated thin film on glass, optical band gap is estimated from the low-energy band edge of the UV-Vis absorption spectrum.

2EH-TIFDKT and **2OD-TIFDKT** exhibit impressive thermal stability with thermolysis onset temperatures of 401 °C and 415 °C, respectively, which enables the semiconductor deposition over a broad range of processing temperature (Figure 2.3.2.a). Both compounds leave 20–40% nonvolatile residues, indicating some degree of chemical decomposition upon heating to > 500 °C. Therefore, semiconductors thin-films fabricated by thermal evaporation technique may be contaminated by decomposition products, which is consistent with the observed OTFT inactivity (vide infra). On the other hand, differential scanning calorimetry (DSC) measurements indicate endotherms at 295 °C and 138 °C for **2EH-TIFDKT** and **2OD-TIFDKT**, respectively, which corresponds to the melting points (T_{mp} = 292–293 °C for **2EH-TIFDKT** and T_{mp} = 135–136 °C for **2OD-TIFDKT**) observed in conventional melting point measurements (Figures 2.3.2.b and 2.3.2.c). The corresponding exothermic crystallization transitions are observed at 288 °C for **2EH-TIFDKT** and at 131 °C for **2OD-TIFDKT** in the reverse scans. In addition, for both compounds endothermic thermal transitions are observed prior to major melting process, which may be attributed to transition from solid state to a liquid crystalline mesophase as a result of lipophilic alky chain melting. The observed melting point for **2EH-TIFDK** is much higher (ΔT_{mp}= 140 °C) than that of the corresponding beta-substituted structure, **β-DD-TIFDKT** (ΔT_{mp}= 152–153 °C). Considering the similar π-core sizes and relatively small changes in molecular weights, the observed large melting point increase indicates more effective solid-state packing, which is most likely due to enhanced intermolecular cohesive forces through dipole-dipole, donor-acceptor, and π-π interactions as a result of enhanced molecular backbone planarity. The single-crystal obtained for the intermediate precursor **2** shows that indeno[1,2-b]fluorene-6,12-dione cores form favorable π-π interactions (3.43 Å) and close dipole-dipole interactions (-C=O/-C=O) with a *parallel*-alignment (vide infra). On the other hand, when the lipophilic alkyl chains are changed to longer 2-octyldodecyl chains, the melting point significantly decreases to T_{mp} = 135–136 °C. This is ∼17 °C lower that of **β-DD-TIFDKT**, which indicates that the structural planarity gained by α,ω-substitution is overweighed by the presence of bulky swallow tail alkyl chains, which deteriorates the intermolecular interactions and results in poor solid-state packing. Based on these thermal studies, 2-ethylhexyl substitution might reflect the ideal balance between good solid-state packing and high solubility, which may lead to the highest OTFT performance from solution processing.

2.3.3. Optical and Electrochemical Properties

The UV-Vis absorption spectra of the present compounds in THF and as thin-films are shown in Figures 2.3.3.a and 2.3.3.c, and optical data are collected in Table 2.3.2. The absorption spectra of **2EH-TIFDKT** and **2OD-TIFDKT** exhibit three maxima, two of them located below 400 nm, and the third one at 556–560 nm. The higher energy maxima (383nm for **2EH-TIFDKT** and 384nm for **2OD-TIFDKT**) correspond to the π-π* transitions of the indenofluorene-thiophene backbone, whereas the weaker absorptions at lower energies (556nm for **2EH-TIFDKT** and 560nm for **2OD-TIFDKT**) are attributed to the symmetry forbidden n-π* transition of the carbonyl group. The optical band gaps are estimated from the low-energy absorption edge as 1.95 eV (**2EH-TIFDKT**) and 1.94 eV (**2OD-TIFDKT**). These gaps are ~0.1 eV smaller than that of **β-DD-TIFDKT** (2.05 eV), and the observed absorption maxima are red-shifted by 5–35 nm compared to that of **β-DD-TIFDKT** (377 nm/525 nm in THF). These changes are indicative of enhanced π-conjugation of the molecular backbone as a result of the planarization of the π-core upon relocating alkyl substituents. For both compounds, significant bathochromic shifts (Δλ = 80–90 nm) are observed in the solid-state UV-Vis absorption spectra, most likely due to molecular planarization and enhanced π-π stacking/donor-acceptor interactions when going from dilute solution to solid-state.

The redox properties of the present compounds were investigated by cyclic voltammetry in solution. The cyclic voltammograms are shown in Figure 2.3.3.b, and electrochemical data are summarized in Table 2.3.2. The measurements were performed in THF by using Pt as the working and counter electrodes, and Ag/AgCl (3M NaCl) as the reference electrode. Both compounds, **2EH-TIFDKT** and **2OD-TIFDKT** exhibit two reversible reduction peaks with the first half-wave potentials ($E_{red}^{1/2}$) located at 0.75 V (vs. Ag/AgCl) and 0.77 V (vs. Ag/AgCl), respectively, which are assigned as reduction of the diketone to the quinonoidal dianion. The reversibility of both reductions demonstrates the good redox stability of these new molecular diketone cores. The LUMO energies are estimated as -3.65eV and -3.63 eV for **2EH-TIFDKT** and **2OD-TIFDKT**, respectively, using the vacuum level energy of the Ag/AgCl as -4.40 eV. The corresponding HOMO

energies of -5.60 eV and -5.57 eV, respectively, are calculated from the optical band gaps. The optical and electrochemical characterizations confirm the theoretically estimated increases in the LUMO (0.05–0.07 eV) and HOMO energy levels (0.15–0.17 eV) after alkyl chain tailoring. From a molecular orbital energetic standpoint, the observed energies for HOMO and LUMO are highly favorable to achieve simultaneous hole and electron transport in these semiconductor thin-films.

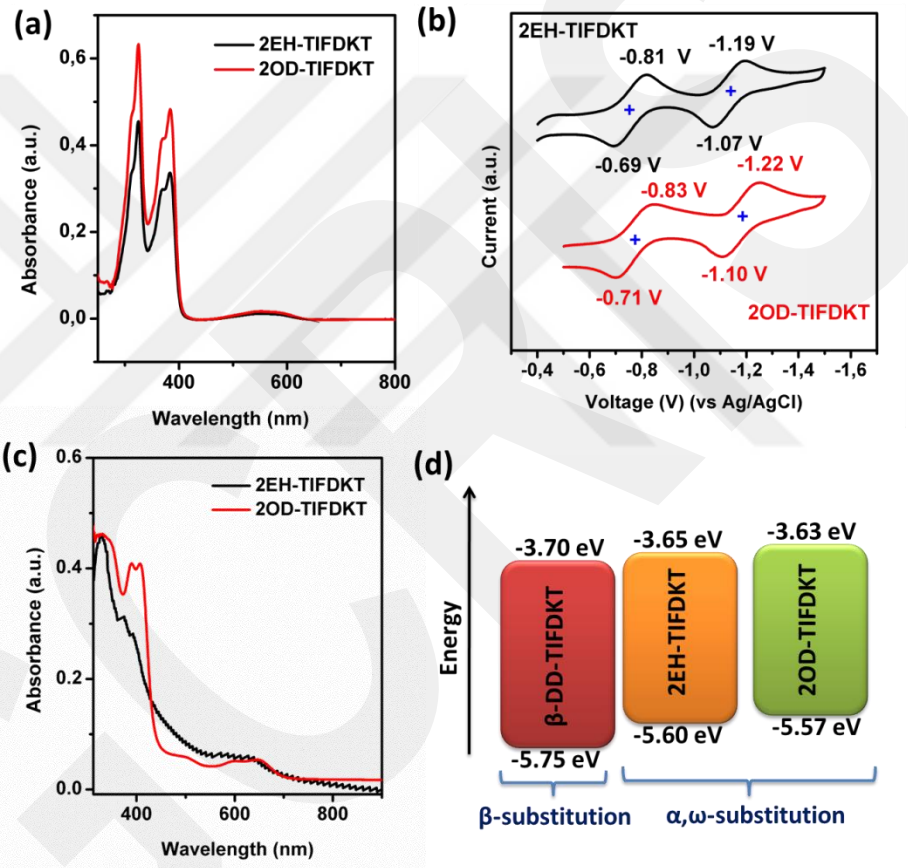

Figure 2.3.3 (a) Optical absorption in THF solution. (b) Cyclic voltammograms in THF (0.1M $Bu_4N^+PF_6^-$, scan rate = 100 $mV \cdot s^{-1}$). (c) Optical absorption as thin-films. (d) Experimentally derived HOMO-LUMO energy levels for **2EH-TIFDKT** and **2OD-TIFDKT**. Note that the energy level values for **β-DD-TIFDKT** is taken from literature[14] measured under the same experimental conditions.

2.3.4. Single-Crystal Structure

Since diffraction-quality single-crystals of the semiconductors, **2EH-TIFDKT** and **2OD-TIFDKT,** were not obtained, we focused on growing the crystals of the intermediate compound **2** to better understand the structural features of the indeno[1,2-b]fluorene-6,12-dione acceptor unit. Single crystals of **2** were grown using physical vapor transport in a thermal gradient under high vacuum (1×10^{-5} Torr), and its solid state structure was confirmed by single-crystal X-ray analysis (Figure 2.3.4.a).

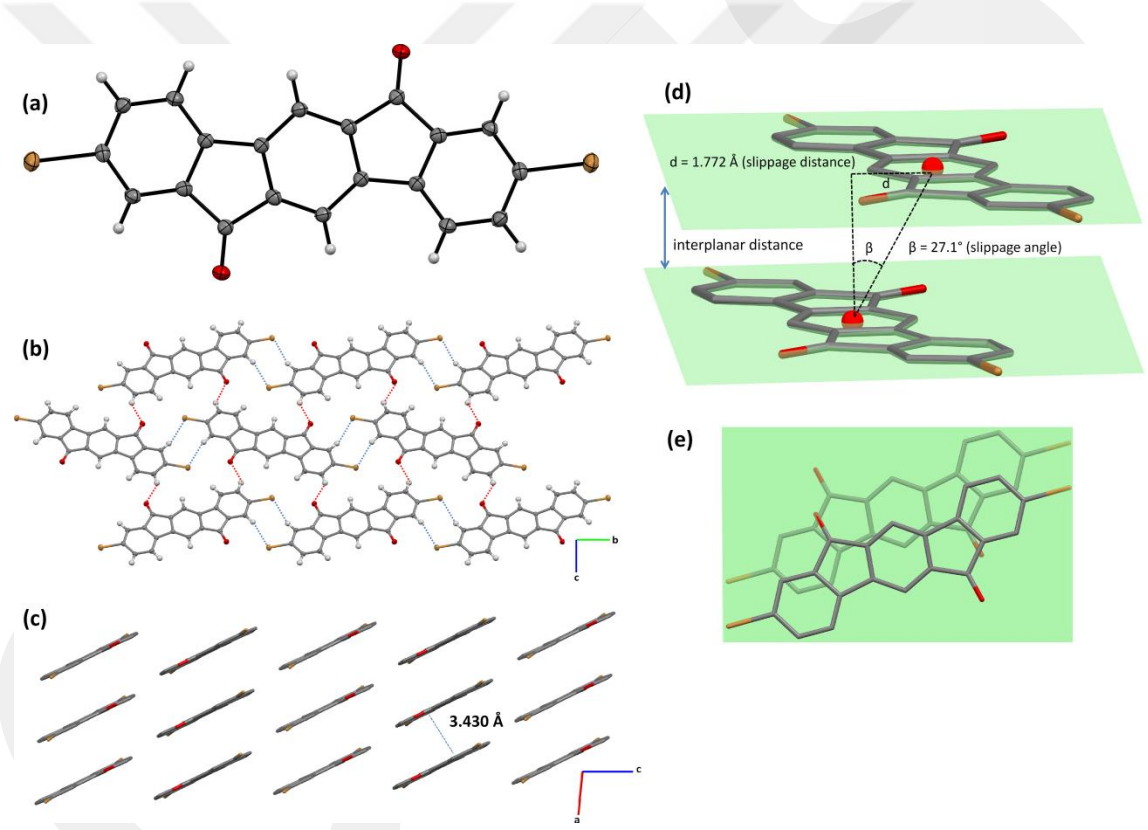

Figure 2.3.4 (a) ORTEP drawings of the crystal structure (50% probability level). **(b)** Perspective view of 2D network via –CH···Br (blue dashed lines) and –CH···O (red dashed lines) contacts. **(c)** Perspective view of brick-wall packing arrangement with an interplanar distance of 3.430 Å. **(d)** and **(e)** Representations of pairs of indeno[1,2-b]fluorene-6,12-dione molecules arranged in a slipped π-stacked fashion (The red, grey, brown, and white coloured atoms represent O, C, Br, and H, respectively).

The conjugated backbone of indeno[1,2-b]fluorene-6,12-dione is found to lie across an inversion center with a substantially planar molecular configuration with negligible interplanar twists. This is consistent with the computational optimization results, and it is similar to the previously reported fluorinated indeno[1,2-b]fluorene-6,12-dione derivative.[89] The carbonyl (–C=O) functionalities are found to stay completely within the molecular plane, which indicates a highly favorable structural conformation for effective π-conjugation between these functionalities and the indeno[1,2-b]fluorene-6,12-dione core. For compound **2**, short –CH···O (2.59 Å) and -CH···Br (3.03 Å) contacts are found to be effective between adjacent molecules (8 interactions per molecule; Fig. 2.3.4.b), which results in the formation of continuous graphene-like two-dimensional π-layers. These interactions take place between benzene hydrogens, which are adjacent to the bromo functionality, and carbonyl oxygen and bromo substituents, respectively, which are ~0.1 Å smaller than the corresponding van der Waals distances (r_{vdw}(O) + r_{vdw}(H) = 2.72 Å and r_{vdw}(Br) + r_{vdw}(H) = 3.05 Å).[90] These 2D layers are packed in a brick-wall packing arrangement (Fig. 6c), which allows π-π-stacking interactions with a favorable interplanar distance of 3.43 Å. In addition, based on the molecular alignments between the layers, strong local dipoles of -C=O groups are found to align parallel to each other with slight slipping (slippage distance d= 1.772 Å, slippage angle β = 27.1°) (Figures 2.3.4.d and 2.3.4.0e). This indicates the presence of dipole–dipole interactions, which may overcome the dominating CH/π interactions (edge-to-face) in the classical herringbone arrangement, and results in the current highly-favorable slipped-cofacial arrangement. Cofacial π-stacked packing motif has been previously shown in high-mobility "TIPS-pentacene" and "TES-ADT" semiconductors.[91] It's noteworthy that although the solid-state packing of **2** does not resemble those of the final semiconductors, it still reveals key structural features of this acceptor core. The favorable structural properties of the indeno[1,2-b]fluorene-6,12-dione core such as short π–π stacking distances, close dipole-dipole interactions, core planarity, cofacial molecular arrangement, and lamellar structure formation hold great promise for their incorporation into larger molecular semiconductors for efficient charge-transport in the solid-state.

2.3.5. Thin-Film Morphology and Microstructure

Microstructural order in the new solution-processed semiconductor thin films was assayed by θ-2θ X-ray diffraction (XRD) scans. As shown in Figures 2.3.5.7, 2.3.5.1, 2.3.5.2, 2.3.5.5, 2.3.5.6 all the semiconductor films exhibit highly crystalline patterns with diffraction peaks up to ninth-order, indicating a high degree of solid state ordering. Based on the highest mobility thin-films achieved via solution-shearing of **2EH-TIFDKT** and **2OD-TIFDKT**, the major primary diffraction peaks (100) are observed at 2θ = 3.52° and 2θ = 2.92°, respectively, corresponding to *d*-spacings of 25.1 Å and 30.2 Å (Figure 2.3.5.7). Although both molecules share exactly the same π-core, thin-films based on **2OD-TIFDKT** show larger *d*-spacings compared to those of **2EH-TIFDKT** as a result of the presence of longer alkyl substituents (2-octyldodecyl *vs.* 2-ethyhexyl).

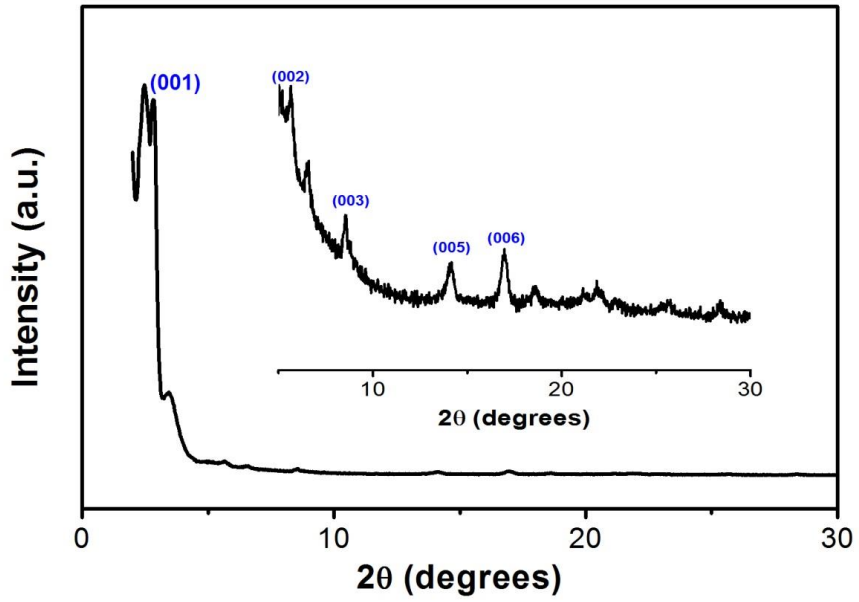

Figure 2.3.5.1 θ-2θ X-ray diffraction (XRD) scans of films fabricated by drop-casting of **2OD-TIFDKT.**

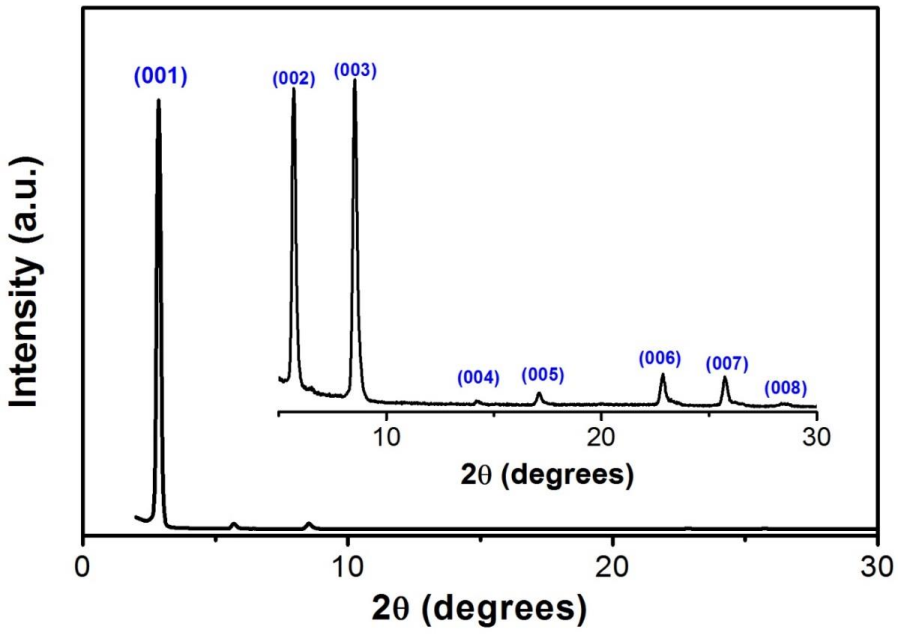

Figure 2.3.5.2 θ-2θ X-ray diffraction (XRD) scans of films fabricated by droplet-pinned crystallization of **2OD-TIFDKT**.

This also indicates that alkyl chains are somewhat aligned along the substrate normal and they are effective in determining the out-of-plane *d*-spacings. These *d*-spacings are considerably smaller than the computed molecular lengths for both compounds (30.5 Å for **2EH-TIFDKT** and 41.7Å for **2OD-TIFDKT**), and longer than the length of **T-IFDK-T** π-core (19.1 Å). This indicates that alkyl chains are interdigitated, and π-cores and/or alkyl chains may be tilted from the substrate normal. Although the tilting angles and the extent of interdigitation together determine the *d*-spacing, based on the good mobilities observed, it's very likely that the molecules are adopting a mostly face-on π-orientation in the out-of-plane microstructure with significant alkyl chain interdigitation.

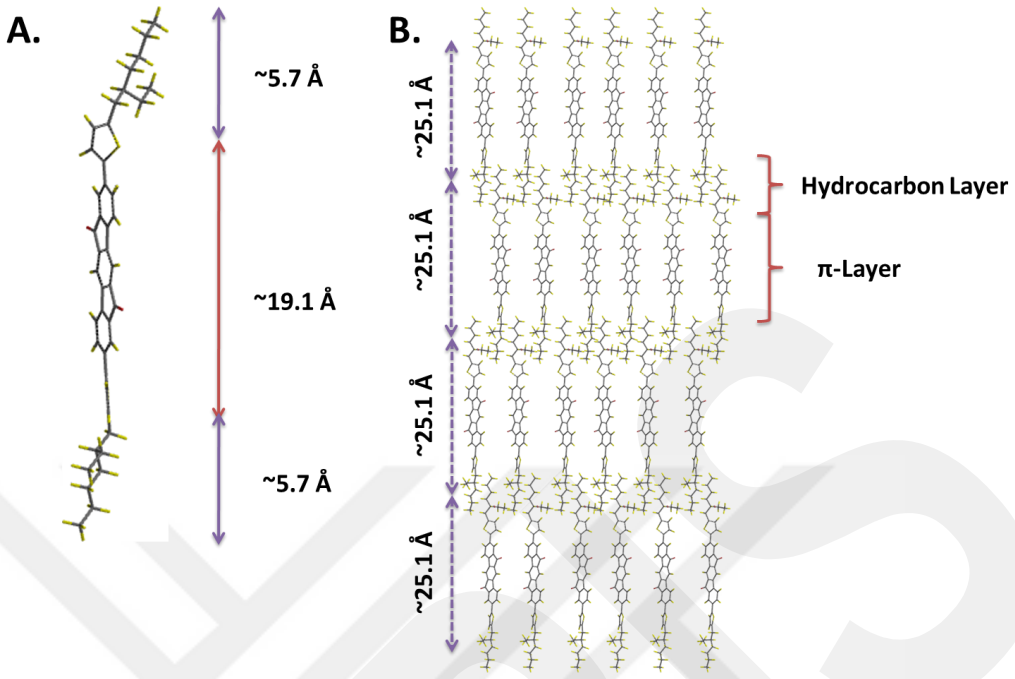

Figure 2.3.5.3 A. The computed molecular dimensions, and B. Proposed thin-film phase packing motif for **2EH-TIFDKT**.

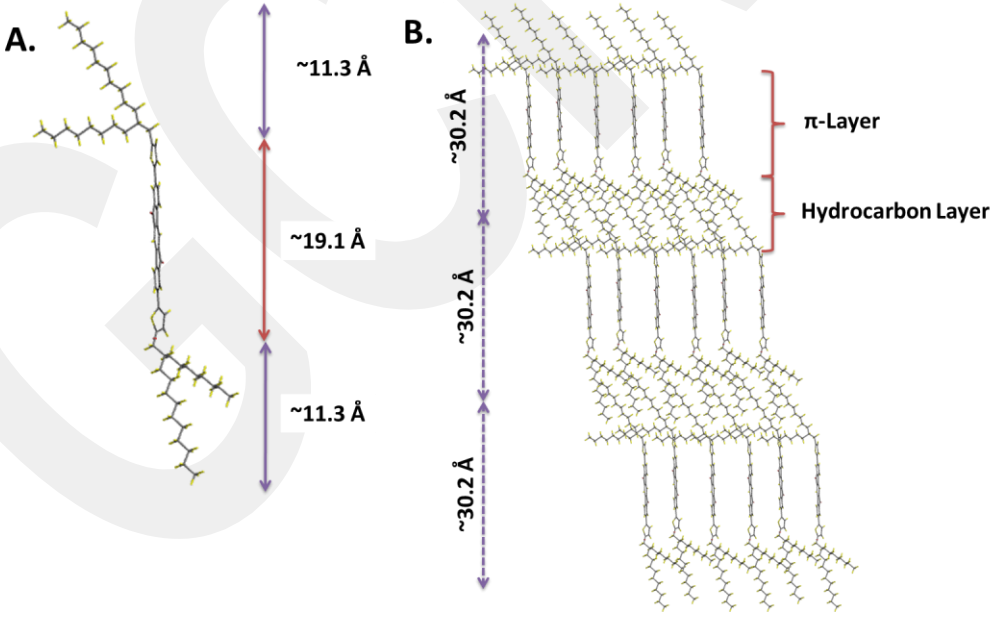

Figure 2.3.5.4 A. The computed molecular dimensions, and B. Proposed thin-film phase packing motif for **2OD-TIFDKT**

This enables the formation of a "layer-by-layer" packing motif consisting of alternately stacked π-cores and intercalated aliphatic chains (Figures 2.3.5.3 and 2.3.5.4), which could explain the good mobilites observed. Surprisingly, a second set of reflections up to the seventh-order is observed in the film of **2EH-TIFDKT**, which points to the presence of a secondary crystalline phase. For **2EH-TIFDKT**-based films, although the diffraction angles remains the same, the relative intensity of the two crystalline phases change with the deposition technique (Figures 2.3.5.5 and 2.3.5.6), and in all cases the lower angle diffraction peaks are found to be the dominant phase.

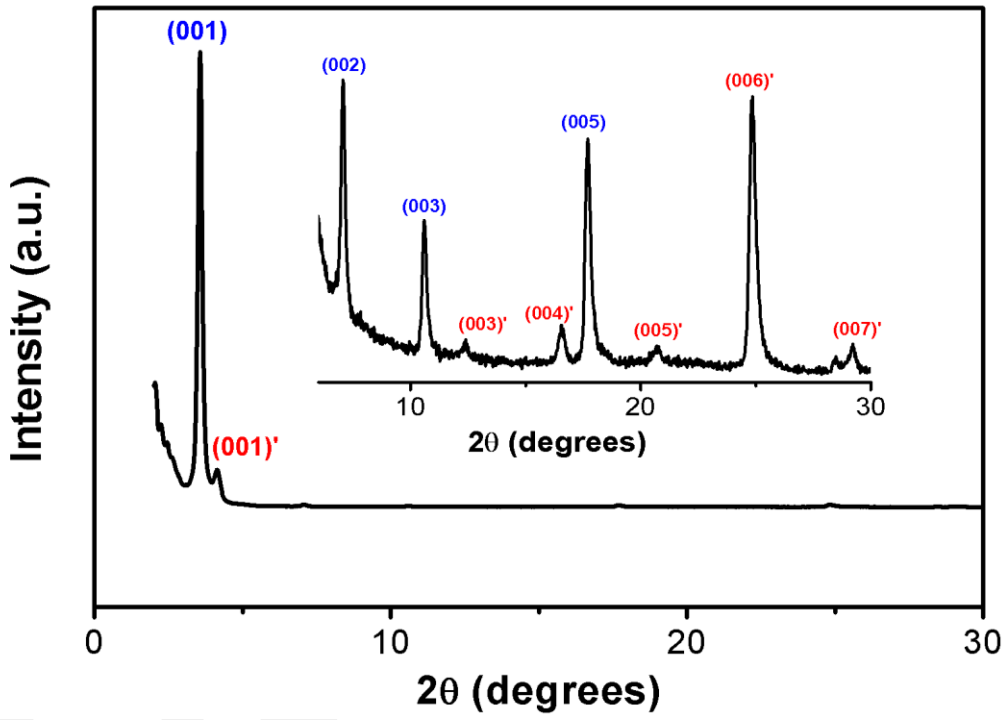

Figure 2.3.5.5 θ-2θ X-ray diffraction (XRD) scans of films fabricated by drop-casting of **2EH-TIFDKT.**

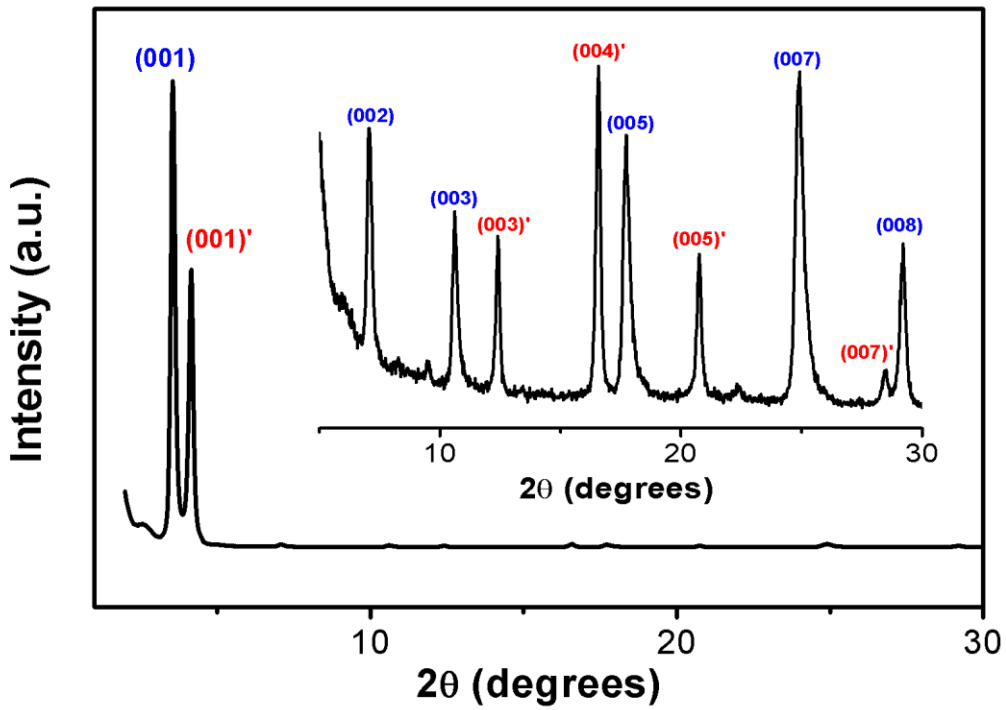

Figure 2.3.5.6 θ-2θ X-ray diffraction (XRD) scans of films fabricated by droplet-pinned crystallization of **2EH-TIFDKT**.

The primary diffraction peak for the secondary phase was at 2θ =4.07° (*d*-spacing = 21.7 Å) corresponding to a likely a more tilted molecular orientation on the surface. Although the presence of two crystalline phases is not unusual for indenofluorene-based thin-films,[81] it is quite surprising that the coexistence of two crystalline phases still leads to good charge carrier mobilities (vide infra).

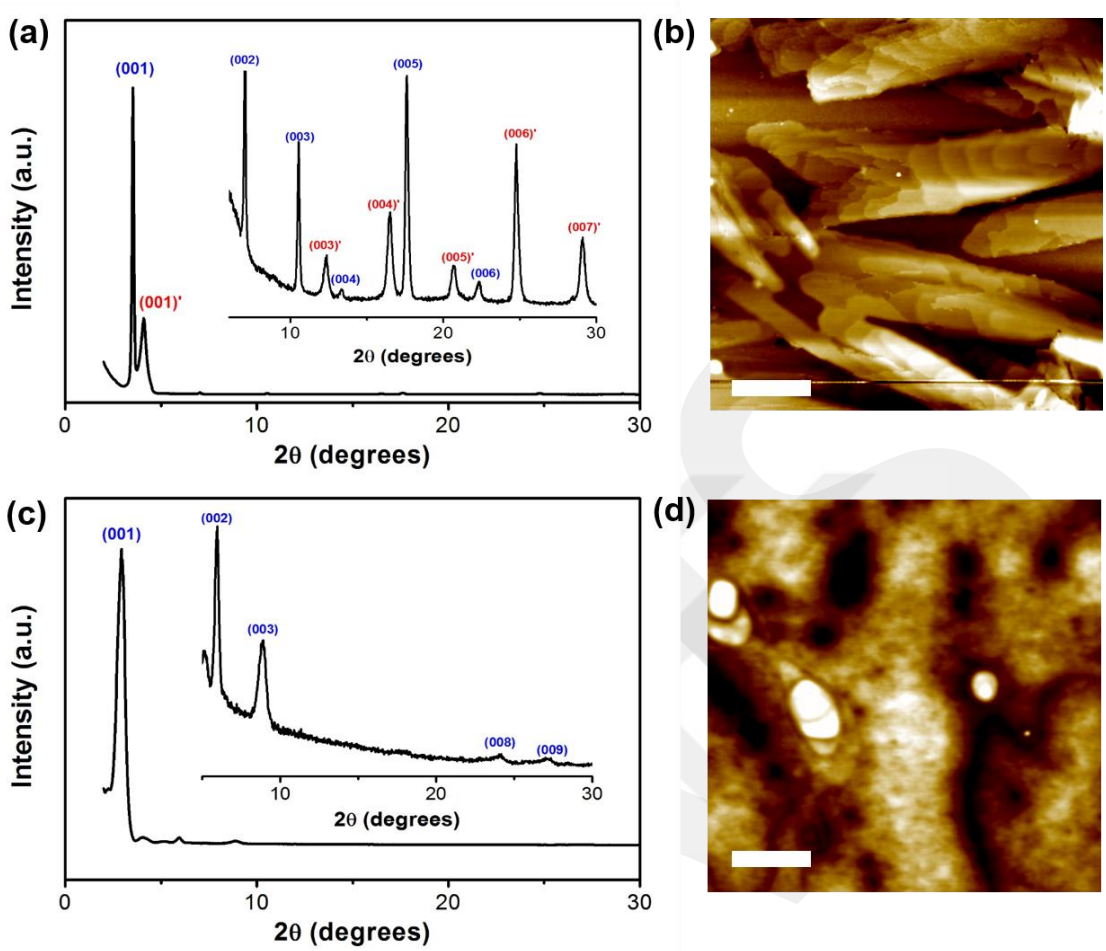

Figure 2.3.5.7 θ-2θ X-ray diffraction (XRD) scans and AFM topographic images of films fabricated by solution shearing of **2EH-TIFDKT** (a and b) and **2OD-TIFDKT** (c and d). Scale bars denote 2 μm.

AFM characterizations of solution-sheared **2EH-TIFDKT** and **2OD-TIFDKT** thin-films reveals relatively homogeneous morphologies with a surface roughness of < 4.28 nm for 10.0 μm × 10.0 μm scan area. For **2EH-TIFDK**, two dimensional platelet grains (~0.5-2.0 μm sizes) grown via layer-by-layer mode are observed. Specifically, grains in solution-sheared thin-films of **2EH-TIFDK** show preferred growth direction on a locale scale forming microscale rods with evident terraced islands. The step heights are ~2.5 nm corresponding to the *d*-spacings obtained from the XRD characterizations. On the other hand, solution-sheared films of **2OD-TIFDKT** exhibit totally different film morphologies with uniform and highly-interconnected isotropic spherulites, which are ~50-200 nm in diameter.

2.3.6. Thin-Film Transistor Device Characterization

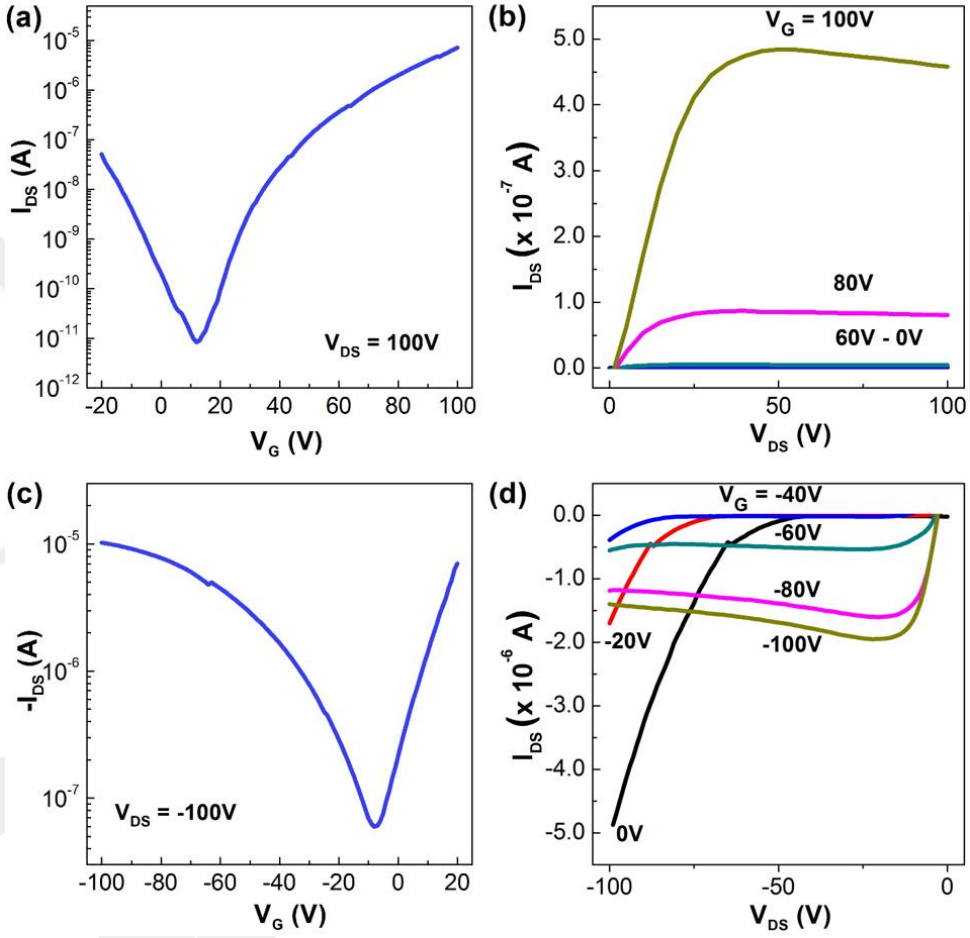

Figure 2.3.6 (a) N type transfer curve, (b) N type output curve, (c) P type transfer curve, and (d) P type output curve of the device with 2EH-TIFDKT

Top-contact/bottom-gate organic thin film transistors (OTFTs) were fabricated with thin-films of **2EH-TIFDKT** and **2OD-TIFDKT** as semiconducting layers via different solution processing methods (solution-shearing (SS), droplet-pinned crystallization (DPC), and drop-casting (DC)) on PS brush-coated Si/SiO_2 substrates.[92]–[95] For solution process, various conditions for the formation of thin-films including solvents (toluene, chlorobenzene, chloroform, *p*-xylene, 1,2-dichlorobenzene, tetralin, and 1,2,4-

trichlorobenzene), concentration of solution, temperature of substrate, and shearing speed were optimized.[96]–[98] Au electrodes were deposited through a shadow mask to define source and drain. Table 2.3.6.2 summarizes the OTFT data, including charge carrier mobility, current on/off ratio, and threshold voltage. As expected from aforementioned physicochemical characterizations, physical vapor deposited films of **2EH-TIFDKT** and **2OD-TIFDKT** were inactive in OTFT devices, which can be attributed to the thermal decomposition of the materials during film deposition. However, solution-processed films of both **2EH-TIFDKT** and **2OD-TIFDKT** exhibit ambipolar behaviors as a result of their reduced band gap and energetically accessible HOMO and LUMO energy levels. It's noteworthy that for the present molecular design, the LUMO energies achieved are not low enough (should be < -4.1 eV) to give ambient-stable electron-transport, and therefore electron mobilities were only observed under vacuum (Table 2.3.6.1).

Table 2.3.6.1. Electrical performances of OTFTs based on Indeno[1,2-b]fluorene-6,12-dione-thiophene derivatives, **2EH-TIFDKT** and **2OD-TIFDKT** measured under ambient condition.

Material	Method	N-channel			P-channel		
		μ_e (cm^2/Vs)	V_T (V)	I_{on}/I_{off}	μ_h (cm^2/Vs)	V_T (V)	I_{on}/I_{off}
2EH-TIFDKT	DC	-	-	-	2.7×10^{-4}	-33	6.3×10^{6}
	DPC	-	-	-	1.6×10^{-4}	-38	2.6×10^{4}
	SS	-	-	-	2.2×10^{-3}	2.8	4.8×10^{2}
2OD-TIFDKT	DC	-	-	-	2.9×10^{-4}	-12	2.0×10^{5}
	DPC	-	-	-	8.0×10^{-4}	-14	8.1×10^{2}
	SS	-	-	-	5.4×10^{-4}	-9.7	5.2×10^{4}

However, electron-transporting high mobility semiconductors with relatively high LUMO energies (> -3.7 eV) are very crucial to the development of green and blue emitting OLET devices.[68] As expected from film morphologies and crystallinities, solution-sheared films of **2EH-TIFDKT** showed the best semiconductor performance with electron and hole mobilities of up to 0.12 $cm^2/V\cdot s$ and 0.02 $cm^2/V\cdot s$, respectively. Among different solution processesing methods applied, SS afforded the highest device performance, compared to DC and DPC. As shown in Table 2.3.6.2, electron and hole mobilities obtained for thin-films formed via DPC and DC methods (~10^{-3}-10^{-4}) were around two orders of magnitude lower than that of SS method. Films of **2OD-TIFDKT** also exhibited ambipolar characteristics

with electron mobility as high as 0.04 $cm^2/V \cdot s$ and hole mobility as high as $3.3\times10^{-4} cm^2/V \cdot s$. For the present semiconductors, the electrical performance of OTFTs is well-correlated with the thin-film microstructures and surface morphologies.

Table 2.3.6.2 Electrical Performance of OTFTs based on Indeno[1,2-b]fluorene-6,12-dione-thiophene Derivatives Developed in this Study.[a]

Material	Method	N-channel			P-channel		
		μ_e (cm^2/Vs)	V_T (V)	I_{on}/I_{off}	μ_h (cm^2/Vs)	V_T (V)	I_{on}/I_{off}
2EH-TIFDKT	DC	1.6×10^{-3}	53	2.8×10^{6}	8.2×10^{-4}	-22	1.5×10^{2}
	DPC	7.7×10^{-4}	46	3.1×10^{2}	2.5×10^{-4}	-4.0	5.3×10^{4}
	SS	0.12	57	8.5×10^{5}	0.02	-62	2.1×10^{2}
2OD-TIFDKT	DC	1.5×10^{-4}	47	6.7×10^{5}	5.3×10^{-7}	-54	5.9×10^{3}
	DPC	0.013	26	1.2×10^{-4}	2.7×10^{-4}	-35	4.2×10^{4}
	SS	0.04	10	2.2×10^{5}	3.3×10^{-4}	-45	1.2×10^{5}

[a]Devices were measured under vacuum.

2.4. Conclusion

In summary, a series of new indeno[1,2-b]fluorene-6,12-dione-thiophene small molecules, **DD-TIFDKT**, **2EH-TIFDKT**, and **2OD-TIFDKT**, has been designed, synthesized and fully characterized. These new semiconductors consist of highly π-conjugated donor-acceptor molecular architectures based on indeno[1,2-b]fluorene-6,12-dione acceptor unit and thiophene donor units, which yields band gaps of 1.7-1.8 eV. The semiconductor structures are α,ω-end-functionalized with linear -*n*-$C_{12}H_{25}$ chains or swallow-tail 2-ethylhexyl-/2-octyldodecyl chains. While the linear -*n*-$C_{12}H_{25}$ chains impart good solubility in β-substituted semiconductor core, they don't provide the desired solubility in α,ω-end-functionalized core. However, 2-ethylhexyl and 2-octyldodecyl chains are found to yield entirely solution-processable molecular systems. The detailed study on the effects of alkyl chain size and orientation on the optoelectronic properties, intermolecular cohesive

forces, thin-film microstructures, and charge transport performances of the new semiconductors reveal crucial structure-property-function relationships. Density functional theory (DFT) calculations are found to be in excellent agreement with the observed electronic structure and physicochemical trends associated with alkyl chain engineering, and provide further insight. In the rational design of the new molecules, the repositioning of the insulating β-substituents to molecular termini is found to significantly enhance the π-core planarity while maintaining a good solubility. 2-Ethylhexyl substitution is shown to provide the finest balance of good solubility, favorable physicochemical/optoelectronic properties, effective solid-state packing and high electrical performance. The solution-processed OTFT devices of the current semiconductors, **2EH-TIFDKT** and **2OD-TIFDKT**, exhibit excellent ambipolar behavior with carrier mobilities of 0.04−0.12 $cm^2/V \cdot s$ and 0.0003−0.02 $cm^2/V \cdot s$ for electrons and holes, respectively, and I_{on}/I_{off} ratios of 10^5-10^6. Specifically, solution-sheared thin-films of **2EH-TIFDKT** show ambipolar device operation with electron and hole mobilities of 0.12 $cm^2/V \cdot s$ and 0.02 $cm^2/V \cdot s$, respectively, with I_{on}/I_{off} ratios of 10^5-10^6, which indicates two-three orders of carrier mobility enhancement compared to those of solution-processed β-substituted counterparts. The findings presented here suggest that through computational modeling guided rational design and synthetic tailoring of insulating alkyl substituents, electron/hole transport characteristics of molecular semiconductors can be significantly enhanced while still maintaining a favorable solution-processibility. We believe that our results will provide key structural/electronic information and additional motivation to investigate and optimize molecular semiconductor structures for high-performance organic optoelectronic devices.

Chapter 3

Solution-Processable BODIPY-Based Small Molecules for Semiconducting Organic Thin-Film Transistors

3.1. Introduction

Solution-processable π-conjugated small molecules allow for the fabrication of thin, low-weight, and flexible organic optoelectronic devices such as field-effect transistors (OFETs)[12], light-emitting transistors (OLETs)[53], and photovoltaics (OPVs)[99]. They offer significant physical/chemical advantages over their inorganic counterparts including low-cost, compatibility with flexible substrates and roll-to-roll printing process, and structural versatility.[60], [100], [101] In the past several decades, the major advances in the performances of organic optoelectronic devices have been mainly due to the development of novel semiconducting structures employing properly designed π-architectures and the detailed understanding of their optoelectronic properties.[43], [102]–[106] Therefore, the continued research efforts for the search of new semiconductor π-structures and elucidating structure-property-device performance relationships is critical to developing novel optoelectronic platforms with varied functionalities. To this end, 4,4-difluoro-4-bora-3a,4a-diaza-s-indacene (BODIPY) stays as a relatively unexplored π-core for use in semiconductor structures, despite it has been heavily studied in the past decades as highly fluorescent functional dyes for chemosensors, fluorescent switches and biochemical labels.[107] BODIPY is a coplanar and highly electron-deficient π-core with a high dipole moment (μ = 3.4-4.2 D), which makes it an ideal π-acceptor unit to build donor-acceptor type semiconductor architectures.[78], [108] Furthermore, considering its excellent photophysical

and photochemical properties, BODIPY-based semiconductors would be ideal functional materials for light-based optoelectronic applications such as OLETs and OPVs.[109] However, to date there has been very few reports on BODIPY-based semiconductor small molecules for optoelectronics with typical charge carrier mobilities of 10^{-5}-10^{-3} $cm^2/V \cdot s$.[110]

In addition, BODIPY system's optical and electronic characteristics are tunable via facile synthetic modifications on the boron-dipyrromethene core.[108], [111] Despite all of these advantages, to date very few BODIPY-based molecular and polymeric semiconductors have been studied in optoelectronics,[112]–[115] and more specifically in organic thin-film transistors (OTFTs), with the most promising ones (**M1** and **M2** in Figure 3.1.1) exhibiting relatively low OTFT charge carrier mobilities of ~10^{-5}-10^{-3} $cm^2/V \cdot s$.[109], [110] To this end, we have recently developed a series of BODIPY-thiophene copolymers, in which the charge carrier mobility was enhanced to μ_h = 0.17 $cm^2/V \cdot s$ (>10000×), remaining the highest mobility BODIPY-based polymer semiconductor (**P1** in Figure 3.1.1).[78] Since such high mobilities were accessible only for BODIPY-based π-conjugated polymeric backbones, the interesting question is whether substantial mobilities are possible for BODIPY-based molecular semiconductors. From a materials perspective, small molecules are advantageous over polymers because of synthetic reproducibility, structural versatility, ease of purification, monodispersity, and high degree of crystallinity.[12], [99], [116]–[118] Thus, the rational engineering of molecular architectures embedding properly designed BODIPY units is very crucial to enhance charge transport as well as to better understand of the properties of BODIPY-based systems. Realization of good charge-transport with BODIPY-based molecular systems is expected to greatly advance technologies where both charge transport and photophysical processes take place such as in organic photovoltaics (OPV), organic light-emitting diodes (OLEDs) and organic light-emitting transistors (OLETs).[42], [119]–[121]

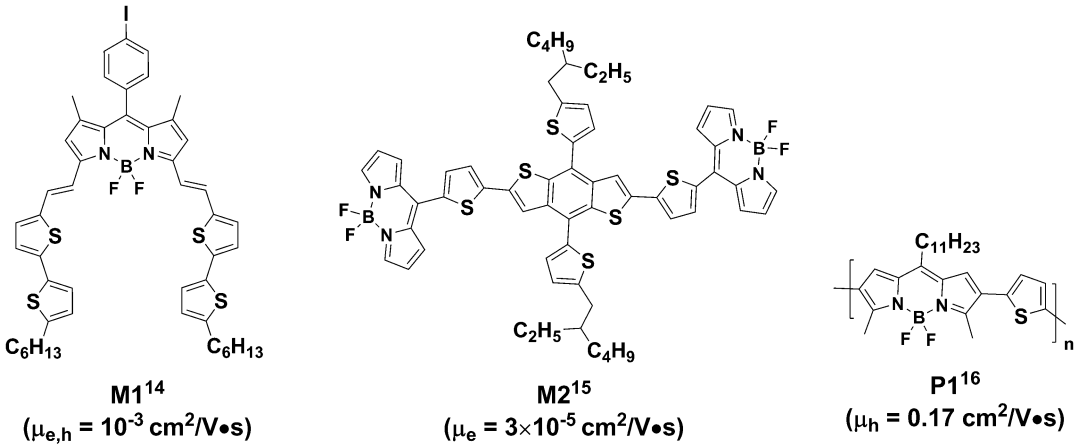

Figure 3.1.1 Chemical structures of previously reported BODIPY-based semiconductors **M1**, **M2** and **P1**.

In this thesis, we report the synthesis, characterization, and field-effect response of a novel two *p*-channel (**BDY-3T-BDY** and **BDY-4T-BDY**), and one *n*-channel (**BDY-PhAc-BDY**) semiconductor molecule, (Figure 3.1.2).

Here, we report the design and synthesis of three new molecular semiconductors **BDY-3T-BDY**, **BDY-4T-BDY** and **BDY-PhAc-BDY** (Figure 3.1.2). Two of them (**BDY-3T-BDY**, **BDY-4T-BDY)**, based on an acceptor-donor-acceptor (A-D-A) molecular architecture, in which BODIPY and terthiophene (3T)/quaterthiophene (4T) units are used as acceptor and donor units, respectively. BODIPYs are connected to the α,ω-oligothiophene cores through their *meso*-positions to achieve linear and symmetrical molecular architectures featuring π-conjugation and optimized molecular energetics. It is noteworthy that the approach of employing π-electron deficient units at the molecular termini of a π-donor has been successfully utilized to enable numerous *n*-channel semiconductors.[77][122] Therefore, in the semiconductor design, we envision that BODIPY may be an ideal acceptor end unit since it has strong electron-withdrawing characteristics, and it may provide negative inductive (-I) and mesomeric (-M) effects. This approach should facilitate the delocalization and stabilization of charge carriers (i.e., electrons). The new semiconductors are designed without any lipophilic substitution on the 4,4'-thiophene and 1,7-BODIPY positions to minimize intramolecular torsions and maximize intermolecular interactions. Furthermore the BODIPY unit exhibits strong dipoles (μ = 3.38 Debye) oriented toward the 4,4′-fluorine

substituents, which could facilitate dipolar intermolecular interactions and result in ordered thin-film phases. This dipole is also expected to enhance the solubility of the current semiconductors *via* dipolar interactions with the solvent molecules. In addition, the presence of fluorine atoms may induce non-bonding intermolecular interactions (e.g. –F···S–, and –F···N–) to enhance thin-film ordering. The new semiconductors were characterized by $^{1}H/^{13}C$ NMR, mass spectrometry, cyclic voltammetry, UV-Vis spectroscopy, differential scanning calorimetry, and thermogravimetric analysis. The single-crystal X-ray diffraction (XRD) characterization of a key intermediate reveals crucial structural properties. Top-contact/bottom-gate OTFT devices were fabricated by physical vapor deposition or solution shearing the semiconductors, and the resulting devices exhibited *n*-channel charge-transport with electron mobilities of up to 0.01 $cm^2/V{\cdot}s$ and current on/off ratio of $>10^8$, which is currently the highest reported to date for BODIPY-based molecular semiconductors. Although these performances are lower than those of the state-of-the-art solution-processed OTFT devices, it is regarded as an important step towards the realization of high performance BODIPY-based semiconductor films.

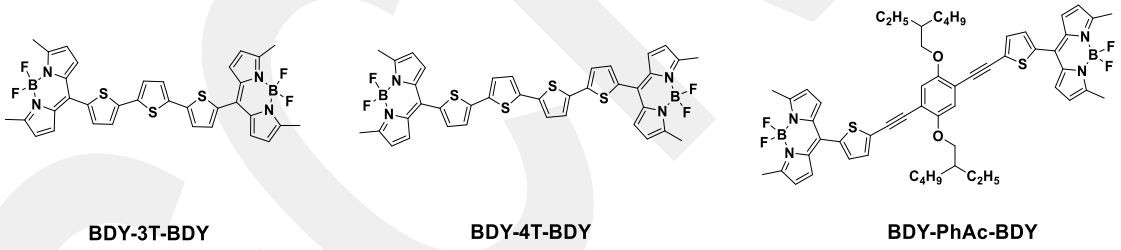

Figure 3.1.2. The chemical structure of **BDY-3T-BDY, BDY-4T-BDY** and **BDY-PhAc-BDY**.

On the other hand, we report the synthesis, characterization, and field-effect response of a novel *n*-channel semiconductor molecule, **BDY-PhAc-BDY** (Figure 3.1.2). In this structure, rod-shaped 1,4-bis-(thienylethynyl)2,5-dialkoxybenzene π-architecture employs 2-ethylhexyloxy electron-donating groups on the central phenyl ring and terminal highly electron-deficient BODIPY π-units. Alkyne linkages are employed between sterically-bulky central phenyl core and thienyl units as a spacer to result in shape-persistent rod-like structure with further extended effective π-conjugation length.[56] Note that, due to its quasi-

cylindrical electronic symmetry, alkyne linkages are advantageous to accommodate steric and conformational constraints. The rationale of having BODIPYs linked to five-membered thiophene units from their meso positions is to minimize inter-ring torsions between donor and acceptor units, and to extend π-conjugation along the molecular backbone. Furthermore, 2-ethylhexyloxy lipophilic substituents provide the required solubility in common organic solvents for convenient purification and thin-film fabrication. Donor-acceptor backbone provides a low optical band gap of 2.2 eV with a relatively stabilized LUMO/HOMO energy level of -3.56/-5.68 eV for unipolar *n*-channel semiconductivity. Single-crystal X-ray diffraction (XRD) analysis shows important structural features about the new semiconductor. The solution-processed **BDY-PhAc-BDY**-based devices exhibit μ_e = 0.004 $cm^2/V \cdot s$ with I_{on}/I_{off} ratios of 10^5-10^6, which is the highest OFET performance reported so far for BODIPY-based small molecules having alkyne linkages. Detailed morphological and microstructural thin-film analysis reveals the formation of highly-crystalline one-dimensional (1-D) microribbons ([010] in the out-of-plane direction) as a result of favorable "-CH···π" and "π···π" intermolecular interactions. Our results clearly offer crucial guidance for the molecular design of BODIPY-based semiconductor molecules and easily fabricable microribbon-based thin-films for *n*-channel OFETs.

3.2. Experimental of Solution-Processable BODIPY-Based Small Molecules for Semiconducting Microfibers in Organic Thin-Film Transistors

3.2.1. Materials and Methods

All reagents were purchased from commercial sources and used without further purification unless otherwise noted. Conventional Schlenk techniques were used, and reactions were carried out under N_2 unless otherwise noted. NMR spectra were recorded on a Bruker 400 spectrometer (^{1}H, 400 MHz; ^{13}C, 100 MHz). Elemental analyses were performed on a LecoTruspec Micro model instrument. MALDI-TOF was performed on a Bruker Microflex LT MALDI-TOF-MS instrument. Thermogravimetric analysis (TGA) and differential scanning calorimetry (DSC) measurements were performed on Perkin Elmer Diamond model instruments under nitrogen at a heating rate of 10 °C/min. UV-Vis absorption measurements were performed on a Shimadzu, UV-1800 UV-Vis Spectrophotometer. Fluorescence emission spectra were recorded on a Varian Eclipse spectrofluorometer using 1 cm path length cuvettes at room temperature. The fluorescence quantum yield values were determined in toluene or THF by comparing with the fluorescence of Rhodamine 6G as the standard (Φ_F = 0.76 in water). Electrochemistry was performed on a C3 Cell Stand electrochemical station equipped with BAS Epsilon software (Bioanalytical Systems, Inc., Lafayette, IN). Prior to the synthesis, the optimization of the molecular geometries and total energy calculations were carried out using density functional theory (DFT) at the B3LYP/6-31G** level by using Gaussian 09.[86]

3.2.2. Crystal Structure Determination

The intensity data for **BDY-1** were collected on an Bruker APEX II QUAZAR three-circle diffractometer using monochromatized Mo K_α X-radiation ($\lambda = 0.71073$ Å). Indexing was performed using APEX2. Data integration and reduction were carried out with SAINT. Absorption correction was performed by multi-scan method implemented in SADABS. The structure was solved and refined using the Bruker SHELXTL Software Package. All non-hydrogen atoms were refined anisotropically using all reflections with $I > 2\sigma(I)$. The C-bound H atoms were positioned geometrically and refined using a riding mode. Crystallographic data and refinement details of the data collection for **BDY-1** are summarized in Table 3.2.2. The final geometrical calculations and the molecular drawings for **BDY-1** were carried out with Platon (version 1.17) and Mercury CSD (version 3.5.1) programs.

Table 3.2.2. Crystal data and refinement parameters for ***BODIPY***.

Empirical Formula	$C_{15}H_{12}BBrF_2N_2S$
Formula weight (g. mol^{-1})	381.05
Temperature (K)	299(2)
Wavelength (Å)	0.71073
Crystal system	Monoclinic
Space group	*P* 2_1/c
a (Å)	6.3938(11)
b (Å)	15.112(2)
c (Å)	15.986(3)
α(°)	90
β(°)	96.680(10)
γ(°)	90
Crystal size (mm)	0.142 x 0.207 x 0.425
V (Å^3)	1534.1(4)
Z	4
ρcalcd (g. cm^{-3})	1.650
μ (mm^{-1})	2.832
F(000)	760
θ range for data collection (°)	1.86 – 26.37
h/k/l	-7/7, -18/18, -19/18
Reflections collected	16075
Independent reflections	3120 [R(int) = 0.0983]
Absorption correction	Multi-scan
Data/restraints/parameters	3120 / 0 / 201
Goodness-of-fit on F^2	1.040
Final R indices [I > 2σ(I)]	R_1= 0.0462, wR_2= 0.1052
R indices (all data)	R_1= 0.0783, wR_2= 0.1199
Largest diff. peak and hole (e.Å^{-3})	0.521 and -0.517

3.2.3. Synthesis and Characterization

3.2.3.1. Synthesis of 5-bromo-2-thiophene carbaldehyde (1).

N-bromosuccinimide (8.7 g, 49.04 mmol) was slowly added to a solution of 2-thiophenecarboxaldehyde (5.0 g, 44.6 mol) in anhydrous $CHCl_3$ (100 mL). The reaction mixture was stirred for 14 h at room temperature. Then, the mixture was extracted with $CHCl_3$, and the organic phase was washed with deionized water, dried over Na_2SO_4, filtered, and evaporated to dryness to give the crude product. Purification by column chromatography on silica gel using $CHCl_3$ as the eluent affords the pure product as a colorless oil (8.3 g, 97.5%). ^{1}H NMR (400 MHz, $CDCl_3$): δ 7.20 (d, H, J = 4.0 Hz), 7.53 (d, H, J = 8.0 Hz), 9.79 (s, H).

3.2.3.2. Synthesis of 8-(2-bromothien-5-yl)-3,5-dimethyl-4,4-difluoro-4-bora-3a,4a-diaza-s-indacene (BDY-1)

To a solution of 5-bromo-2-thiophenecarbaldehyde (**1**) (0.70 g, 3.66 mmol) and 2-methylpyrrole (2) (0.67 g, 8.28 mmol) in degassed CH_2Cl_2 (220 mL) was added trifluoroacetic acid (TFA) (2 drops) under nitrogen, and the mixture was stirred at ambient temperature overnight. Next, 2,3-dichloro-5,6-dicyano-1,4-benzoquinone (DDQ) (0.83 g, 3.66 mmol) was added, and the reaction mixture was stirred for additional 2.5 h. Finally, N,N-diisopropylethylamine $(i\text{-}Pr)_2EtN$ (2.60 g, 20.05 mmol) and boron trifluoride diethyl etherate ($BF_3{\cdot}Et_2O$) (1.81 g, 12.7 mmol) were added, and the reaction mixture was stirred for 2 h. The reaction mixture was poured into water and extracted with CH_2Cl_2. The organic phase was dried over Na_2SO_4, filtered, and evaporated to dryness to give a crude product, which was purified by column chromatography on silica gel using CH_2Cl_2:Hexanes (2:1) as the eluent. The pure product was obtained as a crystalline red solid (0.57 g, 41% yield). m.p.

132-133 °C. ^{1}H NMR (400 MHz, $CDCl_3$): δ 2.68 (s, 6H), 6.32 (d, 2H, J=4.0 Hz), 7.05 (d, 2H, J = 4.0 Hz), 7.19 (m, 2H). ^{13}C NMR (100 MHz, $CDCl_3$): 15.0, 116.9, 119.7, 130.1, 130.6, 131.7, 133.2, 133.9, 136.1, 158.2.

3.2.3.3. Synthesis of 2-methylpyrrole (2)

Pyrrole-2-carboxaldehyde (6.0 g, 63.1 mmol), NaOH (13.2 g, 0.33 mol) and hyrazine hydrate (12.35 g, 0.39 mol) in ethylene glycole (80 mL) were heated at 200 °C under nitrogen for 3 h. During the course of the reaction, an organic phase was distilled via Dean-Stark trap. The distillate was extracted with diethyl ether, and the organic phase was washed with deionized water, dried over Na_2SO_4, filtered, and evaporated to dryness to give the pure product as a colorless oil (4.98 g, 97.5% yield). ^{1}H NMR (400 MHz, $CDCl_3$): δ 2.37 (s, 3H), 6.02 (m, 1H), 6.24 (m, 1H), 6.73 (m, 1H), 7.98 (broad s, 1H).

3.2.3.4. Synthesis of 2,5-dibromothiophene

To a stirred solution of thiophene (1.00 g, 11.89 mmol) in anhydrous DMF (10 ml) at room temperature, N-bromosuccinimide (4.34 g, 24.36 mmol) was added, and the resulting mixture was stirred at room temperature for 20 h. Then, the reaction mixture was poured into water, and the product was extracted with CH_2Cl_2. The organic layer was dried over Na_2SO_4, filtered, and evaporated to dryness to give a crude product. The crude was purified by column chromatography on silica gel using hexanes as the eluent to give the pure product as a colorless oil (1.88 g, 65% yield). ^{1}H NMR (400 MHz, $CDCl_3$): δ 6.86 (s, 2H).

3.2.3.5. Synthesis of 2,5-bis(trimethylstannyl) thiophene (3)

To a solution of 2,5-dibromothiophene (1.05 g, 4.13 mmol) in anhydrous THF (30 ml) at -78 °C, *n*-BuLi (3.47 ml, 8.68 mmol; 2.5 M in hexanes) was added dropwise over 20 min. The reaction mixture was stirred for 1 hour at -78 °C. Then, trimethyltinchloride (1.81 g, 9.1 mmol) was added under nitrogen as a solid, and the resulting mixture was allowed to warm

to ambient temperature overnight. The reaction mixture was quenched with water and extracted with diethyl ether. The organic phase was dried over Na_2SO_4, filtered, and evaporated to dryness to give the pure product as a white solid (1.46 g, 86.5% yield). ^{1}H NMR (400 MHz, $CDCl_3$): δ 0.38 (s, 18H), 7.39 (s, 2H).

3.2.3.6. Synthesis of 5,5'-dibromo-2,2'-bithiophene

To a stirred solution of 2,2'-bithiophene (2.0 g, 12.0 mmol) in acetic acid (30 ml) at room temperature, N-bromosuccinimide (4.49 g, 25.0 mmol) was slowly added, and the reaction mixture was stirred at room temperature for 3 h. Then, the reaction mixture was poured into ice resulting in the formation of a white solid. The white solid was washed with deionized water, dried over Na_2SO_4, filtered, and evaporated to dryness to give a crude product. The crude was purified by column chromatography on silica gel using hexanes as the eluent, and the pure product was obtained as a pale yellow solid (3.84 g, 98.6% yield). ^{1}H NMR (400 MHz, $CDCl_3$): δ 6.87 (d, 2H, J = 4.0 Hz), 6.98 (d, 2H, J = 4.0 Hz).

3.2.3.7. Synthesis of 5,5'-bis(trimethylstannyl)-2-2'-thiophene (4)

To a solution of 5,5'-dibromo 2,2' bithiophene (1.0 g, 3.08 mmol) in anhydrous THF (40 ml) at -78 °C, *n*-BuLi (2.6 ml, 6.48 mmol; 2.5 M in hexane) was added dropwise over 20 min, and the reaction mixture was stirred for 2 hour at -78 °C. Then, trimethyltinchloride (1.35 g, 6.8 mmol) was added under nitrogen as a solid, and the resulting reaction mixture was allowed to warm to ambient temperature overnight. The reaction mixture was quenched with water and extracted with hexanes. The organic phase was dried over Na_2SO_4, filtered, and evaporated to dryness to give a crude product. The crude was recrystallized with ethanol to give the pure product as an off-white crystalline solid (1.19 g, 39.2% yield). ^{1}H NMR (400 MHz, $CDCl_3$): δ 0.39 (s, 18H), 7.10 (d, 2H, J = 3.2 Hz), 7.29 (d, 2H, J = 3.2 Hz).

3.2.3.8. Synthesis of 5,5''-Bis(3,5-dimethyl BODIPY-8-yl)-2,2':5',2''-Terthiophene (BDY-3T-BDY)

The reagents **BDY-1** (0.48 g, 1.25 mmol), 2,5-bis(trimethylstannyl)thiophene (3) (0.24 g, 0.60 mmol), and $Pd(PPh_3)_2Cl_2$ (0.013 g, 17.8 µmol) in anhydrous toluene (30 mL) were heated at 110 °C under nitrogen for 48 h. Then, the reaction mixture was cooled down to room temperature and evaporated to dryness. The crude product was filtered by using methanol, and then washed with methanol to give a dark crude solid, which was purified by column chromatography on silica gel with $CHCl_3$:Hexanes (1:1) as the eluent to give final product as a dark red solid (0.20 g, 49% yield). $T_{decomposition}$ > 250 °C. ^{1}H NMR (400 MHz, $CDCl_3$): δ 2.68 (s, 6H), 6.35 (m, 2H), 7.15(m, 2H), 7.22-7.42 (m, 3H). ^{13}C NMR (100 MHz, $CDCl_3$): 15.0, 119.5, 119.7, 124.4, 124.5, 125.0, 125.2, 125.7, 130.1, 132.6, 132.8, 133.8, 134.7, 140.4, 157.6, 157.7, 158.1. MS(MALDI-TOF) m/z (M^+): calcd. for $C_{34}H_{26}B_2F_4N_4S_3$: 684.14, found: 684.96 $[M+H]^+$, 664.88 $[M-F]^+$, 602.78 $[M-4\times CH_3-F]^+$, 583.70 $[M-4\times CH_3-2\times F]^+$. Anal.calcd. for $C_{34}H_{26}B_2F_4N_4S_3$: C, 59.67; H, 3.83; N, 8.19, Found: C, 59.83; H, 4.07; N, 7.89.

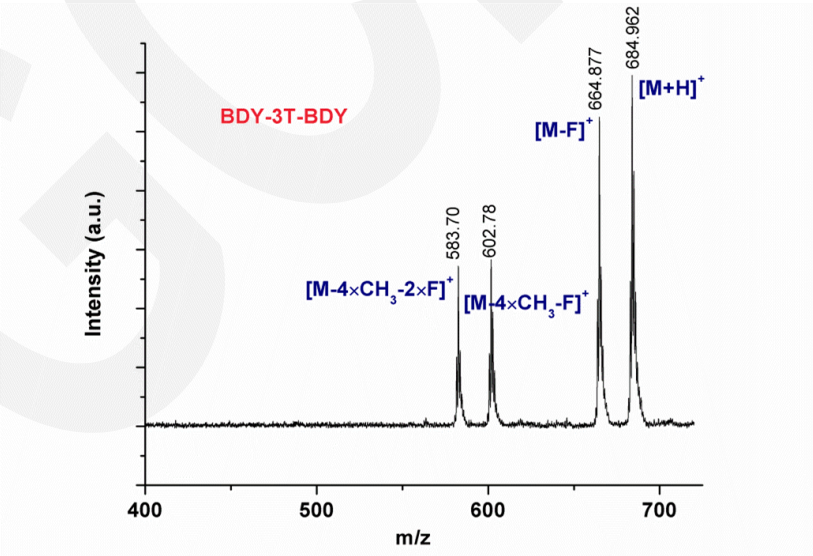

Figure 3.2.3.8 Positive ion and linear mode MALDI TOF-MS spectrum of **BDY-3T-BDY**.

3.2.3.9. Synthesis of 5,5'''-Bis(3,5-dimethyl BODIPY-8-yl)-2,2':5',2'':5'',2'''-Quaterthiophene (BDY-4T-BDY)

The reagents **BDY-1** (0.40 g, 1.05 mmol), 5,5'-bis(trimethylstannyl)-2-2'-thiophene (4) (0.24 g, 0.50 mmol), and $Pd(PPh_3)_2Cl_2$ (0.022 g, 0.03 mmol) in anhydrous toluene (30 mL) were heated at 110 °C under nitrogen for 48 h. Then, the reaction mixture was cooled down to room temperature and evaporated to dryness. The crude product was filtered by using methanol, and then washed with methanol to give a dark crude solid. The crude product was purified by column chromatography on silica gel with CH_2Cl_2:Hexanes (1:1) as the eluent to give final product as a dark red solid (0.17 g, 44% yield). $T_{decomposition}$ > 250 °C. ^1H NMR (400 MHz, $CDCl_3$): δ 2.67 (s, 6H), 6.35 (m, 2H), 7.15-7.42 (m, 6H). ^{13}C NMR (100 MHz, $CDCl_3$): 15.0, 119.6, 119.7, 124.4, 125.0, 125.2, 125.8, 130.1, 132.7, 132.8, 133.6, 133.8, 133.9, 134.7, 135.4, 137.0, 140.4, 141.5, 157.7, 158.0. MS(MALDI-TOF) m/z (M^+): calcd. for $C_{38}H_{28}B_2F_4N_4S_4$: 766.13, found: 767.12 $[M+H]^+$, 748.03 $[M-F]^+$. Anal.calcd. for $C_{38}H_{28}B_2F_4N_4S_4$: C, 59.54; H, 3.68, N, 7.31, Found: C, 59.05; H, 3.84, N, 7.60.

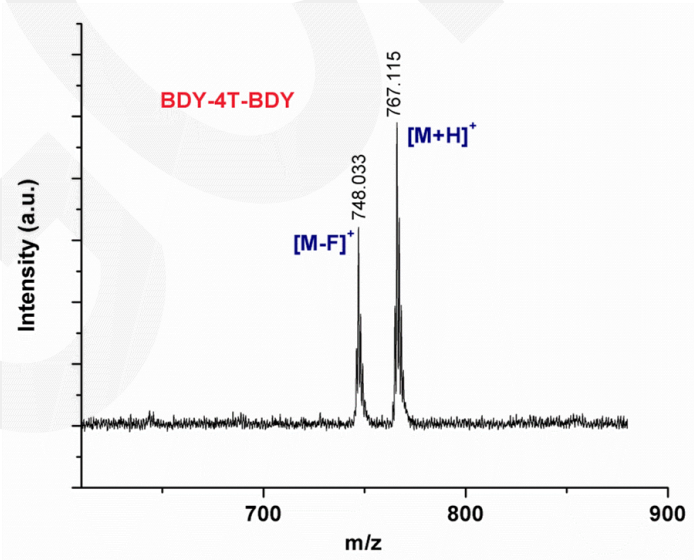

Figure 3.2.3.9. Positive ion and linear mode MALDI TOF-MS spectrum of **BDY-4T-BDY**.

3.2.4. Device Fabrication and Characterization

For the fabrication of top-contact/bottom-gate organic thin film transistors (OTFTs), highly *n*-doped (100) silicon wafers (resistivity < 0.005 Ω·cm) with a 300 nm thermally grown oxide gate dielectric film were used as device substrates. The Si/SiO_2 substrates were washed via sonication in acetone for 10 min, followed by oxygen plasma for 5 min (18 W). The general recipes were employed for the treatment of gate dielectric layers including three self-assembled monolayers (octadecyltrimethoxysilane; OTMS, hexamethyldisilane; HMDS, phenyltrichlorosilane; PTS) and PS-brush.[109] Semiconducting layers (**BDY-3T-BDY** and **BDY-4T-BDY**) were formed via vacuum deposition or solution-shearing (SS). For vacuum deposition, OTMS, HMDS, and PTS substrates were used. Semiconducting layer was deposited under high vacuum (~2×10^{-5} Torr) at various substrate temperatures (T_Ds) of 25, 50, and 80 °C. For solution-shearing process, PS-brush-treated substrates were employed. The solution-shearing process was performed in accordance with the reported procedure. During the solution-shearing process, a few drops of semiconductor solution (~1 mg/mL) were cast onto a heated substrate (1 cm × 2 cm), and the substrate was covered with a dewetting OTS-modified top substrate. The top substrate was fixed with bar to the syringe pump and tilted at small angle (< 10°). The dewetting top substrate was then translated by an electrically-controlled syringe pump at a constant velocity relative to the bottom substrate, gradually uncovering the sandwiched solution, which quickly evaporated and left behind a polycrystalline thin-film seeding from the shearing substrate frontier. Solvent evaporation was controlled by different solution-shearing conditions such as deposition temperature (50-80% of the solvent boiling point) and different solution shearing speed (0.1 – 4 mm/min). The solution-sheared substrates were placed in a vacuum oven at 90 °C overnight to remove the residual solvent. The solution-shearing process was optimized with regards to solvent type, substrate temperature, and shearing speed. Film thicknesses were characterized by profilometer (DEKTAK-XT, Brucker) as 40 – 60 nm (vacuum deposited films) and 300 – 650 nm (solution-sheared films), respectively. Au layers (40 nm) were thermally evaporated through a shadow mask to define source and drain contacts with various channel lengths (L; 100 and 50 μm) and widths (W; 1000 and 500 μm).

The electronic characteristics of OTFTs were measured using a Keithley 4200-SCS in a vacuum probe station ($P < 10^{-5}$ Torr). Carrier mobilities (μ), threshold voltages (V_T), and I_{on}/I_{off} ratios were calculated in the saturation regime by the formula,

$$\mu_{sat} = (2I_{DS}L)/[WC_i(V_G - V_T)^2],$$

where I_{DS} is the source-drain current, L is the channel length, W is the channel width, C_i is the areal capacitance of the gate dielectric (C_i =11.4 nF·cm^{-2}), V_G is the gate voltage, and V_T is the threshold voltage. The reported values are the average of 10 different devices with the standard deviations of less than 5%. The microstructure and surface morphology of thin-films were analyzed by optical microscopy (HDC-SD044S, HDView), atomic force microscope (AFM, NX10, Park systems), X-ray diffraction (XRD, Smartlab, Rigaku), and scanning electron microscope (SEM, JSM-6010LA, JEOL).

3.2.5. Result and Discussion

3.2.5.1. Computational Modeling, Synthesis and Characterization

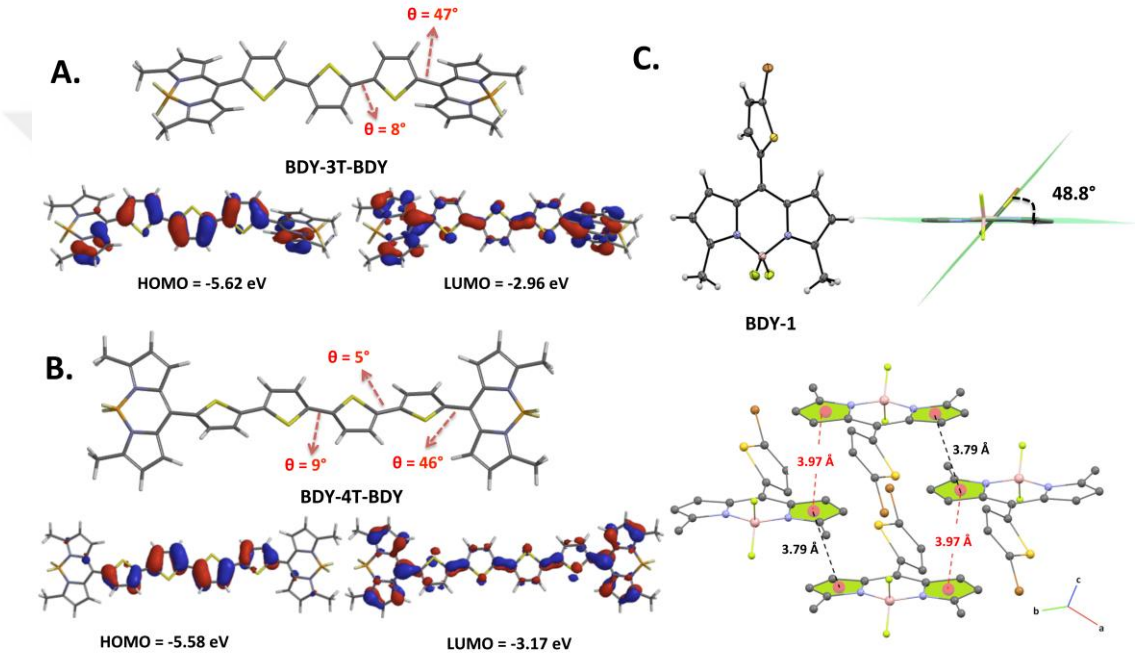

Figure 3.2.5.1.1 Optimized molecular geometries of **BDY-3T-BDY** (A) and **BDY-4T-BDY** (B) showing inter-ring torsional angles (θ), computed HOMO and LUMO energy levels, and molecular orbital topographical representations (DFT, B3LYP/6-31G**). C. ORTEP drawings of the crystal structure of **BDY-1** (20% probability level), and the perspective view of inter-ring dihedral angle between boron-dipyrromethene and *meso*-thiophene planes, and π-π stacking interactions between pyrrole units. (The grey, brown, blue, pink, yellow, and white colored atoms represent C, Br, N, B, F, and H, respectively).

Prior to the synthesis, DFT calculations were performed at the B3LYP/6-31G** level of theory to evaluate molecular geometries and frontier molecular orbital energetics. As shown in Figures 2A and 2B, DFT calculations indicate that the oligothiophene core of both **BDY-3T-BDY** (terthiophene) and **BDY-4T-BDY** (quaterthiophene) molecules are highly planar, featuring maximum inter-ring torsional angles of <10°. This result ensures an efficient π-orbital delocalization along the donor part. On the other hand, large inter-ring

torsional angles (~46-49°) were calculated between the boron-dipyrromethene and the *meso*-thiophene units in both the intermediate compound **BDY-1** (Figure 3.2.5.1.2) and the final compounds **BDY-3T-BDY** and **BDY-4T-BDY** (Figure 3.2.5.1.1A and 2B). These relatively large torsions are confirmed by the single-crystal structure analysis of the subunit **BDY-1** (Figure 3.2.5.1.1C).

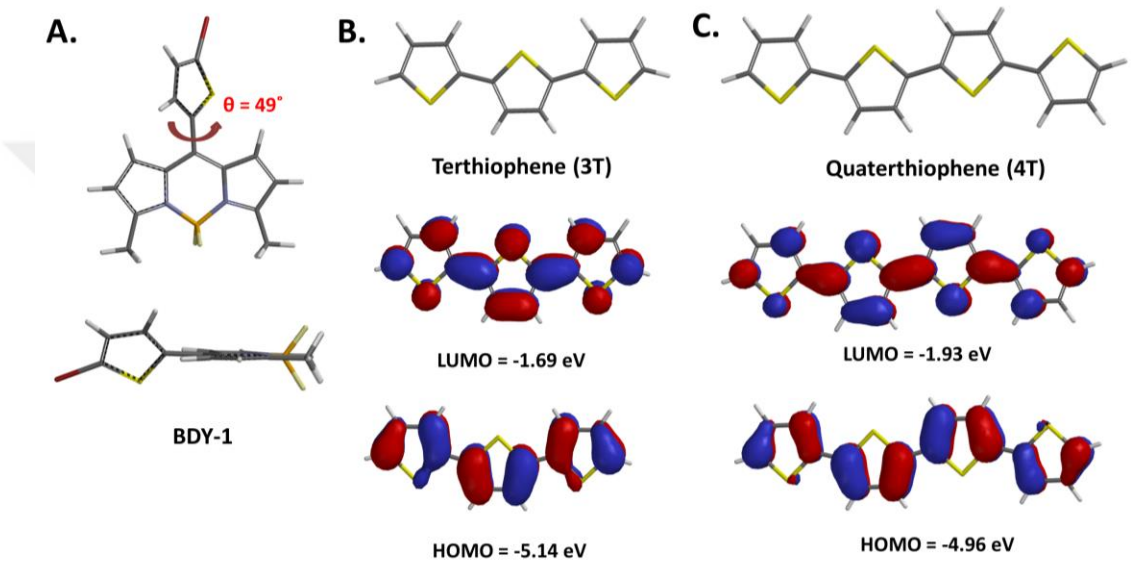

Figure 3.2.5.1.2. Optimized molecular geometries of **BDY-1** (A), 2,2′:5′,2″-terthiophene (B) and 2,2′:5′,2″:5″,2‴-quaterthiophene (C) showing computed HOMO and LUMO energy levels and topographical representations (DFT, B3LYP/6-31G**).

Red crystals of **BDY-1** suitable for single-crystal analysis were obtained in suitable sizes by diffusion of methanol into a chloroform solution at room temperature. **BDY-1** crystallizes in the monoclinic space group $P2_1/c$, and the boron-dipyrromethene core (C_9BN_2) adopting a highly planar geometry with a maximum deviation from the least-squares plane of only 0.070 (3) Å. The inter-ring torsional angle between the *meso*-thiophene group and the boron-dipyrromethene plane is 48.80°, which matches well with the computationally optimized geometries. This angle is small compared to those of previously reported *meso*-aromatic substituted BODIPY small molecules (Figure 3.2.5.1.3, θ = 56-90°), which is probably due to the lack of β-pyrrole substituents and sterically less-encumbered nature of the five-membered thiophene ring.[123]

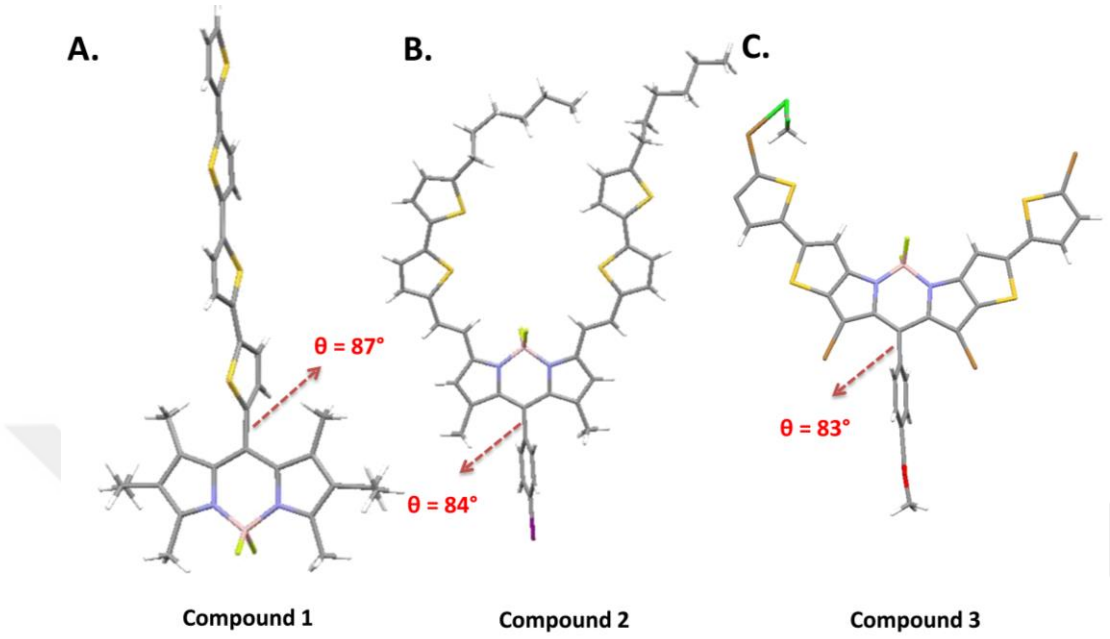

Figure 3.2.5.1.3. The X-ray crystal structures of compounds **1**[124] (A), **2**[110] (B), and **3**[125] (C) reported in the literature, and the perspective views of their inter-ring dihedral angles between boron-dipyrromethene and *meso*-aromatic unit planes.

Thus, our structural approach should offer a significant advantage to enhance charge transport in the solid-state when compared with the previously reported BODIPY-based semiconductors.[73] Comparable donor-acceptor dihedral angles were reported between thiophene and naphthalenediimide(NDI)/perylenediimide(PDI) units in several high-performance *n*-channel semiconductors.[71], [126], [127] The boron-dipyrromethene core in **BDY-1** exhibits slipped cofacial π-stacked packing motif with a favorable interplanar π-π stacking distances of 3.79-3.97 Å through pyrrole rings (Figure 3.2.5.1.1C), again possibly favoring charge carrying properties in the solid-state.

The MO computed HOMO/LUMO energies were found to be -5.62/–2.96 eV for **BDY-3T-BDY** and -5.58/-3.17 eV for **BDY-4T-BDY**, and molecular topology supports highly extended π-orbital delocalizations despite the severe torsions. Since the HOMO is more localized on the oligothiophene π-donor and the LUMO has larger electron density on the terminal BODIPY π-acceptor, HOMO→LUMO optical transitions may be dominated by partial charge transfers (*vide infra*). Compared to π-electron rich terthiophene and

quaterthiophene oligomers (Figure 3.2.5.1.2), MO computations demonstrate that the molecular energy levels of the new A-D-A molecules are found to be highly stabilized (ΔE_{LUMO} = -(1.2-1.3) eV and ΔE_{HOMO} = -(0.5-0.6) eV) as a result of the electron-deficiency of the BODIPY end units. The relatively large LUMO orbital stabilization, and its π-extended delocalization along the molecular backbone with significant spatial orbital distribution on the BODIPYs are expected to facilitate *n*-channel transport in the current semiconductors. The LUMO energy levels are in the range of those calculated for previously reported *n*-channel semiconductors (−2.5 to −4.3 eV), indicating that the new molecules are most likely to exhibit electron-transporting characteristics.[68]

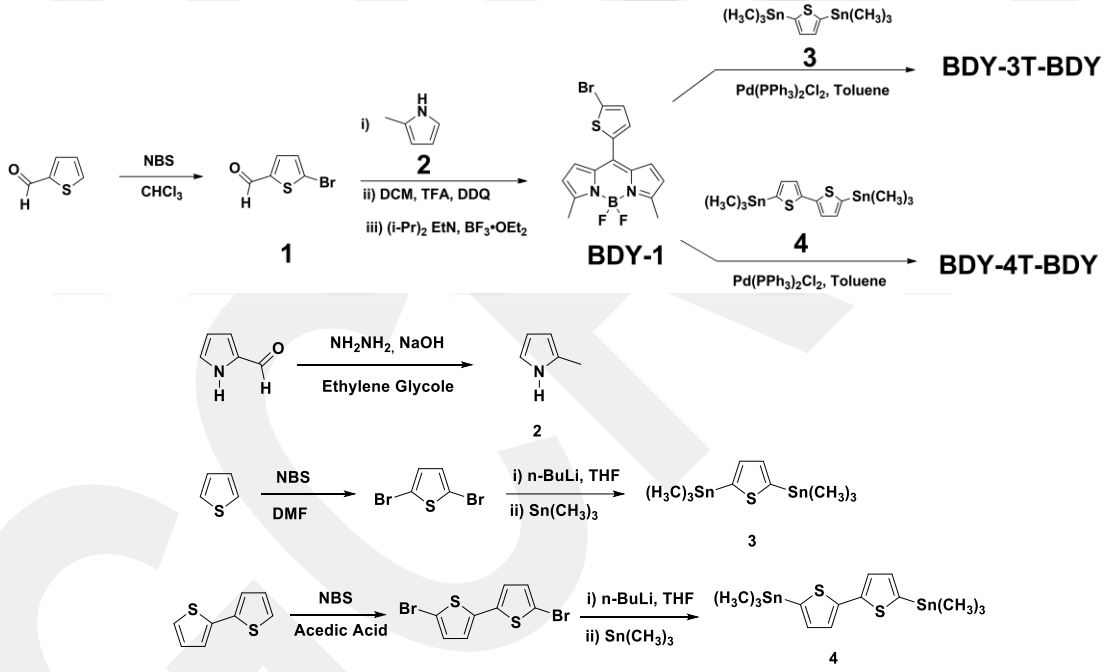

Scheme 3.2.5.1. Synthesis of **BDY-3T-BDY** and **BDY-4T-BDY**.

The synthetic routes to the new semiconductors are shown in Scheme 3.2.5.1. Due to the instability of unsubstituted dipyrromethene, BODIPY end-unit was synthesized with two methyl groups in the α-positions. The common intermediates **2**, **3**, and **4** were prepared according to literature procedures (Scheme 3.2.5.1). The boron-dipyrromethene intermediate **BDY-1** was prepared by first reacting 5-bromo-2-thiophenecarboxaldehyde (**1**) with 2-

methyl pyrrole (**2**) in the presence of catalytic amount of trifluoroacetic acid (TFA), which was subsequently oxidized with 2,3-dichloro-5,6-dicyano-1,4-benzoquinone (DDQ) and coordinated with trifluoroborane dietherate ($BF_3 \cdot OEt_2$) in the presence of $(i\text{-}Pr)_2EtN$ (61% yield). The Stille cross-coupling of **BDY-1** with the corresponding bisstannylthiophene reagents, 2,5- bis(trimethylstannyl)thiophene (**3**) and 5,5'-bis(trimethylstannyl)-2-2'-thiophene (**4**), in toluene using $Pd(PPh_3)_2Cl_2$ as the catalyst yielded semiconductors **BDY-3T-BDY** and **BDY-4T-BDY**, respectively, in 45-50% yields. The new compounds are found to be chemically stable over one year in the solid-state, when stored under ambient conditions without excluding light. In addition, they exhibit good solubility (up to 100 mg/mL) in common organic solvents (dichloromethane, chloroform, toluene, and tetrahydrofuran), which enables convenient purification via column chromatography and device fabrication via solution processing. Attempts to purify **BDY-3T-BDY** and **BDY-4T-BDY** via gradient sublimation under high vacuum (2×10^{-5} Torr) failed, resulting in complete decomposition. This data indicates that the new compounds may not be used to fabricate thin films via physical vapor deposition method, which is in line with the poor charge carrier mobilities obtained for the vapor-deposited OTFTs (*vide infra*). The unusual good solubilities of **BDY-3T-BDY** and **BDY-4T-BDY** despite the absence of long lipophilic alkyl substituents (C_nH_{2n+1}, n >4) may be attributed to inter-ring torsions in solution (*vide infra*) and large dipole moments of BODIPY moieties, which both facilitate interactions with the solvent molecules. This is in sharp contrast to the design principles of the majority of the *n*-type semiconductors reported to date, which has employed linear/branched lipophilic alkyl substituents to ensure good solubility of strong donor-acceptor π-backbones. Thus, this data demonstrates a unique feature of BODIPY building block in the design of solution-processable molecular semiconductors for facile synthesis/purification. In addition, since alkyl substiutents are not needed, the density of insulating σ-electrons can be significantly lowered in BODIPY-based semiconductor solid-state.

The chemical structures and purity of the new compounds were accessed by ^1H NMR, ^{13}C NMR, MALDI-TOF Mass Spectrometry (MS), and Elemental Analysis. It is noteworthy that the MALDI-TOF MS analyses of **BDY-3T-BDY** and **BDY-4T-BDY** exhibited up to four different peak groups corresponding to the protonated molecular ions ($[M+H]^+$) and ions formed by rupture of fluorine atom(s) and/or methyl groups ($[M\text{-}F]^+$, $[M\text{-}4\times CH_3\text{-}F]^+$, [M-

4×CH_3-2F]$^+$) (Figures S3 and S4).[128] Based on conventional melting temperature measurements and differential scanning calorimetry (DSC) analysis, no thermal transitions were observed until decomposition. However, thermogravimetric (TGA) analysis indicates reasonable thermal stability of the new molecules with decomposition thresholds located at ~325 °C (Figure 3.2.5.1.4).

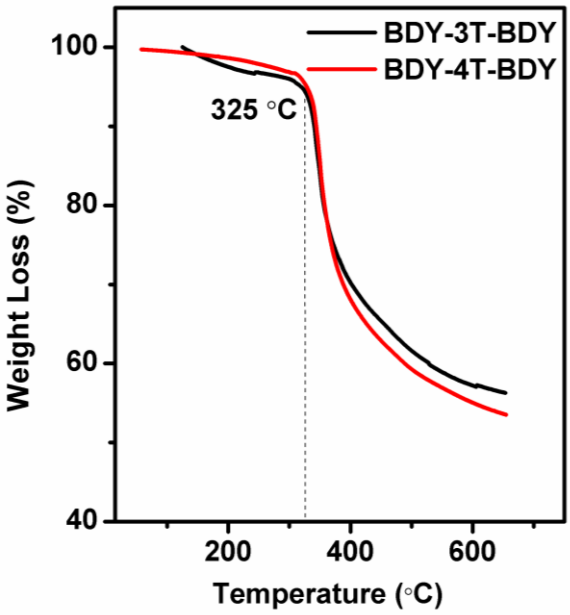

Figure 3.2.5.1.4. Thermogravimetric analysis (TGA) of the compounds **BDY-3T-BDY** and **BDY-4T-BDY** at temperature ramps of 10 °C min^{-1} under N_2.

3.2.5.2. Optoelectronic Characterizations

The optical and electrochemical characteristics of the new compounds were studied by optical absorption and fluorescence spectroscopies as well as cyclic voltammetry. The corresponding spectra and voltammograms are shown in Figures 3.2.5.2.3 and 3.2.5.2.1, and the data is summarized in Table 3.2.5.2. Both compounds exhibit two distinct absorption peaks in THF solution with λ_{max} at 361/526 nm for **BDY-3T-BDY** and at 377/526 nm for **BDY-4T-BDY**. The highly intense absorption peaks observed at 526 nm ($\varepsilon = 2\times10^5$ M^{-1} cm^{-1}) along with the out−of−plane vibronic features at 497 nm (at ~1100 cm^{-1} from the

absorption maximum) are characteristics of the π-π* ($S_0 \rightarrow S_1$) transition of the BODIPY moiety.[107] In addition, this absorption peak matches well with the absorption profile of **BDY-1** (Figure 3.2.5.2.3A, λ_{max} = 525 nm), and it is nearly identical to that of the model compound **BDY-C11**, with *meso*-alkyl substituents (Figure 3.2.5.2.1, λ_{max} = 506 nm). Furthermore, no additional lower energy shoulder corresponding to an intramolecular charge transfer process was observed. The broad, higher energy absorption peaks at 361-377 nm are attributed to interplay of lower-intensity BODIPY-based $S_0 \rightarrow S_2$ and oligothiophene-based π-π* transitions.

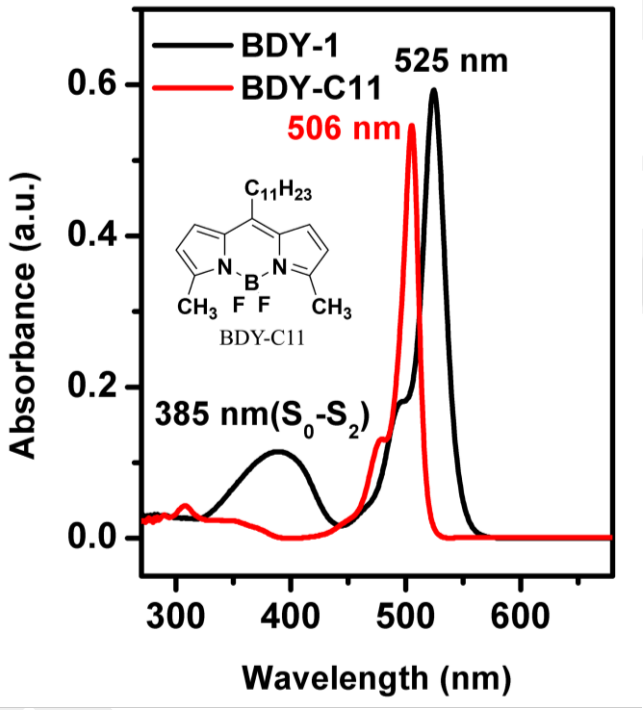

Figure 3.2.5.2.1. Optical absorption spectra of BDY-1 and *meso*-alkyl substituted BODIPY compound BDY-C11 in THF.

Table 3.2.5.2. Summary of Thermal, Optical Absorption, Emission and Electrochemical Properties of Compounds **BDY-3T-BDY** and **BDY-4T-BDY** and Corresponding Estimated Frontier Molecular Orbital Energies.

Compounds	T_{TGA}[a] (°C)	$\lambda_{abs}^{sol.}$ (nm) (E_g (eV))[b]	λ_{abs}^{film} (nm) (E_g (eV))[c]	$\lambda_{em}^{sol.}$ (nm)[d]	$E_{red\text{-}1,2}^{1/2}$ (V)[e]	E_{LUMO} (eV)[f]	E_{HOMO} (eV)[g]
BDY-3T-BDY	325	361,526 (2.23 eV)	349, 555 (1.94 eV)	652 (Φ_F = 0.037) in THF 630 (Φ_F = 0.043) in Toluene	-0.74, -0.84	-3.66	-5.89
BDY-4T-BDY	325	377,526 (2.19 eV)	376, 565 (1.94 eV)	678 (Φ_F = 0.053) in THF 630 (Φ_F = 0.055) in Toluene	-0.73, -0.85	-3.67	-5.86

[a] Onset decomposition temperature measured by TGA under nitrogen at a scan rate of 10 °C/min. [b] From optical absorption in THF, optical band gap is estimated from the low energy band edge of the UV-Vis absorption spectrum. [c] From optical absorption as spin-coated thin film on glass, optical band gap is estimated from the low-energy band edge of the UV-Vis absorption spectrum. [d] From fluorescence spectra in THF or toluene; the fluorescence quantum yield values were determined by comparing with the fluorescence of Rhodamine 6G as the standard (Φ_F = 0.76 in water). [e] Measured in 0.1 M $Bu_4N^+PF_6^-$ in THF at a scan rate of 50 mV/s (*vs.* Ag/AgCl). [f] Estimated from the equation E_{LUMO} = -4.40 eV - $E_{red}^{1/2}$. [g] E_{HOMO} is calculated from $E_g = E_{LUMO} - E_{HOMO}$.

The red-shifted ($\Delta\lambda$ = 16 nm) absorption maximum of **BDY-4T-BDY** for the high-energy region, as compared to that in **BDY-3T-BDY**, correlates well with its further π-extended donor core (quaterthiophene *vs.* terthiophene).[129] These observations indicate minimal ground-state interaction or excitonic coupling between the BODIPY-based π-acceptor and the 3T/4T-based π-donor chromophores in dilute solutions of the present compounds. Therefore, it is very likely that the inter-ring torsional angles between the BODIPY and the *meso*-thiophene units increase in solution ($\theta >> 48°$) compared to those in the solid-state, giving rise to concomitant decrease of electronic interaction between BODIPY and oligothiophene (3T or 4T) π-orbitals, which leads to distinct absorption profiles of two chromophore units. It is noteworthy that this nonplanar geometry undoubtedly contributes to the superior solubility of the present compounds in common organic solvents.

The poor electronic interaction in the ground-state was found to be significantly enhanced in the excited state to facilitate non-radiative decay pathways. Thus, the fluorescence spectra of **BDY-3T-BDY** and **BDY-4T-BDY** in THF solutions (Figure 3.2.5.2.2) exhibit broad emission peaks with maxima at 652 nm and 678 nm, respectively, corresponding to large Stokes shifts of 126-152 nm. The fluorescence quantum yields (Φ_F) were measured as 0.037 (**BDY-3T-BDY**) and 0.053 (**BDY-4T-BDY**).

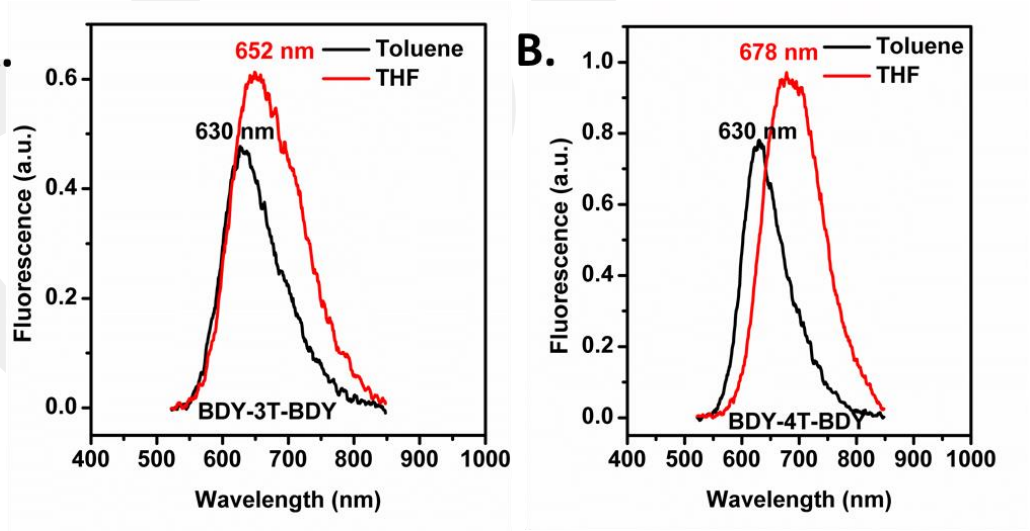

Figure 3.2.5.2.2. Fluorescence emission spectra of **BDY-3T-BDY** (A) and **BDY-4T-BDY** (B) in THF and Toluene solutions ($1x10^{-5}$ M) (Excitation wavelength= 510 nm).

The observed broad emission peaks, large Stokes shifts, and relatively low quantum yields are in contrast to typical BODIPY emission characteristics, and they are indicative of the presence of intramolecular energy-/charge-transfer based non-radiative pathways in the excited-state. Although the absorption spectra of the current compounds are nearly invariant across several solvents, their corresponding fluorescence spectra exhibit positive solvachromatisms (λ_{em} = 630 nm → 652-678 nm; Φ_F = 0.043-0.055 → 0.037-0.053 for toluene (ε = 2.3) → THF (ε = 7.6)) with increasing solvent polarity, associated with concomitant peak broadening and a decreased quantum yield. These observations further support that the final relaxed excited states may have larger dipole moments as a result of charge transfer (CT) between sub-chromophoric units (Figure 3.2.5.2.2). Similar charge-transfer behaviors were observed in the emissive characteristics of previously reported BODIPY dyads.[130]

UV-Vis absorption spectra of the corresponding thin films do not show the obvious BODIPY profiles and exhibit broad and red-shifted maxima at 555 nm and 565 nm for **BDY-3T-BDY** and **BDY-4T-BDY**, respectively. In the solid-state, the low-energy absorption edges exhibit significant bathochromic shifts ($\Delta\lambda$ = 75-80 nm) with onsets located at 635-640 nm indicating reduced solid-state optical band gaps (~1.94 eV) vs. those measured in solution. This result points to enhanced π-core planarization and intermolecular interactions, and some degree of electronic coupling between donor and acceptor subunits in the solid-state. The red-shift in **BDY-4T-BDY** ($\Delta\lambda$ = 39 nm) is more pronounced than **BDY-3T-BDY** ($\Delta\lambda$ = 29 nm), probably reflecting the difference in solid-state ordering levels between these semiconductors and enhanced donor strength of quaterthiophene *vs.* terthiophene.

Based on the cyclic voltammetry (CV) measurements in THF solution, both molecules undergo two reversible reductions with the first and second half-wave potentials ($E_{red}^{1/2}$) located at -0.74/-0.84 V (*vs.* Ag/AgCl) for **BDY-3T-BDY** and -0.73/-0.85 V (*vs.* Ag/AgCl) for **BDY-4T-BDY** (Figure 3.2.5.2.3B). The reversibility of the two reduction processes indicates the good redox stability of the new BODIPY-based molecules. From the CV data, the HOMO/LUMO energy levels are estimated as -3.66/-5.89 eV and -3.67/-5.86 eV for **BDY-3T-BDY** and **BDY-4T-BDY**, respectively. The experimental LUMO energies are in the range of those observed for previously reported *n*-channel semiconductors (-2.9 eV - -4.3 eV), which is in line with the theoretical results. Considering the observed stable *n*-doping/undoping profiles and LUMO energetics, the new molecules are potential *n*-channel semiconductors.

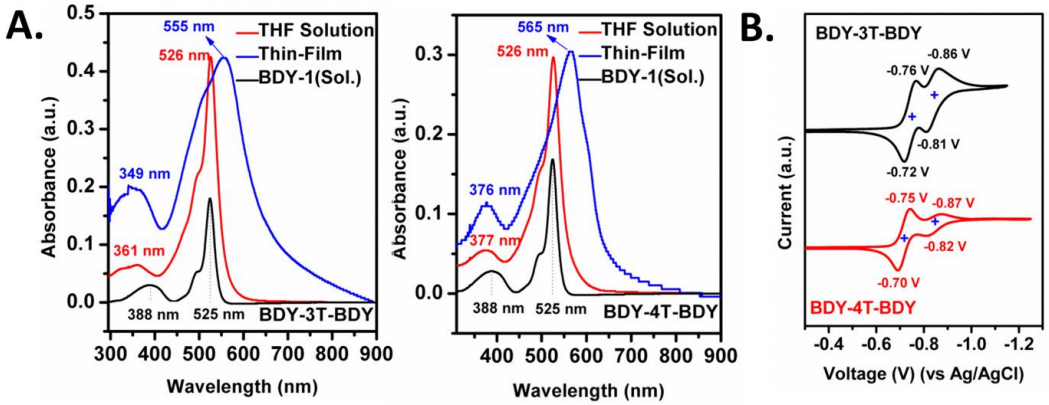

Figure 3.2.5.2.3. A. Optical absorption spectra of **BDY-3T-BDY** and **BDY-4T-BDY** in THF solution and as thin-films. B. Cyclic voltammograms of **BDY-3T-BDY** and **BDY-4T-BDY** in THF (0.1 M $Bu_4N^+PF_6^-$, scan rate = 50 $mV \cdot s^{-1}$).

3.2.5.3. Thin-Film Transistor Characterizations

The semiconductor characteristics of **BDY-3T-BDY** and **BDY-4T-BDY** were measured in a top-contact/bottom-gate (TC-BG) organic thin-film transistor (OTFT) device architecture. The semiconductor thin-films (40 – 60 nm for vapor deposited film, 300 – 600 nm for solution processed film) were deposited *via* physical vapor deposition and solution-shearing methods on pre-treated n^{++}-Si/SiO_2 (300 nm) gate-dielectric substrates. The dielectric surface was functionalized either with a self-assembled monolayer (SAM) for vapor-deposition or with polymer brushes for solution-shearing to achieve a favorable semiconductor-dielectric interface.[87], [131]–[134] Typical transfer and output plots are shown in Figures 3.2.5.2.5.1-3.2.5.3.4, and the OTFT device characteristics are summarized in Tables 2 and 3.2.5.2.5.1.

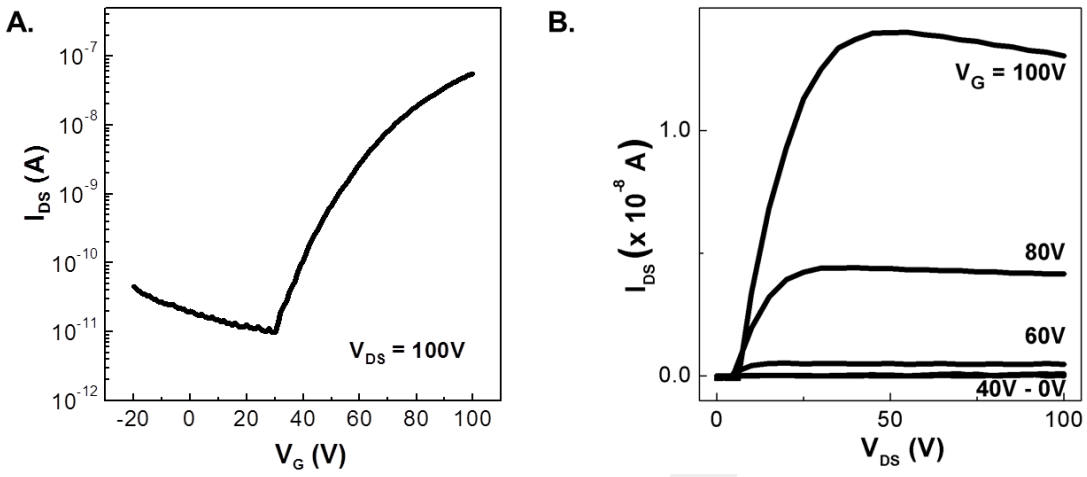

Figure 3.2.5.2.5.1. (a) Transfer and (b) output characteristics of thin-film transistors based on vapor-deposited **BDY-3T-BDY** thin films.

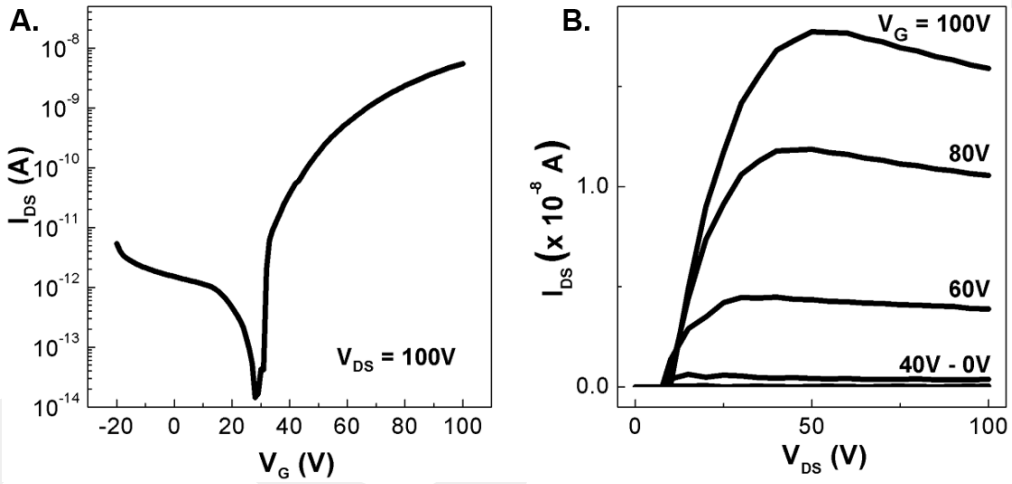

Figure 3.3.2.5.2. (a) Transfer and (b) output characteristics of thin-film transistors based on vapor-deposited **BDY-4T-BDY** thin films.

As a fist approach, **BDY-3T-BDY** and **BDY-4T-BDY** semiconductor films were grown by physical vapor deposition under high vacuum (~2×10^{-5} Torr) at different substrate temperatures (T_D) of 25 °C, 50 °C, and 80 °C. Although, vapor-deposited thin-films of both semiconductors fabricated on n^{++}-Si/SiO_2 substrates maintained a temperature, T_D, of 80 °C were inactive, the devices fabricated at room temperature (T_D = 25 °C) showed a weak *n*-channel behavior with electron mobilities of 2×10^{-4} – 5×10^{-4} $cm^2/V\cdot s$ (Figures 3.2.5.2.5.1 and 3.3.2.5.2, and Table 3.2.5.2.5.1), irrespective of surface treatment for the gate dielectric.

Table 3.2.5.2.5.1. Organic thin-film transistors characteristics based on vacuum-deposited thin films of **BDY-3T-BDY** and **BDY-4T-BDY** at different deposition temperature (T_D). Devices were measured under vacuum.

Compound	T_D (°C)	μ (cm^2/Vs)	V_T (V)	I_{on}/I_{off}
BDY-3T-BDY	20	1.7×10^{-4}	37	9.0×10^{7}
	50	7.3×10^{-5}	53	6.1×10^{5}
	80	-	-	-
BDY-4T-BDY	20	5.3×10^{-4}	75	3.5×10^{5}
	50	2.6×10^{-5}	51	2.4×10^{6}
	80	-	-	-

Next, solution processing of the semiconductor was employed to fabricate the OTFT devices, and among various approaches, solution-shearing was preferred to achieve unidirectional crystalline semiconductor microstructure with favorable carrier transport characteristics. The solution-shearing process was optimized with regards to the solvent type, substrate temperature and shearing speed to fine-tune the rate of semiconductor crystallization in thin-film phase.[96] The optimal conditions were identified as using chlorobenzene solutions (1 mg/mL) at a substrate temperature of 50 – 60 °C and shearing speed of 0.3 – 1 mm/min for both semiconductors. Solution-sheared films of both compounds exhibited typical *n*-channel transport characteristics with those of **BDY-3T-BDY** displaying an electron mobility of 2.7×10^{-4} cm^2/Vs, which is similar to those obtained for vapor-deposited films (Figure 3.2.5.3.3).

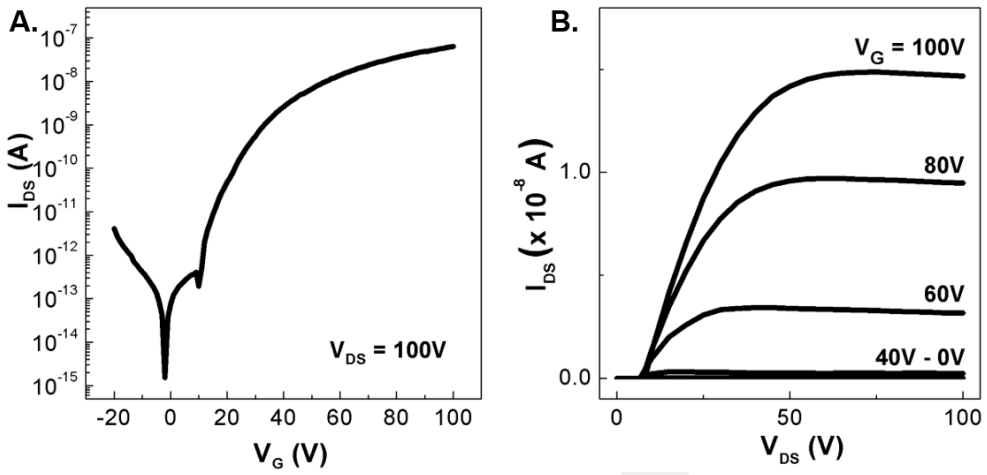

Figure 3.2.5.3.3. (a) Transfer and (b) output characteristics of thin-film transistors based on solution-sheared **BDY-3T-BDY** thin films.

However, **BDY-4T-BDY**-based solution-sheared thin-films, which includes a relatively longer quaterthiophene π-donor part, exhibited higher device performance than those of **BDY-3T-BDY** with shorter π-donor of terthiophene. The OTFTs fabricated with **BDY-4T-BDY** showed electron mobility as high as 0.011 $cm^2/V{\cdot}s$ with an impressive current on/off ratio of $>10^8$ (Figure 3.2.5.3.4). Note that this electron mobility is obtained for devices having the source-drain electrodes deposited perpendicular to the major fiber alignment direction (*vide infra*). To the best of our knowledge, this is the highest OTFT device performance reported to date for a BODIPY-based small molecule.[135] The extremely low off current ($\sim10^{-13}$ A) and the high $I_{on/off}$ ratio ($>10^8$) points to the favorable current modulation characteristics of **BDY-4T-BDY** thin-films. The higher electron mobility of solution-sheared **BDY-4T-BDY** thin-films correlates well with its relatively lower charge-carrier trap density ($N_T = 7.4\times10^{11}$ cm^{-2}) among the current BODIPY-based OTFT devices, which leads to more favorable charge-transport (Tables 3.3.2.5.2 and 3.2.5.2.5.1).[136]–[138]

Table 3.3.2.5.2. Organic thin-film transistor characteristics based on thin films of **BDY-3T-BDY** and **BDY-4T-BDY**.[a,b]

Compound	Method	μ (cm^2/Vs)	V_T (V)	I_{on}/I_{off}	SS (V/dec)	N_T (cm^{-2})
BDY-3T-BDY	Vacuum Deposition	1.7×10^{-4}	37	9.0×10^{7}	32.2	1.2×10^{12}
	Solution Shear	2.7×10^{-4}	43	9.6×10^{5}	17.9	2.1×10^{12}
BDY-4T-BDY	Vacuum Deposition	5.3×10^{-4}	75	3.5×10^{5}	18.4	1.7×10^{12}
	Solution Shear	0.011	19	1.5×10^{8}	9.35	7.4×10^{11}

[a] The OTFT electrical characteristics were measured in a vacuum probe station ($P < 10^{-5}$ Torr). [b] The mobility values, threshold voltages, and I_{on}/I_{off} ratios given are the average values for 10 devices with the standard deviations of less than 5%.

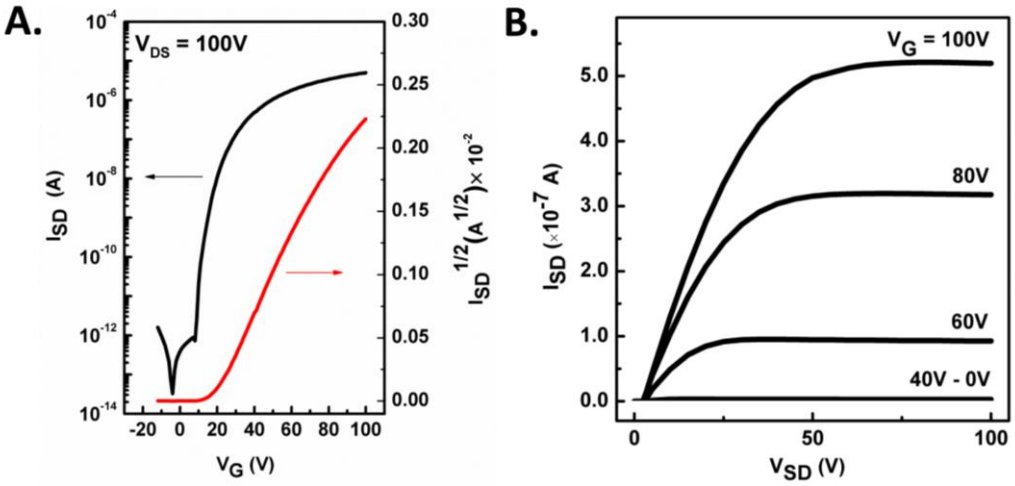

Figure 3.2.5.3.4. Representative OTFT transfer (A) and output (B) plots for devices fabricated with solution-sheared **BDY-4T-BDY** thin films.

3.2.5.4. Thin-Film Microstructure and Morphology

The microstructure and morphology of the present semiconductor thin-films were studied by θ-2θ X-ray diffraction (XRD), atomic force microscopy (AFM) and scanning electron microscopy (SEM) to rationalize the observed device performances. The corresponding XRD profiles and AFM/SEM images are shown in Figures 5 and 16. XRD scans reveal that vapor-deposited thin-films of both semiconductors and solution-sheared

thin-films of **BDY-3T-BDY** are essentially amorphous (Figure 3.2.5.4.1), and that only the solution-sheared thin-film of **BDY-4T-BDY** is highly textured (Figure 3.2.5.4.2).

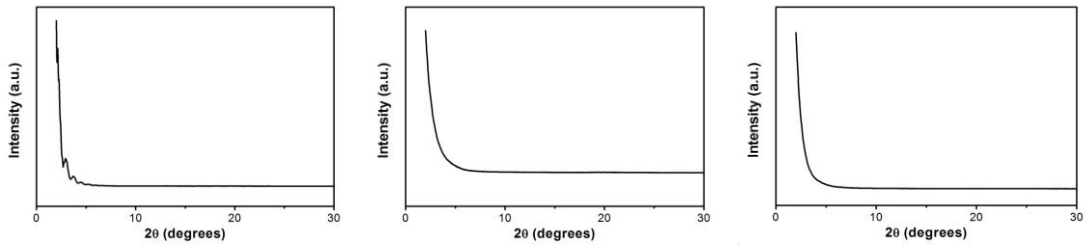

Figure 3.2.5.4.1. θ-2θ X-ray diffraction (XRD) scans of solution-sheared **BDY-3T-BDY** thin film, vacuum-deposited **BDY-3T-BDY** thin film and vacuum-deposited **BDY-4T-BDY** thin film.

For solution-sheared thin-films of **BDY-4T-BDY**, no first-order reflection was observed at low-angles ($2\theta < 10°$), which indicates the absence of typical edge-on molecular long-axis orientation on the substrate. Based on the computed molecular lengths (~2.4 nm), one would expect to see the first-order diffraction peak at $2\theta \sim 4\text{-}5°$ if the molecules are oriented with their long axis along the substrate normal. However, a major reflection is observed at $2\theta = 13.1°$ along with the second order peak at $2\theta = 26.4°$, which shows that **BDY-4T-BDY** thin-films include a major crystalline phase with an interlayer *d*-spacings of 6.8 Å along the substrate normal. This is much smaller than the computed long-axis molecular lengths (~2.4 nm), and consistent with the computed length of **BDY-4T-BDY** along the short molecular axis (~7 Å). Therefore, it is very likely that BODIPY-based molecules adopt an unusual molecular packing in the thin-film phase, either featuring a highly tilted molecular orientation on the substrate ($\theta > 70°$) or, more likely, aligning with their short axis along the substrate normal. Note that self-assembly of **BDY-4T-BDY** semiconductor molecules into well-defined microfibers (*vide infra*) in thin-film phase is more consistent with the short-axis molecular orientation, which enables strong π-π interactions along the fiber long-axis.[139] A secondary crystalline phase ($2\theta = 13.6°$) with a lower intensity and additional higher angle diffraction peaks at $2\theta = 18.1°$ and 19.8° were also evident from the XRD spectra. Although end-functionalized oligothiophenes such α,ω-dihexyl-terthiophene and α,ω-dihexyl-quaterthiophene typically shows long-axis molecular edge-on orientations on various dielectrics including polymeric surfaces,[140][131] the current rather unusual thin-film microstructure is probably due to the chemical nature of BODIPY end-units and

the absence of long lipophilic alkyl substituents, which both influence the current semiconductor physisorption characteristics on the polymeric dielectric surface.

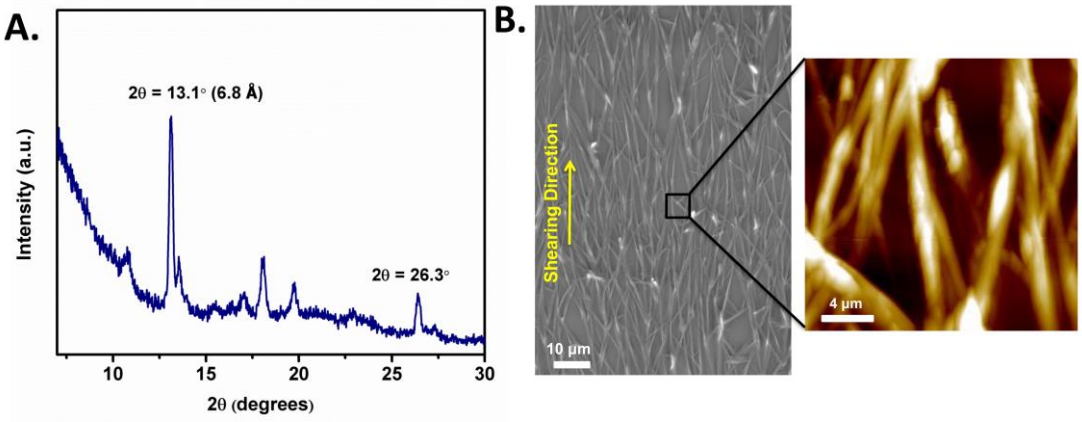

Figure 3.2.5.4.2. A. θ-2θ X-ray diffraction (XRD) scans of solution-sheared **BDY-4T-BDY** films. B. Top-view SEM images (left) and AFM topographic images (right) of solution-sheared **BDY-4T-BDY** films indicating the solution-shearing and major fiber alignment directions.

The AFM and top-view SEM images were recorded to characterize the film surface morphology. As shown in Figure 3.2.5.4.2B, the surface topology of solution-sheared **BDY-4T-BDY** thin film shows anisotropic micron-sized crystalline fiber structures that grow along the shearing direction. The widths of the microfibers were as large as 1 – 2 μm and their lengths can reach to ~0.1 mm. As seen from the optical microscopy images (Figure 3.2.5.4.3), these microfibers exhibit a directional and highly homogeneous distribution in an area of 1 mm × 1 mm, and they are aligned mainly along the shearing direction.

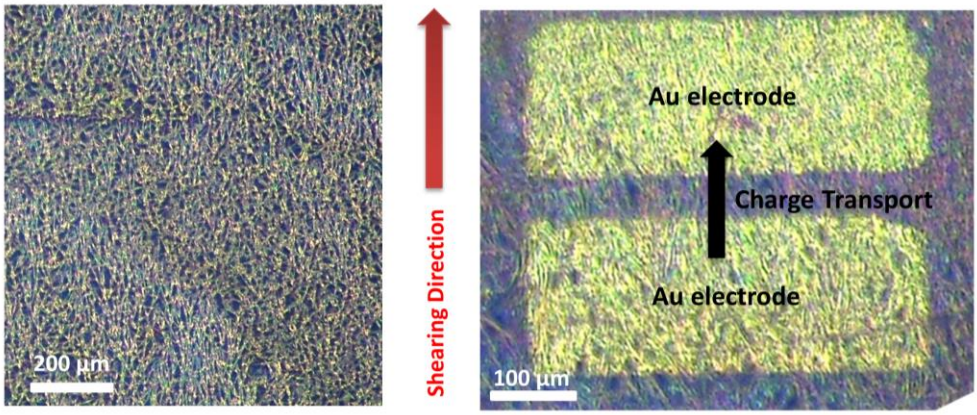

Figure 3.2.5.4.3. Optical microscopy images of solution-sheared **BDY-4T-BDY** thin film showing the source-drain electrodes, and the directions of solution-shearing and charge-transport.

Close inspection of these fibers via AFM indicates the presence of grain bundles with much smaller dimensions (~100-200 nm), giving information about the mechanism how these fibers form. Since uniaxially aligned fiber-based semiconductor morphologies were obtained with **BDY-4T-BDY**-based films, charge carrier mobilities were measured in two different source-drain electrode configurations with electrodes being deposited perpendicular or parallel to the major fiber alignment direction. As shown in Figure 3.2.5.4.5B, electron mobilities of 0.001 $cm^2/V \cdot s$ (Figure 3.2.5.4.4) were measured for the OTFTs with the charge transport direction perpendicular to the major fiber alignment direction.

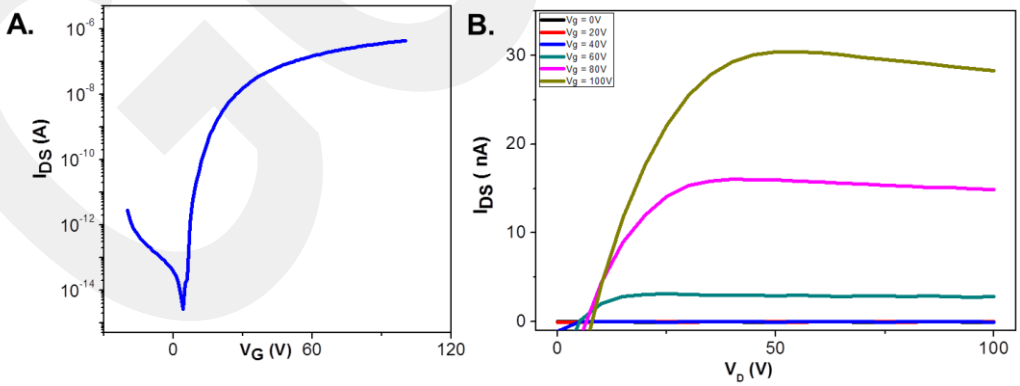

Figure 3.2.5.4.4. Transfer (A) and output (B) characteristics of thin-film transistors based on solution-sheared **BDY-4T-BDY** thin films with source-drain electodes deposited parallel to the major fiber alignment direction.

This mobility value is one order of magnitude lower than the electron mobilities measured in OTFTs having charge transport along the major fiber alignment direction

(Figure 3.2.5.4.5A), indicating the presence of fiber-alignment-induced charge transport anisotropy ($\mu_{\parallel}/\mu_{\perp}$~10). Similar anisotropic charge-transport properties were observed with highly oriented semiconducting polymers[141][142] , thus the alignment of semiconducting fibers along the conduction channel is very crucial to enhance macroscopic charge transport.[143]

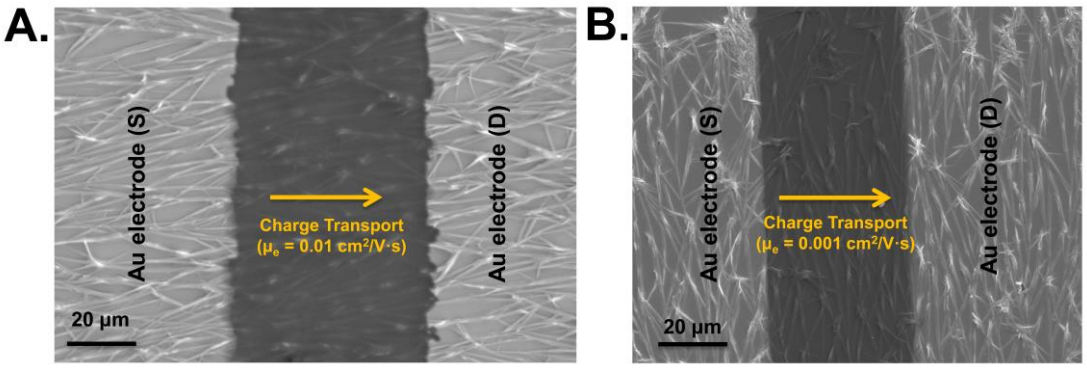

Figure 3.2.5.4.5. Top-view SEM images of OTFT devices fabricated via solution shearing of BDY-4T-BDY with source-drain electrodes deposited perpendicular (A) and parallel (B) to the major fiber alignment direction.

The solution-processed thin-films of **BDY-3T-BDY** showed fiber-like, randomly-aligned anisotropic features with much smaller widths and lengths compared to those of **BDY-4T-BDY** (Figure 3.2.5.4.6). The interconnectivity between these features was found to be poor compared to that of **BDY-4T-BDY**. On the other hand, vacuum-deposited thin-films of **BDY-3T-BDY** and **BDY-4T-BDY** showed completely different morphologies with relatively smooth (RMS surface roughness < 9.1nm for 5.0 μm × 5.0 μm scan area) and isotropic spherulites of ~100 nm in diameter (Figure 3.2.5.4.7). Therefore, on the contrary of **BDY-4T-BDY** solution-sheared films, the absence of thin-film texturing and poor film morphology are consistent with the poor electron mobility of these semiconductor films.

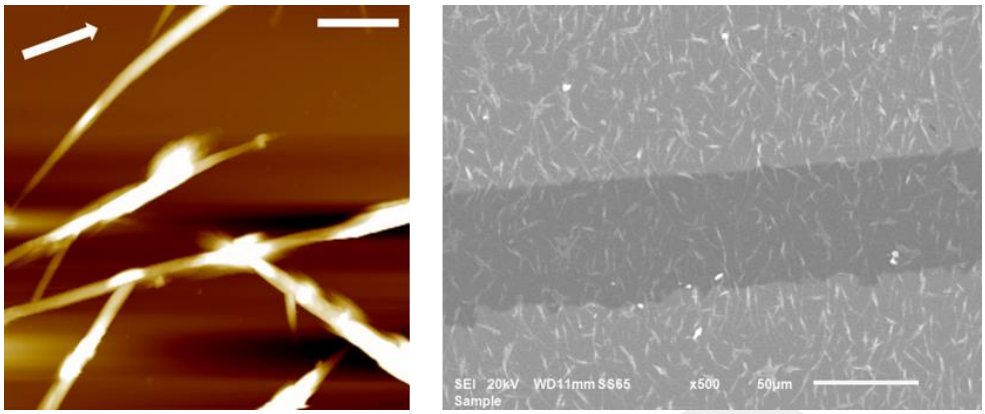

Figure 3.2.5.4.6. AFM topographic image (left) and top-view SEM images (right) of solution-sheared **BDY-3T-BDY** thin film. Scale bar denotes 4 μm in AFM and 50 μm in SEM image. Arrow shows the direction of solution shearing.

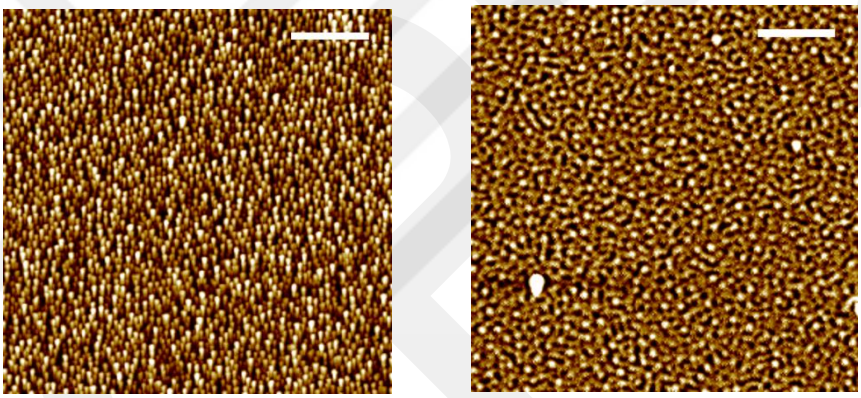

Figure 3.2.5.4.7. AFM image of vacuum-deposited **BDY-3T-BDY and BDY-4T-BDY** thin film. Scale bar denotes 1 μm.

3.2.6. Conclusion

In conclusion, we have demonstrated the design, synthesis and characterization of a new class BODIPY-based semiconductors (**BDY-3T-BDY** and **BDY-4T-BDY**) with an acceptor-donor-acceptor (A-D-A) molecular architecture. The structural, optoelectronic and physicochemical properties of the new semiconductors were investigated in details. Single-crystal XRD characterization of the key intermediate, **BDY-1**, reveals crucial structural properties. Top-contact/bottom-gate OTFTs were fabricated with these semiconductors and relatively high electron mobilities of 0.01 $cm^2/V \cdot s$ and excellent

current on/off ratios of $>10^8$ have been obtained for solution-processed semiconductor films. To the best of our knowledge, these values are the highest reported to date for a BODIPY-based small molecular OTFT semiconductor. The microstructural and morphological characterizations of the new semiconductor thin-films explain the observed relatively high charge carrier mobilities. Specifically, for **BDY-4T-BDY**-based thin-films, highly crystalline, relatively long (~0.1 mm) and micron-sized (1-2 μm) fibers were obtained along the shearing direction from source to drain, which allows for efficient long-range S→D charge transport. This result is consistent with its relatively high electron mobility among the present semiconductor films. In addition, fiber-alignment-induced charge transport anisotropy ($\mu_{\parallel}/\mu_{\perp}$~10) was observed resulting in one order of magnitude difference in electron mobilities of solution-sheared semiconductor films. Undoubtedly, our results provide important guidelines for designing BODIPY-based molecular semiconductors, indicating that through rational design and synthesis, BODIPY can be a highly favorable building block for efficient electron charge transport in solution-processed optoelectronics.

3.3. Experimental of A New Rod-Shaped BODIPY-Acetylene Molecule for Solution-Processed Semiconducting Microribbons in N-Channel Organic Field-Effect Transistors

3.3.1. Materials and Methods

Schlenk techniques were used in the reactions, and the reactions were carried out under N_2 unless otherwise noted. All reagents were obtained from commercial sources and used without any purification unless otherwise noted. $^1H/^{13}C$ NMR characterizations were performed on a Bruker 400 spectrometer (^1H, 400 MHz; ^{13}C, 100 MHz). Elemental analyses were done on a LecoTruspec Micro model instrument. MALDI-TOF was performed on a Bruker Microflex LT MALDI-TOF-MS Instrument. Thermogravimetric analysis (TGA) and differential scanning calorimetry (DSC) measurements were

performed on Perkin Elmer Diamond model instruments at a heating rate of 10 °C/min under nitrogen. UV-Vis absorption and fluorescence emission measurements were performed on a Shimadzu, UV-1800 UV-Vis Spectrophotometer and a Varian Eclipse spectrofluorometer, respectively. The fluorescence quantum yield was determined in dichloromethane as compared to the fluorescence of Rhodamine 6G standart (Φ_F = 0.76 in water). Electrochemistry was performed on a C3 cell stand electrochemical station equipped with BAS-Epsilon software (Bioanalytical Systems, Inc. Lafayette, IN). The molecular geometry optimizations and total energy calculations were carried out using density functional theory (DFT) at the B3LYP/6-31G** level by using Gaussian 09.[86]

3.3.2. Synthesis and Characterization

The synthesis of 5-bromo-2-thiophenecarbaldehyde and 2-methylpyrrole reagents were performed in accordance with our previously reported procedures.[1]

3.3.2.1. Synthesis of 1,4-dibromo-2,5-bis((2-ethylhexyl)oxy)-2,5-diethynylbenzene (1)

A mixture of potassium carbonate (4.0 g, 28.97 mmol) and 2-ethylhexyl bromide (8.24 g, 40.55 mmol) was dissolved in 40 mL DMF under nitrogen. 2,5-dibromohydroquinone (3.88 g, 14.48 mmol) was added slowly to this mixture, and the resulting reaction solution was stirred at 100 °C for 48 h. The mixture was then cooled to room temperature and quenched with water. The reaction mixture was extracted with dichloromethane, and the organic phase was washed with water, dried over Na_2SO_4, filtered, and evaporated to dryness to give the crude product. The crude was then purified by column chromatography on silica gel using hexane as the eluent to give compound **1** as a colorless oil (6.9 g, 97%). ^{1}H NMR (400 MHz, $CDCl_3$) δ 7.09 (s, 2H), 3.83 (d, 4H, J=8.0 Hz), 1.76 (m, 2H, J=12.0 Hz), 1.43-1.57 (m, 8H), 1.32-1.35 (m, 8H), 0.91-0.96 (m, 12H). ^{13}C NMR (100 MHz, $CDCl_3$): 150.1, 118.1, 111.0, 72.5, 39.4, 30.4, 29.0, 23.8, 23.0, 14.1, 11.1.

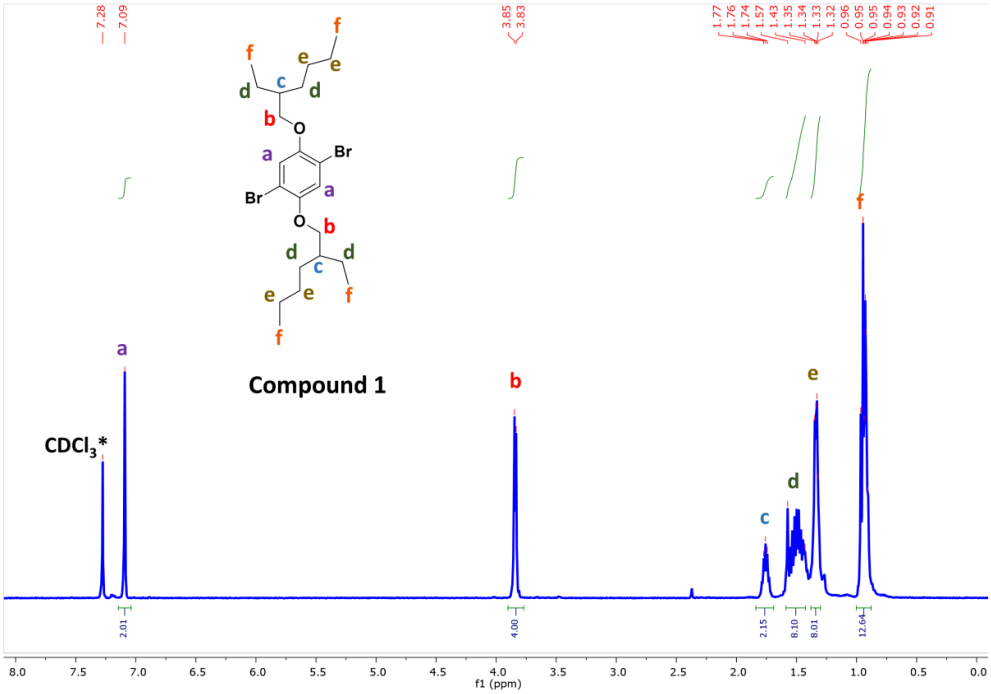

Figure 3.3.2.1. ^{1}H NMR spectra of compound **1** in $CDCl_3$ at room temperature.

3.3.2.2. Synthesis of ((2,5-bis((2-ethylhexyl)oxy)-1,4-phenylene)bis(ethyne-2,1-diyl)) bis (trimethylsilane) (2)

A mixture of 1,4-dibromo-2,5-bis((2-ethylhexyl)oxy)-2,5-diethynylbenzene (**1**) (2.0 g, 4.06 mmol), $Pd(PPh_3)_2Cl_2$ (0.1.71 g, 0.243 mmol), and CuI (0.039 g, 0.203 mmol) in Et_3N (40 mL) was stirred 5 minutes. Next, ethynyltrimethylsilane (1.0 g, 10.16 mmol) was added, and the reaction was heated at 90 °C under nitrogen for 48 h. Then, the reaction mixture was cooled down to room temperature and filtered; the filtrate was evaporated to dryness to yield a crude. The crude was then purified by column chromatography on silica gel using hexane:ethylacetate (30:1) as the eluent to compound **2** as a yellow oil (1.69 g, 79%). ^{1}H NMR (400 MHz, $CDCl_3$) δ 6.89 (s, 2H), 3.81-3.86 (dd, 4H), 1.72-1.75 (m, 2H, J=12.0 Hz), 1.44-1.58 (m, 8H), 1.32-1.34 (m, 8H), 0.91-0.96 (m, 12H), 0.26 (s, 18H).

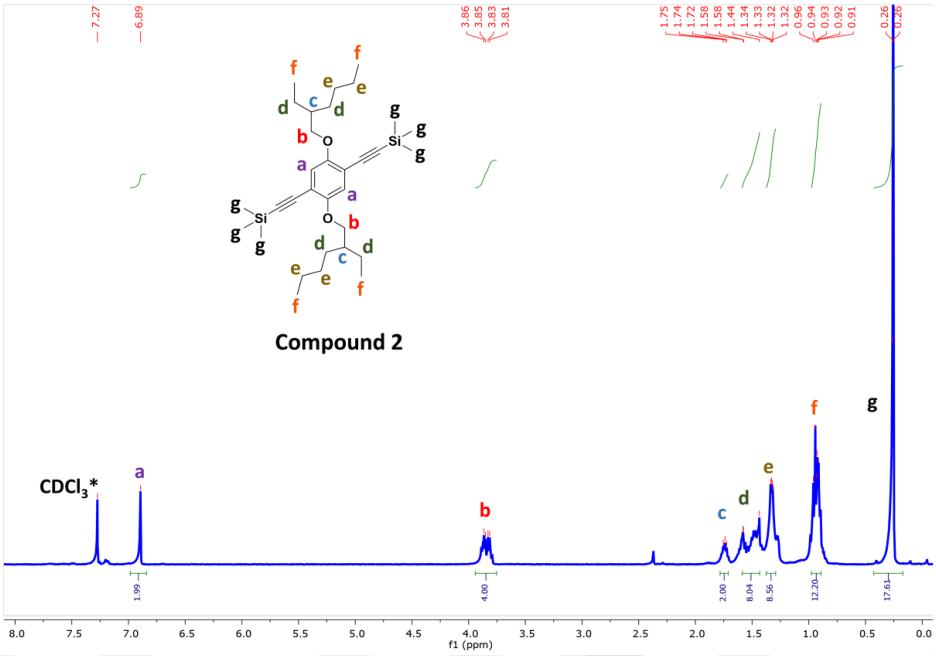

Figure 3.3.2.2. ^{1}H NMR spectra of compound **2** in $CDCl_3$ at room temperature.

3.3.2.3. Synthesis of 1,4-bis((2-ethylhexyl)oxy)-2,5-diethynylbenzene (3)

The suspension of ((2,5-bis((2-ethylhexyl)oxy)-1,4-phenylene)bis(ethyne-2,1-diyl))bis(trimethylsilane) (**2**) (0.29 g, 0.55 mmol) and KOH (0.93 g, 16.51 mmol) in THF:methanol (9:1) (30 mL) was stirred at room temperature for 1 h. Then, the reaction was quenched with water, and the resulting mixture was extracted with dichloromethane. The organic phase was washed with water, dried over Na_2SO_4, filtered, and evaporated to dryness to compound **3** as a yellow oil-solid (0.21 g, 100% yield). ^{1}H NMR (400 MHz, $CDCl_3$): δ 6.96 (s, 2H), 3.85-3.86 (d, 4H, J=4.0 Hz), 3.33 (s, 2H), 1.75-1.78 (m, 2H), 1.46-1.57 (m, 8H), 1.27-1.34 (m, 8H), 0.91-0.96 (m, 12H).

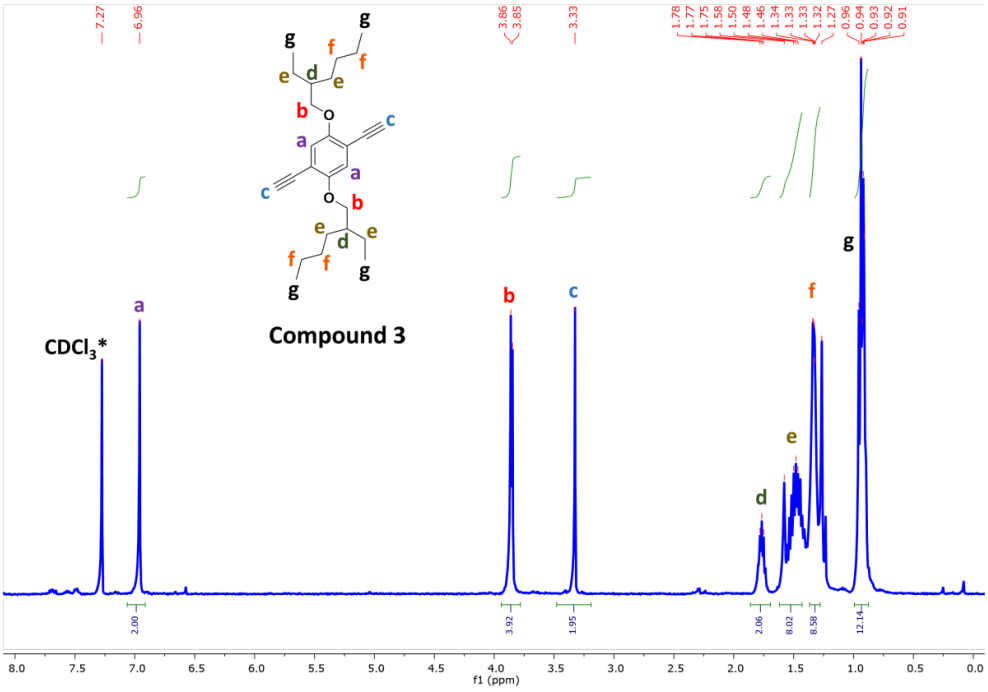

Figure 3.3.2.3. ^{1}H NMR spectra of compound **3** in $CDCl_3$ at room temperature.

3.3.2.4. Synthesis of 8-(2-bromothien-5-yl)-3,5-dimethyl-4,4-difluoro-4-bora-3a,4a-diaza-s-indacene (BDY-Th-Br)

Trifluoroacetic acid (TFA) (4 drops) was added to a solution of 5-bromo-2-thiophenecarbaldehyde (0.90 g, 4.70 mmol) and 2-methylpyrrole (0.86 g, 10.64 mmol) in degassed CH_2Cl_2 (300 mL), and the resulting mixture was stirred at room temperature overnight. Next, 2,3-dichloro-5,6-dicyano-1,4-benzoquinone (DDQ) (1.06 g, 4.70 mmol) was added, and the reaction mixture was stirred for additional 2.5 h. Finally, N,N-diisopropylethylamine $(i\text{-}Pr)_2EtN$ (1.33 g, 10.31 mmol) and boron trifluoride diethyl etherate ($BF_3{\cdot}Et_2O$) (2.33 g, 16.44 mmol) were added, and the reaction mixture was stirred for additional 2 h. The reaction mixture was poured into water and extracted with CH_2Cl_2. The organic phase was dried over Na_2SO_4, filtered, and evaporated to dryness to give a crude product, which was further purified by column chromatography on silica gel using CH_2Cl_2:Hexanes (2:1) as the eluent. The pure product was obtained as a crystalline

red solid (0.78 g, 44% yield). m.p. 132-133 °C. ^{1}H NMR (400 MHz, $CDCl_3$): δ 7.18 (m, 2H), 7.05 (d, 2H, J = 4.0 Hz), 6.31 (d, 2H, J=4.0 Hz), 2.66 (s, 6H). ^{13}C NMR (100 MHz, $CDCl_3$): 15.0, 116.9, 119.7, 130.1, 130.6, 131.7, 133.2, 133.9, 136.1, 158.2.

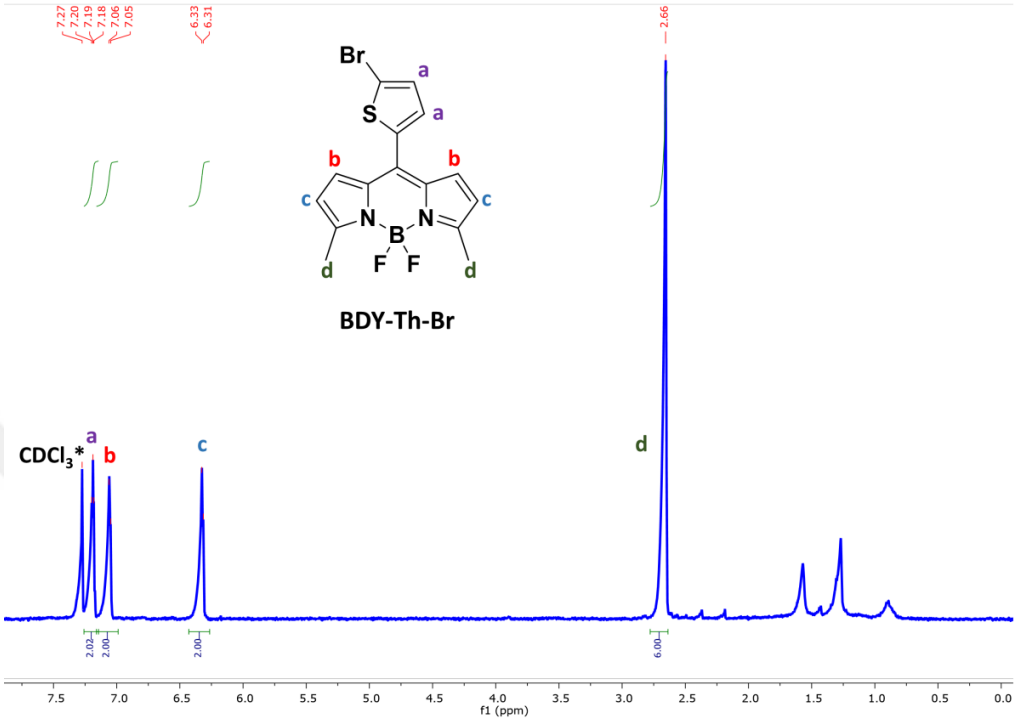

Figure 3.3.2.4. ^{1}H NMR spectra of compound **BDY-Th-Br** in $CDCl_3$ at room temperature.

3.3.2.5. Synthesis of 10-(5-((4-((5-(5,5-difluoro 3,7-dimethyl-5H-4l4,5l4-dipyrrolo[1,2-c:2',1'-f][1,3,2]diazaborinin-10-yl)thiophen-2-yl)ethynyl)-2,5-bis((2-ethylhexyl)oxy)phenyl)ethynyl)thiophen-2-yl)-5,5-difluoro-3,7-dimethyl-5H-4l4,5l4-dipyrrolo[1,2-c:2',1'-f][1,3,2]diazaborinine (BDY-PhAc-BDY)

The reagents 8-(2-bromothien-5-yl)-3,5-dimethyl-4,4-difluoro-4-bora-3a,4a-diaza-s-indacene (**BDY-Th-Br**) (0.675 g, 1.77 mmol), CuI (0.0076 g, 0.040 mmol) and $Pd(PPh_3)_2Cl_2$ (0.056 g 0.08 mmol) in Et_3N:THF (2:1) (21 mL) were stirred for 5 minutes. Then, 1,4-bis((2-ethylhexyl)oxy)-2,5-diethynylbenzene (**3**) (0.308 g, 0.8 mmol) in 5 mL of THF was added, and the resulting mixture was heated at 80 °C under nitrogen for 24 h. Then, the reaction mixture was cooled to room temperature and evaporated to dryness. The crude was then purified by column chromatography on silica gel using dichloromethane as the eluent to give the pure product as a dark red solid (0.228 g, 29%). ^{1}H NMR (400 MHz, $CDCl_3$): δ 7.34 (m, 4H), 7.09 (d, 4H, J= 4.0 Hz), 7.02 (s, 2H), 6.33 (d, 4H, J= 4.0 Hz), 3.94 (m, 4H), 2.67 (s, 12.0 H), 1.80 (m, 2H), 1.52-1.58 (m, 8H), 1.27-1.36 (m, 8H), 0.98 (t, 6H), 0.90 (t, 6H). ^{13}C NMR (100 MHz, $CDCl_3$):δ 158.0, 153.9, 136.0, 134.0, 133.6, 132.0, 131.6, 130.2, 127.9, 119.6, 116.0, 113.7, 93.1, 87.5, 72.0, 39.6, 30.7, 29.1, 24.1, 23.1, 15.0, 14.1, 11.4. m.p. = 196-197 °C. MS(MALDI-TOF) m/z (M^+): calcd. for $C_{56}H_{60}B_2F_4N_4O_2S_2$: 982.43, found: 983.302 $[M+H]^+$, 963.534 $[M-F]^+$, 870.685 $[M-1\times(2\text{-EH})]^+$, 758.961 $[M-2\times(2\text{-EH})]^+$. Anal.calcd. for $C_{56}H_{60}B_2F_4N_4O_2S_2$: C, 68.43; H, 6.15; N, 5.70, Found: C, 68.78; H, 6.25; N, 5.74.

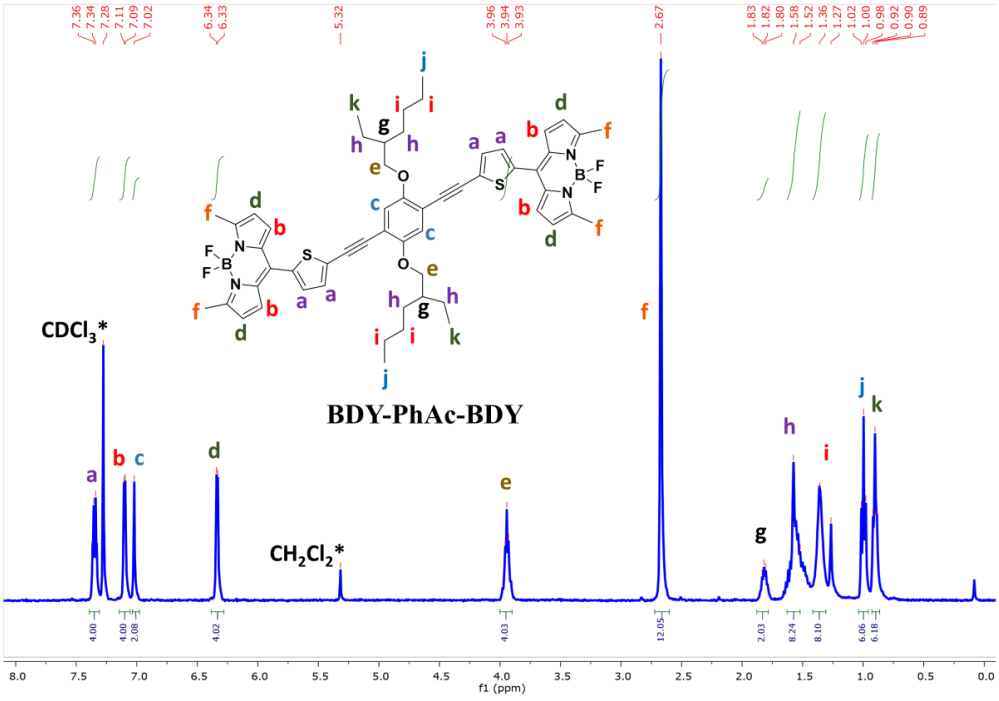

Figure 3.3.2.5.1 ^{1}H NMR spectra of compound **BDY-PhAc-BDY** in $CDCl_3$ at room temperature.

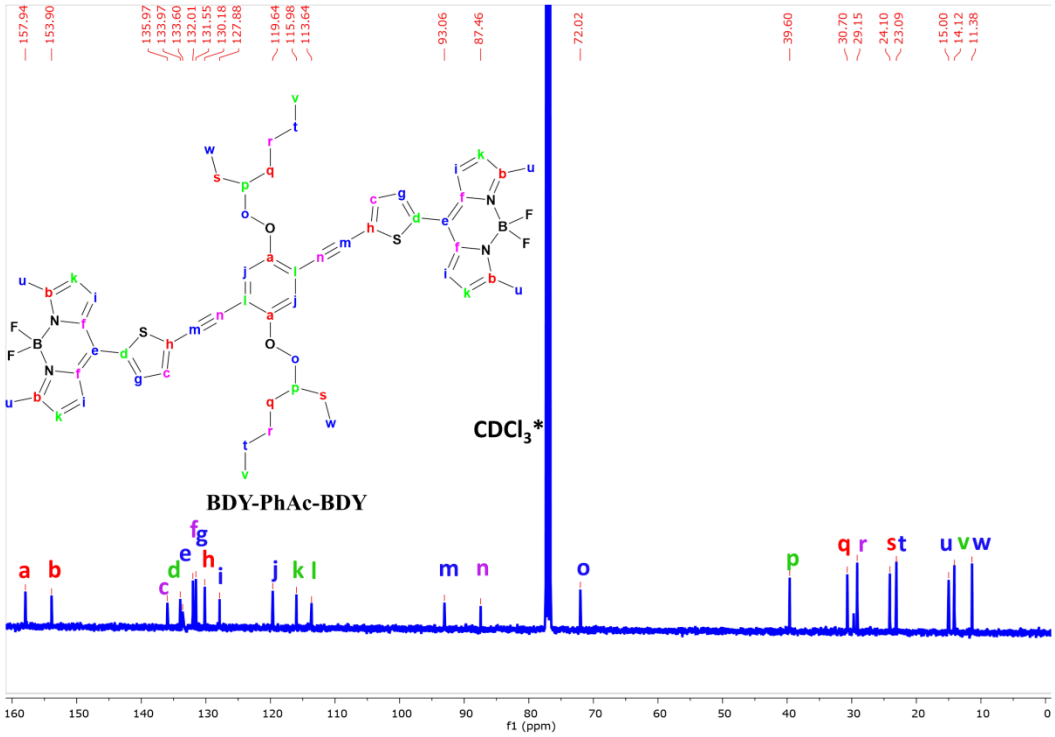

Figure 3.3.2.5.2. ^{13}C NMR spectra of compound **BDY-PhAc-BDY** in $CDCl_3$ at room temperature.

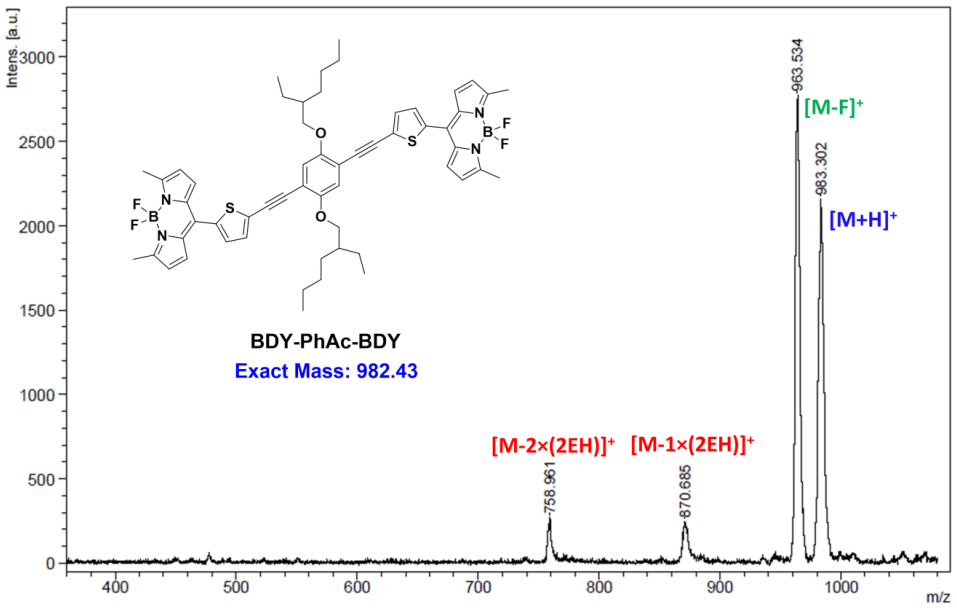

Figure 3.3.2.5.3. Positive ion and linear mode MALDI TOF-MS spectrum of **BDY-PhAc-BDY**.

3.3.3. Device Fabrication and Characterization

The OTFTs were fabricated by the bottom-gate/top-contact (BG/TC) structure. Highly n-doped silicon wafers (capacitance per unit area C_i =11.4 nF·cm^{-2}) with thermally oxidized 300 nm SiO_2 layer were cleaned via acetone sonication for 10 min and oxygen plasma cleaning for 5 min (Harrick plasma, PDC-32G, 18 W). The organic layers of BDY-PhAc-BDY were deposited via solution-shearing on PS-brush-treated substrates. The PS-brush (Mw = 10 kg/mol) treatments were implemented by the general recipe[87] and the solution-shearing process was accomplished as the reported procedure.[93] The solution-sheared substrates were annealed in a vacuum oven at 100 °C for 24 h to remove the residual solvent. The concentration of BDY-PhAc-BDY solution (1 – 2 mg/mL), solvent type, substrate temperature (50 – 80 % of the solvent boiling point), and shearing speed (0.5 – 8 mm/min) were optimized. The thickness of organic films (40 – 62 nm) were measured by the profilometer (DEKTAK-XT, Brucker). The Au layers (40 nm) with various channel widths (W; 1000 and 500 μm) and lengths (L; 100 and 50 μm) were thermally evaporated to define the source and drain electrodes. The electronic performances of OTFTs were characterized in vacuum condition (<10-2 Torr) at room temperature with the probe station (Keithely 4200-SCS). The microstructure and surface morphology of thin-films were measured by atomic force microscope (AFM, NX10, Park systems), scanning electron microscope (SEM, JSM-6010LA, JEOL), and X-ray diffraction (XRD, Smartlab, Rigaku).

3.3.4. Result and Discussion

3.3.4.1. Synthesis, Single-Crystal Structure and Thermal Characterizations

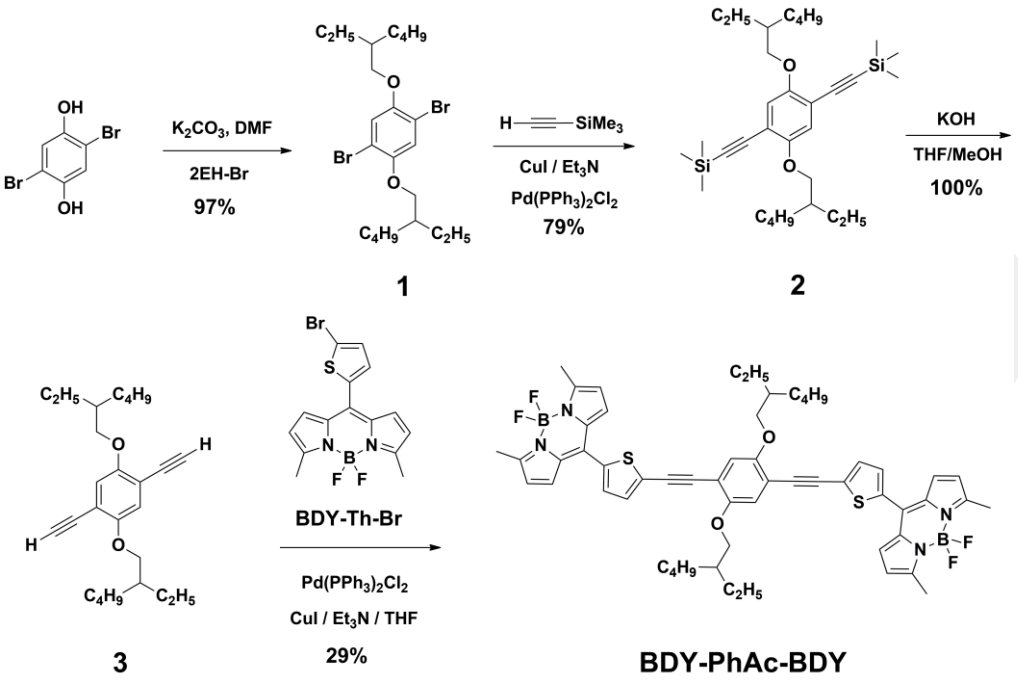

Scheme 3.3.4.1. Synthetic route to **BDY-PhAc-BDY**.

The synthesis of **BDY-PhAc-BDY** is shown in Scheme 1. 2,5-Dibromohydroquinone was first reacted with 2-ethylhexylbromide (2EH-Br) in the presence of K_2CO_3 base in DMF to yield double alkylated product **1** in 97% yield. Double alkynylation reaction of **1** was performed via Sonogashira cross-coupling reaction with ethynyltrimethylsilane ($HC{\equiv}C\text{-}SiMe_3$) by using $Pd(PPh_3)_2Cl_2$ catalyst in the presence of CuI/Et_3N. This reaction yielded **2** in 79% yield, which then underwent quantitative (100% yield) desilylation with KOH to form hydrogen-ended ethynyl groups in compound **3**. In the final Sonogashira cross-coupling reaction, **3** was reacted with **BDY-Th-Br** in the presence of $Pd(PPh_3)_2Cl_2$ catalyst and CuI/Et_3N cocatalyst/base mixture. Note that **BDY-Th-Br** was prepared in accordance with our reported procedure**.**[1] Thanks to the good

solubility of the target small molecule in common organic solvents, the purification was carried out via column chromatography using $CHCl_3$ as eluent (29% yield). The chemical structure and purity of the intermediate compounds and the resulting small molecule, **BDY-PhAc-BDY**, were characterized by $^{1}H/^{13}C$ NMR, MALDI-TOF, and Elemental Analysis. Diffraction-quality single-crystals of **BDY-PhAc-BDY** were obtained by diffusion of methanol into a chloroform solution at room temperature, and the corresponding solid-state structure was confirmed by single-crystal X-ray analysis (Figure 3.3.4.1.1). **BDY-PhAc-BDY** is crystallized in the triclinic space group P-1 and it is located on a crystallographic inversion center. BODIPY frame (C_9BN_2) adopts a nearly coplanar π-structure with the boron atom locating slightly out of this plane by 0.159(10) Å. As shown in Figure 3.3.4.1.1B, BODIPY π-core shows a dihedral angle ($\theta_{dihedral}$) of 44.94° with the *meso*-thiophene ring, which is slightly lower than our previously reported "BODIPY-Thiophene" dihedral angle (48.80°). Moreover, this is much smaller than those measured between the dipyrrin framework and the *meso*-phenyl and thienyl units in previously reported BODIPY small molecules ($\theta_{dihedral} > 54-90°$).[124], [144]–[146] This co-planarization reflects the structural advantages of the current π-system including absence of β-pyrrole substitutions and sterically-confined nature of the five-membered thiophene ring. The B1–F1 (1.385(11) Å) and B1–F2 (1.378(10) Å) bond distances and F1–B1–F2 (110.1(7)°), N1–B1–N2 (106.8(7)°), and N–B–F (av. 109.975°) bond angles are similar to those found in the literature.[147] As shown in Figure 3.3.4.1.1C, the detailed crystal packing analysis of **BDY-PhAc-BDY** indicates that the presence of 2-ethylhexyloxy moieties on the central benzene ring prevents the π-π stacking interactions to occur between the complete molecular π-backbones. However, BODIPY π-cores are still found to employ antiparallel arranged, π-stacked dimers with an interplanar distance of 3.93 Å in the unit cell (Figure 3.3.4.1.1D). This arrangement is most likely a result of the energetically favorable antiparallel dipole-dipole interactions between the BODIPY cores' strong molecular dipole moments (μ = 3.38 Debye)[148] oriented toward the 4,4′-fluorine substituents. In addition, relatively weaker "π···π" (~4.51 Å) interactions were observed between ethynyl (-C≡C-) groups which, in combination with the strong edge-to-face "C-H···π (*dialkoxyphenylic*) (~2.85Å)" interactions between π-electron-deficient BODIPY-pyrrole hydrogens and the central π-electron-rich dialkoxybenzene ring or ethynyl (-C≡C-) group, is found to play a critical role not only in solid-state formation, but also in thin-film crystallization to form highly crystalline microribbons (Figure 3.6.3.2C, *vide infra*).

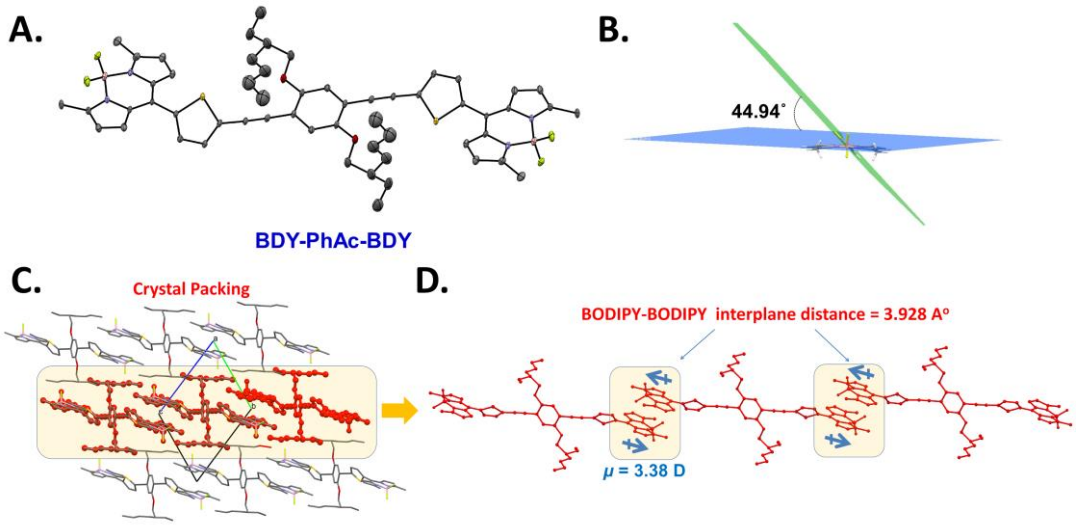

Figure 3.3.4.1.1. A. X-ray crystal structure of **BDY-PhAc-BDY** with 20% ellipsoids. The grey, blue, red, pink, yellow, and white coloured atoms represent C, N, O, B, F, and H, respectively, B. the perspective view of the inter-ring dihedral angle between boron-dipyrromethene and *meso*-aromatic unit planes, C. Crystal packing of **BDY-PhAc-BDY**, and D. The perspective view of antiparallel arranged, π-stacked dimers (3.928 Å) occurred between two BODIPY units. The local dipole moments (μ = 3.38 Debye) of BODIPY cores are shown in blue.

As shown in Figure 3.3.4.1.2, **BDY-PhAc-BDY** was found to be highly thermally stable with the thermolysis onset temperature (5% mass loss) located at 300 °C. A two-step decomposition behavior was observed with a small step at ~87% of the original weight, corresponding to the mass loss of one of the alkyl substituents (-$CH_2CH(C_2H_5)(C_4H_9)$). Differential scanning calorimetry (DSC) measurement shows a sharp endothermic peak at 198 °C with an enthalpy of 62.65 J/g. This peak indicates the thermal transition of the crystalline **BDY-PhAc-BDY** solid into an isotropic liquid, which was further confirmed by conventional melting-temperature measurement ($T_{m.p.}$ = 196-197 °C). This is very different from our previously reported non-substituted BODIPY-small molecules, **BDY-3T-BDY/BDY-4T-BDY**, which have showed thermal decompositions with no observable melting points.[149] This reflects the critical role of flexible swallow-tailed 2-ethylhexyloxy substituents to tune intermolecular interactions, which eventually induces melting process. Note that once the crystalline solid obtained from chromatographic purification melts to an isotropic liquid, no corresponding crystallization peak was observed in the cooling cycle. This indicates that **BDY-PhAc-BDY** adopts an amorphous solid-state upon cooling and it does not exhibit further melting peak in the second-heating cycle (Figure 3.3.4.1.2B).

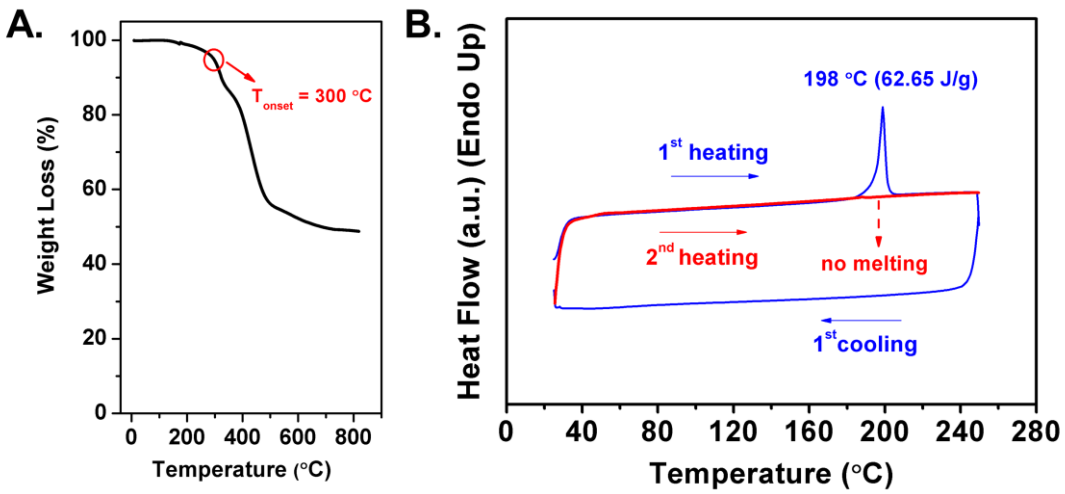

Figure 3.3.4.1.2. A. Thermogravimetric analysis (TGA), and B. Differential scanning calorimetry (DSC) measurement curves of **BDY-PhAc-BDY** at a temperature ramp of 10 °C/min under N_2.

3.3.4.2. Optical and Electrochemical Properties

The electrochemical and optical properties of **BDY-PhAc-BDY** were evaluated by UV-vis absorption and photoluminescence spectroscopies, and cyclic voltammetry. **BDY-PhAc-BDY** exhibits two absorption peaks in dichloromethane solution with λ_{max} located at 355 nm and 527 nm. The large molar extinction coefficient ($\varepsilon = 1 \times 10^5$ M^{-1} cm^{-1}) for the absorption peak at 527 nm and the out-of-plane vibronic feature at 495 nm (~1200 cm^{-1} shift from λ_{max}) are unique features of the BODIPY-based π–π^* ($S_0 \rightarrow S_1$) transition.[107] The broad peak with lower intensity at 355 nm is ascribed to a combination of BODIPY-based $S_0 \rightarrow S_2$ and 1,4-bis-(thienylethynyl)2,5-dialkoxybenzene-based π–π^* transitions. The optical band gap is estimated as 2.22 eV from the low-energy absorption edge. In the thin-film state (spin-coated on glass substrate), the absorption maxima show bathochromic shifts (λ_{max} = 365/543 nm) and the optical band gap is lowered to 2.06 eV (solid-state) with respect to those in the solution. This is indicative of molecular π-backbone planarization and solid-state ordering as compared to the solution phase. The fluorescence spectrum of **BDY-PhAc-BDY** in dichloromethane solution (Figure 3.3.4.2.1) exhibits a broad emission peak with a largely shifted maxima of 646 nm (Stokes shift = 119 nm) and a very low quantum yield (Φ_F) of ~0.02%. This is very different from typical BODIPY emission features such as high

quantum yield and extremely low Stokes shifts, and it reflects most likely the presence of nonradiative pathways in the excited state via intra-/inter-molecular charge transfer processes.[130] When the solvent dielectric constant is lowered (THF ($\varepsilon = 8.9$) → toluene ($\varepsilon = 2.3$)), a highly blue-shifted PL spectra was measured in toluene (Figure 3.3.4.2.1, λ_{em} = 578 nm) indicating positive solvachromatism.

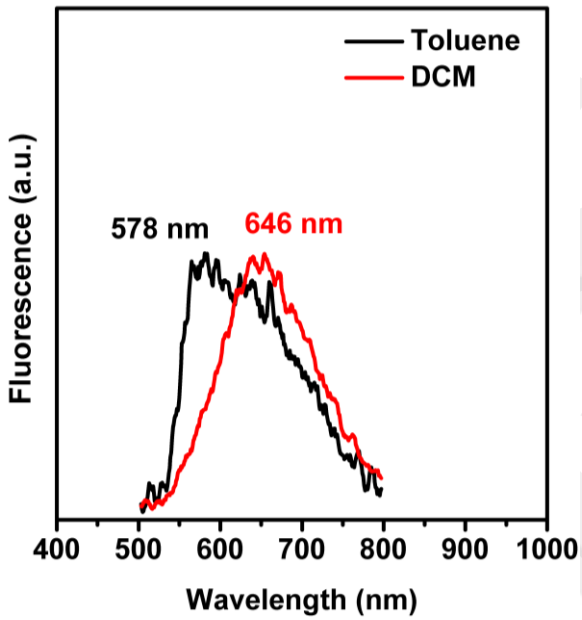

Figure 3.3.4.2.1. Fluorescence emission spectra of **BDY-PhAc-BDY** in dichloromethane (DCM) and toluene solutions ($1x10^{-5}$ M) (Excitation wavelength= 510 nm).

This further confirms that the final relaxed excited state employs a large dipole moment as a result of charge transfer (CT) between subchromophoric units. Based on the DFT calculations (B3LYP/6-31G** level of theory), lowest unoccupied molecular orbital (LUMO) of **BDY-PhAc-BDY** is found to be symmetrically localized on the outer BODIPY π-acceptor units, while highest occupied molecular orbital (HOMO) is delocalized only on the central π-donor part with noticeable contributions from the oxygens on the alkoxy groups (Figure 3.3.4.2.2-inset). This further supports the emission characteristics of **BDY-PhAc-BDY**, that the photoexcitation is probably accompanied with an intramolecular charge-transfer (CT) in the excited state from donor to acceptor unit (HOMO → LUMO). Cyclic voltammetry measurements reveal two reversible reductions and one quasi-reversible oxidation for **BDY-PhAc-BDY** with the first half-wave reduction-potential ($E_{1/2}^{red-1}$) located at -0.84 V and the first onset oxidation-potential (E_{onset}^{ox-1}) located at 1.28 V. The electrochemical band gap (2.12 eV) shows

excellent agreement with the optical band gap (2.22 eV) measured in solution. The HOMO and LUMO energy levels are estimated as −5.68 eV and −3.56 eV, respectively. Note that, as a result of π-electron deficiency of the *meso*-substituted BODIPY's at the molecular termini, LUMO energy level of the new molecule is sufficiently stabilized to be in the energetic range of previously reported *n*-channel semiconductors (−2.9 to −4.3 eV).[150] Furthermore, when compared with the observed *p*-doping characteristics, highly reversible and favorable reductive properties of **BDY-PhAc-BDY** are indicative of its electron-transporting semiconductor potential.

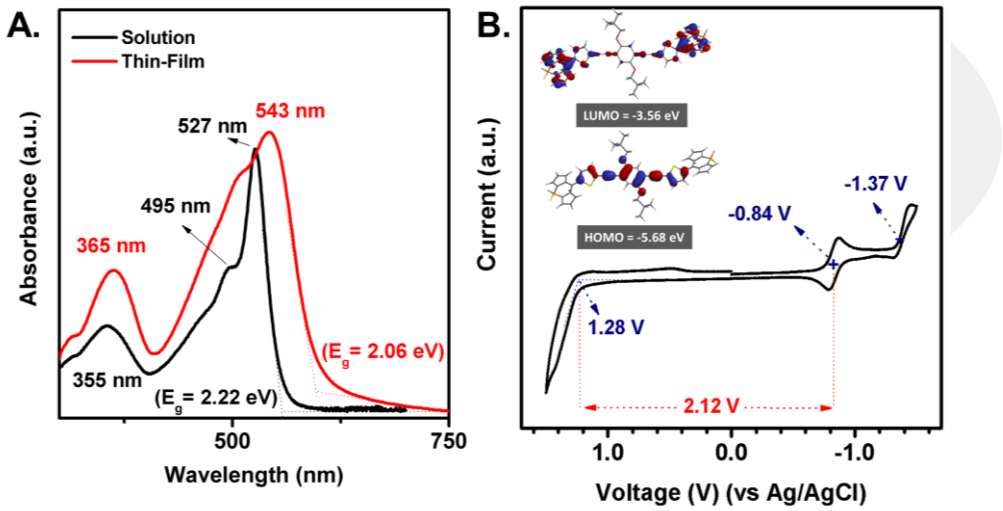

Figure 3.3.4.2.2. A. Optical absorption in dichloromethane solution (black line) and as thin-film (red line) of **BDY-PhAc-BDY**, and B. Cyclic voltammogram of **BDY-PhAc-BDY** in dichloromethane (0.1M $Bu_4N^+PF_6^-$, scan rate = 50 $mV \cdot s^{-1}$). Inset shows the calculated (DFT, B3LYP/6-31G**) topographical orbital representations and experimentally estimated HOMO and LUMO energy levels.

3.3.4.3. Thin-Film Microstructure/ Morphology and Field-Effect Transistor Characterization

The semiconductor thin-films (40-62 nm) were fabricated by solution-shearing **BDY-PhAc-BDY** solution in 1,2,4-trichlorobenzene (1.0 mg/mL) on PS (polystyrene)-brush treated n^{++}-Si/SiO_2 substrates. Bottom-gate/top-contact (BG/TC) OFETs were

completed by thermal evaporation of source and drain Au electrodes (40 nm) via thermal evaporation (deposition rate = 0.2 Å/s) to yield various channel lengths (L: 100 and 50 μm) and widths (W: 1000 and 500 μm). The microstructure of solution-sheared **BDY-PhAc-BDY** thin-film was investigated by out-of-plane X-ray diffraction measurement, which displays a major diffraction peak at 2θ = 8.94° (Figure 3.3.4.3.2A). The second and third order diffractions of the same crystalline phase were also observed revealing a high degree of ordering across the thin-film thickness. The simulation of the powder pattern based on the single-crystal structure of **BDY-PhAc-BDY** (Figure 3.3.4.3.1) shows that all these peaks are well indexed along the (010) lattice plane, and second and third order diffractions correspond to (020) and (030), respectively.

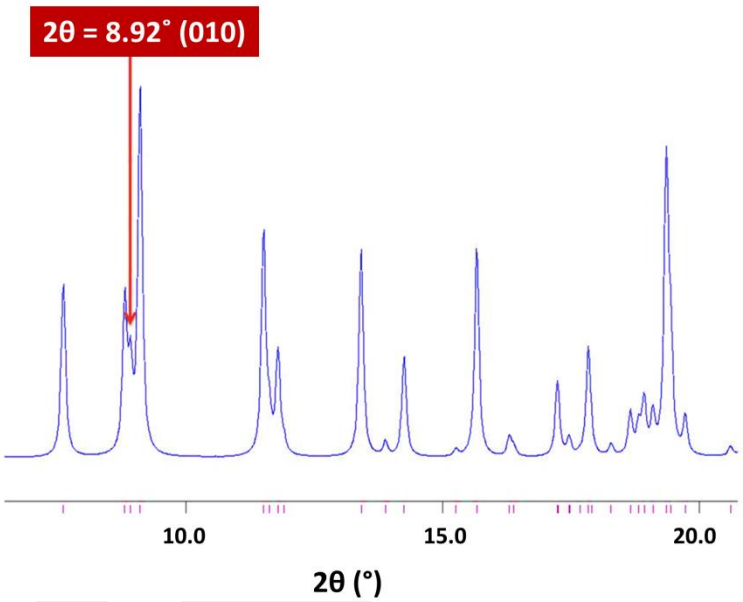

Figure 3.3.4.3.1. Simulated XRD powder pattern of **BDY-PhAc-BDY** with the selected matching peak at 2θ = 8.92˚ corresponding to (010) diffraction plane.

The periodicity (*d*-spacing) of the (010) plane in thin-film phase is measured as 9.88 Å, which corresponds to "*b*-axis (10.928 Å) × sin α (66.26˚)" and suggests that the molecules are adopting a highly tilted molecular orientation on the substrate (Figure 3.3.4.3.2C). Atomic force microscopy (AFM) and scanning electron microscopy (SEM) characterizations show that the morphology of the solution-sheared thin-film of **BDY-PhAc-BDY** consists of one-dimensional (1-D) highly crystalline micron-sized ribbons, which are perfectly aligned along the shearing direction (Figure 3.3.4.3.2B). The lengths of the microribbons can reach to ~0.1 mm and their widths were ~0.5-2.0 μm. Detailed

analysis of the AFM image also shows the formation of well-connected smaller grains having ~200-500 nm lengths along the ribbon long-axis. In order to elucidate the structural packing in these micro-ribbons, the BFDH (Bravais, Friedel, Donnay, and Harker) theoretical crystal morphology was used, which predicts a high aspect ratio crystal growth perpendicular to the [010] out-of-plane direction. Since the self-assembly process during thin-film crystallization may be similar to single-crystal formation, the thermodynamically/kinetically more favored primary crystal growth along the [100] crystallographic direction most likely reflects the anisotropic ribbon growth due to similar directional intermolecular forces.[151]–[153] This shows that the major intermolecular interactions governing the thin-film crystallization are: (i) strong "-CH···π" contacts (~2.85Å) between π-deficient BODIPY-pyrrole hydrogens and the central π-electron rich dialkoxybenzene ring/ethynyl (-C≡C-) groups, (ii) "π···π" (~4.5Å) interactions between ethynyl (-C≡C-) groups, and (iii) "π···π" (~3.9 Å) and dipole-dipole interactions between antiparallel arranged BODIPY frameworks (*vide infra*). It appears to us that also the directional solution-shearing process used for the current thin-film fabrications might play a key role to facilitate **BDY-PhAc-BDY**'s molecular self-assembly into anisotropic ribbons along the shearing direction.[93] The formation of ribbon-like morphology with the solution-shearing method is consistent with our previous rod-like BODIPY small molecules (**BDY-3T/4T-BDY**) which has also yielded high-aspect ratio microfibers in thin-film.

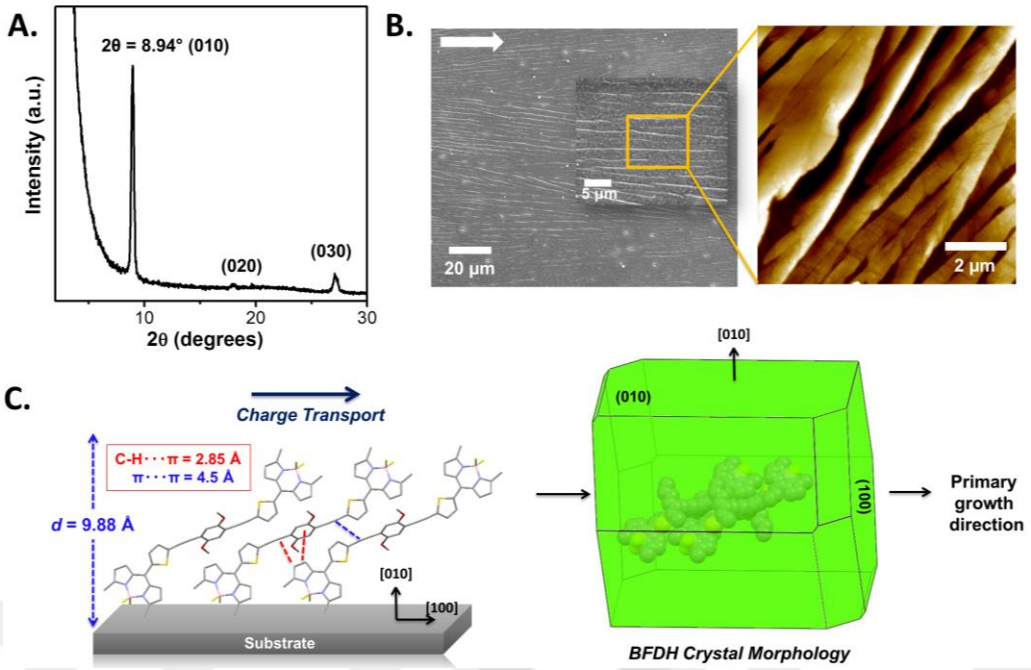

Figure 3.3.4.3.2. *θ*-2*θ* X-ray diffraction (XRD) scans (A) and SEM/AFM-topographic images (B) of solution-sheared **BDY-PhAc-BDY** thin-film. (C) The molecular arragement in the out-of-plane [010] direction and the BFDH (Bravais, Friedel, Donnay and Harker) theoretical crystal morphology showing the primary crystal growth direction ([100]). The arrow shows the shearing direction. "-CH···π" contacts (~2.85Å) and "π···π" (~4.5Å) interactions are shown between two representative molecules.

OFET device characteristics were measured wih a Keithley 4200-SCS semiconductor characterization system at room temperature. The transistor characteristics in the saturation regime such as charge carrier mobilities (μ) and threshold voltages (V_T) were extracted from the equation:

$$\mu_{sat} = (2I_{DS}L)/[WC_i(V_G - V_T)^2]$$

where I_{DS} is the drain current, L and W are the channel length and width, respectively, C_i is the areal capacitance of the gate dielectric, V_G is the gate voltage, and V_T is the threshold voltage. Typical transfer and output curves are shown in Figures 3.3.4.3.3 and 3.3.4.3.4. Consistent with the theoretical and experimental optoelectronic characterizations on the small molecule (*vide supra*), these devices exhibited *n*-channel behavior with μ_e = 0.004 $cm^2/V \cdot s$ and $I_{on}/I_{off} = 10^5$-10^6. This clearly shows that BODIPY is an effective π-acceptor unit to afford a substantial lowering of the LUMO level and to

induce *n*-channel semiconductivity in π-conjugated small molecules for use in optoelectronic devices.

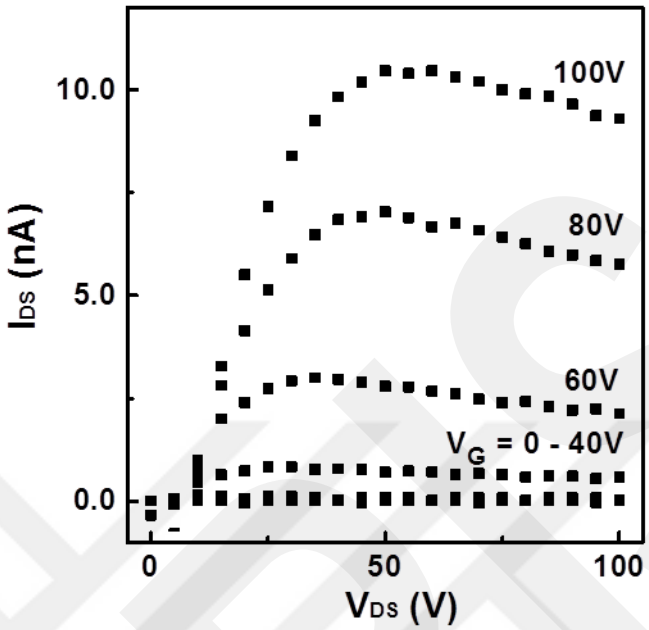

Figure 3.3.4.3.3. Representative output plot for the OFET devices fabricated with solution-sheared **BDY-PhAc-BDY** thin-film.

Although the current electron mobility for **BDY-PhAc-BDY** thin-film is much lower than the state-of-the-art performances achieved previously with other molecular π-systems, it is still remarkable from a molecular design perspective since it is the highest reported to date for a BODIPY-based small molecular semiconductor having alkyne linkages. Besides, the growth of well-oriented micro- and nano-sized organic semiconductor structures from solution phase has always been challenging in the literature and it offers great advantages in fabricating transistor arrays for circuit design.[152][153][154] Although π-π stacking between whole molecular skeletons are not evident along the charge-transport (in-plane) direction, the localized π-π stackings between individual acceptor or donor units in the twisted arrangement of A-D-A π-architecture,[155] and strong "-CH···π" interactions in the face-to-edge herringbone packing may still contribute to 3-D charge transport, which, along with the highly-crystalline microstructure, explains the observed mobility. Since the thin-film crystallinity and morphology of the current semiconductor remains similar to our previously reported non-substituted semiconductor, **BDY-4T-BDY**, the slightly reduced

(2.5×) OFET performance is most likely related to the presence of σ-insulating alkyl substituents on the central benzene ring. Based on our findings, note that BODIPY π-core offers unique advantage by providing good solubility to the molecular π-system even in the absence of alkyl substituent. Therefore, for the future development of solution-processable BODIPY-based semiconductors, we rationalize that non-substituted systems should be preferred to yield higher mobilities.

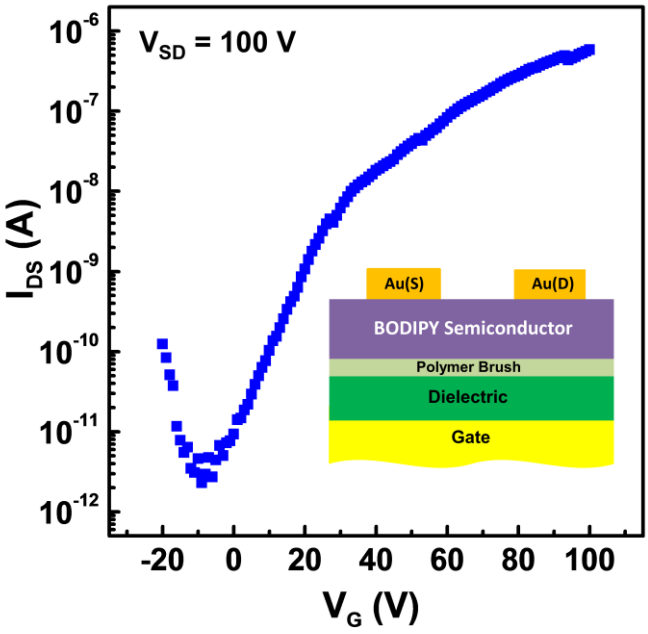

Figure 3.3.4.3.4. Representative transfer plot in the *n*-channel region for bottom-gate/top-contact (BG/TC) OFET devices fabricated with solution-sheared **BDY-PhAc-BDY** thin-film.

3.3.5. Conclusion

A new solution-processable BODIPY-Acetylene small molecule, **BDY-PhAc-BDY**, based on A-D-A π-architecture was designed, synthesized and fully characterized. The new semiconductor exhibited a low solid-state optical band gap of 2.06 eV with stabilized HOMO and LUMO energy levels of -5.68 eV and -3.56 eV. Single-crystal X-ray diffraction (XRD) analysis reveals crucial structural features and intermolecular interactions such as relatively low "BODIPY-*meso*-thiophene" dihedral angle ($\theta_{dihedral}$ = 44.94°) and antiparallel π-stacked BODIPY dimers with an interplanar distance of 3.93 Å. Highly crystalline one-dimensional (1-D) microribbons of **BDY-PhAc-BDY** were

grown from the chloroform solution on PS (polystyrene)-brush treated substrates via solution-shearing method. Strong edge-to-face "C-H(*pyrrolic*)···π(*dialkoxyphenylic*) (~2.85Å)" and relatively weaker "π(*ethynyl*)···π(*ethynyl*)" (~4.51 Å) directional interactions are found to be effective in the formation of current highly crystalline microribbons along the [100] direction. The bottom-gate/top-contact OFET devices based on these microribbons exhibited clear *n*-channel operation and afforded electron mobility of 0.004 $cm^2/V \cdot s$ and the on/off current ratio of 10^5-10^6, which is the highest reported till now for BODIPY-based small molecular semiconductors with alkyne linkages. Our findings clearly demonstrate that BODIPY is an effective π-acceptor unit to realize solution-processable donor-acceptor type small molecules for electron-transport. Here, we also offer crucial guidance for the design of future BODIPY-based semiconductor molecules with further improved electrical performances and also easily fabricable 1-D semiconductor thin-film morphologies for fundamental/applied research in organic optoelectronics.

Chapter 4

Semiconducting Copolymers based on meso-Substituted BODIPY for Inverted Organic Solar Cells and Field-Effect Transistors

4.1. Introduction

The development of novel solution-processable semiconducting polymers for organic optoelectronic technologies has grown rapidly within the recent decades, because of their emerging applications in new generation flexible and roll-to-roll processed electronic devices such as organic field-effect transistors (OFETs) and bulk-heterojunction organic photovoltaics (BHJ-OPVs).[101], [156]–[163] This progress is mainly driven by a combination of rational materials design and extensive exploratory synthesis.[56], [73], [99], [104], [164], [165] In particular, donor-acceptor (D-A) conjugated polymers with alternating electron-rich (D) and electron-deficient (A) units offer the great advantage of fine-tuning optoelectronic/physicochemical properties.[73], [166]–[170] This allows the realization of any desired copolymer property for a particular application by simply choosing the proper D/A units. Importantly, this strategy can yield low band-gap (<1.5 eV) copolymers with highly extended π-conjugations, providing access to a variety of state-of-the-art performances in polymer-based OFETs and OPVs. Specifically, the reported charge carrier mobilities with D-A copolymers in OFETs are now routinely higher than that of amorphous silicon (>0.5-1.0 $cm^2/V \cdot s$) and power conversion efficiencies (PCEs) of 10-12% are now available with D-A copolymer-based BHJ solar cells.[171]–[180] Despite these recent advances in polymer-based optoelectronics, there is still only a handful example of π-acceptor building blocks realized in the structure of D-A copolymers, which are mainly based on

diketopyrrolopyrrole (DPP),[177], [181], [182] isoindigo,[183] benzo(bis)thiadiazole,[184] rylenediimide,[185][20][71][127][186][187] and thieno[3,4-c]pyrrole-4,6-dione[185] π-acceptor units. Therefore, from synthetic chemistry and materials design perspectives, the development of new π-acceptor building blocks is of great importance to diversify the chemistry of charge-transporting polymeric materials and to realize novel properties in advanced optoelectronic technologies.

BODIPY (4,4-difluoro-4-bora-3a,4a-diaza-sindacene) π-core, structurally considered as "porphyrin's little sister", has attracted significant interest because of its potential technological applications in various fields including biochemical labeling, fluorescent switching, and photodynamic therapy.[1], [188]–[191] Recently, BODIPY-based semiconductors are attracting considerable attention for their applications in the organic electronics.[110], [192], [193] This is not only due to BODIPY π-core's facile synthesis/modification but also because of its advantageous structural/electronic properties such as co-planarity, low LUMO level, good solubility, and high dipole-moment[1], [78], [194]–[199] To this end, it has been recently demonstrated by several research groups that BODIPY has a very unique electronic structure that charge-carrier type is highly dependent on its π-architecture.[109], [110], [200] While π-extension on BODIPY's *meso*-position leads to *n*-channel semiconductivity (as in the case of **BDY-4T-BDY**, μ_e = 0.01 $cm^2/V \cdot s$),[1][109] aromatic substitutions on 2,6-positions yields *p*-channel semiconductors (Figure 4.1).[78] By means of this unique electronic feature, some of us have recently demonstrated solution-processed *p*-channel OFETs based on a semicrystalline BODIPY-thiophene copolymer **P(C11-BDY-T)** (Figure 4.1),[78] which is still holding the record for charge-carrier mobility (μ_h = 0.17 $cm^2/V \cdot s$) among all known BODIPY-based semiconductors. In these studies, BODIPY core stands out as a promising, highly electron-deficient and versatile π-acceptor building block with superior solution processibility. However, BODIPY-based donor polymers still show very poor solar cell performances with PCEs of only ~1-2% in fullerene-based BHJ devices.[192], [201]–[203] The reported solar cells consisting of BODIPY-based polymers and PCBM suffered from one or more of these following complications: low short-circuit current (J_{SC}) mainly due to poor solubility of polymer donors, mismatched energy levels, and unoptimized BHJ morphology with fullerene acceptors, which prevents efficient charge transport and generation. Therefore, further research is required to design and develop new polymerizable BODIPY-based building blocks and to investigate their properties in semiconducting copolymers for use in OPVs

and OFETs. To this end, the development of BODIPY-based polymers, which can yield high PCEs in inverted solar cell device structure, is especially very important. This is because, compared with conventional BHJ-OPV devices, inverted structure has the advantage of improved long-term ambient stability since corrosive/hygroscopic hole-transporting poly(3,4-ethylenedioxylenethiophene):poly(styrenesulphonicacid) (PEDOT:PSS) and low-work-function metal cathode are not needed, and these devices are self-encapsulated.[172], [173] In addition, inverted devices can show favorable vertical phase separation and concentration gradient in the active layer.[204]

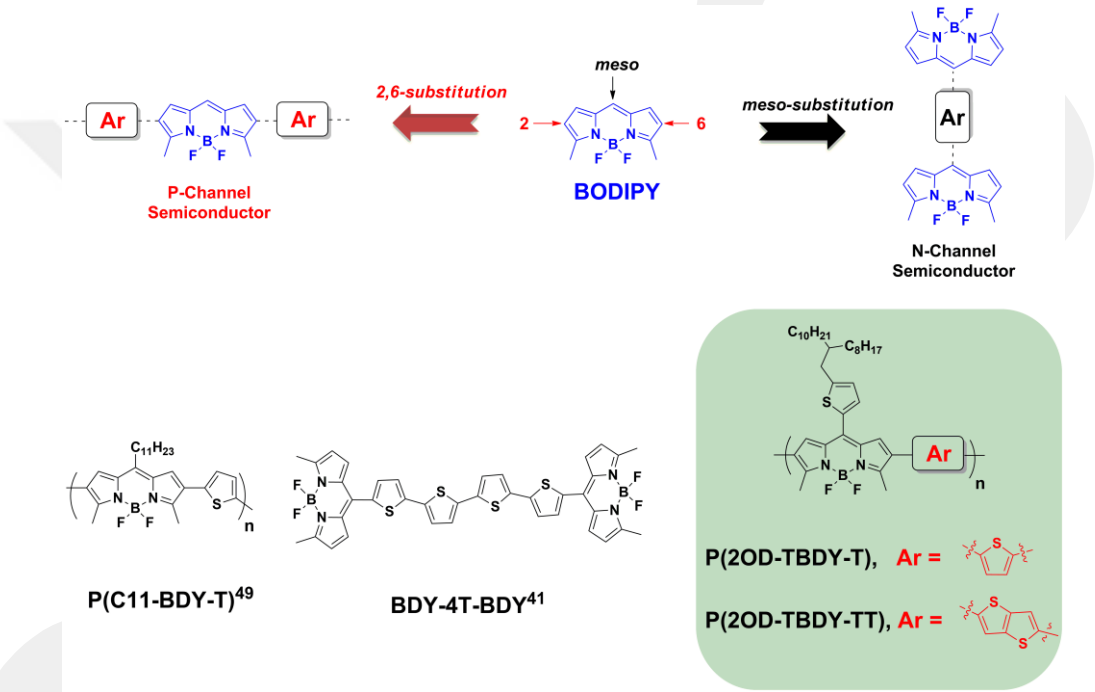

Figure 4.1. The effect of aromatic substitutions at *meso*- and *2,6*-positions of the BODIPY π-core on the charge-carrier type, the chemical structures of previously developed semiconductors **P(C11-BDY-T)**[78] and **BDY-4T-BDY(1)**, and the copolymers **P(2OD-TBDY-T)** and **P(2OD-TBDY-TT)** developed in this study.

In this paper, a highly electron-deficient and soluble *meso*-heteroaromatic substituted π-acceptor building block, **2OD-TBDY-Br$_2$** (Scheme 4.3.1), is developed. When compared with *meso*-alkyl substituted BODIPY monomers, π-delocalization for the lowest unoccupied molecular orbital (LUMO) in this building block is found to be extended towards the *meso*-thienyl π-core, which yields highly favorable structural/electronic properties. Based on the previous findings that *meso*-heteroaromatic substituted BODIPY π-systems are efficient electron-transporting semiconductors, we

envision a similar rationale that *meso*-heteroaromatic substitutions on BODIPY-based monomers may lead to enhanced electron-acceptor characteristics.[1], [109], [205] **2OD-TBDY-Br$_2$** was copolymerized with thiophene and thieno[3,2-b]thiophene donor moieties to yield two new low band-gap (E_g = 1.31-1.35 eV) donor-acceptor semiconducting copolymers **P(2OD-TBDY-T**) and **P(2OD-TBDY-TT**), respectively (Figure 4.1). The polymeric semiconductor thin-films prepared by spin-coating show isotropic nodule-like grains with essentially no microstructural ordering in the out-of-plane direction. The polymer solutions and the corresponding thin-films exhibit strong aggregation-dependent excitonic properties, as studied by temperature-dependent UV-Vis absorption spectroscopy. Enhanced π-coherence was evident in solution even at high temperature as a result of strong interchain interactions. OFETs in bottom-gate/top-contact device geometry featuring polymer semiconductor thin-films demonstrate hole mobilites of 0.005 $cm^2/V{\cdot}s$ and 0.0002 $cm^2/V{\cdot}s$ for **P(2OD-TBDY-T)** and **P(2OD-TBDY-TT)**, respectively, with I_{on}/I_{off} ratios of 10^4–10^6 in ambient. BHJ-OPVs consisting of **P(2OD-TBDY-T)** donor polymer and $PC_{71}BM$ acceptor had the power conversion efficiency (PCE) of 6.16% with high short-circuit current (J_{SC}) value of 16.63 mA/cm^2. To the best of our knowledge, the PCE value is the highest achieved to date for the OPVs based on BODIPY-based donor polymer, and, more generally, on the boron-containing donor polymers.

4.2. Experimental

4.2.1. Materials and Methods

All reagents were used as obtained from commercial sources without any purification unless otherwise noted. Schlenk techniques were employed in the reactions by using a vacuum-nitrogen manifold system, and the reactions were carried out under N_2 unless otherwise noted. $^1H/^{13}C$ NMR spectra were recorded on a Bruker-400 spectrometer (^1H, 400 MHz; ^{13}C, 100 MHz) and thin-layer chromatography (TLC) was performed on silica gel plates coated with fluorescent indicator F254. Elemental analyses were done on a LecoTruspec Micro model instrument. MALDI-TOF characterization was

performed on a Bruker Microflex LT MALDI-TOF-MS Instrument. Polymer molecular weights were determined on a Waters GPC system (Waters Pump 510) in THF at room temperature vs polystyrene standards. Thermogravimetric analysis (TGA) and differential scanning calorimetry (DSC) measurements were performed on Perkin Elmer Diamond model instruments at a heating rate of 10 °C/min under nitrogen. Dynamic light-scattering (DLS) measurements were performed on a Malvern, Nano ZS Zetasizer. UV-Vis absorption measurements were performed on a Shimadzu, UV-1800 UV-Vis Spectrophotometer. Electrochemical measurements were performed on a C3 cell stand electrochemical station equipped with BAS-Epsilon software (Bioanalytical Systems, Inc. Lafayette, IN). The molecular geometry optimizations and total energy calculations were carried out using density functional theory (DFT) at the B3LYP/6-31G** level by using Gaussian 09.[86]

4.2.2. Synthesis and Characterization

The synthesis of 2-(2-octyldodecyl)thiophene (**1**),[116] 2-methylpyrrole,[1] 2,5-bis(trimethylstannyl)thiophene,[1] 2,5-bis(trimethylstannyl)thieno[3,2-b]thiophene,[206] and 5,5'-bis(trimethylstannyl)-2,2'-bithiophene[207] reagents were performed in accordance with the previously reported procedures.

4.2.2.1. Synthesis of 5-(2-octyldodecyl)thiophene -2-carbaldehyde (2).

To a solution of 2-(2-octyldodecyl)thiophene (**1**) (1.7 g, 4.66 mmol) in THF (30 mL) at −78 °C was added 1.96 mL (4.89 mmol) of *n*-butyllithium (2.5 M in *n*-hexane) under nitrogen. The mixture was stirred at −78 °C for 30 min and at room temperature for 1 h. Then, N,N-dimethylformamide (0.375 g, 5.13 mmol) was added slowly at −78 °C, and the resulting reaction mixture was allowed to warm to room temperature overnight. The reaction mixture was quenched with water, and the product was extracted with hexanes. The organic phase was washed with water, dried over Na_2SO_4, filtered, and

evaporated to dryness to give a crude product, which was purified by column chromatography on silica-gel using hexanes:ethyl acetate (10:1) as the eluent. The pure product was obtained as a dark yellow oil (1.48 g, 81%). ^{1}H NMR ($CDCl_3$, 400 MHz): 0.89 (t, 6H, J = 6.4 Hz), 1.25-1.35 (m, 33H), 2.81 (d, 2H, J = 6.8 Hz), 6.88 (d, 1H, J = 3.6 Hz), 7.62 (d, 1H, J = 3.6 Hz), 9.83 (s, 1H).

4.2.2.2. Synthesis of 10-(5-octyldodecylthiophen-2-yl)-5,5-difluoro-3,7-dimethyl-5,10a-dihydro-1H-5l4,6l4-dipyrrolo[1,2-c:2',1'-f][1,3,2]diazaborinine (2OD-TBDY).

A degassed solution of 5-(2-octyldodecyl)thiophene-2-carbaldehyde (**2**) (0.70 g, 1.78 mmol) and 2-methylpyrrole (0.33 g, 4.03 mmol) in CH_2Cl_2 (~250 mL) was prepared under nitrogen and trifluoroacetic acid (TFA) (2 drops) was added. The reaction mixture was stirred at ambient temperature overnight. Next, 2,3-dichloro-5,6-dicyano-1,4-benzoquinone (DDQ) (0.40 g, 1.78 mmol) was added, and the reaction mixture was stirred for additional 2.5 h. Finally, N,N-diisopropylethylamine $(i\text{-}Pr)_2EtN$ (1.26 g, 9.77 mmol) and boron trifluoride diethyl etherate ($BF_3{\cdot}Et_2O$) (0.88 g, 6.22 mmol) were added, and the reaction mixture was stirred for 2 h. The reaction mixture was poured into water and extracted with CH_2Cl_2. The organic phase was dried over Na_2SO_4, filtered, and evaporated to dryness to give a crude product, which was purified by column chromatography on silica gel using CH_2Cl_2:Hexanes (2:3) as the eluent. The pure product was obtained as red oil (0.29 g, 28% yield). ^{1}H NMR (400 MHz, $CDCl_3$): δ 0.89 (t, 6H, J = 6.0 Hz), 1.27-1.33 (m, 33H), 2.66 (s, 6H), 2.82 (d, 2H, J=6.8 Hz), 6.30 (d, 2H, J=4.4 Hz), 6.86 (d, 1H, J=4.0 Hz), 7.11 (d, 2H, J = 4.4 Hz), 7.29 (d, 1H, J = 4.0 Hz). ^{13}C NMR (100 MHz, $CDCl_3$): 14.1, 14.9, 22.7, 26.6, 29.3, 29.4, 29.6, 29.7, 29.8, 30.0, 31.9, 33.3, 34.7, 40.1, 119.1, 126.1, 130.3, 131.9, 132.3, 133.9, 135.4, 150.3, 157.0. MS(MALDI-TOF) m/z (M^+): calcd. for $C_{35}H_{53}BF_2N_2S$: 582.40, found: 582.762 $[M]^+$, 562.709 $[M\text{-}F]^+$, 534.745 $[M\text{-}F\text{-}2\times(CH_3)]^+$. Anal.calcd. for $C_{35}H_{53}BF_2N_2S$: C, 72.14; H, 9.17; N, 4.81, Found: C, 72.47; H, 9.53; N, 4.98.

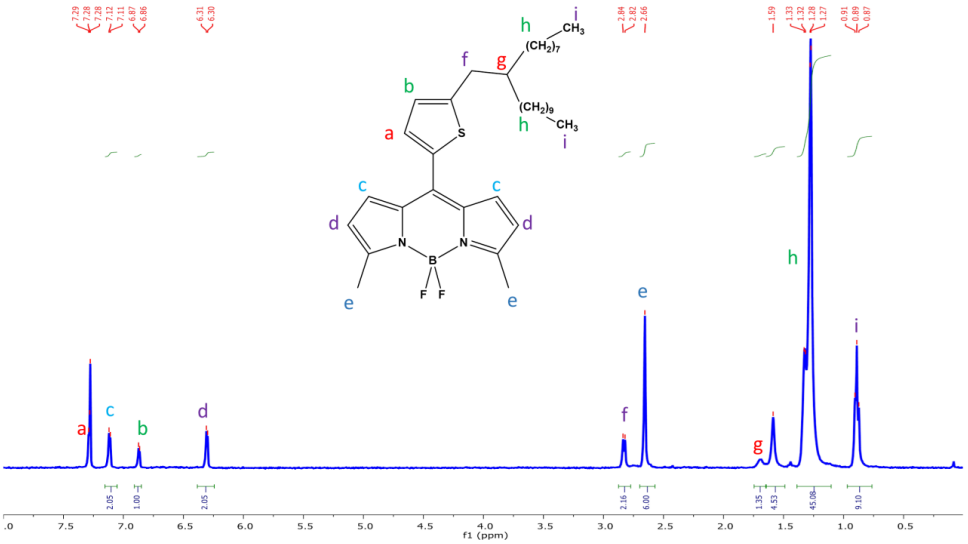

Figure 4.2.2.2.1 ^{1}H NMR spectra of 2OD-TBDY in $CDCl_3$ at room temperature.

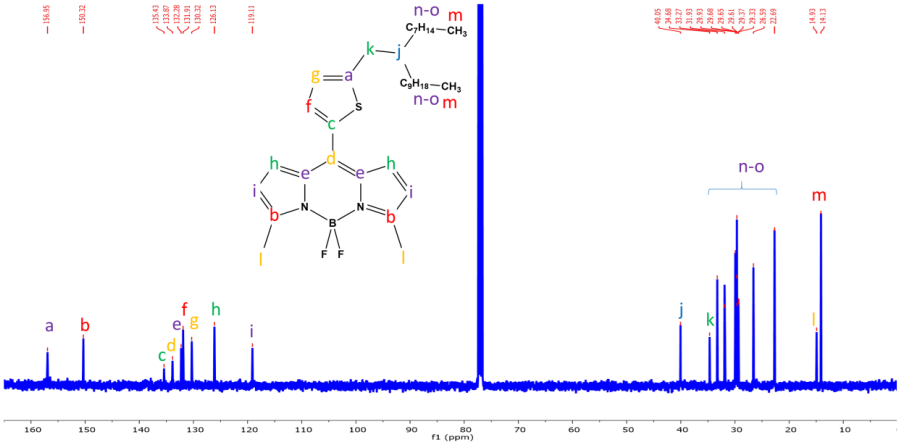

Figure 4.2.2.2.2 ^{13}C NMR spectra of 2OD-TBDY in $CDCl_3$ at room temperature.

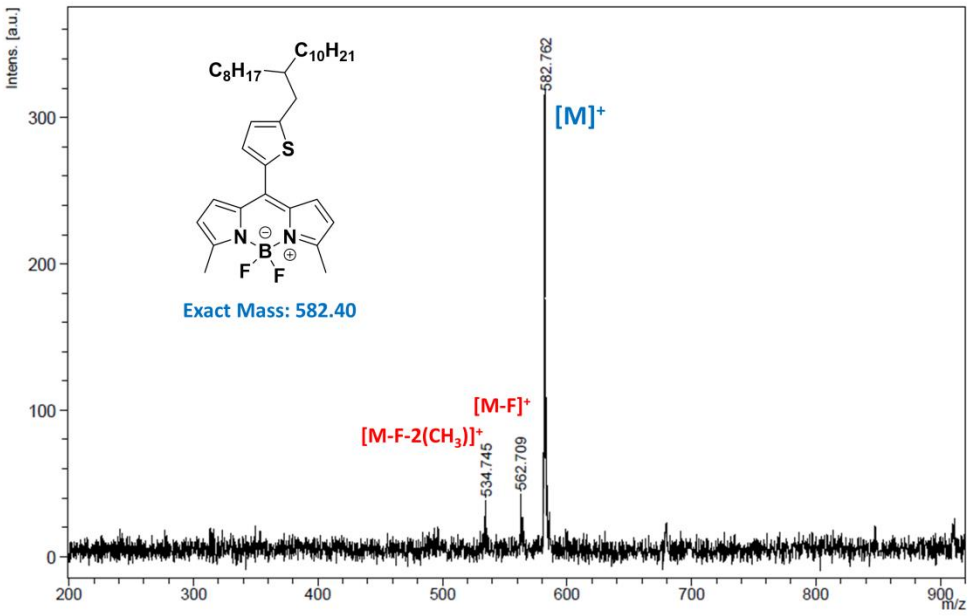

Figure 4.2.2.2.3 Positive ion and linear mode MALDI TOF-MS spectrum of 2OD-TBDY.

4.2.2.3. Synthesis of 2,8-dibromo-10-(5-ethylthiophen-2-yl)-5,5-difluoro-3,7-dimethyl-5,10a-dihydro-1H-5l4,6l4-dipyrrolo[1,2-c:2',1'-f][1,3,2] diazaborinine (2OD-TBDY-Br2)

To a solution of 10-(5-octyldodecylthiophen-2-yl)-5,5-difluoro-3,7-dimethyl-5,10a-dihydro-1H-5l4,6l4-dipyrrolo[1,2-c:2',1'-f][1,3,2]diazaborinine (**2OD-TBDY**) (0.289 g, 0.496 mmol) in dry CH_2Cl_2: DMF (6 mL:6 mL) was added N-bromosuccinimide (0.181 g, 1.02 mmol) in CH_2Cl_2 (3 mL) under nitrogen, and the mixture was stirred at ambient temperature for 2 h. The reaction mixture was evaporated to dryness to give a crude product, which was purified by column chromatography on silica gel using CH_2Cl_2:Hexanes (1:1) as the eluent. The pure product was obtained as dark red oil (0.33 g, 91% yield). ^{1}H NMR (400 MHz, $CDCl_3$): δ 0.88 (t, 6H, J = 6.0 Hz), 1.27-1.33 (m, 33H), 2.63 (s, 6H), 2.85 (d, 2H, J=6.4 Hz), 6.90 (d, 1H, J = 3.6 Hz), 7.20

(s, 2H), 7.30 (d, 1H, J = 3.6 Hz). ^{13}C NMR (100 MHz, $CDCl_3$): 13.4, 14.1, 22.7, 26.6, 29.3, 29.4, 29.6, 29.7, 29.8, 29.9, 31.8, 31.9, 33.3, 34.8, 40.1, 108.6, 126.7, 130.3, 131.4, 132.3, 132.9, 135.2, 152.1, 154.9. MS(MALDI-TOF) m/z (M^+): calcd. for $C_{35}H_{51}BBr_2F_2N_2S$: 738.22, found: 738.357 $[M]^+$, 720.638 $[M\text{-}F]^+$. Anal.calcd. for $C_{35}H_{53}BF_2N_2S$: C, 56.77; H, 6.94; N, 3.78, Found: C, 56.97; H, 6.85; N, 3.85.

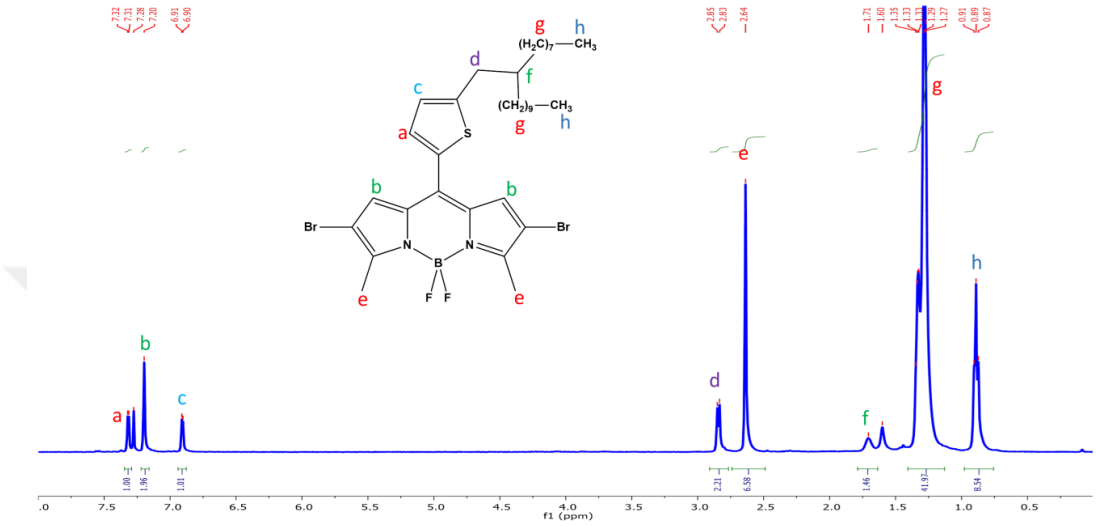

Figure 4.2.2.3.1 ^{1}H NMR spectra of 2OD-TBDY-Br_2 in $CDCl_3$ at room temperature.

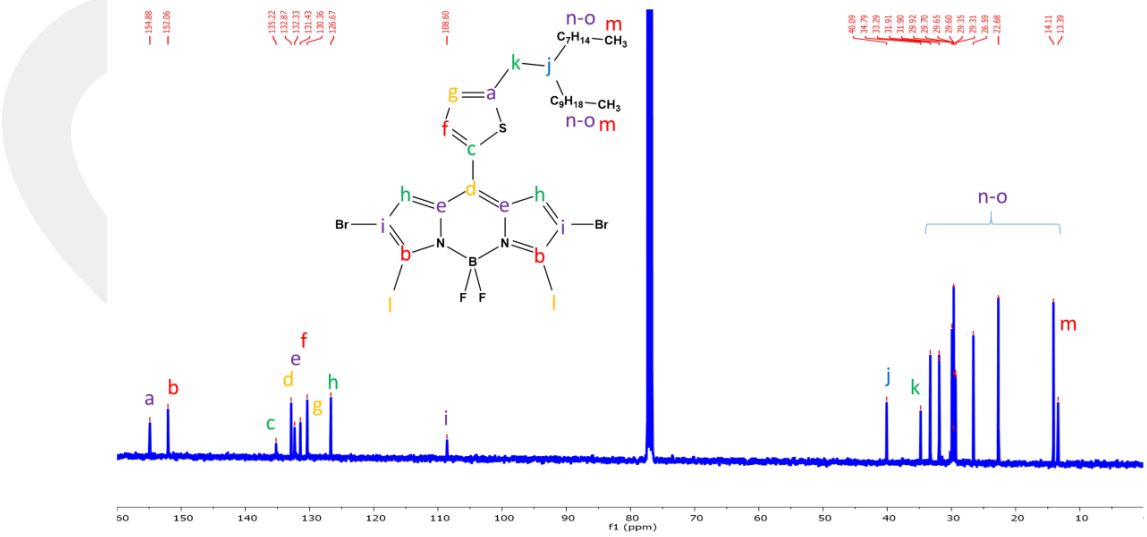

Figure 4.2.2.3.2 ^{13}C NMR spectra of 2OD-TBDY-Br_2 in $CDCl_3$ at room temperature.

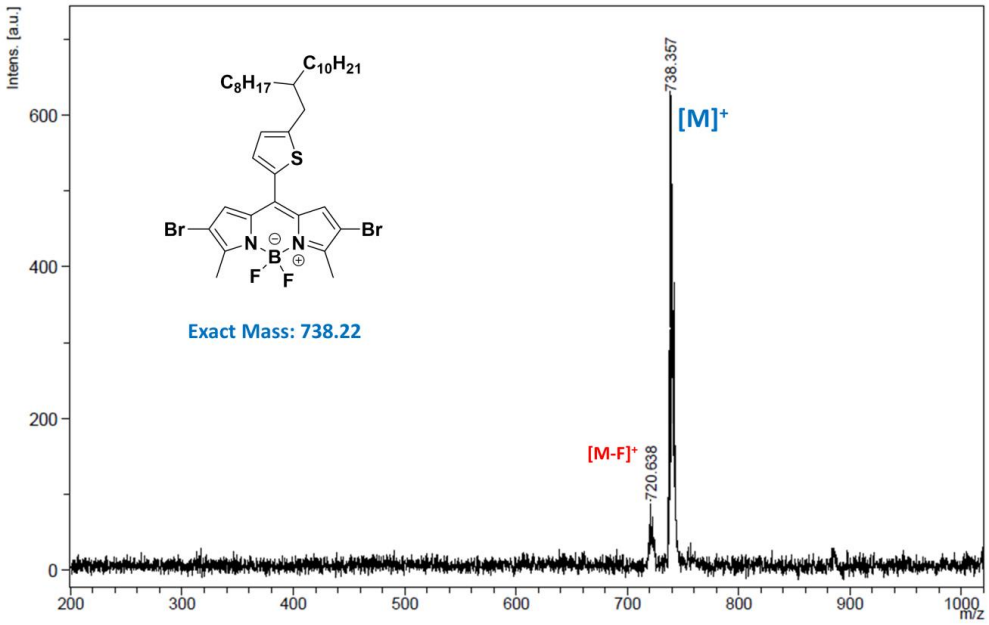

Figure 4.2.2.3.3 Positive ion and linear mode MALDI TOF-MS spectrum of 2OD-TBDY-Br_2.

4.2.2.4. Synthesis of P(2OD-TBDY-T)

A mixture of **2OD-TBDY-Br_2** (0.23 g, 0.310 mmol, 1.0 equiv.), 2,5-bis(trimethylstannyl)thiophene (0.127 g, 0.310 mmol, 1.0 equiv), $Pd_2(dba)_3$ (14.22 mg, 0.016 mmol, 0.05 equiv), and P(*o*-tolyl)$_3$ (37.8 mg, 0.124 mmol, 0.4 equiv) in anhydrous toluene (25 mL) was heated at 120 °C for 16 h in a sealed flask under nitrogen. Then, the polymerization mixture was cooled to room temperature, and the viscous mixture was poured into methanol (~200 mL). After stirring for 1h, the precipitated dark solid was collected by gravity filtration. The crude polymer solid was subjected to sequential soxhlet extractions with methanol, acetone, hexanes, and chloroform. Finally, the concentrated chloroform solution (~10 mL) was precipitated into methanol (~200 mL). The extraction/precipitation procedure was repeated three times in total. The final precipitate was collected by vacuum filtration and dried under reduced pressure to give the pure polymer as a dark colored solid (186 mg, 91% yield). Elemental analysis calcd for $C_{39}H_{53}BF_2N_2S_2$: C, 70.67; H, 8.06; N, 4.23; found: C, 70.86; H, 8.15; N, 4.55; GPC (RT in THF): Mn = 75.3 kDa, Mw = 398.6 kDa, and PDI = 5.29 (against PS standard).

4.2.2.5. Synthesis of P(2OD-TBDY-TT)

A mixture of **2OD-TBDY-Br$_2$** (0.44 g, 0.59 mmol, 1.0 equiv.), 2,5-bis(trimethylstannyl)thieno[3,2-b]thiophene (0.285 g, 0.59 mmol, 1.0 equiv), $Pd_2(dba)_3$ (20.72 mg, 29 μ mol, 0.05 equiv), and P(*o*-tolyl)$_3$ (72.3 mg, 237.6 μ mol, 0.4 equiv) in anhydrous toluene (50 mL) was heated at 120 °C for 5 min in a sealed flask under nitrogen. Then, the polymerization mixture was cooled to room temperature, and the viscous mixture was poured into methanol (~750 mL). After stirring for 1h, the precipitated dark solid was collected by gravity filtration. The crude polymer solid was subjected to sequential soxhlet extractions with methanol, acetone, hexanes, and chloroform. Finally, the concentrated chloroform solution (~100 mL) was precipitated into methanol (~2000 mL). The extraction/precipitation procedure was repeated three times in total. The final precipitate was collected by vacuum filtration and dried under reduced pressure to give the pure polymer as a dark colored solid (85 mg, 20% yield). Elemental analysis calcd for $C_{41}H_{53}BF_2N_2S_3$: C, 68.50; H, 7.43; N, 3.90; found: C, 68.78; H, 7.85; N, 3.65; GPC (RT in THF): Mn = 11.0 kDa, Mw = 112.0 kDa, and PDI = 10.21 (against PS standard).

4.2.3. Fabrication and characterization of OFET devices

All OFETs were fabricated on highly *n*-doped silicon wafers having thermally oxidized 300 nm-SiO_2 dielectric (capacitance per unit area, C_i =11.4 nF/cm^2) by adopting the top-contact/bottom-gate (TC/BG) device architecture. The substrates were cleaned via sonication in acetone for 10 min and followed by oxygen plasma cleaning for 5 min (Harrick plasma, PDC-32G, 18 W). The PS (polystyrene)-brush treatment was performed in accordance with the reported procedures (M_w = 1.7 – 10 kg/mol) to achieve favorable dielectric-semiconductor interfaces.[87] The polymeric semiconductor films (**P(2OD-TBDY-T)** and **P(2OD-TBDY-TT)**) were deposited via spin-coating (~5-7 mg/mL in chloroform) on PS-brush-treated substrates, followed by thermal annealing at 70 °C to remove residual solvents. The profilometer (DEKTAK-XT, Brucker) was used to measure the polymer film thicknesses (~50 – 60 nm). The top electrodes were thermally

evaporated (deposition rate = 0.2 Å/s) as Au layers (50 nm) with various channel widths (W; 1000 and 500 μm) and lengths (L; 100 and 50 μm). Keithley 4200-SCS was used to characterize the electrical performances of OFETs in ambient at room temperature. The electronic performance in the saturation region such as charge carrier mobilities (μ) and threshold voltages (V_T) were extracted from the equation:

$$\mu_{sat} = (2I_{DS}L)/[WC_i(V_G - V_T)^2]$$

where I_{DS} is the drain current, L and W are the channel length and width, respectively, C_i is the areal capacitance of the gate dielectric, V_G is the gate voltage, and V_T is the threshold voltage. The surface morphology and microstructure of thin-films were measured by atomic force microscopy (AFM, NX10, Park systems), field-emission scanning electron microscope (FE-SEM, Zeiss EVO LS 10), and X-ray diffraction (XRD, Smartlab, Rigaku), respectively.

4.2.4. Fabrication and characterization of Inverted OPV devices

The BHJ-OPV devices of inverted type were fabricated with the structure of ITO/ZnO/active layer (P(2OD-TBDY-T):PC71BM))/MoO3/Ag. The patterned ITO substrates were cleaned by ultra-sonication in acetone, DI water, and isopropyl alcohol for 20min at each step. Then, the ITO substrates were dried for 60 min in an oven at 80 °C. The ITO substrates were treated with plasma prior to the spin-coating of ZnO solution at 4000 rpm for 40 s and baking for 20 min at 200 °C in ambient air. The devices were transferred to a N2-filled glovebox. P(2OD-TBDY-T):PC71BM (ratio 1:1.5 w/w) dissolved in chloroform (12 mg/mL) with or without 3 vol% 1,8-diiodooctane (DIO) additive was spin-coated onto the ZnO layer at 3000 rpm for 40 s. 10 nm of MoO3 layer followed by a Ag layer (120 nm) were thermally evaporated under high vacuum (< 10-6 Torr). The J-V characteristics of the devices were measured with a Keithley 2400 SMU under AM 1.5G (100 mW cm-2) solar irradiation (Peccell: PEC-L01). The EQE was obtained using a solar cell spectral response measurement system (K3100 IQX, McScience Inc.) at ambient conditions. A monochromatic light from a xenon arc lamp at

300 W processed by a monochromator (Newport) and an optical chopper (MC 2000 Thorlabs) was used to apply this spectral measurement system. The morphology of the polymer:fullerene blend was studied by atomic force microscopy (AFM) (Veeco Dimension 3100) in tapping mode and a transmission electron microscopy (TEM) (JEM-3011, JEOL).

4.3. Results and Discussion

4.3.1. Computational Design, Synthesis and Characterization

Explored via computational modeling, the structural and electronic properties of the building block, **2OD-TBDY**, were found to be highly attractive for a strong π-acceptor building block. Note that the molecular structure of **2OD-TBDY** monomer developed herein employs an alkyl substituent modification of an original *meso*-thiophene substituted BODIPY monomer reported by Chochos et al.[192] In the structure of **2OD-TBDY**, five-membered thienyl aromatic unit is placed at *meso*-position to minimize the dihedral angle ($\theta_{Th\text{-}BODIPY} \approx 47°$) with highly coplanar dipyrromethene π-core. This is consistent with the previously measured thienyl-dipyrromethene dihedral angles ($\theta_{Th\text{-}BODIPY} \approx 45\text{-}48°$) in single-crystal structures, and it could contribute to efficient π-π stacking and C-H···π interactions in the copolymer solid-state.[1], [205] As shown in Figure 4.3.1.3, π-delocalization of the LUMO frontier orbital is found to be extended towards the *meso*-thienyl unit, which results in lowered LUMO energy (-2.48 eV → -2.64 eV) as compared to the alkyl-substituted monomer **C11-BDY**. As expected, the HOMO energy level remains the same (≈ -5.50 eV) since the corresponding π-electron density is found to be delocalized only on the boron-dipyrromethene π-core. Thus, the HOMO-LUMO gap for **2OD-TBDY** is found to be reduced by ≈0.16 eV as compared to that of **C11-BDY**. On the other hand, the presence of thienyl unit at *meso*-position significantly increases the magnitude of the ground-state dipole moment from 3.83 D (for **C11-BDY**) to 4.75 D (**2OD-TBDY**) while the direction remains the same pointing towards the 4,4'-difluorine substituents. This could enhance backbone-ordering and interchain interactions

in the corresponding copolymer thin-films as a result of strong dipolar interactions.[19] In order to demonstrate that improved acceptor property of **2OD-TBDY** could translate into donor-acceptor type π-backbones, we performed DFT calculations on D-A-D model units (**T-C11-BDY-T** and **T-2OD-TBDY-T** in Figure 4.3.1.1) by employing thiophene donors at 2,6-positions of the BODIPY unit. These results also demonstrate energetically stabilized and delocalized LUMO, and reduced band gap for **2OD-TBDY**-based D-A-D system as compared with that based on *meso*-alkyl substituted **C11-BDY** acceptor.

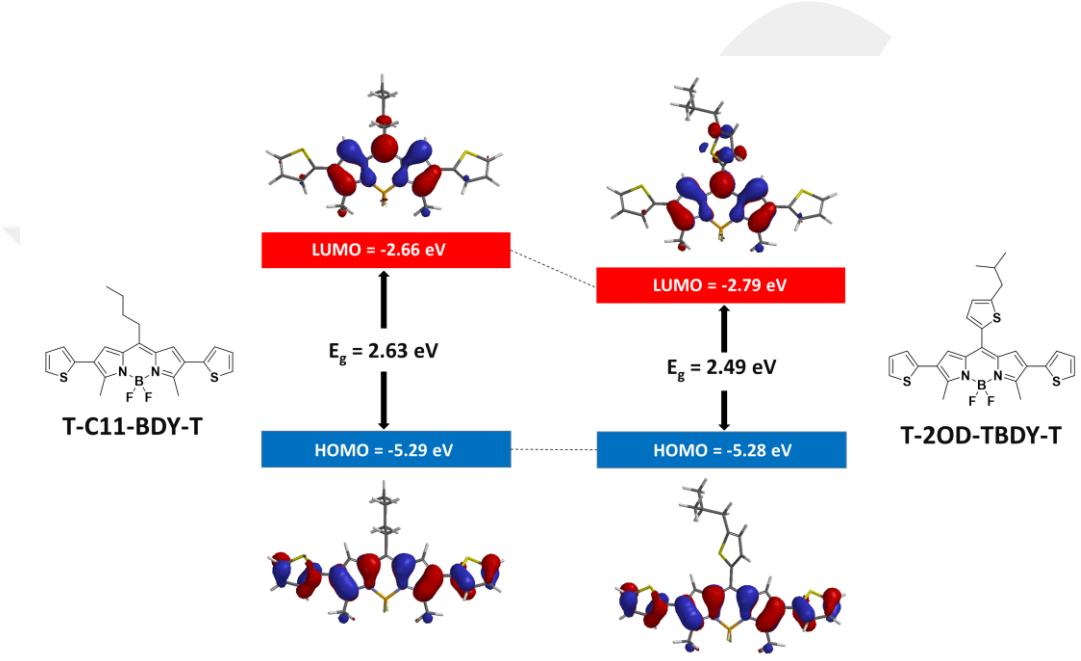

Figure 4.3.1.1 Calculated frontier molecular orbital (HOMO/LUMO) energy levels and pictorial representations for donor-acceptor-donor model units (T-C11-BDY-T and T-2OD-TBDY-T) with thiophene donors (B3LYP/6-31G** level of theory).

Furthermore, according to recent findings by L. Yu et al.[54] and J. Hou et al.[179] on fluorinated small molecules and polymers, fluorination increases ground-state dipole moment and yields higher π-system polarization, which effectively lowers the exciton Coulomb binding energy and leads to faster charge separation kinetics in photovoltaics. Therefore, we envision that the new D-A copolymers employing **2OD-TBDY** π-acceptor may show improved photovoltaic performances in BHJ devices. Sterically encumbered swallow-tailed alkyl substituent (2-octyldodecyl) is placed at α-position of the *meso*-thienyl unit, which provides increased solubility to the corresponding copolymers while keeping the insulating C-C/C-H σ-bonds further away from the semiconducting π-system. This type of structural strategy of physically separating σ-alkyl chain and π-system has recently been shown to yield efficient charge-transport properties in isoindigo-based

copolymers.[208] From a structural and electronic standpoint, **2OD-TBDY** has much improved π-acceptor characteristics as compared to *meso*-alkyl substituted BODIPY monomer **C11-BDY** (Figure 4.3.1.3), and it has similar properties to some of the commonly known electron-deficient building blocks (dithienyldiketopyrrolopyrrole (T-DPP-T) (LUMO = –2.50 eV, μ = 0.15 D); isoindigo (LUMO = –2.64 eV, μ = 0.49 D); naphthalenediimide (NDI) (LUMO = –3.37 eV, μ = 0 D); Figure 4.3.1.2), which were reported to yield low band-gap polymers.[209]–[211]

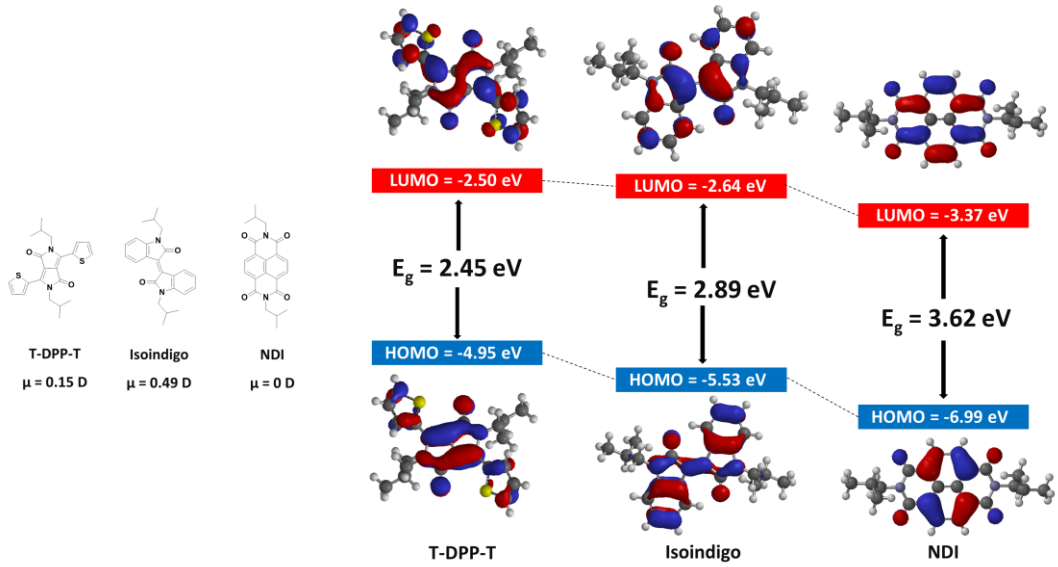

Figure 4.3.1.2 The chemical structures, molecular dipole moments (μ), HOMO/LUMO energies and the corresponding pictorial orbital representations for commonly known π-acceptor building blocks dithienyldiketopyrrolopyrrole (T-DPP-T), isoindigo, and naphthalenediimide (NDI).

Therefore, we envision that **2OD-TBDY** building block should be a promising π-acceptor for use in low band-gap semiconducting copolymer backbones.

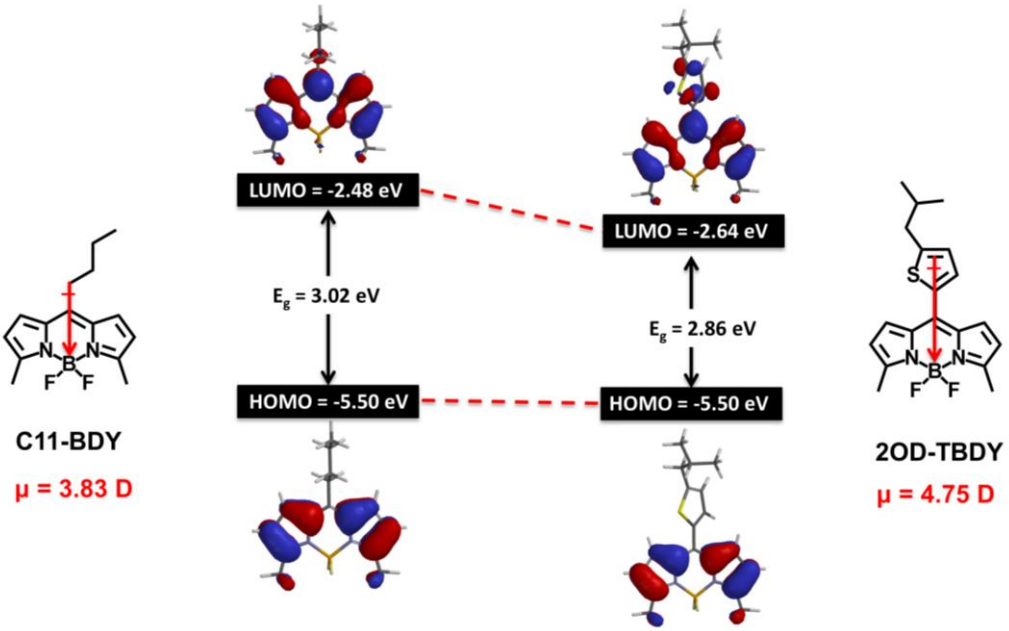

Figure 4.3.1.3 Calculated frontier molecular orbital (HOMO/LUMO) energy levels and pictorial representations, and molecular dipole moments (μ) of model monomers for *meso*-alkyl substituted **C11-BDY**[78] and *meso*-thiophene substituted **2OD-TBDY** developed in this study (B3LYP/6-31G** level of theory).

The synthetic routes to the **2OD-TBDY-Br$_2$** monomer, and its corresponding copolymers **P(2OD-TBDY-T)** and **P(2OD-TBDY-TT)** are shown in Scheme 4.3.1. 5-(2-octyldodecyl)-2-thiophenecarboxaldehyde compound **2** was prepared in two steps (40% total yield) by first lithiation/alkylation of thiophene at *5*-position to give compound **1**, which was subsequently lithiated and reacted with DMF to form the carboxaldehyde functionality at *2*-position. The boron-dipyrromethene π-core **2OD-TBDY** was prepared by reacting 5-(2-octyldodecyl)-2-thiophenecarboxaldehyde (**2**) with 2-methyl pyrrole in the presence of a catalytic amount of trifluoroacetic acid (TFA), which was subsequently oxidized with 2,3-dichloro-5,6-dicyano-1,4-benzoquinone (DDQ) and coordinated with trifluoroborane dietherate ($BF_3{\cdot}OEt_2$) in the presence of (i-Pr)$_2$EtN (28% yield). Bromination at the 2- and 6- positions was selectively accomplished with *N*-bromosuccinimide, which afforded the dibromo-functionalized BODIPY monomer **2OD-TBDY-Br$_2$** in 91% yield. The chemical structures and purities of the intermediate compounds and the resulting monomer, **2OD-TBDY-Br$_2$**, were characterized by ^{1}H/^{13}C NMR, MALDI-TOF (Figures 4.2.2.3.1 and 4.2.2.3.3), and elemental analysis. Stille polycondensation protocols were employed for the copolymerization reactions of **2OD-TBDY-Br$_2$** with 2,5-bis(trimethylstannyl)thiophene and 2,5-

bis(trimethylstannyl)thieno[3,2-b]thiophene in toluene using $Pd_2(dba)_3$/P(*o*-tolyl)$_3$ as the catalyst/ligand system. During the copolymerization of **2OD-TBDY-Br$_2$** with 2,5-bis(trimethylstannyl)thieno[3,2-b]thiophene, the reaction was stopped after 5 minutes; otherwise, the copolymers were found to be insoluble. The obtained **P(2OD-TBDY-T)** and **P(2OD-TBDY-TT)** solids were purified by sequential soxhlet extractions (methanol-acetone-hexane) and multiple dissolution-precipitation processes with methanol/chloroform to yield dark colored solids in 91% and 20% yields, respectively. The copolymers' purities were evaluated by elemental analysis and molecular weights were determined by gel permeation chromatography (GPC) with THF as the eluent against polystyrene standards, which indicated number-average molecular weights (M_n) of 75.3 kDa for **P(2OD-TBDY-T)** and 11.0 kDa for **P(2OD-TBDY-TT)**. The relatively lower molecular weight of **P(2OD-TBDY-TT)** can be explained by the fact that the corresponding polymerization reaction was stopped at its earlier stage to obtain a soluble polymer. The good solubility of the current copolymers should enable the solution-based fabrication of copolymer thin-films for use in BHJ-OPV and OFET devices.

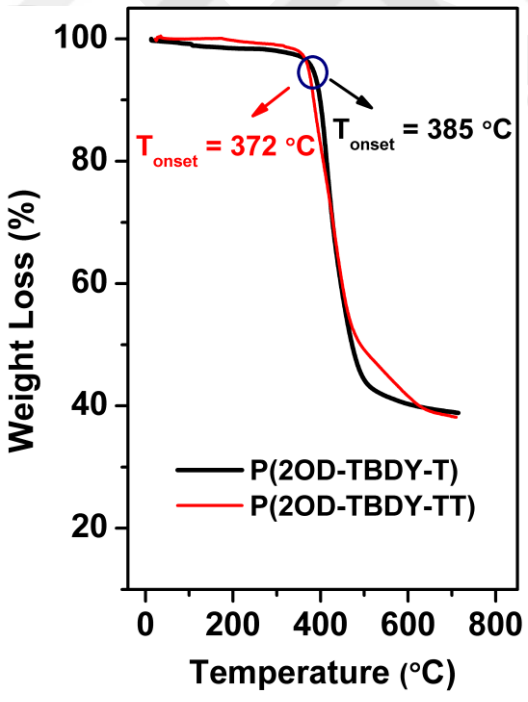

Figure 4.3.1.4 Thermogravimetric analysis (TGA) curves of P(2OD-TBDY-T) and P(2OD-TBDY-TT) measured at a temperature ramp of 10 °C/min under N_2.

Both copolymers show good thermal stabilities with decomposition onset temperatures (5% mass loss) at 372-384 °C (Figure 4.3.1.4). No apparent phase

transitions were observed for both copolymers in the range of 25 °C to 350 °C by differential scanning calorimetry (DSC).

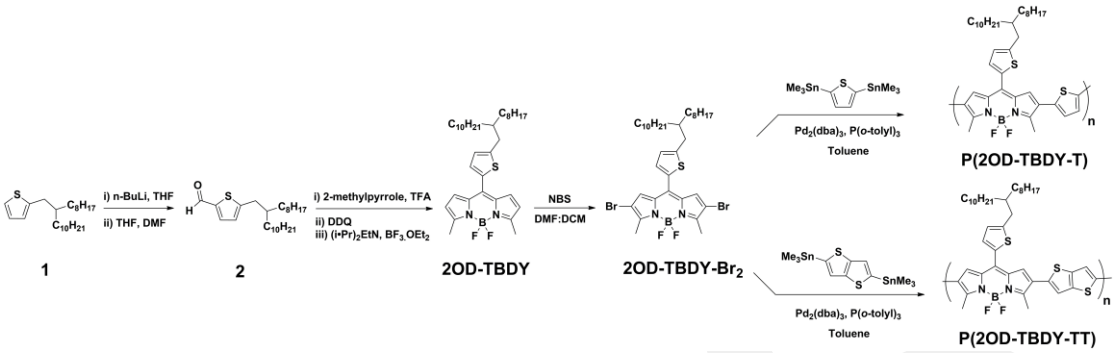

Scheme 4.3.1 Synthesis of *meso*-thiophene substituted monomer **2OD-TBDY-Br2** and the corresponding copolymers **P(2OD-TBDY-T**) and **P(2OD-TBDY-TT**).

4.3.2. Optoelectronic Characterizations

The optical characteristics of the new copolymers were studied by UV-Vis absorption spectroscopy in dilute solutions ($CHCl_3$, 10^{-5} M) and thin-film states (as spin-coated thin-films on glass). As shown in Figure 4.3.2.3.a, the copolymers exhibit two low-energy absorption maxima at 838/736 nm for **P(2OD-TBDY-T)** and 834/730 nm for **P(2OD-TBDY-TT)** corresponding to π–π* excitations. In order to elucidate the origin of these peaks, which are separated by ~0.2-0.3 eV, temperature-dependent UV-Vis absorption spectra of the current polymers were recorded in chloroform and toluene solutions. As shown in Figure 4.3.2.3.b, upon progressive heating (25 °C → 60 °C) of **P(2OD-TBDY-T)** solution in chloroform, while the absorbance at the lower energy peak (838 nm) greatly decreases, the absorbance at the higher energy peak (736 nm) gradually increases with a blue-shift of ~12 nm. In addition, an isosbestic point was observed at 756 nm.

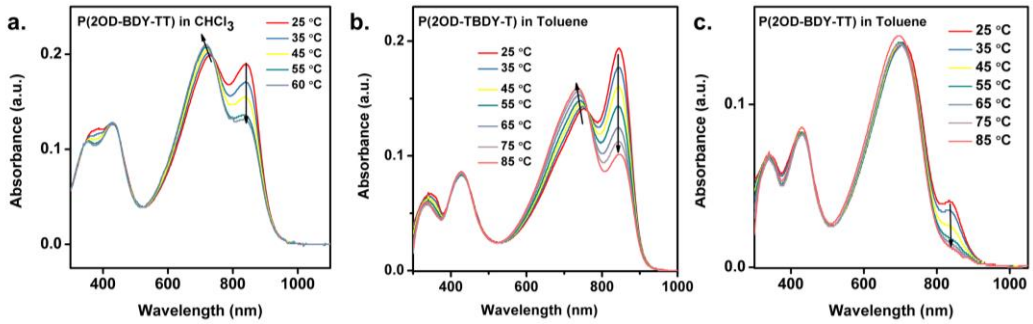

Figure 4.3.2.1 Temperature-dependent UV-Vis absorption spectra of **P(2OD-TBDY-TT)** in chloroform (a) and toluene (c) solutions, and **(2OD-TBDY-T)** in toluene (b) solution (concentrations ~ 1.0×10^{-5} M) (arrows indicate the trends upon temperature increases).

Likewise, the chloroform solution of **P(2OD-TBDY-TT)** exhibits similar trends but with much smaller changes in absorbance values (Figure 4.3.2.1.a), which indicates the difference between the polymers' temperature-dependent aggregation behaviors. Based on these results, we assign the absorbance at higher energy peak (736 and 730 nm) to disaggregated (isolated) polymer chains and the absorbance at lower energy peak (838 and 834 nm) to aggregated polymer chains in solution (enhanced π-coherence as a result of interchain interactions). On the other hand, when high-boiling point solvent (i.e., toluene) was used for **P(2OD-TBDY-T)**, the presence of higher-energy shoulder even at 85 °C indicates strong aggregation tendency of the current D-A copolymer in toluene even at high temperature (Figure 4.3.2.1.b). Note that **P(2OD-TBDY-TT)** solution in toluene shows mostly disaggregated (isolated) polymer chains and the aggregation peak almost disappears at 85 °C (Figure 4.3.2.1.c). When BODIPY acceptor, **2OD-TBDY**, is copolymerized with thiophene-based donors (i.e., T and TT) through 2,6-positions, the corresponding absorption profiles were found to significantly red-shift ($\Delta\lambda_{max}$ ~ 315 nm and $\Delta\lambda_{onset}$ ~ 360 nm in Figure 4.3.2.2), which indicates highly extended electronic communication (effective π-conjugation) between BODIPY-based acceptor and thiophene-based donor units along the current polymer backbones.

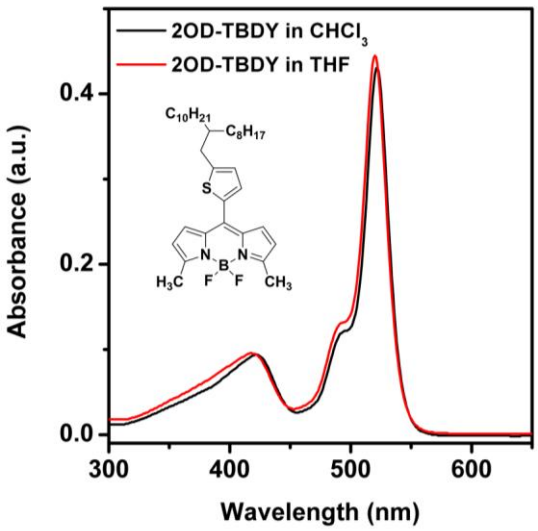

Figure 4.3.2.2 Optical absorption spectra of the newly designed acceptor building block **2OD-TBDY** in solution (chloroform, 1.0×10^{-5} M). Inset shows the chemical structure.

This is in sharp contrast to the observations on BODIPY-oligothiophene π-systems, since they exhibit very limited electronic communications between boron-dipyrromethene and oligothiophene moieties when linked through BODIPY's *meso*-position.[1], [205] Note that, when the new copolymer **P(2OD-TBDY-T)** is compared with structurally related **P(C11-BDY-T)** (Figure 4.1),[78] the low-energy absorption maxima and onset were found to be significantly red-shifted ($\Delta\lambda_{max} \approx 136$ nm; $\Delta\lambda_{onset} \approx 75$ nm), indicating more favorable electronic/structural properties of the new acceptor unit (**2OD-TBDY**) to enhance π-conjugation, donor-acceptor interactions, and aggregation (interchain interactions).

The absorption maximum for spin-coated copolymer thin-films are significantly red-shifted ($\Delta\lambda_{max} \approx 120$ nm) compared to those in chloroform solution. For both copolymers, going from solution to solid-state, the lower-energy aggregation peak becomes stronger and the disaggregation absorbance becomes a shoulder peak, which suggests the existence of strong interchain interactions (enhanced π-coherence) in the solid-state. The solid-state optical band gaps are estimated from the low-energy band edges as 1.35 eV and 1.31 eV for **P(2OD-TBDY-T)** and **P(2OD-TBDY-TT)**, respectively. These low optical bands make the new copolymers quite attractive for various optoelectronic applications.[99] The observed aggregation properties both in solution and solid-state for the present copolymers could be attributed to strong interchain interactions (π-π stacking, donor-acceptor, and dipolar) between polymer chains, resulting in enhanced π-coherence. Similar temperature-dependent aggregation behaviors

in solution and strong aggregations in solid-state were previously reported for several donor-acceptor copolymers characterized in high-performing BHJ-OPVs based on isoindigo[212], B←N bridged bipyridine[213], naphthalene diimide[210], and difluoro-benzothiadiazole[174] acceptors.

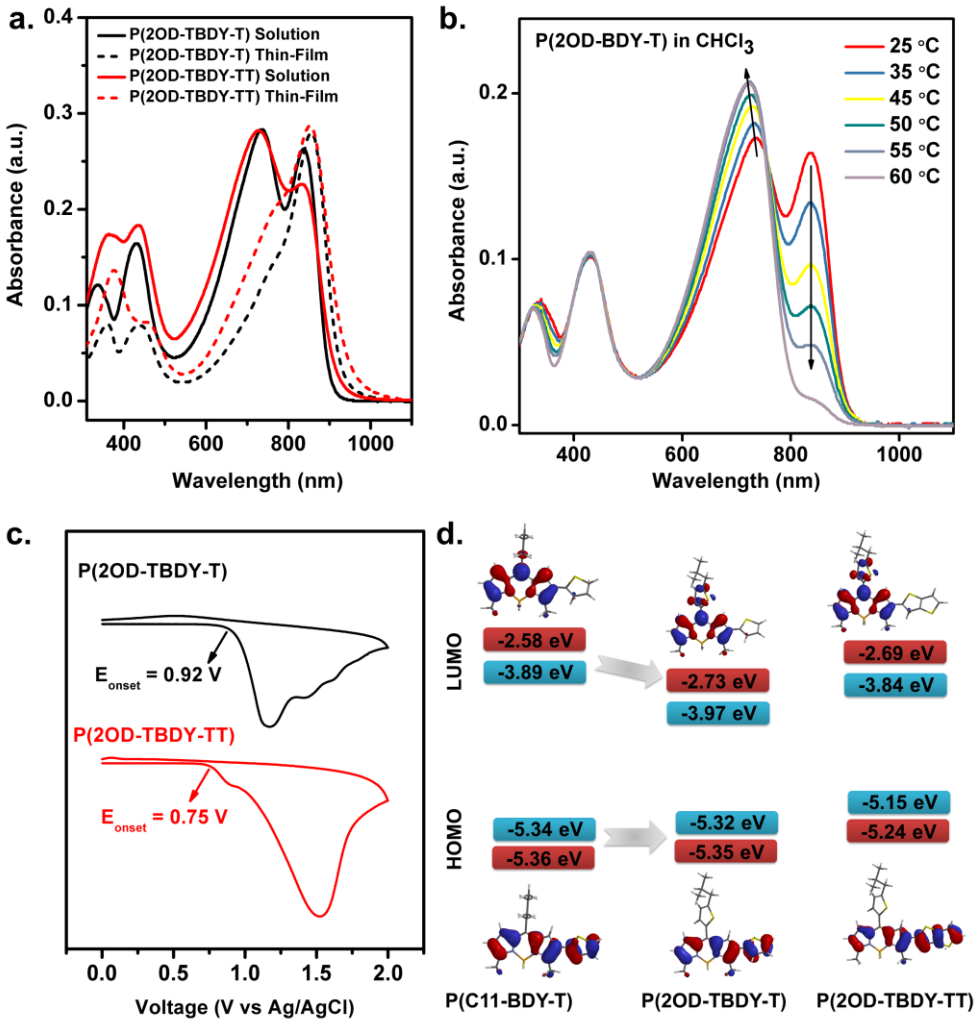

Figure 4.3.2.3 a. Optical absorption spectra in chloroform (solid lines, 1.0×10^{-5} M) and as spin-coated thin-films on glass (dashed lines) for copolymers **P(2OD-TBDY-T)** and **P(2OD-TBDY-TT)**, b. Temperature-dependent UV-Vis absorption spectra of **P(2OD-TBDY-T)** in chloroform solution (0.6×10^{-5} M) (arrows indicate the trends upon temperature increases), c. Cyclic voltammograms as thin-films in 0.1 M $TBAPF_6$/MeCN solution vs. Ag/AgCl (3.0 M NaCl) at a scan rate of 100 mV/s, and d. Energy diagrams showing theoretically calculated (red) (for model monomers) and experimentally estimated (blue) HOMO/LUMO energy levels as well as their topographical representations. Note that P(C11-BDY-T) is our previously reported BODIPY-based copolymer.[78]

We also studied the aggregate formation via solvent-dependent absorption spectra by adding a non-solvent (ethanol, ε = 24.5) to a well dissolved copolymer solution in

chloroform. As shown in Figure **4.3.2.5.**, both copolymers show gradual reduction of the intensities for the higher energy peaks at 730/736 nm and concurrent increase in the intensities of the lower-energy peaks at 834/838 nm. These spectral changes were successively controlled by continually increasing the volume fraction of ethanol from 0% to 36%, and well-defined isosbestic points were observed for both copolymers at 764/774 nm indicating that aggregation occurs under thermodynamic control.[214], [215] Similar aggregation behavior was also observed when a different non-solvent (hexane) and a bad solvent (THF) having relatively lower dielectric constants (ε_{hexane} = 2.0; ε_{THF} = 7.6) were added to copolymer solutions in chloroform (Figure 4.3.2.4), indicating that the dielectric constant of the added solvent does not play a major role in aggregation mechanism.

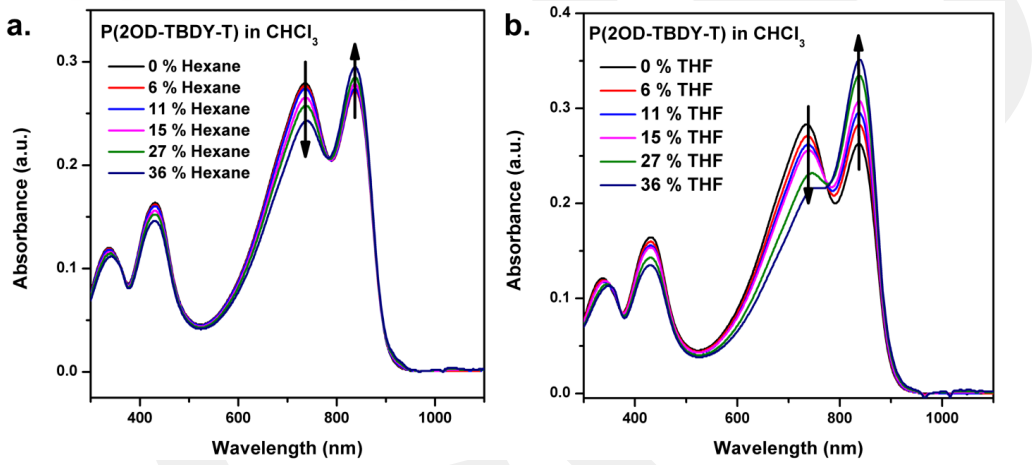

Figure 4.3.2.4 Solvent-dependent optical absorption spectra of P(2OD-TBDY-T) chloroform–hexane (a) and chloroform-THF (b) mixtures at room temperature starting in pure chloroform (black lines) and successively increasing the volume fraction of non-solvent/bad solvent.

Next, we analyzed the suspended aggregated particle size of **P(2OD-TBDY-T)**, formed in aggregated solution, by dynamic light-scattering (DLS) technique, which indicates a significant increase in average particle size upon ethanol addition (insets in Figures 4.3.2.5c and 4.3.2.5d). In order to obtain more information on these aggregates, the corresponding solutions were drop-casted on Si(100) and their morphologies were determined by scanning electron microscopy (SEM). As shown in Figures 4.3.2.5c and 4.3.2.5d, while the film drop-casted from chloroform solution shows a very smooth morphology with no observable microscopic aggregates, the film drop-casted from chloroform:ethanol (64:36, v/v) shows a three-dimensional (3-D) polymeric network consisting of numerous, irregular, entangled nanoparticles and micron-sized aggregates

with sizes ranging from ~50-100 nm to >1 μm, which is consistent with the DLS particle size distribution (Figure 4.3.2.5.d-inset). Thus, we propose that these particulates observed in the SEM image are mostly formed in the chloroform-ethanol solution; they are not purely based on polymer precipitation during solvent evaporation in drop-casting. Note that this type of 3-D micro-/nanostructured organic surface morphologies, which can be prepared via simple solution processing, might be quite advantageous for low-cost Surface-Enhanced Raman Scattering (SERS) platforms and catalysis applications.[206]

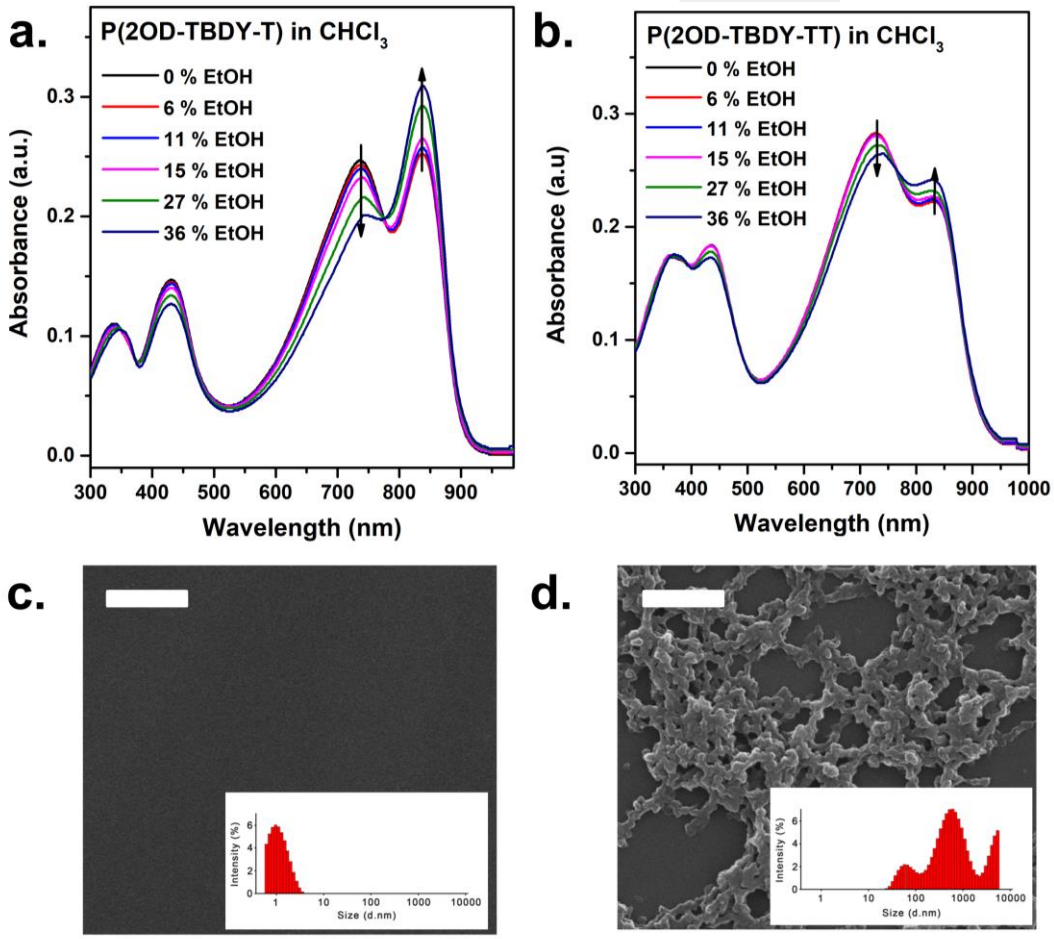

Figure 4.3.2.5. Solvent-dependent optical absorption spectra of **P(2OD-TBDY-T)** (a) and **P(2OD-TBDY-TT)** (b) in chloroform–ethanol mixtures at room temperature starting in pure chloroform (black line) and successively increasing the volume fraction (from 0% to 36%) of ethanol. Arrows indicate the spectral changes upon non-solvent addition. SEM images for P(2OD-TBDY-T) films drop-casted on Si(100) from chloroform (c) and chloroform:ethanol (64:36, v/v) (d) solutions. Insets show the size distributions of the corresponding drop-casting solutions determined by dynamic light scattering (DLS). Scale bars denote 1 μm.

The cyclic voltammograms of the **P(2OD-TBDY-T**) and **P(2OD-TBDY-TT**) copolymeric films drop-casted on platinum electrodes are shown in Figure 4.3.2.3.c The measurements were performed in 0.1 M $TBAPF_6$ solution in acetonitrile against Ag/AgCl (3.0 M NaCl) reference electrode. For **P(2OD-TBDY-T)** and **P(2OD-TBDY-TT)**, only oxidation peaks were observed and the onset of the oxidation potentials are located at 0.92 V (*vs* Ag/AgCl) and 0.75 V (*vs* Ag/AgCl), respectively, from which solid-state HOMO energies are estimated as -5.32 eV and -5.15 eV, respectively. The solid-state LUMO energies are estimated using the thin-film optical bandgaps as -3.97 eV for **P(2OD-TBDY-T)** and -3.84 eV for **P(2OD-TBDY-TT)**. When the energy levels of **P(2OD-TBDY-TT)** are compared with those of **P(2OD-TBDY-T)**, the increases (Δ~0.15 eV) in both HOMO and LUMO energies reflect relatively more π-extended electronic structure of thieno[3,2-b]thiophene donor unit versus thiophene. On the other hand, for the copolymers embedding the same thiophene donor unit, the new copolymer **P(2OD-TBDY-T)** has a relatively lower LUMO energy level and similar HOMO energy level as compared to the previously reported copolymer **P(C11-BDY-T)**,[78] which reflects better electron-acceptor characteristics of the new building block **2OD-TBDY** as compared to **C11-BDY** (*vide supra*). All these trends in the experimental HOMO/LUMO energy levels (blue) correlate well with the theoretically calculated values (red) on the model repeating units (Figure 4.3.2.3.d). It is noteworthy that the HOMO energies of the current copolymers are typical of ambient-stable *p*-channel semiconductors.[99] However, although LUMO energies of these copolymers are quite stabilized and they are even in the energetic regime of the ambient-stable *n*-channel semiconductors ($\leq$ -3.8 eV), no electron transport was observed under vacuum and in ambient (*vide infra*).

4.3.3. Thin-Film Fabrication, Characterization, and Field-Effect Transistor Devices

The semiconductor characteristics of the current copolymers **P(2OD-TBDY-T)** and **P(2OD-TBDY-TT)** were studied in OFETs in a bottom-gate/top-contact (BG-TC) device architecture. The semiconductor thin-films (~50-60 nm) were prepared by spin-coating

copolymer solutions (~5-7 mg/mL in chloroform) on PS-brush treated n^{++}-Si/SiO_2(300 nm) gate-dielectric substrates, which was followed by drying at 70 °C under vacuum to remove residual solvents. Note that this temperature is an acceptable temperature for industrial applications and no further thermal annealing was needed. The reason for dielectric surface functionalization with PS brushes was to achieve a favorable semiconductor−dielectric interface.[87] Polymeric thin-film microstructures and morphologies were studied by θ-2θ XRD and AFM. As shown in Figures 4.3.3.3a and 4.3.3.3b, XRD profiles do not exhibit any low-angle ($2\theta < 10°$) diffraction peak, which indicates the lack of lamellar crystalline regions in the out-of-plane direction.[216] For both polymer thin-films, the only noticeable diffractions show highly broadened peaks centered at $2\theta \sim 22°$. Since the reference XRD scan on pristine PS-brush treated n^{++}-Si/SiO_2(300 nm) substrate does not exhibit similar broadened peak, these peaks are assigned to short-range ordered π-π interactions originating from the polymer semiconductor film. This corresponds to π-π stacking distances of ~4.0 Å.[172], [217] Indeed, the XRD profiles obtained for the current copolymers could be attributed to the presence of bulkyl swallow-tailed 2OD alkyl substituents on BODIPY unit, which prevents the formation of lamellar ordering in the out-of-plane crystallographic direction.[216], [218], [219] These microstructural observations agree well with the AFM characterizations, which reveal relatively homogeneous morphologies with extremely smooth surfaces (root-mean-square roughness < 1 nm for 5.0 μm × 5.0 μm scan area). As shown in Figures 4.3.3.3c and 4.3.3.3d, both films show highly interconnected isotropic nodule-like domains (~50–100 nm in diameter). OFET device characteristics were measured in ambient conditions, and typical transfer and output plots are shown in Figures 4.3.3.3 and 4.3.3.1.

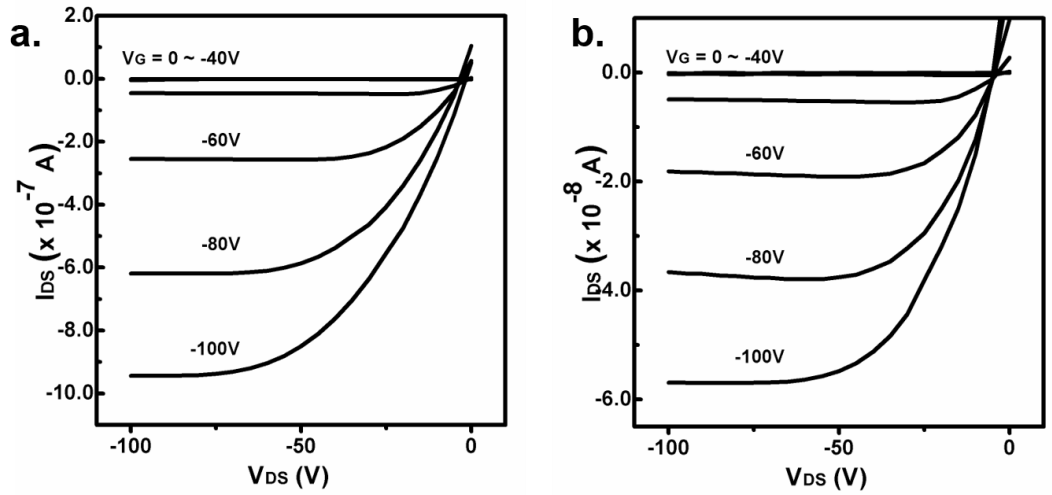

Figure 4.3.3.1. Output curves for the OFET devices fabricated with copolymers P(2OD-TBDY-T) (a) and P(2OD-TBDY-TT) (b).

Consistent with the pre-fabrication theoretical and experimental optoelectronic characterizations, these devices exhibit unipolar *p*-channel operation with μ_h = 0.005 $cm^2/V \cdot s$ ($I_{on}/I_{off} = 10^4$-10^5) and μ_h = 0.0002 $cm^2/V \cdot s$ ($I_{on}/I_{off} = 10^4$-10^6) for **P(2OD-TBDY-T)** and **P(2OD-TBDY-TT)**, respectively. Note that these devices were dried/annealed only at 70 °C, and post-deposition thermal annealing at higher temperatures did not further improve the transistor performance as well as the polymer crystallinity/morphology. Since no evident microstructural and morphological differences were revealed between two polymer thin-films, the inferior device performance of P(2OD-TBDY-TT), as compared with P(2OD-TBDY-T), should originate from its much lower molecular weight (M_n = 11.0 kDa *vs* 75.3 kDa).[220] From frontier-orbital energetics perspective, one would expect the current copolymers to exhibit also *n*-channel semiconductivity, because the present LUMOs are in the energetic range of those measured for typical *n*-channel semiconductors.[99], [116], [221] Therefore, we performed DFT calculations on trimer and tetramer models of the repeating units, which shows localization on specific BODIPY units for LUMO π-electron density and complete delocalization along the π-backbone for HOMO (Figure 4.3.3.2).

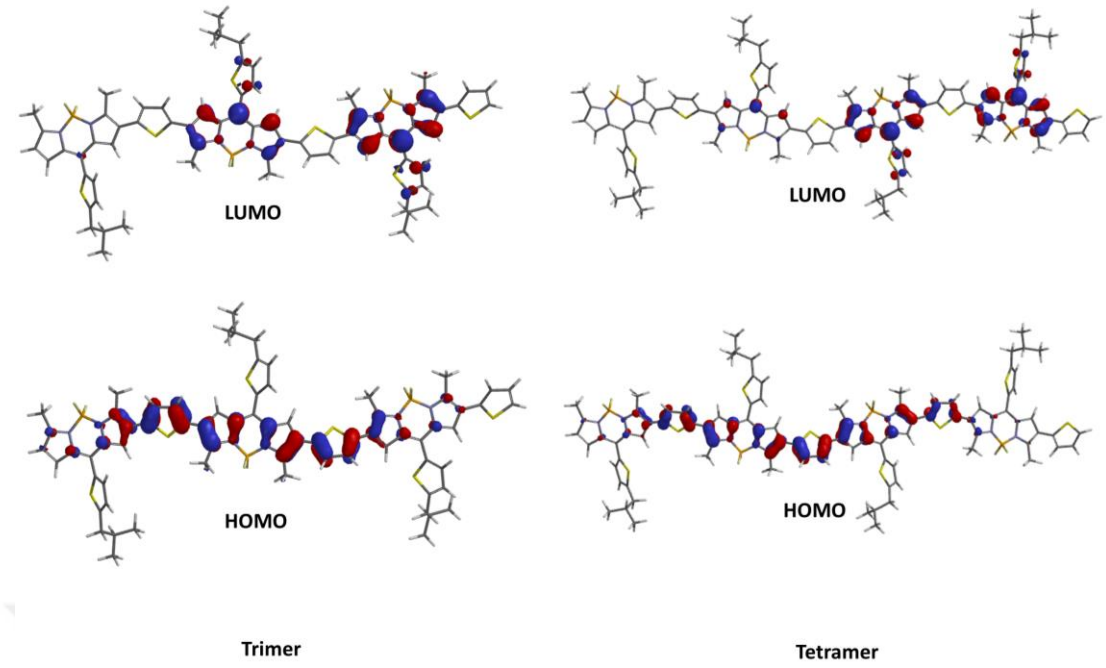

Figure 4.3.3.2. Calculated pictorial representations for frontier molecular orbitals (HOMO/LUMO) of trimer and tetramer models of the repeating units for P(2OD-TBDY-T) (B3LYP/6-31G** level of theory).

Therefore, it seems that the major charge carrier type (hole *vs* electron) of the current polymers are directed by the corresponding π-orbital distributions. Note that the semiconductivity in polymeric films will occur mainly through intra- and inter-chain charge transports, which relies on the formation of radical cationic species (polarons) on isolated and aggregated conjugated segments of the polymer chains, respectively.[222] Therefore, it's quite crucial to have highly π-conjugated polymer chains with good inter-chain interactions in the solid-state, which agrees well with the current polymeric thin-films. Since the length of a single copolymer chain – even in its fully extended conformation – is much smaller than the device channel lengths (~50-100 μm), π-π stacked regions are still very crucial to enable interchain hopping processes for an efficient charge-transport from source to drain. Note that although the current charge carrier mobilities are short of the state-of-the art performances recently achieved with D-A copolymers, they are among the highest for BODIPY-based semiconductor polymers measured in BG-TC OFETs.

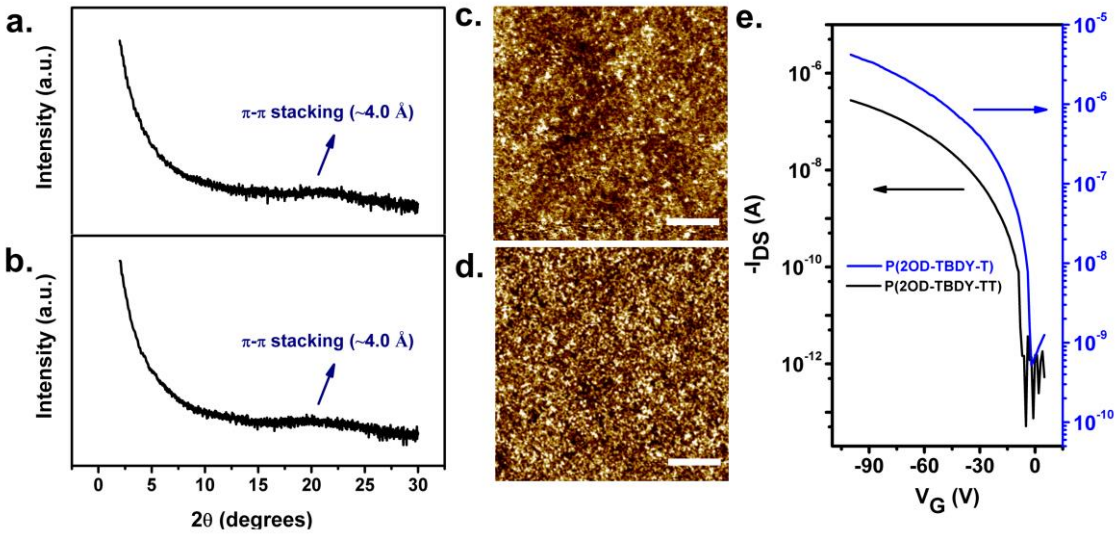

Figure 4.3.3.3. θ-2θ X-ray diffraction (XRD) scans and atomic force microscopy (AFM) topographic images for spin-coated thin-films of **P(2OD-TBDY-T)** (a and c) and **P(2OD-TBDY-TT)** (b and d). P-channel transfer curves (V_{DS} = -100 V) for bottom-gate/top-contact OFET devices fabricated with spin-coated copolymer thin-films (e). Scale bars in AFM images denote 1 μm.

4.3.4. Bulk-Heterojunction Inverted Solar Cell Devices

Next, we investigated the photovoltaic performance of **P(2OD-TBDY-T)** as polymer donor by fabricating the inverted bulk-heterojunction (BHJ) solar cells with a device architecture of ITO/ZnO/active layer (P(2OD-TBDY-T):$PC_{71}BM$)/MoO_3/Ag (see the Experimental Section for device fabrication details). The inverted device structure was preferred due to better device stability in air when compared with the normal type structure. This is because high work–function metal anodes (resistant to oxidation in air) are used in inverted structures and acidic PEDOT:PSS layer is not required, which leads to much superior long-term stability.[223]–[225] The optimal polymer:fullerene blend weight ratio in the active layer was found to be 1:1.5 (w/w), and chloroform was used as the processing solvent. In general, the addition of solvent additives optimizes the BHJ morphology, which plays a crucial role in determining the corresponding device performance.[226] Therefore, we studied **P(2OD-TBDY-T):$PC_{71}BM$** device characteristics with or without 1,8-diiodooctane (DIO) additive in the processing solvent. Figure 4.3.4.2 shows the *J-V* curves and external quantum efficiency (EQE) responses of

the devices under AM 1.5G illumination (100 mW/cm^2), and the corresponding photovoltaic parameters are summarized in Table 4.3.4. The devices without DIO additive exhibited an impressive PCE of 5.12% with V_{oc} of 0.73 V, J_{sc} of 13.08 mA cm^{-2}, and FF = 0.53. The devices with 3 vol% DIO additive showed further improved photovoltaic performance with PCE of 6.16%, V_{oc} of 0.66 V, J_{sc} of 16.36 mA cm^{-2} and FF = 0.56, which is a record high PCE value among the solar cells based on BODIPY-polymer donor. Although the use of the DIO additive resulted in a slight decrease of V_{oc} value by ~10%, the J_{sc} value was increased by ~21 %, resulting in a significant improvement (~20%) in the PCE value. The decrease of V_{oc} and the increase of J_{sc} are fairly common for the active layer film processed with DIO additive in polymer solar cells reported to date.[227]–[232] To support these changes in V_{oc} and J_{sc} values after the addition of DIO additive, we measured the absorption spectra of the P(2OD-TBDY-T):$PC_{71}BM$ blend films without or with DIO additive (Figure 4.3.4.1).

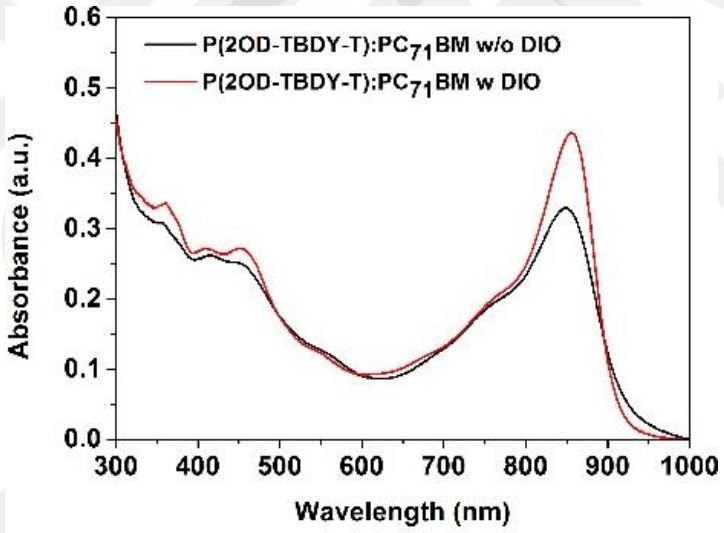

Figure 4.3.4.1. UV-vis spectra of P(2OD-TBDY-T):$PC_{71}BM$ blend films prepared without or with DIO additive.

It was clearly observed that absorption peak of the blend film with DIO additive increased in intensity in the range of 800-900 nm, and slightly red-shifted from 849 nm to 855 nm, indicating an increased structural ordering and interchain interactions for polymer donor.[233]–[235] The variations of the absorption spectra for blend films without and with DIO additive were closely correlated with the photovoltaic parameters of the devices. As shown in Figure 4.3.4.2b, the **P(2OD-TBDY-T):$PC_{71}BM$** devices were observed to effectively generate photocurrent in a broad spectral range of 400-900

nm. The active layer with DIO additive showed higher EQE values than that without DIO additive in the entire spectral range, even leading to maximum EQE values of >65% at 450-500 nm. The *J*sc values calculated from EQE spectrum of P(2OD-TBDY-T):$PC_{71}BM$ without and with DIO additive were 12.53 or 15.87 mA cm^{-2}, respectively, which agree well with the corresponding *J*sc values from *J-V* curves within an acceptable error of ~5%. The hole (μ_h) and electron (μ_e) mobilities of the P(2OD-TBDY-T):$PC_{71}BM$ with DIO additive device were measured by the SCLC method under optimized device condition, which were calculated as 3.56×10^{-5} cm^2 $V^{-1}s^{-1}$ and 2.75×10^{-5} cm^2 $V^{-1}s^{-1}$, respectively. Notably, the hole and electron mobilities are well-balanced (μ_h/μ_e = 1.29), which can contribute to efficient charge transport.[236]

Table 4.3.4. Photovoltaic characteristics of P(2OD-TBDY-T):PC71BM device without or with 1,8-diiodooctane (DIO) additive.

Active layer (donor:acceptor)	DIO additive (3vol%)	V_{oc} (V)	J_{sc} (mA cm^{-2})	FF	PCE_{max} a) (PCE_{avg}) (%)
P(2OD-TBDY-T): PC71BM	w/o	0.73	13.08	0.53	5.12(5.10)
	w	0.66	16.63	0.56	6.16(6.11)

a) The average PCEs were obtained from at least ten different devices for each system.

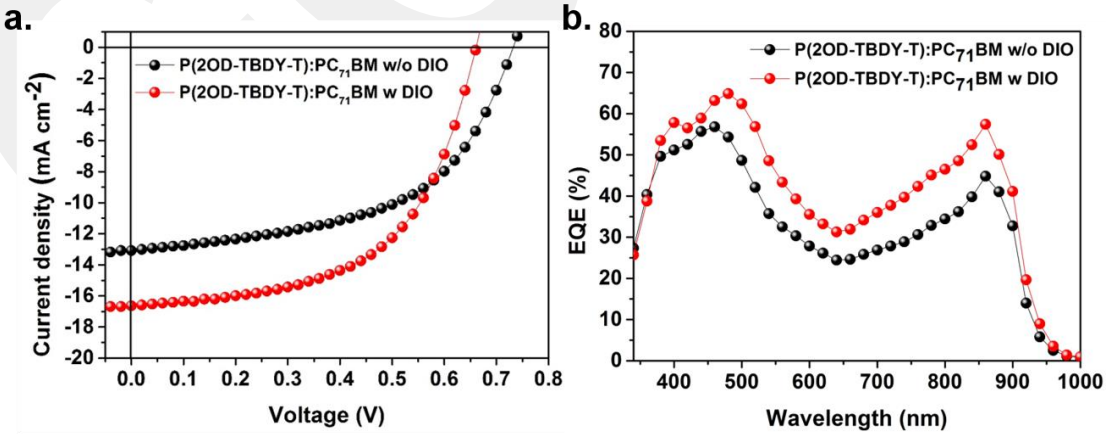

Figure 4.3.4.2. J-V characteristics (a) and EQE responses (b) of **P(2OD-TBDY-T)**:$PC_{71}BM$ without or with 1,8-diiodooctane (DIO) additive.

The morphology of the polymer/fullerene blend active layer plays a critical role in device performance, and continuous interpenetrating donor/acceptor domains with limited sizes are typically needed for efficient exciton dissociation and charge carrier transport/extraction. We compared the BHJ morphologies of **P(2OD-TBDY-T):PC$_{71}$BM** blend film without or with DIO additive using TEM and AFM measurements (Figures 4.3.4.3 and 4.3.2.4). The blend film without DIO additive had continuous network of polymer donor and **PC$_{71}$BM** phases, but their length scale of phase separation (i.e., large dark PCBM-rich domains (> 80-110 nm)) is significantly larger than the typical exciton diffusion length of ~10-20 nm.[237] In contrast, blend films with DIO additive exhibited highly-interpenetrated domains with much decreased domain sizes (< 20-40 nm), producing much larger interfacial area between **P(2OD-TBDY-T)** and PC$_{71}$BM. Importantly, the contrast between the **P(2OD-TBDY-T)** and PC$_{71}$BM is greatly enhanced, suggesting that the relative purity of each domain is higher, which is beneficial for efficient charge transport and suppressed bimolecular charge recombination in the **P(2OD-TBDY-T)/**PC$_{71}$BM devices with DIO additive.[238], [239] The observations from TEM data clearly explain the enhanced $J_{sc,}$ FF and PCE values of **P(2OD-TBDY-T)/**PC$_{71}$BM devices with DIO additive.

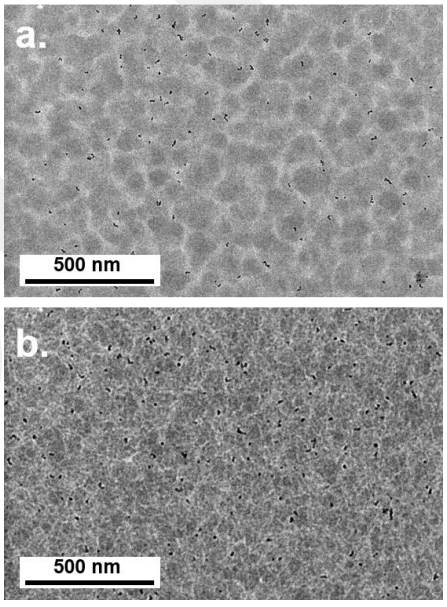

Figure 4.3.4.3. Transmission electron microscopy (TEM) images of **P(2OD-TBDY-T):PC$_{71}$BM** blend films (a) without or (b) with DIO additive.

Moreover, the AFM images (Figure 4.3.4.4) confirm the domain size differences between these blend films, and the blend film with DIO additive showed smaller domains with smoother surface roughness (RMS roughness = 1.1 nm) as compared to that without DIO additive (RMS roughness = 1.7 nm). To the best of our knowledge, these photovoltaic performances are the highest reported to date for a BODIPY-based donor polymer and, more generally, for a boron-containing polymer donor showing the potential of properly designed BODIPY monomer as a promising acceptor building block for OPVs. Considering that the previous research on BODIPY-based donor polymers have only achieved <1.5-2% PCEs in photovoltaic devices, the significantly enhanced photovoltaic performance (>3-4×) of the new donor polymer is mainly attributed to the well matched energy levels with fullerene acceptors, low optical band gap, as well as the favorable BHJ morphology yielding effective charge generation and transport.

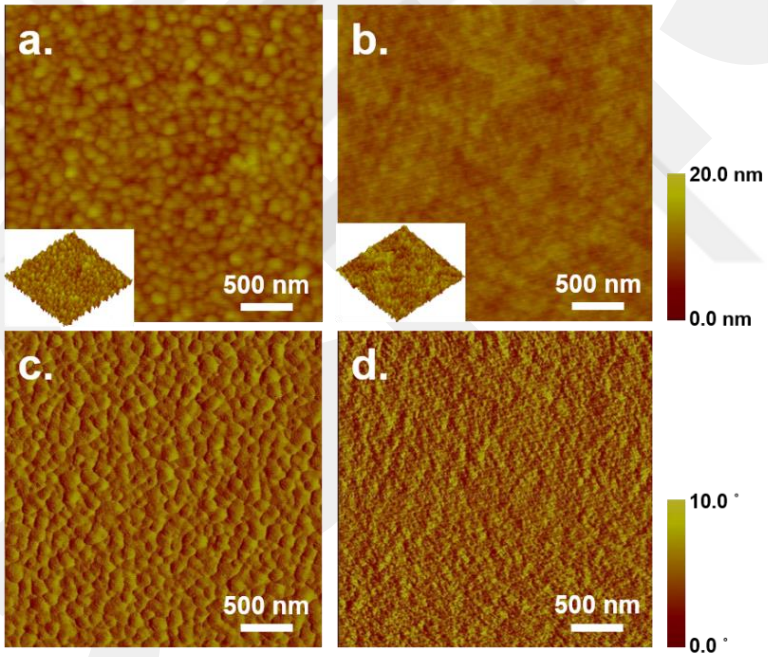

Figure 4.3.4.4. Atomic force microscopy (AFM) images of P(2OD-TBDY-T):$PC_{71}BM$ blend films without (height (a) and phase (c)) or with 1,8-diiodooctane (DIO) additive (height (b) and phase (d)).

4.4. Conclusion

In summary, we have demonstrated the design, synthesis, and physicochemical/optoelectronic characterizations of two new low band-gap (~1.3 eV) D-A copolymers (**P(2OD-TBDY-T)** and **P(2OD-TBDY-TT)**) based on a highly electron-deficient *meso*-thiophene substituted BODIPY π-acceptor **2OD-TBDY**. The thin-films of these polymers exhibit nano-scale isotropic nodule-like domains with essentially no ordering in the out-of-plane direction. The semiconductor characteristics of the new polymers tested in BG-TC OFET devices demonstrated hole mobilities of up to ~0.005 $cm^2/V \cdot s$. By employing **P(2OD-TBDY-T)** as the electron donor and $PC_{71}BM$ as the electron acceptor in active layer, inverted BHJ-OPV devices with high PCE of ~6.2% have been achieved. This is, to the best of our knowledge, a record high value for a boron-containing donor polymer. Since BODIPY-based polymers have only recently attracted research interest for OPV technologies, yet with much lower performances (PCEs < 2%) in previous research; our findings clearly demonstrate that they can play a pronounced role in the design of high-performance donor polymers in BHJ-OPV devices.

Chapter 5

Conclusion and Future Prospect

5.1. Conclusion

This thesis includes a series of new semiconducting materials for OTFT and OPV applications. They were fully characterized by $^{1}H/^{13}C$ NMR, mass spectrometry, cyclic voltammetry, UV-Vis absorption spectroscopy, differential scanning calorimetry, thermogravimetric analysis, melting point measurements, and solution-processed thin-film morphologies/microstructures.

IFDK-based novel semiconducting materials, DD-TIFDKT, 2EH-TIFDKT, and 2OD-TIFDKT, have donor-acceptor-donor architectures in which thiophene is the donor and indeno[1,2-b]fluorene-6,12-dione is the acceptor unit. Both *n*-$C_{12}H_{25}$ linear chains and 2-ethylhexyl-/2-octyldodecyl swallow-tail chains were used as solubilizing groups at the position of α,ω-molecular terminals. 2-ethylhexyl-/2-octyldodecyl swallow-tail chains were found to be soluble in common organic solvents while -*n*-$C_{12}H_{25}$ linear chains were insoluble at α,ω-positions. On the other hand, linear alkyl chain provided good solubility at β-position. Density functional theory (DFT) calculations revealed that the computational results are consistent with the experimental results. Replacement of *n*-$C_{12}H_{25}$ linear chains with 2-Ethylhexyl resulted in not only good solubility but also good physicochemical/optoelectronic properties, effective solid-state packing, and high electrical performance. 2EH-TIFDKT and 2OD-TIFDKT-based solution-processible devices exhibited perfect ambipolar behavior including charge carrier mobilities of 0.04−0.12 $cm^2/V{\cdot}s$ and 0.0003−0.02 $cm^2/V{\cdot}s$ for electrons and holes, respectively, and I_{on}/I_{off} ratios of 10^5-10^6.

BODIPY-based new small molecular semiconductors, BDY-3T-BDY, BDY-4T-BDY, and BDY-PhAc-BDY have acceptor-donor-acceptor (A-D-A) molecular architecture. Solution processed thin-film transistors were fabricated with top-

contact/bottom-gate architecture. Stabilized frontier molecular orbital energies of these materials were found as -5.89 eV and -3.66 eV for BDY-3T-BDY, -5.86 eV and -3.67 eV for BDY-4T-BDY, and -5.68 eV and -3.56 eV for BDY-PhAc-BDY. Both BDY-3T-BDY and BDY-4T-BDY small molecules exhibited a low solid-state optical energy band gap of 1.94 eV, and BDY-PhAc-BDY showed band gap energy of 2.06 eV. BDY-4T-BDY-based OTFT devices exhibited perfect on-to-off current ratios of $>10^8$ and relatively high electron mobilities of 0.01 $cm^2/V{\cdot}s$. BDY-3T-BDY and BDY-PhAc-BDY exhibited electron mobilities of 2.7×10^{-4} $cm^2/V{\cdot}s$ and 0.004 $cm^2/V{\cdot}s$, and I_{on}/I_{off} ratios of 9.6×10^5 and 10^5-10^6, respectively. Since BDY-4T-BDY-based thin-films was highly crystalline, and fiber formation was observed through the solution-shearing direction. On the other hand, microribbons formation was detected in BDY-PhAc-BDY-based thin-films.

Boron based polymeric semiconducting materials with low band gap, (P(2OD-TBDY-T) and P(2OD-TBDY-TT) was designed, synthesized and fully characterized. These polymers based on D-A architecture in which highly electron deficient *meso*-thiophene substituted BODIPY, 2OD-TBDY was the π-acceptor unit. The thin-film morphology and microstructures characterizations showed nano-scale isotropic nodule-like domains. P(2OD-TBDY-T) and P(2OD-TBDY-TT)-based bottom-gate/top-contact OTFT devices possessed hole mobilities of ca. 0.005 $cm^2/V{\cdot}s$. OPV applications of these polymers were studied within the device architecture of inverted BHJ-OPV. The active layer of this device was consisted of $PC_{71}BM$ electron acceptor and P(2OD-TBDY-T) donor units. P(2OD-TBDY-T): $PC_{71}BM$-based inverted BHJ-OPV devices exhibited one of the highest PCEs of ~6.2% when compared to other boron containing polymeric donor materials.

Certainly, our results provide important rationales for the design of IFDK-based and BODIPY-based semiconducting materials for OTFT and OPV device applications. Clearly, our findings also present a new molecular design approach for the preparation of both molecular and polymeric solution-processable unipolar/ambipolar semiconductors. The current organic semiconductors could be promising materials for high-performance optoelectronic applications.

5.2. Future Prospect

The detailed study conducted in this thesis on the effects of molecular structures and substitutions/functionalizations on the optoelectronic properties, intermolecular cohesive forces, thin-film microstructures, and charge transport performances of semiconductors revealed crucial structure–property–function relationships. Furthermore, density functional theory (DFT) calculations were found to be in excellent agreement with the observed electronic structure and physicochemical trends and provided further insight. Therefore, we strongly envision that further structural tailoring could be performed on each molecular family shown in this thesis to further improve their (opto)electronic performances and realize new functions. In the rational design of the molecules presented in Chapter 2, further repositioning of the insulating substituents could potentially enhance the π-core planarity and improve device performances. These modifications could result in two dimensional stacking in thin-film, which is more favorable for high performance optoelectronic devices. Also, thiazole aromatic units could be used to further planarize the structures. Thiazole-based donor units have some superior structural properties over thiophene, possessing higher molecular dipole and lower LUMO energy levels. Thus, thiazole could be used to increase charge carrier mobility, especially electron mobility. The design strategy and choosing proper alkyl substituents are also very crucial for BODIPY-based small molecules. The electron mobility of OTFT devices could be further improved to values in excess of 0.01 cm2/V·s by using more electron deficient groups, which also offers some future prospects in OTFT applications. Using thiazole instead of thiophene at the meso-position of BODIPY could result in the decrease in the dihedral angle between these two which enhance the planarity of π-system. Furthermore, dipole moment of overall system could increase. All these parameters make thiazole unit a very promising candidate to develop novel donor materials with higher power conversion efficiency in BHJ-OPVs. Finally, device performances of both OTFT and OPV devices could be further optimized by employing various device structures (i.e. bottom gate bottom contact (BG-BC) and top-gate coplanar or staggered for OTFT) (i.e. tandem geometry and normal geometry for OPV) and conductor-dielectric-interfacial materials (i.e. Polyvinyl alcohol (PVA) and Al2O3).

BIBLIOGRAPHY

[1] M. Ozdemir *et al.*, "Solution-Processable BODIPY-Based Small Molecules for Semiconducting Microfibers in Organic Thin-Film Transistors," *ACS Appl. Mater. Interfaces*, vol. 8, no. 22, pp. 14077–14087, Jun. 2016.

[2] S. Theses, *Short-Channel Organic Thin-Film Transistors*. .

[3] T. H. E. Definitive and V. Guide, *The definitive visual guide*. .

[4] *No Title*. .

[5] B. S. Ong, Y. Wu, P. Liu, and S. Gardner, "Structurally Ordered Polythiophene Nanoparticles for High-Performance Organic Thin-Film Transistors," *Adv. Mater.*, vol. 17, no. 9, pp. 1141–1144.

[6] H. Sirringhaus, P. J. Brown, R. H. Friend, M. M. Nielsen, K. Bechgaard, and A. J. H. Spiering, "Two-dimensional charge transport in conjugated polymers," pp. 685–688, 1999.

[7] Y. D. Park, J. A. Lim, H. S. Lee, and K. Cho, "Interface engineering in organic transistors," *Mater. Today*, vol. 10, no. 3, pp. 46–54, 2007.

[8] V. A. Online, S. B. Darling, and F. You, "RSC Advances The case for organic photovoltaics," pp. 17633–17648, 2015.

[9] R. J. Kline, M. D. Mcgehee, E. N. Kadnikova, J. Liu, J. M. J. Fre, and M. F. Toney, "Dependence of Regioregular Poly (3-hexylthiophene) Film Morphology and Field-Effect Mobility on Molecular Weight," pp. 3312–3319, 2005.

[10] A. Zen *et al.*, "Effect of Molecular Weight on the Structure and Crystallinity of Poly(3-hexylthiophene)," *Macromolecules*, vol. 39, no. 6, pp. 2162–2171, Mar. 2006.

[11] R. Zhang *et al.*, "Nanostructure Dependence of Field-Effect Mobility in Regioregular Poly(3-hexylthiophene) Thin Film Field Effect Transistors," *J. Am. Chem. Soc.*, vol. 128, no. 11, pp. 3480–3481, Mar. 2006.

[12] S. O. F. Transistors *et al.*, "Highly Soluble [1] Benzothieno [3 , 2-b] benzothiophene (BTBT) Derivatives for," no. Table 1, pp. 15732–15733, 2007.

[13] T. Lei, J.-H. Dou, and J. Pei, "Influence of Alkyl Chain Branching Positions on the Hole Mobilities of Polymer Thin-Film Transistors," *Adv. Mater.*, vol. 24, no. 48, pp. 6457–6461, Sep. 2012.

[14] J. Li *et al.*, "A stable solution-processed polymer semiconductor with record high-mobility for printed transistors," *Sci. Rep.*, vol. 2, p. 754, Oct. 2012.

[15] I. Kang, H.-J. Yun, D. S. Chung, S.-K. Kwon, and Y.-H. Kim, "Record High Hole Mobility in Polymer Semiconductors via Side-Chain Engineering," *J. Am. Chem. Soc.*, vol. 135, no. 40, pp. 14896–14899, Oct. 2013.

[16] K. Takimiya, H. Ebata, K. Sakamoto, T. Izawa, T. Otsubo, and Y. Kunugi, "2,7-Diphenyl[1]benzothieno[3,2-b]benzothiophene, A New Organic Semiconductor for Air-Stable Organic Field-Effect Transistors with Mobilities up to 2.0 cm2 V-1 s-1," *J. Am. Chem. Soc.*, vol. 128, no. 39, pp. 12604–12605, Oct. 2006.

[17] H. Cho *et al.*, "High-Mobility Pyrene-Based Semiconductor for Organic Thin-Film Transistors," *ACS Appl. Mater. Interfaces*, vol. 5, no. 9, pp. 3855–3860, May 2013.

[18] A. L. Briseno *et al.*, "Self-Assembly, Molecular Packing, and Electron Transport in n-Type Polymer Semiconductor Nanobelts," *Chem. Mater.*, vol. 20, no. 14, pp. 4712–4719, Jul. 2008.

[19] J. A. Letizia, M. R. Salata, C. M. Tribout, A. Facchetti, M. A. Ratner, and T. J. Marks, "n-Channel Polymers by Design : Optimizing the Interplay of Solubilizing Substituents , Crystal Packing , and Field-Effect Transistor Characteristics in Polymeric Bithiophene-Imide Semiconductors," no. 12, pp. 9679–9694, 2008.

[20] X. Zhan *et al.*, "A High-Mobility Electron-Transport Polymer with Broad Absorption and Its Use in Field-Effect Transistors and All-Polymer Solar Cells," pp. 7246–7247, 2007.

[21] T. Lei, J.-H. Dou, X.-Y. Cao, J.-Y. Wang, and J. Pei, "Electron-Deficient Poly(p-phenylene vinylene) Provides Electron Mobility over 1 cm2 V–1 s–1 under Ambient Conditions," *J. Am. Chem. Soc.*, vol. 135, no. 33, pp. 12168–12171, Aug. 2013.

[22] C. Kanimozhi, N. Yaacobi-Gross, K. W. Chou, A. Amassian, T. D. Anthopoulos, and S. Patil, "Diketopyrrolopyrrole–Diketopyrrolopyrrole-Based Conjugated Copolymer for High-Mobility Organic Field-Effect Transistors," *J. Am. Chem. Soc.*, vol. 134, no. 40, pp. 16532–16535, Oct. 2012.

[23] A. Facchetti, M. Mushrush, M.-H. Yoon, G. R. Hutchison, M. A. Ratner, and T. J. Marks, "Building Blocks for n-Type Molecular and Polymeric Electronics. Perfluoroalkyl- versus Alkyl-Functionalized Oligothiophenes (nT; n = 2−6). Systematics of Thin Film Microstructure, Semiconductor Performance, and Modeling of Majority Charge Injection in Field-Effect Transistors," *J. Am. Chem. Soc.*, vol. 126, no. 42, pp. 13859–13874, Oct. 2004.

[24] A. Facchetti, M.-H. Yoon, C. L. Stern, H. E. Katz, and T. J. Marks, "Building Blocks for n-Type Organic Electronics: Regiochemically Modulated Inversion of Majority Carrier Sign in Perfluoroarene-Modified Polythiophene Semiconductors," *Angew. Chemie Int. Ed.*, vol. 42, no. 33, pp. 3900–3903, Aug. 2003.

[25] P. H. Wöbkenberg *et al.*, "Fluorine containing C60 derivatives for high-performance electron transporting field-effect transistors and integrated circuits," *Appl. Phys. Lett.*, vol. 92, no. 14, p. 143310, Apr. 2008.

[26] H. E. Katz, J. Johnson, A. J. Lovinger, and W. Li, "Naphthalenetetracarboxylic Diimide-Based n-Channel Transistor Semiconductors: Structural Variation and Thiol-Enhanced Gold Contacts," *J. Am. Chem. Soc.*, vol. 122, no. 32, pp. 7787–7792, Aug. 2000.

[27] E. J. Meijer *et al.*, "Corrigendum: Solution-processed ambipolar organic field-effect transistors and inverters," *Nat. Mater.*, vol. 2, p. 834, Dec. 2003.

[28] F. S. Kim, X. Guo, M. D. Watson, and S. A. Jenekhe, "High-mobility Ambipolar Transistors and High-gain Inverters from a Donor–Acceptor Copolymer Semiconductor," *Adv. Mater.*, vol. 22, no. 4, pp. 478–482, Jan. 2010.

[29] T. T. Steckler *et al.*, "A Spray-Processable, Low Bandgap, and Ambipolar Donor−Acceptor Conjugated Polymer," *J. Am. Chem. Soc.*, vol. 131, no. 8, pp. 2824–2826, Mar. 2009.

[30] T. Lei *et al.*, "Ambipolar Polymer Field-Effect Transistors Based on Fluorinated Isoindigo: High Performance and Improved Ambient Stability," *J. Am. Chem. Soc.*, vol. 134, no. 49, pp. 20025–20028, Dec. 2012.

[31] L. Wang, X. Zhang, H. Tian, Y. Lu, Y. Geng, and F. Wang, "A cyano-terminated dithienyldiketopyrrolopyrrole dimer as a solution processable ambipolar semiconductor under ambient conditions," *Chem. Commun.*, vol. 49, no. 96, pp. 11272–11274, 2013.

[32] H. N. Tsao, W. Pisula, Z. Liu, W. Osikowicz, W. R. Salaneck, and K. Müllen, "From Ambi- to Unipolar Behavior in Discotic Dye Field-Effect Transistors," *Adv.*

Mater., vol. 20, no. 14, pp. 2715–2719, Jul. 2008.
[33] U. Schoeler, K. H. Tews, and H. Kuhn, "Potential model of dye molecule from measurements of the photocurrent in monolayer assemblies," *J. Chem. Phys.*, vol. 61, no. 12, pp. 5009–5016, Dec. 1974.
[34] P. Liu, Q. Li, M. Huang, W. Pan, and W. Deng, "High open circuit voltage organic photovoltaic cells based on oligothiophene derivatives," *Appl. Phys. Lett.*, vol. 89, no. 21, p. 213501, Nov. 2006.
[35] L. Guan *et al.*, "Synthesis and Photovoltaic Properties of Donor–Acceptor Oligothiophene Derivatives Possessing Mesogenic Properties," *Synth. Commun.*, vol. 41, no. 24, pp. 3662–3670, Dec. 2011.
[36] R. Fitzner *et al.*, "Interrelation between Crystal Packing and Small-Molecule Organic Solar Cell Performance," *Adv. Mater.*, vol. 24, no. 5, pp. 675–680, Jan. 2012.
[37] K. Schulze, M. Riede, E. Brier, E. Reinold, P. Bäuerle, and K. Leo, "Dicyanovinyl-quinquethiophenes with varying alkyl chain lengths: Investigation of their performance in organic devices," *J. Appl. Phys.*, vol. 104, no. 7, p. 74511, Oct. 2008.
[38] S. Steinberger *et al.*, "Vacuum-processed small molecule solar cells based on terminal acceptor-substituted low-band gap oligothiophenes," *Chem. Commun.*, vol. 47, no. 7, pp. 1982–1984, 2011.
[39] D. Demeter, T. Rousseau, and J. Roncali, "3,4-Ethylenedioxythiophene (EDOT) as building block for the design of small molecular donors for organic solar cells," *RSC Adv.*, vol. 3, no. 3, pp. 704–707, 2013.
[40] H. Sirringhaus, "25th Anniversary Article : Organic Field-Effect Transistors : The Path Beyond Amorphous Silicon," pp. 1319–1335, 2014.
[41] J. E. Anthony, "Functionalized Acenes and Heteroacenes for Organic Electronics," pp. 5028–5048, 2006.
[42] B. Vercelli, A. Berlin, J. Casado, J. T. Lo, and G. Zotti, "Phenyl- and Thienyl-Ended Symmetric Azomethines and Azines as Model Compounds for n - Channel Organic Field-E ff ect Transistors : An Electrochemical and Computational Study," 2014.
[43] R. P. Ortiz *et al.*, "Molecular and Electronic-Structure Basis of the Ambipolar Behavior of Naphthalimide – Terthiophene Derivatives : Implementation in Organic Field-Effect Transistors," pp. 12458–12467, 2013.
[44] M. Chen *et al.*, "and their functionalized derivatives for organic thin-film transistors w," pp. 1846–1848, 2009.
[45] L. Chen, T. Hu, P. Huang, and C. Kim, "Enhanced Performance of Solution-Processed TESPE-ADT Thin-Film Transistors **," pp. 2772–2776, 2013.
[46] H. Lin *et al.*, "High-Performance Non-Fullerene Polymer Solar Cells Based on a Pair of Donor – Acceptor Materials with Complementary Absorption Properties," pp. 7299–7304, 2015.
[47] Y. Liu *et al.*, "Efficient non-fullerene polymer solar cells enabled by tetrahedron-shaped core based 3D-structure small-molecular electron acceptors," pp. 13632–13636, 2015.
[48] A. K. Palai *et al.*, "RSC Advances electron donating thienylethyl moieties and," pp. 41476–41482, 2014.
[49] J. Kim, M. Ko, N. Cho, S. Paek, K. Lee, and J. Ko, "RSC Advances Efficient small molecule organic semiconductor containing bis- dimethylfluorenyl amino benzo [b] thiophene for high open circuit voltage in high efficiency solution processed organic solar cell {," vol. 1, pp. 2692–2695, 2012.

[50] A. Pierre, M. Sadeghi, M. M. Payne, A. Facchetti, J. E. Anthony, and A. C. Arias, “All-Printed Flexible Organic Transistors Enabled by Surface Tension-Guided Blade Coating,” pp. 5722–5727, 2014.
[51] L. Basiricò, P. Cosseddu, B. Fraboni, and A. Bonfiglio, “Inkjet printing of transparent , flexible , organic transistors,” *Thin Solid Films*, vol. 520, no. 4, pp. 1291–1294, 2011.
[52] K. C. Dickey *et al.*, “Large-area patterning of a solution-processable organic semiconductor to reduce parasitic leakage and off currents in thin-film transistors Large-area patterning of a solution-processable organic semiconductor to reduce parasitic leakage and off currents ,” vol. 244103, no. 2007, pp. 28–31, 2014.
[53] R. Capelli, S. Toffanin, G. Generali, H. Usta, A. Facchetti, and M. Muccini, “light-emitting diodes,” *Nat. Mater.*, vol. 9, no. 6, pp. 496–503, 2010.
[54] B. Carsten *et al.*, “Mediating Solar Cell Performance by Controlling the Internal Dipole Change in Organic Photovoltaic Polymers,” 2012.
[55] A. Broggi, I. Tomasi, L. Bianchi, and A. Marrocchi, “Small Molecular Aryl Acetylenes : Chemically Tailoring High-Efficiency Organic Semiconductors for Solar Cells and Field-Effect Transistors,” pp. 486–507, 2014.
[56] F. Silvestri *et al.*, “Solution-Processable Low-Molecular Weight Extended Arylacetylenes : Versatile p-Type Semiconductors for Field-Effect Transistors and Bulk Heterojunction Solar Cells,” no. m, pp. 6108–6123, 2010.
[57] A. Marrocchi, F. Silvestri, M. Seri, A. Facchetti, and T. J. Marks, “Conjugated anthracene derivatives as donor materials for bulk heterojunction solar cells : olefinic versus acetylenic spacers w,” no. Scheme 1, pp. 1380–1382, 2009.
[58] M. Cai, T. Xiao, E. Hellerich, Y. Chen, R. Shinar, and J. Shinar, “High-Effi ciency Solution-Processed Small Molecule Electrophosphorescent Organic Light-Emitting Diodes,” pp. 3590–3596, 2011.
[59] Y. Kajiyama, K. Kajiyama, and H. Aziz, “Maskless RGB color patterning of vacuum- deposited small molecule OLED displays by diffusion of luminescent dopant molecules,” vol. 23, no. 13, pp. 2250–2258, 2015.
[60] H. E. Katz, Z. Bao, and S. L. Gilat, “Synthetic Chemistry for Ultrapure , Processable , and High-Mobility Organic Transistor Semiconductors,” vol. 34, no. 5, pp. 359–369, 2001.
[61] M. Ozdemir, S. Genc, R. Ozdemir, Y. Altintas, and M. Citir, “Trans – cis isomerization assisted synthesis of solution-processable yellow fl uorescent maleic anhydrides for white-light generation,” vol. 210, pp. 192–200, 2015.
[62] W. Wu, Y. Liu, and D. Zhu, “p -Conjugated molecules with fused rings for organic field-effect transistors : design , synthesis and applications,” pp. 1489–1502, 2010.
[63] V. A. Online *et al.*, “Materials Chemistry C,” pp. 8892–8902, 2014.
[64] M. Zambianchi *et al.*, “Synergic e ff ect of unsaturated inner bridges and polymorphism for tuning the optoelectronic properties of 2 , 3-thieno (bis) imide based materials †,” pp. 121–131, 2015.
[65] K. Niimi, S. Shinamura, I. Osaka, E. Miyazaki, and K. Takimiya, “Characterization , and FET Characteristics of New π -Extended Heteroarene with Eight Fused Aromatic Rings,” pp. 8732–8739, 2011.
[66] P. Kumaresan *et al.*, “Fused-Thiophene Based Materials for Organic Photovoltaics and Dye-Sensitized Solar Cells,” pp. 2645–2669, 2014.
[67] J. Li, F. Yan, J. Gao, P. Li, W. Xiong, and Y. Zhao, “Dyes and Pigments Synthesis , physical properties and OLED performance of azatetracenes,” *Dye. Pigment.*, vol. 112, pp. 93–98, 2015.
[68] H. Usta *et al.*, “Per fl uoroalkyl-Functionalized Thiazole − Thiophene Oligomers

as N - Channel Semiconductors in Organic Field-E ff ect and Light- Emitting Transistors," 2014.
[69] D. T. Chase *et al.*, "6,12-Diarylindeno[1,2- b] fl uorenes: Syntheses, Photophysics, and Ambipolar OFETs," pp. 2–5, 2012.
[70] J. Mei, Y. Diao, A. L. Appleton, L. Fang, and Z. Bao, "Integrated Materials Design of Organic Semiconductors for Field- E ff ect Transistors," 2013.
[71] H. Usta, C. Newman, Z. Chen, and A. Facchetti, "Dithienocoronenediimide-Based Copolymers as Novel Ambipolar Semiconductors for Organic Thin-Film Transistors," pp. 3678–3684, 2012.
[72] A. J. Kronemeijer *et al.*, "A Selenophene-Based Low-Bandgap Donor – Acceptor Polymer Leading to Fast Ambipolar Logic," pp. 1558–1565, 2012.
[73] S. Fabiano, H. Usta, R. Forchheimer, X. Crispin, and A. Facchetti, "Selective Remanent Ambipolar Charge Transport in Polymeric Field-Effect Transistors For High-Performance Logic Circuits Fabricated in Ambient," pp. 7438–7443, 2014.
[74] A. C. Arias, J. D. Mackenzie, I. Mcculloch, J. Rivnay, and A. Salleo, "Materials and Applications for Large Area Electronics : Solution-Based Approaches," pp. 3–24, 2010.
[75] K. Baeg, M. Caironi, and Y. Noh, "Toward Printed Integrated Circuits based on Unipolar or Ambipolar Polymer Semiconductors," pp. 4210–4244, 2013.
[76] V. A. Online *et al.*, "Materials Chemistry C," pp. 6376–6386, 2014.
[77] R. P. Ortiz, H. Yan, A. Facchetti, and T. J. Marks, "Azine- and Azole-Functionalized Oligo´ and Polythiophene Semiconductors for Organic Thin-Film Transistors," pp. 1533–1558, 2010.
[78] H. Usta *et al.*, "BODIPY-Thiophene Copolymers as p -Channel Semiconductors for Organic Thin-Film Transistors," *Adv. Mater.*, vol. 25, no. 31, pp. 4327–4334, Aug. 2013.
[79] E. Environ, "Environmental Science High mobility organic thin film transistor and efficient photovoltaic devices using versatile donor – acceptor polymer semiconductor by molecular design," pp. 2288–2296, 2011.
[80] H. Usta, A. Facchetti, and T. J. Marks, "Air-Stable , Solution-Processable n -Channel and Ambipolar Semiconductors for Thin-Film Transistors Based on the Indenofluorenebis (dicyanovinylene) Core," vol. 3, pp. 8580–8581, 2008.
[81] H. Usta *et al.*, "Design , Synthesis , and Characterization of Ladder-Type Molecules and Polymers . Air-Stable , Solution-Processable n -Channel and Ambipolar Semiconductors for Thin-Film Transistors via Experiment and Theory," no. 3, pp. 5586–5608, 2009.
[82] J. Mei and Z. Bao, "Side Chain Engineering in Solution-Processable Conjugated Polymers," 2014.
[83] J. Min *et al.*, "Alkyl Chain Engineering of Solution-Processable Star-Shaped Molecules for High-Performance Organic Solar Cells," pp. 1–10, 2014.
[84] A. Han, G. K. Dutta, J. Lee, H. R. Lee, and S. M. Lee, "ε -Branched Flexible Side Chain Substituted Diketopyrrolopyrrole-Containing Polymers Designed for High Hole and Electron Mobilities," pp. 247–254, 2015.
[85] J. Lee, A. Han, H. Yu, T. J. Shin, C. Yang, and J. H. Oh, "Boosting the Ambipolar Performance of Solution-Processable Polymer Semiconductors via Hybrid Side-Chain Engineering," 2013.
[86] M. J. Frisch *et al.*, "Gaussian 09, Revision C.01." Gaussian, Inc., Wallingford CT, 2010.
[87] S. H. Park *et al.*, "A polymer brush organic interlayer improves the overlying pentacene nanostructure and organic field-effect transistor performance," *J. Mater.*

Chem., vol. 21, no. 39, p. 15580, 2011.
[88] V. A. Online, "RSC Advances," pp. 13078–13084, 2014.
[89] T. Nakagawa *et al.*, "High Performance n-Type Field-Effect Transistors Based on Indenofluorenedione and Diindenopyrazinedione Derivatives cording to a reported method . 5 The dihalogenated derivatives 1b - d were prepared by a method similar to that described Organic field-eff," pp. 2615–2617, 2008.
[90] D. Waals, D. Waals, and D. Waals, "OF," 1964.
[91] J. E. Anthony, D. L. Eaton, and S. R. Parkin, "LETTERS A Road Map to Stable , Soluble , Easily Crystallized Pentacene Derivatives," pp. 1–4, 2002.
[92] P. Huang *et al.*, "High-Performance Bottom-Contact Organic Thin-Film Transistors Based on Benzo [d , d ′] thieno [3 , 2 - b ; 4 , 5 - b ′] dithiophenes (BTDTs) Derivatives," pp. 4–10, 2012.
[93] M. F. Toney and Z. Bao, "semiconductors using lattice strain," pp. 4–9, 2011.
[94] B. K. C. Dickey, J. E. Anthony, and Y. Loo, "Improving Organic Thin-Film Transistor Performance through Solvent-Vapor Annealing of Solution-Processable Triethylsilylethynyl Anthradithiophene **," pp. 1721–1726, 2006.
[95] A. Becerril, M. E. Roberts, Z. Liu, J. Locklin, and Z. Bao, "High-Performance Organic Thin-Film Transistors through Solution-Sheared Deposition of Small-Molecule Organic Semiconductors **," pp. 2588–2594, 2008.
[96] Z. Liu, S. Member, H. A. Becerril, M. E. Roberts, Y. Nishi, and Z. Bao, "Experimental Study and Statistical Analysis of Solution-Shearing Processed Organic Transistors Based on an Asymmetric Small-Molecule Semiconductor," *IEEE Trans. Electron Devices*, vol. 56, no. 2, pp. 176–185, 2009.
[97] C. S. Kim *et al.*, "Solvent-dependent electrical characteristics and stability of organic thin-film transistors with drop cast bis (triisopropylsilylethynyl) pentacene Solvent-dependent electrical characteristics and stability of organic thin-film transistors with drop cas," vol. 103302, pp. 1–4, 2008.
[98] J. Chang *et al.*, "Enhanced Mobility of Poly (3-hexylthiophene) Transistors by Spin-Coating from High-Boiling-Point Solvents," no. 7, pp. 4772–4776, 2004.
[99] A. Facchetti, "π-Conjugated Polymers for Organic Electronics and Photovoltaic Cell Applications," *Chem. Mater.*, vol. 23, no. 3, pp. 733–758, Feb. 2011.
[100] L. Chua, J. Zaumseil, J. Chang, and E. C. Ou, "General observation of n-type field-effect behaviour in organic semiconductors," vol. 434, no. March, pp. 194–199, 2005.
[101] M.-C. Chen *et al.*, "Asymmetric fused thiophenes for field-effect transistors: crystal structure–film microstructure–transistor performance correlations," *J. Mater. Chem. C*, vol. 2, no. 42, pp. 8892–8902, 2014.
[102] S. Allard, M. Forster, B. Souharce, and H. Thiem, "Organic Electronics Organic Semiconductors for Solution-Processable Field-Effect Transistors (OFETs) Angewandte," pp. 4070–4098, 2008.
[103] M. Sawamoto, M. J. Kang, E. Miyazaki, H. Sugino, I. Osaka, and K. Takimiya, "Masanori Sawamoto, § , ¶ Myeong Jin Kang, † Eigo Miyazaki, † Hiroyoshi Sugino, § Itaru Osaka, § and Kazuo Takimiya * , § , † §," 2016.
[104] L. Zhang *et al.*, "Bistetracene: An Air-Stable, High-Mobility Organic Semiconductor with Extended Conjugation," *J. Am. Chem. Soc.*, vol. 136, no. 26, pp. 9248–9251, Jul. 2014.
[105] M. Durso *et al.*, "Synthesis , size-dependent optoelectronic and charge transport properties of thieno (bis) imide end-substituted molecular semiconductors," *Org. Electron.*, vol. 14, no. 11, pp. 3089–3097, 2013.
[106] V. A. Online, "donating small molecules on their molecular packing," pp. 14538–

14547, 2013.
[107] J. M. Chem, A. C. Benniston, G. Copley, A. Harriman, and R. Ryan, “Thermoresponsive fluorescent polymers based on a quaterthiophene- containing boron dipyrromethene (Bodipy) dyad dispersed in silicone rubber †,” pp. 2601–2608, 2011.
[108] G. S. Hanan and G. S. Hanan, “Chem Soc Rev their applications in organic photovoltaic devices,” no. September 2002, pp. 3342–3405, 2014.
[109] A. M. Poe, A. M. Della Pelle, A. V Subrahmanyam, W. White, G. Wantz, and S. Thayumanavan, “Small molecule BODIPY dyes as non-fullerene acceptors in bulk heterojunction organic photovoltaics,” *Chem. Commun.*, vol. 50, no. 22, pp. 2913–2915, 2014.
[110] T. Bura *et al.*, “High-Performance Solution-Processed Solar Cells and Ambipolar Behavior in Organic Field-Effect Transistors with Thienyl-BODIPY Scaffoldings,” *J. Am. Chem. Soc.*, vol. 134, no. 42, pp. 17404–17407, Oct. 2012.
[111] D. A. Links, “Chem Soc Rev Fluorescent indicators based on BODIPY,” pp. 1130–1172, 2012.
[112] W. Liu, A. Tang, J. Chen, Y. Wu, C. Zhan, and J. Yao, “Photocurrent Enhancement of BODIPY-Based Solution-Processed Small-Molecule Solar Cells by Dimerization via the Meso Position,” 2014.
[113] J. J. Chen, S. M. Conron, P. Erwin, M. Dimitriou, K. Mcalahney, and M. E. Thompson, “High-E ffi ciency BODIPY-Based Organic Photovoltaics,” 2015.
[114] D. Cortizo-lacalle *et al.*, “Solution processable diketopyrrolopyrrole (DPP) cored small molecules with BODIPY end groups as novel donors for organic solar cells,” pp. 2683–2695.
[115] C. T. P. Applications, “Revealing the Charge-Transfer Interactions in Self-Assembled Organic Cocrystals: Two-Dimensional Photonic Applications**,” pp. 6785–6789, 2015.
[116] M. Ozdemir *et al.*, “Design, synthesis, and characterization of α,ω-disubstituted indeno[1,2-b]fluorene-6,12-dione-thiophene molecular semiconductors. Enhancement of ambipolar charge transport through synthetic tailoring of alkyl substituents,” *RSC Adv.*, vol. 6, no. 1, pp. 212–226, 2016.
[117] M. A. Reyes-martinez, A. J. Crosby, and A. L. Briseno, “via conducting channel wrinkling,” *Nat. Commun.*, vol. 6, no. May, pp. 1–8, 2015.
[118] Y. Zhang, A. J. Wise, M. D. Barnes, and A. L. Briseno, “A forrest of crystals,” *Biochem. Pharmacol.*, vol. 17, no. 9, pp. 464–465, 2014.
[119] R. Turrisi *et al.*, “acceptor perylenemonoimides for luminescent solar concentrators †,” no. 2, pp. 8045–8054, 2015.
[120] F. Meinardi *et al.*, “Large-area luminescent solar concentrators based on ‘Stokes-shift-engineered’ nanocrystals in a mass-polymerized PMMA matrix,” vol. 8, no. May, 2014.
[121] A. Sanguineti *et al.*, “High Stokes shift perylene dyes for luminescent solar concentrators †,” no. c, pp. 1618–1620, 2013.
[122] L. Beverina and G. A. Pagani, “π - Conjugated Zwitterions as Paradigm of Donor À Acceptor Building Blocks in Organic-Based Materials,” vol. 47, no. 2, pp. 319–329, 2014.
[123] C. F. Macrae *et al.*, “Mercury : visualization and analysis of crystal structures,” pp. 453–457, 2006.
[124] A. C. Benniston, G. Copley, A. Harriman, D. B. Rewinska, R. W. Harrington, and W. Clegg, “A Donor - Acceptor Molecular Dyad Showing Multiple Electronic Energy-Transfer Processes in Crystalline and Amorphous States,” pp. 7174–7175,

2008.
[125] S. Zhen, “As featured in :,” no. 207890, pp. 3940–3943, 2013.
[126] J. Choi *et al.*, “Importance of Electron Transport Ability in Naphthalene Diimide-Based Polymer Acceptors for High-Performance, Additive-Free, All- Polymer Solar Cells,” 2015.
[127] Z. Chen, Y. Zheng, H. Yan, and A. Facchetti, “Naphthalenedicarboximide- vs Perylenedicarboximide-Based Copolymers . Synthesis and Semiconducting Properties in Bottom-Gate N-Channel Organic Transistors,” pp. 8–9, 2009.
[128] I. F. Sengul, E. Okutan, H. Kandemir, E. Astarc, and B. Ços, “Dyes and Pigments Carbazole substituted BODIPY dyes : Synthesis , photophysical properties and antitumor activity,” vol. 123, pp. 32–38, 2015.
[129] B. Acceptors *et al.*, “Engineering Tuneable Light-Harvesting Systems with Oligothiophene Donors and Mono- or interest 7 - 10 because it exhibits sharp fluorescence emissions and high quantum yields in addition to elevated chemical and photostabilities . 11 Bodipy has very recen,” vol. 17, no. c, pp. 1563–1566, 2008.
[130] M. T. Whited *et al.*, “ChemComm Symmetry-breaking intramolecular charge transfer in the excited state of meso -linked BODIPY dyads w,” pp. 284–286, 2012.
[131] M. Yoon, C. Kim, A. Facchetti, and T. J. Marks, “Gate Dielectric Chemical Structure - Organic Field-Effect Transistor Performance Correlations for Electron , Hole , and Ambipolar Organic Semiconductors,” no. d, pp. 12851–12869, 2006.
[132] S. Kobayashi *et al.*, “Control of carrier density by self-assembled monolayers in organic field-effect transistors,” vol. 3, no. May, pp. 317–322, 2004.
[133] A. Von Mühlenen, M. Castellani, M. Schaer, and L. Zuppiroli, “solidi,” vol. 1174, no. 6, pp. 1170–1174, 2008.
[134] K. P. Pernstich *et al.*, “Threshold voltage shift in organic field effect transistors by dipole monolayers on the gate insulator Threshold voltage shift in organic field effect transistors by dipole monolayers on the gate insulator,” vol. 6431, 2004.
[135] Y. Wang *et al.*, “Synthesis and properties of novel near-infrared dye based on BODIPY and diketopyrrolopyrrole units,” *Mater. Lett.*, vol. 139, pp. 130–133, 2015.
[136] M. Mcdowell, I. G. Hill, J. E. Mcdermott, S. L. Bernasek, and J. Schwartz, “Improved organic thin-film transistor performance using novel self-assembled monolayers Improved organic thin-film transistor performance using novel self-assembled monolayers,” vol. 073505, no. 2006, pp. 39–42, 2014.
[137] Y. Woo and H. Klauk, “Conducting polymers for carbon electronics themed issue Organic thin-film transistors w,” no. 7, 2010.
[138] S. Cheng *et al.*, “Solution-Processed Small-Molecule Bulk Heterojunction Ambipolar Transistors,” pp. 2057–2063, 2014.
[139] A. L. Briseno, S. C. B. Mannsfeld, S. A. Jenekhe, Z. Bao, and Y. Xia, “Introducing organic nanowire transistors semiconductors , and review some of the advances in this field .,” vol. 11, no. 4, pp. 38–47, 2008.
[140] A. Facchetti, M. Mushrush, M. Yoon, G. R. Hutchison, M. A. Ratner, and T. J. Marks, “Building Blocks for n-Type Molecular and Polymeric Microstructure , Semiconductor Performance , and Modeling of Majority Charge Injection in Field-Effect Transistors,” no. i, pp. 13859–13874, 2004.
[141] K. Tremel *et al.*, “Charge Transport Anisotropy in Highly Oriented Thin Films of the Acceptor Polymer P (NDI2OD-T2),” pp. 1–13, 2014.
[142] E. J. W. Crossland, K. Tremel, F. Fischer, and K. Rahimi, “Anisotropic Charge Transport in Spherulitic Poly (3-hexylthiophene) Films,” pp. 839–844, 2012.

[143] J. Rivnay *et al.*, “microstructure in organic thin films,” *Nat. Mater.*, vol. 8, no. 12, pp. 952–958, 2009.
[144] T. Bura *et al.*, “High-Performance Solution-Processed Solar Cells and Ambipolar Behavior in Organic Field-E ff ect Transistors with Thienyl-BODIPY Sca ff oldings,” pp. 2–5, 2012.
[145] P. E. Kesavan, S. Das, M. Y. Lone, P. C. Jha, S. Mori, and I. Gupta, “Bridged bis-BODIPYs: their synthesis, structures and properties,” pp. 17209–17221, 2015.
[146] H. L. Kee *et al.*, “Structural Control of the Photodynamics of Boron - Dipyrrin Complexes,” pp. 20433–20443, 2005.
[147] D. Ayd, G. Viswanathan, and Z. Topal, “Biomolecular Chemistry Antimicrobial activity of a quaternized BODIPY against Staphylococcus strains †,” vol. 979886, pp. 2665–2670, 2016.
[148] H. Usta *et al.*, “COMMUNICATION BODIPY – Thiophene Copolymers as p - Channel Semiconductors for Organic Thin-Film Transistors,” pp. 4327–4334, 2013.
[149] M. Ozdemir *et al.*, “Solution-Processable BODIPY-Based Small Molecules for Semiconducting Micro fi bers in Organic Thin-Film Transistors,” 2016.
[150] T. J. Marks, “n -Channel Semiconductor Materials Design for Organic Complementary Circuits,” vol. 44, no. 7, pp. 501–510, 2011.
[151] G. K. Veits, K. K. Carter, S. J. Cox, and A. J. Mcneil, “Developing a Gel-Based Sensor Using Crystal Morphology Prediction,” 2016.
[152] M. Wang, J. Li, G. Zhao, Q. Wu, Y. Huang, and W. Hu, “High-Performance Organic Field-Effect Transistors Based on Single and Large-Area Aligned Crystalline Microribbons of 6 , 13-Dichloropentacene,” pp. 2229–2233, 2013.
[153] T. He, M. Stolte, and F. Würthner, “Air-Stable n-Channel Organic Single Crystal Field-Effect Transistors Based on Microribbons of Core-Chlorinated Naphthalene Diimide,” pp. 6951–6955, 2013.
[154] Z. Bao, “High-Mobility Field-Effect Transistors from Large-Area Solution-Grown Aligned C 60 Single Crystals,” 2012.
[155] M. Gsänger *et al.*, “A Crystal-Engineered Hydrogen-Bonded Octachloroperylene Diimide with a Twisted Core : An n-Channel Organic Semiconductor **,” pp. 740–743, 2010.
[156] V. Shrotriya, “Organic photovoltaics: Polymer power,” *Nat. Photonics*, vol. 3, no. 8, pp. 447–449, Aug. 2009.
[157] M. Kaltenbrunner *et al.*, “Ultrathin and lightweight organic solar cells with high flexibility,” *Nat. Commun.*, vol. 3, p. 770, Apr. 2012.
[158] T. Kim *et al.*, “Flexible , highly efficient all-polymer solar cells,” *Nat. Commun.*, vol. 6, no. May, pp. 1–7, 2015.
[159] H. T. Yi, M. M. Payne, J. E. Anthony, and V. Podzorov, “Ultra-flexible solution-processed organic field-effect transistors,” *Nat. Commun.*, vol. 3, no. May, p. 1259, Dec. 2012.
[160] C.-H. Cho, H. J. Kim, H. Kang, T. J. Shin, and B. J. Kim, “The effect of side-chain length on regioregular poly[3-(4-n-alkyl)phenylthiophene]/PCBM and ICBA polymer solar cells,” *J. Mater. Chem.*, vol. 22, no. 28, p. 14236, 2012.
[161] T. E. Kang *et al.*, “Photoinduced Charge Transfer in Donor–Acceptor (DA) Copolymer: Fullerene Bis-adduct Polymer Solar Cells,” *ACS Appl. Mater. Interfaces*, vol. 5, no. 3, pp. 861–868, Feb. 2013.
[162] S. S. Cheng *et al.*, “Solution-processed small-molecule bulk heterojunction ambipolar transistors,” *Adv. Funct. Mater.*, vol. 24, no. 14, pp. 2057–2063, 2014.
[163] L. Zhang, N. S. Colella, B. P. Cherniawski, S. C. B. Mannsfeld, and A. L. Briseno,

"Oligothiophene Semiconductors : Synthesis , Characterization , and Applications for Organic Devices," 2014.
[164] V. Fig *et al.*, "Symmetric naphthalenediimidequaterthiophenes for electropolymerized electrochromic thin films †," pp. 5985–5994, 2015.
[165] L. Vaccaro, A. Marrocchi, D. Lanari, S. Santoro, and A. Facchetti, "Click-chemistry approaches to π-conjugated polymers for organic electronics applications," *Chem. Sci.*, 2016.
[166] C. Grand *et al.*, "Structure-Property Relationships Directing Transport and Charge Separation in Isoindigo Polymers," *Macromolecules*, vol. 49, no. 11, pp. 4008–4022, Jun. 2016.
[167] T. Lei, Y. Cao, Y. Fan, C. Liu, S. Yuan, and J. Pei, "High-Performance Air-Stable Organic Field-Effect Transistors: Isoindigo-Based Conjugated Polymers," pp. 6099–6101, 2011.
[168] I. Meager *et al.*, "Thieno [3 , 2- b] thiophene Flanked Isoindigo Polymers for High Performance Ambipolar OFET Applications," pp. 7109–7115, 2014.
[169] Y. Cheng, S. Yang, and C. Hsu, "Synthesis of Conjugated Polymers for Organic Solar Cell Applications," pp. 5868–5923, 2009.
[170] H. Zhou, L. Yang, and W. You, "Rational Design of High Performance Conjugated Polymers for Organic Solar Cells," 2012.
[171] Y. Liang *et al.*, "Highly Efficient Solar Cell Polymers Developed via Fine-Tuning of Structural and Electronic Properties," no. d, pp. 7792–7799, 2009.
[172] V. Vohra *et al.*, "Efficient inverted polymer solar cells employing favourable molecular orientation," *Nat. Photonics*, vol. 9, no. 6, pp. 403–408, May 2015.
[173] Z. He, C. Zhong, S. Su, M. Xu, H. Wu, and Y. Cao, "Enhanced power-conversion efficiency in polymer solar cells using an inverted device structure," vol. 6, no. September, pp. 591–595, 2012.
[174] Y. Liu *et al.*, "Aggregation and morphology control enables multiple cases of high-efficiency polymer solar cells," *Nat. Commun.*, vol. 5, no. 9, pp. 1–8, 2014.
[175] H. Hu *et al.*, "Terthiophene-Based D − A Polymer with an Asymmetric Arrangement of Alkyl Chains That Enables E ffi cient Polymer Solar Cells," 2015.
[176] T. E. Kang, K.-H. Kim, and B. J. Kim, "Design of terpolymers as electron donors for highly efficient polymer solar cells," *J. Mater. Chem. A*, vol. 2, no. 37, p. 15252, Jun. 2014.
[177] K. Kim, S. Park, H. Yu, H. Kang, I. Song, and J. H. Oh, "Determining Optimal Crystallinity of Diketopyrrolopyrrole-Based Terpolymers for Highly E ffi cient Polymer Solar Cells and Transistors," 2014.
[178] Y. Lin and X. Zhan, "Oligomer Molecules for Efficient Organic Photovoltaics," *Acc. Chem. Res.*, vol. 49, no. 2, pp. 175–183, Feb. 2016.
[179] W. Zhao *et al.*, "Molecular Optimization Enables over 13% Efficiency in Organic Solar Cells," *J. Am. Chem. Soc.*, vol. 139, no. 21, pp. 7148–7151, May 2017.
[180] W. Zhao *et al.*, "Fullerene-Free Polymer Solar Cells with over 11% Efficiency and Excellent Thermal Stability," *Adv. Mater.*, vol. 28, no. 23, pp. 4734–4739, Jun. 2016.
[181] K. H. Hendriks, G. H. L. Heintges, V. S. Gevaerts, M. M. Wienk, and R. A. J. Janssen, "High-Molecular-Weight Regular Alternating Diketopyrrolopyrrole-based Terpolymers for Efficient Organic Solar Cells," *Angew. Chemie Int. Ed.*, vol. 52, no. 32, pp. 8341–8344, Aug. 2013.
[182] H. Bronstein *et al.*, "Thieno[3,2- b]thiophene−Diketopyrrolopyrrole-Containing Polymers for High-Performance Organic Field-Effect Transistors and Organic Photovoltaic Devices," *J. Am. Chem. Soc.*, vol. 133, no. 10, pp. 3272–3275, Mar.

2011.
[183] E. Wang, Z. Zhang, K. Vandewal, P. Henriksson, F. Zhang, and M. R. Andersson, “An Easily Accessible Isoindigo-Based Polymer for High-Performance Polymer Solar Cells,” pp. 14244–14247, 2011.
[184] K. Kranthiraja *et al.*, “High-Performance Long-Term-Stable Dopant-Free Perovskite Solar Cells and Additive-Free Organic Solar Cells by Employing Newly Designed Multirole π-Conjugated Polymers,” *Adv. Mater.*, vol. 29, no. 23, p. 1700183, Jun. 2017.
[185] N. Zhou *et al.*, “All-Polymer Solar Cell Performance Optimized via Systematic Molecular Weight Tuning of Both Donor and Acceptor Polymers,” 2016.
[186] E. Zhou, J. Cong, Q. Wei, K. Tajima, C. Yang, and K. Hashimoto, “All-Polymer Solar Cells from Perylene Diimide Based Copolymers : Material Design and Phase Separation Control,” pp. 2799–2803, 2011.
[187] C. Lee *et al.*, “High-Performance All-Polymer Solar Cells Via Side-Chain Engineering of the Polymer Acceptor : The Importance of the Polymer Packing Structure and the Nanoscale Blend Morphology,” pp. 2466–2471, 2015.
[188] L. Huang *et al.*, “Ultralow-Power Near Infrared Lamp Light Operable Targeted Organic Nanoparticle Photodynamic Therapy,” pp. 6–11, 2016.
[189] C. L. Teoh *et al.*, “Chemical Fluorescent Probe for Detection of Aβ Oligomers,” *J. Am. Chem. Soc.*, vol. 137, no. 42, pp. 13503–13509, Oct. 2015.
[190] K. Tanaka and Y. Chujo, “Advanced Luminescent Materials Based on Organoboron Polymers,” pp. 1235–1255.
[191] A. Nagai, J. Miyake, K. Kokado, Y. Nagata, and Y. Chujo, “Highly Luminescent BODIPY-Based Organoboron Polymer Exhibiting Supramolecular Self-Assemble Structure,” pp. 15276–15278, 2008.
[192] B. M. Squeo *et al.*, “Ultra low band gap α,β-unsubstituted BODIPY-based copolymer synthesized by palladium catalyzed cross-coupling polymerization for near infrared organic photovoltaics,” *J. Mater. Chem. A*, vol. 3, no. 31, pp. 16279–16286, 2015.
[193] F. Li, Y. Chen, C. Ma, U. Buttner, K. Leo, and T. Wu, “High-Performance Near-Infrared Phototransistor Based on n-Type Small-Molecular Organic Semiconductor,” *Adv. Electron. Mater.*, vol. 3, no. 1, p. 1600430, Jan. 2017.
[194] I. Bulut *et al.*, “Rational Engineering of BODIPY-Bridged Trisindole Derivatives for Solar Cell Applications,” *ChemSusChem*, vol. 10, no. 9, pp. 1878–1882, May 2017.
[195] V. Leen, P. Yuan, L. Wang, N. Boens, and W. Dehaen, “Synthesis of Meso -Halogenated BODIPYs and Access to Meso -Substituted Analogues,” *Org. Lett.*, vol. 14, no. 24, pp. 6150–6153, Dec. 2012.
[196] Y. Hayashi, S. Yamaguchi, W. Y. Cha, D. Kim, and H. Shinokubo, “Synthesis of Directly Connected BODIPY Oligomers through Suzuki–Miyaura Coupling,” *Org. Lett.*, vol. 13, no. 12, pp. 2992–2995, Jun. 2011.
[197] A. Poirel, A. De Nicola, P. Retailleau, and R. Ziessel, “Oxidative Coupling of 1,7,8-Unsubstituted BODIPYs: Synthesis and Electrochemical and Spectroscopic Properties,” *J. Org. Chem.*, vol. 77, no. 17, pp. 7512–7525, Sep. 2012.
[198] L. Jiao *et al.*, “Regioselective Stepwise Bromination of Boron Dipyrromethene (BODIPY) Dyes,” 2011.
[199] A. B. Nepomnyashchii, M. Bröring, J. Ahrens, and A. J. Bard, “Synthesis, Photophysical, Electrochemical, and Electrogenerated Chemiluminescence Studies. Multiple Sequential Electron Transfers in BODIPY Monomers, Dimers, Trimers, and Polymer,” *J. Am. Chem. Soc.*, vol. 133, no. 22, pp. 8633–8645, Jun.

2011.
[200] B. M. Squeo *et al.*, “Progress in Polymer Science BODIPY-based polymeric dyes as emerging horizon materials for biological sensing and organic electronic applications,” *Prog. Polym. Sci.*, vol. 71, pp. 26–52, 2017.
[201] D. Cortizo-Lacalle *et al.*, “BODIPY-based conjugated polymers for broadband light sensing and harvesting applications,” *J. Mater. Chem.*, vol. 22, no. 28, p. 14119, 2012.
[202] B. Kim, V. R. Donuru, H. Liu, and J. M. J. Fre, “Bodipy-backboned polymers as electron donor in bulk heterojunction solar cells w,” pp. 4148–4150, 2010.
[203] W. He, Y. Jiang, and Y. Qin, “Synthesis and photovoltaic properties of a low bandgap BODIPY–Pt conjugated polymer,” *Polym. Chem.*, vol. 5, no. 4, pp. 1298–1304, 2014.
[204] Z. Xu *et al.*, “Vertical Phase Separation in Poly(3-hexylthiophene): Fullerene Derivative Blends and its Advantage for Inverted Structure Solar Cells,” *Adv. Funct. Mater.*, vol. 19, no. 8, pp. 1227–1234, Apr. 2009.
[205] M. Ozdemir *et al.*, “A new rod-shaped BODIPY-acetylene molecule for solution-processed semiconducting microribbons in n-channel organic field-effect transistors,” pp. 6232–6240, 2017.
[206] M. Yilmaz, M. Erkartal, M. Ozdemir, U. Sen, H. Usta, and G. Demirel, “Three-Dimensional Au-Coated Electrosprayed Nanostructured BODIPY Films on Aluminum Foil as Surface-Enhanced Raman Scattering Platforms and Their Catalytic Applications,” 2017.
[207] S. Subramaniyan, H. Xin, F. S. Kim, and S. A. Jenekhe, “New Thiazolothiazole Copolymer Semiconductors for Highly Efficient Solar Cells,” pp. 6245–6248, 2011.
[208] T. Lei, J. Dou, and J. Pei, “Infl uence of Alkyl Chain Branching Positions on the Hole Mobilities of Polymer Thin-Film Transistors,” pp. 6457–6461, 2012.
[209] H. Hu *et al.*, “Influence of fluorination on the properties and performance of isoindigo–quaterthiophene-based polymers,” *J. Mater. Chem. A*, vol. 4, no. 14, pp. 5039–5043, 2016.
[210] S. Shi, J. Yuan, G. Ding, M. Ford, K. Lu, and G. Shi, “Improved All-Polymer Solar Cell Performance by Using Matched Polymer Acceptor,” pp. 5669–5678, 2016.
[211] S. Lu *et al.*, “3,6-Dithiophen-2-yl-diketopyrrolo[3,2- b]pyrrole (isoDPPT) as an Acceptor Building Block for Organic Opto-Electronics,” *Macromolecules*, vol. 46, no. 10, pp. 3895–3906, May 2013.
[212] H. Hu *et al.*, “Influence of fluorination on the properties and performance of isoindigo-quaterthiophene-based polymers,” *J. Mater. Chem. A*, vol. 4, no. 14, pp. 5039–5043, 2016.
[213] X. Long, Z. Ding, C. Dou, J. Zhang, J. Liu, and L. Wang, “Polymer Acceptor Based on Double B←N Bridged Bipyridine (BNBP) Unit for High-Efficiency All-Polymer Solar Cells,” *Adv. Mater.*, vol. 28, no. 30, pp. 6504–6508, Aug. 2016.
[214] A. Zitzler-Kunkel, M. R. Lenze, K. Meerholz, and F. Würthner, “Enhanced photocurrent generation by folding-driven H-aggregate formation,” *Chem. Sci.*, vol. 4, no. 5, pp. 2071–2075, 2013.
[215] H. Kar and S. Ghosh, “J-aggregation of a sulfur-substituted naphthalenediimide (NDI) with remarkably bright fluorescence,” pp. 8818–8821, 2016.
[216] J. Y. Na, B. Kang, D. H. Sin, K. Cho, and Y. D. Park, “Understanding Solidification of Polythiophene Thin Films during Spin-Coating: Effects of Spin-Coating Time and Processing Additives,” *Sci. Rep.*, vol. 5, no. 1, p. 13288, Oct. 2015.

[217] X. Guo *et al.*, "Bithiopheneimide–Dithienosilole/Dithienogermole Copolymers for Efficient Solar Cells: Information from Structure–Property–Device Performance Correlations and Comparison to Thieno[3,4- c]pyrrole-4,6-dione Analogues," *J. Am. Chem. Soc.*, vol. 134, no. 44, pp. 18427–18439, Nov. 2012.
[218] S. G. J. Mathijssen *et al.*, "Dynamics of Threshold Voltage Shifts in Organic and Amorphous Silicon Field-Effect Transistors," *Adv. Mater.*, vol. 19, no. 19, pp. 2785–2789, Oct. 2007.
[219] M. Kastler *et al.*, "ARTICLES A high-mobility electron-transporting polymer for printed transistors," vol. 457, no. February, 2009.
[220] R. J. Kline, M. D. McGehee, E. N. Kadnikova, J. Liu, J. M. J. Frechet, and M. F. Toney, "Dependence of Regioregular Poly(3-hexylthiophene) Film Morphology and Field-Effect Mobility on Molecular Weight," *Macromolecules*, vol. 38, no. 8, pp. 3312–3319, Apr. 2005.
[221] R. P. Ortiz, H. Herrera, C. Seoane, J. L. Segura, A. Facchetti, and T. J. Marks, "Rational Design of Ambipolar Organic Semiconductors: Is Core Planarity Central to Ambipolarity in Thiophene-Naphthalene Semiconductors?," *Chem. - A Eur. J.*, vol. 18, no. 2, pp. 532–543, Jan. 2012.
[222] H. Sirringhaus *et al.*, "Two-dimensional charge transport in self-organized, high-mobility conjugated polymers," *Nature*, vol. 401, no. 6754, pp. 685–688, Oct. 1999.
[223] S. K. Hau, H. Yip, and A. K. Jen, "A Review on the Development of the Inverted Polymer Solar Cell Architecture," vol. 3724, 2010.
[224] K.-H. Kim, H. Kang, H. J. Kim, P. S. Kim, S. C. Yoon, and B. J. Kim, "Effects of Solubilizing Group Modification in Fullerene Bis-Adducts on Normal and Inverted Type Polymer Solar Cells," *Chem. Mater.*, vol. 24, no. 12, pp. 2373–2381, Jun. 2012.
[225] D. J. Kang, H. Kang, K. Kim, and B. J. Kim, "Nanosphere Templated Continuous PEDOT : PSS Films with Low Percolation Threshold for Application in E ffi cient Polymer Solar Cells," no. 9, pp. 7902–7909, 2012.
[226] H. Kang *et al.*, "Determining the Role of Polymer Molecular Weight for High-Performance All-Polymer Solar Cells: Its Effect on Polymer Aggregation and Phase Separation," *J. Am. Chem. Soc.*, vol. 137, no. 6, pp. 2359–2365, Feb. 2015.
[227] K. Gao *et al.*, "Multi-Length-Scale Morphologies Driven by Mixed Additives in Porphyrin-Based Organic Photovoltaics," pp. 4727–4733, 2016.
[228] J. Chen, L. Zhang, X. Jiang, K. Gao, F. Liu, and X. Gong, "Using o - Chlorobenzaldehyde as a Fast Removable Solvent Additive during Spin-Coating PTB7-Based Active Layers : High Efficiency Thick-Film Polymer Solar Cells," pp. 1–8, 2017.
[229] D. H. Wang, P.-O. Morin, C.-L. Lee, A. K. Ko Kyaw, M. Leclerc, and A. J. Heeger, "Effect of processing additive on morphology and charge extraction in bulk-heterojunction solar cells," *J. Mater. Chem. A*, vol. 2, no. 36, pp. 15052–15057, 2014.
[230] G. Zhang, Y. Fu, Q. Zhang, and Z. Xie, "Benzo[1,2-b:4,5-b′]dithiophene-dioxopyrrolothiophen copolymers for high performance solar cells," *Chem. Commun.*, vol. 46, no. 27, p. 4997, 2010.
[231] L. Huo, T. Liu, X. Sun, Y. Cai, A. J. Heeger, and Y. Sun, "Single-Junction Organic Solar Cells Based on a Novel Wide-Bandgap Polymer with Effi ciency of 9 . 7 %," pp. 2938–2944, 2015.
[232] H. Qin *et al.*, "Solution-processed bulk heterojunction solar cells based on a porphyrin small molecule with 7% power conversion efficiency," *Energy Environ.*

Sci., vol. 7, no. 4, pp. 1397–1401, 2014.
[233] G. Ren, E. Ahmed, and S. A. Jenekhe, "Non-Fullerene Acceptor-Based Bulk Heterojunction Polymer Solar Cells : Engineering the Nanomorphology via Processing Additives," pp. 946–953, 2011.
[234] P. Cheng, L. Ye, X. Zhao, J. Hou, Y. Li, and X. Zhan, "Binary additives synergistically boost the efficiency of all-polymer solar cells up to 3.45%," *Energy Environ. Sci.*, vol. 7, no. 4, pp. 1351–1356, 2014.
[235] J. Peet *et al.*, "Efficiency enhancement in low-bandgap polymer solar cells by processing with alkane dithiols," pp. 497–500, 2007.
[236] Z. Li *et al.*, "High Performance All-Polymer Solar Cells by Synergistic Effects of Fine-Tuned Crystallinity and Solvent Annealing," *J. Am. Chem. Soc.*, vol. 138, no. 34, pp. 10935–10944, Aug. 2016.
[237] G. Li, R. Zhu, and Y. Yang, "Polymer solar cells," vol. 6, no. MARCH, 2012.
[238] S. Mukherjee, C. M. Proctor, J. R. Tumbleston, G. C. Bazan, T.-Q. Nguyen, and H. Ade, "Importance of Domain Purity and Molecular Packing in Efficient Solution-Processed Small-Molecule Solar Cells," *Adv. Mater.*, vol. 27, no. 6, pp. 1105–1111, Feb. 2015.
[239] W. Ma, J. R. Tumbleston, M. Wang, E. Gann, F. Huang, and H. Ade, "Domain Purity , Miscibility , and Molecular Orientation at Donor / Acceptor Interfaces in High Performance Organic Solar Cells : Paths to Further Improvement," pp. 864–872, 2013.